The many faces of alpha synuclein:

From phospholipid bilayer interactions to amyloid aggregation

De vele gezichten van alfa synucleine:

Van fosfolipide dubbellaag interacties tot amyloïde aggregatie

Aditya Iyer

Members of the thesis committee

Prof. Dr. V. Subramaniam	University of Twente (Promotor)
Prof. Dr. ir. M.M.A.E Claessens	University of Twente (Co-promotor)
Prof. Dr. ir. J. van der Gucht	Wageningen University
Prof. Dr. D. F. Stamatialis	University of Twente
Prof. Dr. ir. P. Jonkheijm	University of Twente
Prof. Dr. J. Antoinette Killian	Utrecht University
Prof. Dr. T. J. Aartsma	Leiden University

The work described in this thesis is a part of a project titled "A Single Molecule View on Protein Aggregation" (Nr. 127) funded by Foundation for Fundamental Research on Matter (FOM) which is part of the Netherlands Organization for Scientific Research (NWO).
The research described in this thesis was carried out at:

1. Nanobiophysics group,
   MESA+ Institute for Nanotechnology
   Faculty of Science and Technology
   University of Twente
   P.O. Box 217
   7500 AE Enschede
   The Netherlands

UNIVERSITY OF TWENTE.

2. Nanoscale Biophysics group
   FOM Institute AMOLF
   Science Park 104
   1098 XG Amsterdam
   The Netherlands

FOM Institute AMOLF

ISBN: 978-90-365-4086-5
DOI: 10.3990/1.9789036540865

A digital version of this thesis is available at doc.utwente.nl and www.amolf.nl/publications/theses. Printed copies can be obtained by request to the library at FOM Institute AMOLF, library@amolf.nl

THE MANY FACES OF ALPHA SYNUCLEIN:

FROM PHOSPHOLIPID BILAYER INTERACTIONS TO AMYLOID AGGREGATION

DISSERTATION

to obtain

the degree of doctor at the University of Twente,

under the authority of the rector magnificus,

Prof. Dr. H. Brinksma,

on account of the decision of the graduation committee,

to be publicly defended

on Wednesday 6th of April 2016 at 16:45 h

by

Aditya Iyer

born on 22nd of December 1986

in Vapi, India

Dit proefschrift is goedgekeurd door:

Prof. Dr. Vinod Subramaniam en Prof. Dr. ir. Mireille Claessens

"A model is a lie that helps you see the truth"
– Howard Skipper

Table of Contents

1

Introduction

1.1 Protein (mis)folding and associated diseases

Proteins are integral components of every living cell; they give structure to cells or exert specific functions. Common examples include enzymes, molecular motors, receptors, hormones, cytoskeletal networks, exoskeletons and components of the extracellular matrix. The functional diversity of proteins is made possible by their three-dimensional structures, typically stabilized by non-covalent interactions and in some cases covalent bonds. Proteins are constantly synthesized and recycled/degraded in the cellular cytoplasm, both metabolic processes being tightly regulated. Synthesized from 20 different amino acids, the total number of endogenous proteins in humans has been estimated to be close to a million[1]. Typically, upon synthesis every protein folds spontaneously or with the help of chaperones into a structurally/functionally active three dimensional structure. The exception to this are intrinsically disordered proteins (IDPs), which approximately make up 30% of all mammalian proteins[2]. Upon synthesis, IDPs remain either entirely or partly unstructured and sample multiple conformations in the absence of binding partners[3,4]. A number of proteins involved in cellular processes such as cell-cell communication, growth, transcriptional regulation and apoptosis require the conformational flexibility that arises from this intrinsic structural disorder[5]. Given the abundance of IDPs in the cellular cytoplasm, their levels must be regulated to prevent non-specific interactions, and in many but not all cases, to prevent self association/aggregation. This is because not all IDPs are prone to aggregation but the ones that are aggregation-prone can contribute to the etiology of many diseases. Parkinson's disease (PD), Alzheimer's disease (AD), Huntington's disease (HD) are believed to be caused by abnormal accumulations and aggregation of the IDPs alpha synuclein (αS), tau and/or Aβ or huntingtin protein polyQ fragments respectively[6,7]. Such protein aggregates arise from intermolecular contacts when hydrophobic stretches are exposed and not protected by chaperones[8,9] and/or the protein is not degraded/removed by the ubiquitin-proteasome system (UPS)[10] or the autophagy system as shown in **Figure 1.1**.

Generally, self-aggregation of structurally ordered proteins requires partial or complete unfolding. IDPs are already unfolded which makes them more amenable to aggregation and which interferes with cellular processes. To circumvent this, cellular systems have evolved to contain a *proteostasis* network that mitigates accumulation of aggregated proteins which may arise from misfolding of ordered proteins or results from abnormal accumulation of IDPs[11]. A number of deficiencies in maintaining this *proteostasis* can arise from numerous factors like mutations, oxidative stress or chemical modifications in the involved proteostatic machinery or from an overload of aggregates. This can result in the accumulation of partially folded or misfolded proteins which can often no longer exert their specific biological function leading to degenerative protein misfolding diseases that fall into the category of "loss-of-function"

diseases like cystic fibrosis, familial hypercholesterolemia and 1-antitrypsin deficiency. Under some conditions, accumulation of IDPs or misfolded proteins leads to the formation of stable amorphous or fibrillar protein aggregates which are cytotoxic and result in most cases, cell death. These diseases fall into the category of "gain-of-toxicity" diseases.

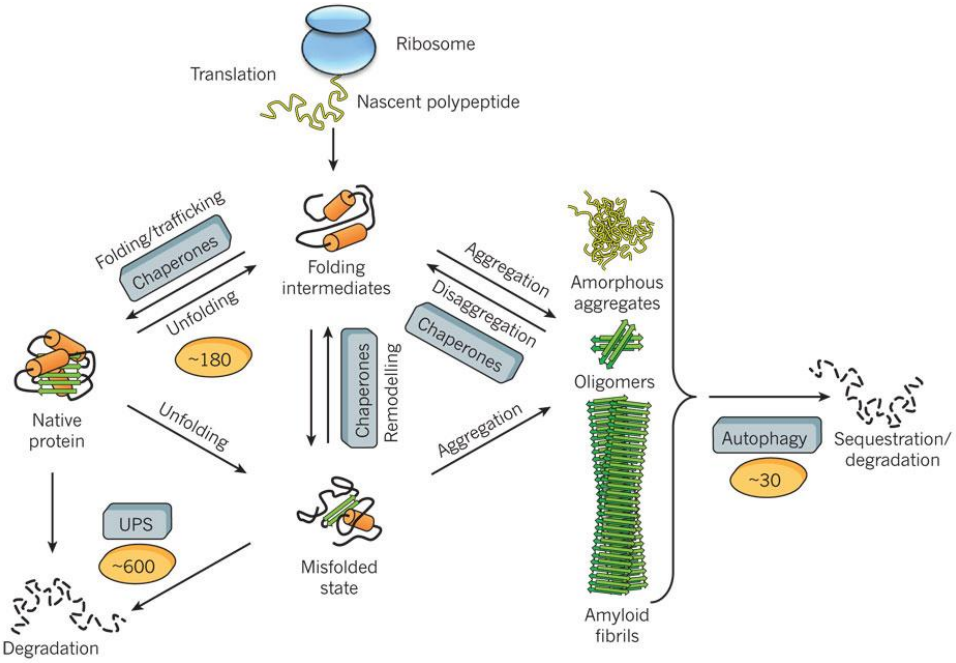

Figure 1.1: Fate of proteins in the proteostasis network. A number of cellular pathways including the ubiquitin-proteasome system (UPS) ensure minimal levels of misfolded proteins. Numbers in parenthesis indicate the approximate number of components comprising the system. Figure reprinted with permission from Hartl et al[11].

It is interesting to note that upon aggregation, a number of IDPs form "rod-like" fibrillar protein aggregates with a strikingly similar appearance. Several decades of research has shown that these similarities in fibrillar protein aggregates are unlikely to depend on the amino acid sequence of the proteins involved, but rather reflect common structural features in their organization[12,13]. Protein aggregates containing these structural features are broadly termed as "amyloids". A brief history of amyloids in discussed in the following section.

1.2 From generic amyloids to amyloids of alpha synuclein

The term "amyloid" as we use it today, refers in general to fibrillar protein structures typically ranging from 5-10 nm in width that have a characteristic cross β sheet secondary structure. Less than two centuries ago, amyloids were believed to be carbohydrates and their relevance to disease was believed to be circumstantial[14,15]. It was in 1859 when Friedreich and Kekulé showed that amyloid plaques mainly contained proteins, that the entire research attention shifted to the study of amyloids as *protein* aggregates[16] (**Figure 1.2**).

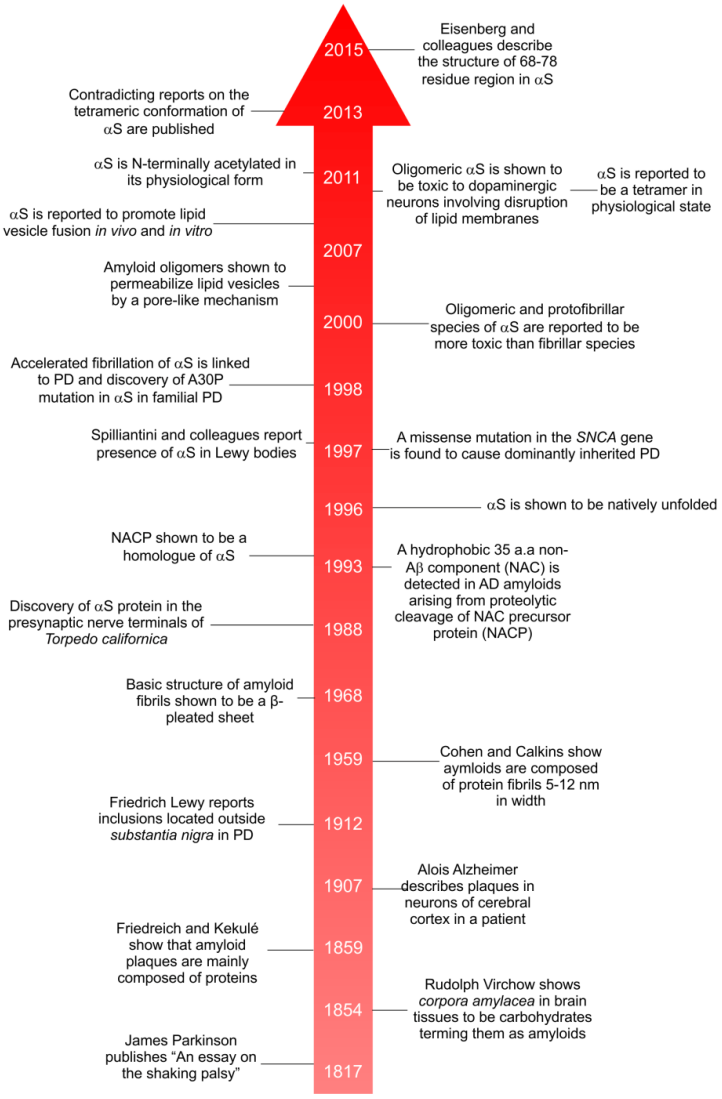

Figure 1.2: Timeline of selected events relating to amyloids.

The presence of amyloids was now thought to be a consequence of aging and other conditions including cancer and many auto-immune diseases rather than a cause of disease. In 1912, Friedrich Lewy described proteinaceous inclusion bodies in neurons of patients suffering from PD (which would later be recognized as a pathological hallmark of PD). More than 4 decades later, Cohen and Calkins, using electron microscopy showed that amyloids had a characteristic fibrillar ultra-structure with dimensions ranging between 50-120 Å in width[17]. Further studies showed

that amyloid fibrils, irrespective of their origin, were composed of even thinner fibrils designated as protofibrils[18,19]. The following year, the basic structure of amyloid fibrils was shown to be a β-pleated sheet[20]. Since then, numerous reports, using high resolution techniques like solid state nuclear magnetic resonance (ssNMR), magic angle spinning nuclear magnetic resonance (MAS-NMR), x-ray fiber diffraction (XRD) and two-dimensional infra-red spectroscopy (2D-IR), have tremendously fuelled the understanding of the amyloid state of numerous proteins. It is now known that amyloid formation is *not* a rare phenomenon associated merely with diseases but rather it defines a structurally and thermodynamically stable form of proteins. The amyloid fibril is an alternative to the native state, which can in principle be adopted by many, if not all, polypeptide sequences[21]. There are now about 50 known disorders with widely disparate symptoms each of which involve conversion of normally soluble and functional peptides/proteins (possessing a distinct secondary structure or intrinsically disordered) into amyloid fibrils[6]. An example of this is the aggregation of alpha synuclein (αS) in PD.

The protein αS was initially found in the synapse and in the nuclear envelope of the electric ray, *Torpedo californica*[22] in 1988 when proteins involved at the neurological synapse were being investigated. The connection of αS to neurodegenerative disorders was not established until the discovery of a distinct peptide component in the amyloid plaques in AD[23]. This ~ 35 amino acid peptide component was referred to as the non-Aβ component (NAC) which was shown to be generated from proteolytic cleavage of a 140 amino acid protein called NAC precursor protein, NACP (which was later shown to be a homologue of human αS[24,25]). The NAC peptide itself was shown to be highly amyloidogenic and antibodies raised against synthetic NAC peptides recognized amyloid fibrils in AD plaques[23,26]. NACP was subsequently described as a natively unfolded protein[27] that loosely associated with synaptic vesicles[25,28] and expressed abnormally in the presynpatic terminals of neuronal cells of the central nervous system in patients afflicted with AD[25,29].

The link between αS/NACP and PD was established in 1997, when a point mutation (A53T)[1] in the αS gene was identified in families with autosomal dominant PD[30] followed by the seminal discovery of αS as a major component of Lewy bodies from brain tissues of sporadic PD cases[31] and the positive immunostaining of these Lewy bodies with anti-NACP antibodies[32]. The following year, it was shown that αS in Lewy bodies was present as 5-10 nm thick filaments (αS amyloids), with αS monomers running parallel to the filament axis[33]. These discoveries triggered tremendous scientific interest in αS and the possible causality of αS aggregation in the development of PD. The following year, reports surfaced showing point

[1] A point mutation due to a single nucleotide substitution in the human αS gene leading to production of a αS variant in which the amino acid alanine at position 53 is substituted by threonine.

mutants of αS that accelerated fibril formation which could be directly linked early to onset of PD[34]. Further, triplication of αS gene was shown to cause PD[35] and it was found that mRNA levels of αS were consistently elevated in brains of both early onset familial PD[36] and idiopathic PD patients[37]. αS was also detected in several other neurodegenerative diseases, including multiple system atrophy (MSA), amyotrophic lateral sclerosis (ALS), dementia with Lewy bodies (DLB) and Hallervorden-Spatz syndrome. These diseases have now been collectively referred to as synucleinopathies[38]. Till today, 5 additional point mutations in the αS gene have been identified that lead to protein variants found in familial forms of PD: A30P[39], E46K[40], A53E[41], H50Q[42] and G51D[43]. Yet, finding the mechanism that causes cellular damage in PD remains a holy grail and the role of αS in the disease etiology is constantly debated.

1.3 αS amyloids and mechanisms of cellular toxicity

1.3.1 The "Janus" face of αS

It was already known that αS was a natively unfolded protein[27] prior to its discovery as a major component in Lewy bodies along with other proteins like ubiquitin, neurofilament proteins and lipids[44 31,33,45]. To explain the role of the conformational transition of αS from its disordered state to the fibrillar state to PD etiology, several mechanisms of αS mediated cellular toxicity and death have been postulated. These mechanisms can be grouped into two major classes: a toxic gain of function or a toxic loss of function both of which include failure of the ubiquitin-proteasome system (UPS), oxidative stress, impaired axonal transport and mitochondrial damage[38,46-55]. Although not established, given the intricacy of these cellular processes, these postulated mechanisms may not be mutually exclusive but could possibly act synergistically. Due to the synergy of different cellular processes, it has been difficult to pinpoint till date the intracellular location or pathway that is involved in the early stages of PD leading to neuronal cell death. Existing reports suggest contrasting roles of αS and are reminiscent of the mythological two-faced Roman god *Janus*. On one hand, the failure of the above mentioned cellular processes in both familial/idiopathic cases of PD[56,38,57] are shown to stem from the overexpression, point mutations and aggregation of αS into toxic pre-fibrillar/oligomeric/fibrillar species[58,59]. Amongst these factors, soluble oligomeric species of αS have been shown to be the most potent toxic species in both in vitro and in vivo systems[60-64]. On the other hand, a number of reports suggest that overexpression of αS *per se* and aggregation into soluble oligomeric species (formed in presence of dopamine) and fibrillar species could have a neuroprotective role in PD[38,53,65-67]. This neuroprotective role of αS is also supported by the fact that PD and the associated death of dopaminergic neurons can also

occur without formation of Lewy bodies[68,69], raising questions about the precise role of αS in PD.

The *Janus* face of αS is particularly evident in its interactions with cell membranes. On the one hand, interactions of αS with lipid membranes are thought to be necessary for cellular processes like synaptic vesicle fusion, regulation of the synaptic vesicle pool, regulation of phosphatidic acid (PA) synthesis and preventing lipid oxidation[70-72]. The sequence homology of αS to adipophilin/perilipin family of proteins that regulate lipid storage and metabolism also suggests a functional link to lipid membranes[73]. On the other hand, interactions with cell membranes have been suggested to trigger aggregation into (amyloid) oligomers which are shown to be toxic in vivo[74,75] and permeabilize cell membrane mimicking lipid vesicles[76-79]. The aggregation of αS into oligomers can occur with/without membranes but it is not clear if aggregation initiates from the unstructured or membrane-bound state of the protein.

Although the role of αS remains debated in the physiological environment, both function and toxicity seem to involve interactions with cellular membranes. Interactions of αS relating to its putative functional role seem to be intricately dependent on their interactions with lipid membranes whilst the very same interactions can apparently lead to cell death. The membrane-associated state of αS is thus likely of great significance to both its physiological function and its role in PD etiology.

1.4 αS and phospholipid membrane interactions

Full length monomeric αS comprises of 140 amino acids and consists of three major structural regions: an N-terminal region comprising of amino acid residues that are believed to involved in lipid membrane binding, a hydrophobic NAC region required for aggregation and more recently found necessary in defining the affinity of αS for lipid membranes[80], and a negatively charged C-terminus (95-140) that is highly unstructured and experiences weak and transient interactions, if any, with model lipid membranes[80] (**Figure 1.3**). The C-terminus is also known to modulate aggregation of αS into amyloids[81-83] and contains sites that can be post-translationally modified by e.g. nitration and phosphorylation[84-86]. The N-terminal residue (methionine) of αS was recently shown to be acetylated in its physiological form[87,88] and αS has been reported to exist as a stable tetramer resisting aggregation[87,89]. Subsequent reports from other labs have not been able attest to the existence of a αS tetramer and the subject remains a matter of debate[88,90].

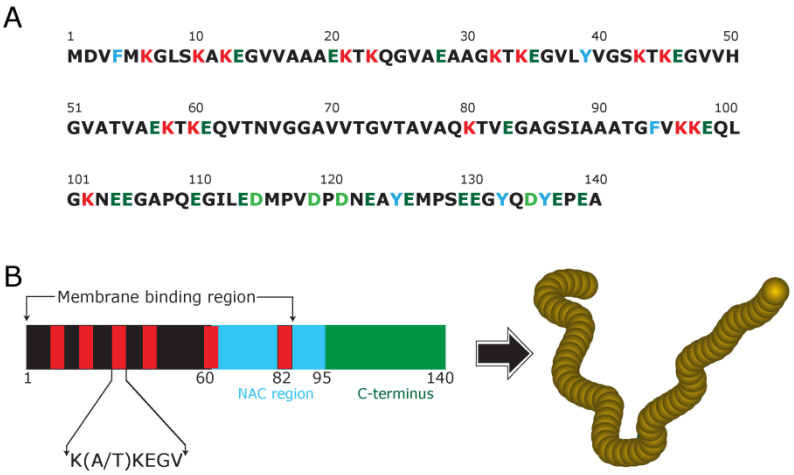

Figure 1.3: Amino-acid sequence and domains in αS. A) αS primary amino acid sequence (top panel) with acidic (green), lysine (red) and aromatic (light blue) residues highlighted. B) Schematic representation of αS with amphipathic repeats housed in the membrane binding region, Non-Amyloid β Component (NAC) region and the acidic region (green). The bottom right panel shows a pictorial representation of the disordered state of the protein.

The loose association of αS to lipid bilayers with reported dissociation constants in micromolar ranges *in vivo* is counter-intuitive because of the presence of imperfect 11-amino acid residue repeats that resemble those found in strongly membrane binding apolipoproteins. These repeats contain a K(A/T)TKEGV consensus that is consistent with the capacity to fold into an amphipathic helix[91]. It has been proposed that the weak affinity of αS for membranes could hint at a regulatory role of αS in maintenance of a lipid vesicle pool at the synapse[71,92,93]. The equilibrium between the membrane-bound and free state of αS is tightly regulated and approximately 15% of αS is bound within membranes at the synaptic termini[50,94].

Association of the unstructured monomeric αS with phospholipid membranes is accompanied by a dramatic increase in the helical content (from 3% to ~ 80%)[91]. In a report by Eliezer and colleagues in 2001, αS was shown to assume a bipartite structure with residues 1-102 bound to SDS micelles while the remaining residues remaining disordered[95]. The conformation of the membrane-bound helical segment of αS has been a matter of debate as to whether it is a fully extended helix[96-98], a broken helix[99,100] or co-existence of both[101]. It seems that a range of structural architectures probably due to variable helix break positions[97] between these two conformations may be sampled by αS. It has been shown by NMR that αS binds to lipid bilayers via distinct binding modes[102] that can be tuned by changing the lipid-to-protein ratio.

1.4.1 Physicochemical properties of lipids aiding αS membrane interaction

There is now strong evidence that the population of the lipid-bound state of αS is regulated not only by the intrinsic structural properties of αS but also by the exact chemical composition

and physical properties of the phospholipid bilayer, such as anionic charge, curvature and packing defects, phase state and degree of hydration[91,99,103-105].

1.4.1.1 Anionic charge density

The preferential binding of αS to negatively charged surfaces like anionic lipid membranes in comparison to neutral surfaces is attributable to electrostatic attractions from multiple lysine residues found in its N-terminus. The involvement of electrostatics is corroborated by studies showing reduced αS binding to anionic lipid vesicles with increasing ionic strengths[106] and enhanced αS binding to phosphatidic acid (PA) and phosphatidylinositol(PI) from bovine liver lipids that have a slightly higher negative charge compared to phosphatidylserine (PS) and phosphatidylglycerol (PG)[105-108].

1.4.1.2 Membrane curvature

It has been argued that membrane binding of αS is not purely mediated by electrostatic interactions but also involves hydrophobic interactions of αS regions with the acyl chain[91]. The membrane binding region of αS stays at the interface of the headgroup and acyl chains while the NAC domain is shown to penetrate deeper into the apolar acyl chain region[109]. The curvature sensitivity of αS probably stems from the presence of packing defects in lipid vesicles that increase as the vesicle diameter approaches the lipid bilayer thickness. Small unilamellar vesicles (SUVs) that are ~ 25-40 nm in diameter are well known to bind αS better than large unilamellar vesicles (LUVs). Interestingly, αS not only binds preferentially to curved lipid membranes but has also been shown to *induce* local curvature and cause remodeling in lipid membranes[110,111]. Similarly, increasing the fraction of inverted cone-shaped lipids wherein the acyl chains occupy a larger area than their headgroups like phosphatidylethanolamine (PE) in anionic lipid vesicles enhance binding of αS[106,112].

1.4.1.3 Membrane phase state

The lipid acyl chain has been shown to enhance αS-lipid membrane binding as well. Compared to saturated lipids, binding of αS to membranes of unsaturated lipids of the same length is higher because of a relatively lower lipid packing density and reduced screening of the apolar acyl chains[108].

1.4.1.4 Specific interactions

Besides its preference for binding negatively charged phospholipid bilayers, αS has been shown to interact specifically with sphingolipids like GMs by forming a hydrogen-bonded network between its side chains and hydroxyl groups[113,114]. More recently, it was shown that the physiological form of αS is N-terminally acetylated[87,115] and this post-translational

modification improves αS binding to GM lipids[116]. Reports have also indicated the presence of a cholesterol binding domain in αS[117].

1.4.2 Lipid membranes: sites of αS amyloid assembly or αS function?

Interactions of globular proteins with hydrophobic or charged surfaces exposing different functional groups can induce local or extensive protein unfolding[118,119]. IDPs like αS bind membranes and contain hydrophobic amino acid patches that can potentially aggregate on the membrane due to the high effective concentration on the lipid membrane. This high effective concentration may speed up their aggregation rate which is often limited by slow nucleation[120]. The aggregation kinetics and the morphology of the resulting aggregates of amyloid forming IDPs has been shown to be influenced by both charged and hydrophobic surfaces like mica, gold, graphite and Teflon[121-124]. Aggregation of αS on mica (a hydrophilic substrate) led to fibril growth along two directions separated by 120°. These two directions probably reflect the pseudo-hexagonal geometry of mica. αS aggregation under similar conditions on highly oriented pyrolytic graphite, HOPG (a hydrophobic substrate) resulted in spheroidal aggregates[121] as depicted in **Figure 1.4**.

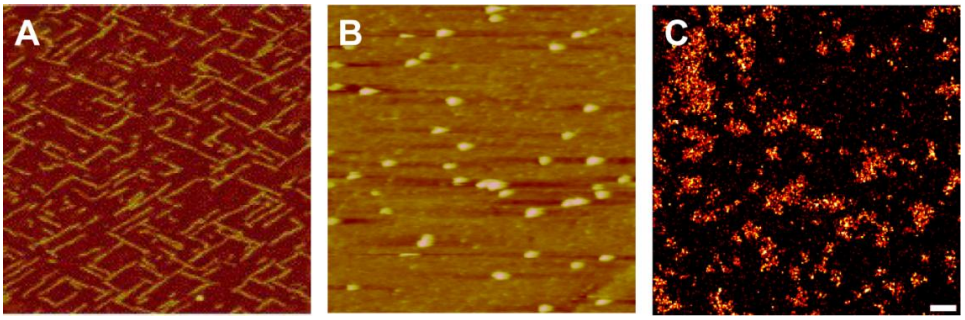

Figure 1.4: Influence of type of surface on the morphology of αS amyloid aggregates. The above panels are AFM images (in solution) of αS aggregates obtained on mica (panel A) and highly oriented pyrolytic graphite, HOPG (panel B). Panel C shows super-resolution images of AlexaFluor 647 labeled αS amorphous aggregates on POPC:POPG supported lipid bilayers. The scale bar is 1 μm. Panels A and B (1 μm x 1 μm) are reprinted with permission from Hoyer et al[121]. Panel C (10 μm x 10 μm) was obtained in collaboration with Pim van den Berg at the University of Twente, Enschede, The Netherlands using dSTORM technique.

Aggregation of αS monitored on POPC:POPG supported lipid bilayers visualized using super-resolution (dSTORM) microscopy (**Figure 1.4**,**panel C**) appears to result in amorphous aggregates. Although αS has been show to aggregate into amyloid fibrils on other surfaces, membrane-bound αS has not been observed to aggregate into amyloid fibrils with a typical "rod-like" morphology on lipid membranes even at saturating concentrations but rather form amorphous aggregates[125-127]. A recent study has shown that αS fibrils can bind cell membranes of both neuroblastoma cell lines and hippocampal primary neurons and induce cell

death when endogenous αS monomers are additionally present[128]. The apparent amorphous morphology of the αS aggregates on lipid membranes suggests that the conformation of αS in the monomeric state can influence the structure and morphology of the resulting aggregates. The aggregation of αS in presence of lipid membranes also depends on degree of unsaturation and acyl chain length. Polyunsaturated fatty acids (PUFAs) are found abundantly in neuronal membranes and are shown to promote αS aggregation while saturated lipids inhibit αS oligomerization in living mesenchephalic neurons[74]. Thus not only interactions of αS with lipid membranes, but also the lipid composition plays a relevant role in the aggregation process.

Akin to artificial solid surfaces, interactions of proteins with lipid membranes, apart from partially restricting their conformational dynamics and possibly aiding aggregation, can lead to localized protein clustering and formation of lipid domains with distinct properties that forms the basis of the biochemical functioning and signaling of a lot of proteins in living cells[129-134]. Accordingly, the association of αS to raft-like membrane micro-domains (typically *liquid-ordered*) composed of cholesterol and sphingomylein has been linked to its function in eukaryotic cells[114,86,135]. However, *in vitro* observations indicate selective binding of αS to *liquid-disordered* regions in anionic lipid membranes[108,136]. This discrepancy between *in vivo* and *in vitro* observations remains unsolved. Typically, raft-associated proteins like the amyloid precursor protein or prion proteins have transmembrane domains, a feature lacking in αS[114] which may suggest distinct mechanisms of interaction and function.

Taken together, the wealth of data obtained in the last two decades points towards a cloudy scenario wherein lipid membranes could aid αS aggregation by creating an environment that enhances early aggregate assembly. αS aggregates that form either in solution or on cell membranes have been shown to result in cellular dysfunction and even cell death. The effect of lipid membranes on the aggregation rate of αS remains controversial to date with many unanswered questions. What makes an amyloid aggregate toxic: its structure/morphology or its interactions with lipid membranes? How do early interactions of lipid membranes with αS trigger aggregation of αS and in turn how do such early aggregates impact lipid membranes? What are the cellular triggers for aggregation of αS? A better knowledge of the formation of early αS aggregates preceding the appearance of mature fibrils is pertinent in understanding the etiology of the pathological nature of early αS aggregates/amyloids associated not only with PD, but also with other neurodegenerative conditions involving amyloids.

1.5 Outline of the thesis

Despite extensive studies on amyloid formation of αS in bulk solution, αS aggregation at biological interfaces like lipid membranes remains far from understood. Interactions of αS with phospholipid membranes have been increasingly thought to be crucial in the pathogenic aggregation of αS into amyloid structures and therefore understanding the basic mechanisms behind these interactions are crucial. In this work, I aim to investigate the early interactions of monomeric αS with model phospholipid membranes. In particular, we focus on the following questions:

- How are physical properties of phospholipid membranes affected by αS binding and aggregation and vice versa?
- How do early amyloid aggregates of αS perturb phospholipid membranes?
- What is the role of N-terminal acetylation in αS on its membrane binding properties and aggregation propensities?
- How do electrostatic interactions affect the morphology of αS amyloid aggregates?

These questions are key to understand the fundamental biophysical interactions of αS with phospholipid membranes. The inherent compositional complexities in biological membranes and unknown function of αS in cellular cytoplasm are likely to occlude our ability to unravel the details of the fundamental physicochemical interactions between αS and lipid membranes and the potential role of these interactions in PD. Understanding the fundamental physical chemistry behind these interactions requires controlled model phospholipid membrane systems which I chose to work with in this thesis.

To answer these questions, supported lipid bilayers (SLBs) were chosen as model lipid system and I used a wide range of *in vitro* biochemical and biophysical techniques to probe interactions with αS. Given, the fragile nature of lipid membranes and difficulties associated with preparing defect-free SLBs, stable preparations of SLBs are necessary to be able to draw conclusions from experiments with αS. Rigorous optimization of SLB preparation and characterization using confocal fluorescence microscopy and fluorescence recovery after photobleaching experiments was primarily done to ensure this as described in **Chapter 2**.

First we probed for changes in the physical properties of lipid membranes upon interactions of monomeric αS with SLBs. Using fluorescence anisotropy and FRAP experiments we show how lipid order and effective lateral lipid diffusion in SLBs are affected as a result of αS interaction and discus their significance in detail in **Chapter 3**.

To better understand the role of αS amyloid formation in phospholipid membrane damage, we looked at monomeric αS interactions with SLBs at longer timescales. We observe amyloid formation to be dependent of the protein-to-lipid ratios and anionic charge fraction in SLB.

Our results point towards the requirement of amyloid structure for phospholipid membrane damage and the details of the possible damage mechanism and its significance are discussed in **Chapter 4**.

During the realization of experiments in **Chapter 4**, it was reported that αS is N-terminally acetylated in its physiological environment in eukaryotic cells. We obtained αS not only from recombinant expression in *E.coli* (with and without N-terminal acetylation), but also endogenous protein from human red blood cells. The role of this modification in αS on binding to phospholipid membrane binding and aggregation into amyloid fibrils was investigated in **Chapter 5**.

To better understand aggregation of αS on phospholipid membranes, it is essential not only to study the interplay of αS and phospholipid membranes, but also the aggregation in the absence of phospholipid membranes. To probe the influence of terminal regions of αS on its aggregation, we investigated the structural features of amyloid fibrils prepared from truncated variants of αS (**Chapter 6**) and discuss their implications on fibril structure and morphology.

In the final chapter of this thesis, we summarize and discuss all results obtained and suggest future directions.

1.6 Acknowledgements

I wish to thank Dr. Wolfgang Hoyer from Universität Düsseldorf for providing original high resolution images for **Figure 1.4 (panel A-B)**.

2

Supported lipid bilayers: preparation & characterization

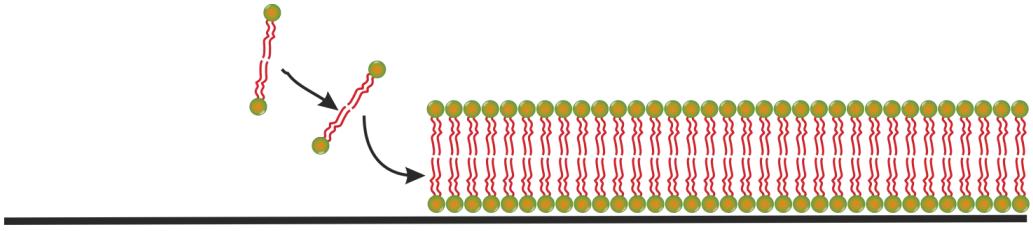

2.1 Introduction

Biological membranes are ubiquitous elements in all living cells that are essential for the very existence of life. For the unique properties and functions of membranes, lipid molecules are as important as proteins. The predominant lipid species of biological membranes are anionic and zwitterionic phospholipids (varying in acyl chain lengths, headgroups and saturation), sphingolipids (also with various modifications) and cholesterol. Every phospholipid molecule has a polar (headgroup) and a non-polar segment (composed of fatty-acids) covalently linked to a glycerol moiety via an ester bond as shown in **Figure 2.1** (**left panel**). Fatty-acids are long chain hydrocarbons (saturated/unsaturated) with a carboxyl group. The length of these fatty-acids and the degree of unsaturation (presence of double bonds between carbons) can vary in a single phospholipid molecule. The length of these fatty-acids determines the thickness, and the degree of unsaturation determines the phase behavior of the resulting bilayer. Covalent attachment of polar groups like phosphatidylcholine, phosphatidylserine, phosphatidylglycerol, sugar groups etc to the glycerol backbone imparts water solubility. Phospholipids usually have two fatty-acids and the third position on the glycerol occupied by a polar headgroup. Often cellular systems use sphingosine (a long-chain amine) instead of glycerol for the above chemistry, resulting in sphingolipids. This large lipid compositional heterogeneity is thought to play a role in the modulation of relevant physical properties of natural membranes and influences the lateral segregation of lipids therein. Currently, models of biological membranes are unclear on the existence of certain nano-domains or so-called 'rafts', in live cell membranes. Cholesterol and sphingolipids are now known to be enriched in these rafts, leading to a local membrane structure that is thought to play a role in membrane-protein sorting and the formation of signaling complexes[137].

The aforementioned amphiphilic nature of phospholipid molecules results in hydrophobic attraction which drives their assembly. Whether lipids self assemble into planar bilayers, micelles, or cubic phases depends on their shape. The shape of lipid molecules resembles cylindrical rods with a typical cross-sectional area of 0.65 nm^2 and an average length between 1 and 3 nm. The effective shape of a lipid molecule determines its ability to form a stable lipid bilayer. This is described by a packing parameter called P, where

$$P = \frac{v}{a * l}$$

and *a* represents the cross sectional area of the headgroup region, *v* represents the volume occupied by the non-polar segments and *l*, the length of the non-polar segment.

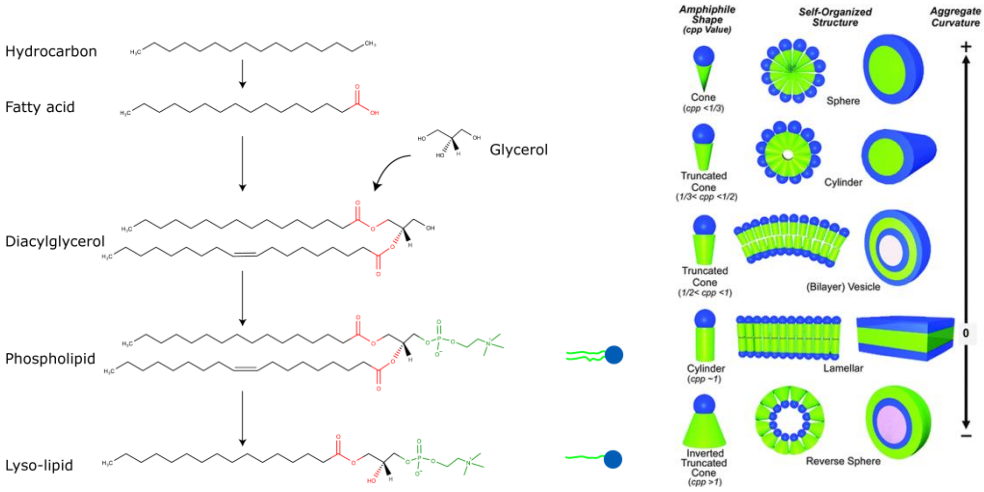

Figure 2.1: Phospholipid structure and influence of shape on self-assembled structures. The left panel indicates the structural aspect of a lipid molecule and the right panel shows how variation in the packing parameter P, or shape of the lipid molecule, results in the self-assembly of structures with different geometries. The figure (right panel) depicts different structures that result at different packing parameters. Figure (right panel) is reprinted with permission from Ramanathan et al[138].

As shown in **Figure 2.1** (**right panel**)**,** for an ideal cylinder P=1 and lipid molecules with such packing parameters (for example DOPC) preferably form planar bilayers. Lipids having P>1 (for example DOPE) tend to form inverse cones while lipids having P<1 (lysophosphocholine, LPC) tend to form cones. The larger the difference of P from unity, the higher the stress when monolayers of these lipids are forced into planar structures.

When lipid bilayers self-assemble on solid supports they are referred to as supported lipid bilayers (SLBs)[139]. SLBs are very practical membrane model systems and of scientific interest as they can easily be prepared onto large areas of solid substrates (in the order of cm^2), which provide excellent mechanical stability, while the lipids in the bilayer maintain their mobility[140]. This characteristic of SLBs is the reason for their extensive use to explore lipid-protein interactions in model cell membranes[125,141-145]. SLBs also allow the realization of experiments which are difficult to perform/interpret with black lipid membranes or spherical vesicle systems. Such free-standing membranes may e.g. interfere with unraveling certain membrane damage mechanisms, as the line tension of the edge of a membrane defect or pore ensures defect closure. In SLBs, interactions with the underlying surface and the fixed membrane surface area will prevent defect closure[146]. Considering the cytoskeletal support of many membranes *in vivo*, SLBs may also give better insight into possible membrane disruption mechanisms.

The preparation of SLBs is fairly straightforward when zwitterionic lipids are used. A solution of lipid vesicles incubated over cleaned glass substrates results in the formation of uniform and homogeneous SLBs. Model lipid compositions mimicking biological membranes often

contain a significant fraction of anionic lipids. In this case, repulsive electrostatic forces between the anionic lipid headgroups and the negatively charged glass substrates are large, making SLB preparations difficult. Considering that the preparation of SLBs of anionic lipids is challenging, I will describe this tricky preparation procedure in detail in this chapter.

2.2 Lipids used to mimic biological membranes

The type of lipids used for preparing SLBs typically depends on the research question. SLBs are formed to mimic cellular lipid compositions and the exact composition of biological membranes in eukaryotic cells remains unclear. This arises from the fact that eukaryotic cell membranes are asymmetric, and typically contain hundreds of different lipids. Additionally the lipid composition of eukaryotic membranes is highly dynamic[147] and can vary with environmental stresses like temperature, light and salt availability[148,149]. Even sub-cellular organelles differ both quantitatively and qualitatively in their lipid composition[150]. Measurements on purified membranes to delineate the composition of different eukaryotic cellular membranes provide approximations[150,151] for the composition. The use of model membrane compositions mimicking either the anionic charge fraction, cholesterol content or membrane phase of biological membranes has provided tremendous insights into various biological mechanisms involving lipid membranes[125,127,144,152-158].

To vary the surface charge densities in SLBs, membranes containing a fraction of lipids with charged headgroups like POPG or POPS have been used. Membrane compositions mimicking anionic charge fraction of the inner leaflet of the plasma membrane typically contain 20-30% of anionic lipids supplemented with neutral lipids like POPC. By varying the chain length and chain unstauration, the phase behavior of lipids can be controlled, and changes in phase behavior in the presence/absence of proteins have been used to elucidate lipid-protein interactions. Below a certain temperature (called phase transition temperature, T_m), lipids in a bilayer have a regular structure as in a crystalline solid while above the T_m, lipids are positionally disordered as in a liquid. Such states are called solid-ordered and liquid disordered phases respectively. The phase change of lipid bilayers (between liquid ordered and disordered states) has also been used to understand formation of lipid nanodomains (often called rafts) and protein function[114,135,137,158]. In plasma membranes, cholesterol and phospholipids are reported to be present in an equimolar concentration[151] though most studies use equimolar concentrations of cholesterol, sphingolipids and phosphatidylcholine to mimic the plasma membrane composition[136,158-161]. Simpler plasma membrane mimics use between 20-30% of POPS, a lipid molecule found extensively in the inner plasma membrane leaflet, in combination with a zwitterionic lipid. Some lipids are found preferentially in certain cellular organelles; an example is cardiolipin which is found mainly in mitochondrial membranes[162]. Model liposome systems mimicking these entities have employed such lipids[79,163,164].

Functionalization of lipids (both headgroup/chain) including biotinylation, His-tagging, coupling to fluorophores, and PEGylation have paved the road towards understanding mechanistic aspects of the functioning of trans-membrane proteins[165], ion channels[166,167], membrane active proteins[168], and receptor signaling[169]. The analysis of physical membrane properties including the determination of the diffusion coefficient of lipids in the SLB has contributed to unraveling the how these proteins fulfill their function. A list of commonly used lipids for preparing model phospholipid SLBs is given in **Table 2.1**.

Table 2.1: Commonly used lipids in SLB preparation

	Lipid Type	Structure	Net Charge
Phosphatidylcholine (PC)	POPC	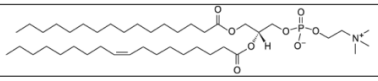	0
	DOPC	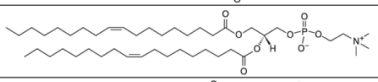	0
	DPPC	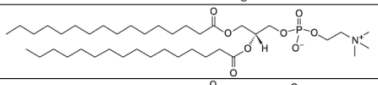	0
Phosphatidylglycerol (PG)	POPG	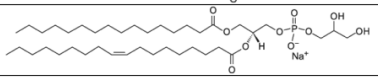	-1
	DOPG	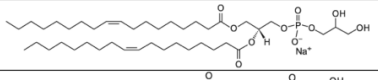	-1
	DPPG	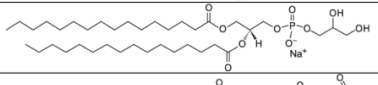	-1
Phosphatidylserine (PS)	POPS	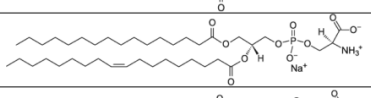	-1
	DOPS	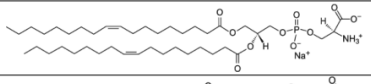	-1
	DPPS	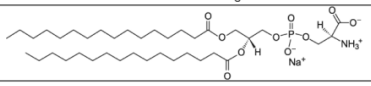	-1
Fluorescent lipids			
NBD-PC Excitation/Emission : 460/534 nm		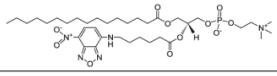	0
NBD-PS Excitation/Emission : 460/534 nm		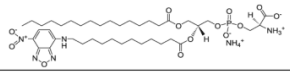	-1
Lissamine Rhodamine-PE Excitation/Emission : 560/583 nm		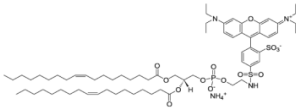	-1
BODIPY-PC Excitation/Emission : 500/550 nm		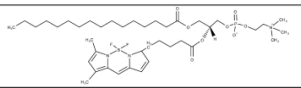	0

2.3 Methods of lipid vesicle preparation

Lipid vesicles are lipid bilayers that are closed upon themselves to form spherical shells. Depending on the number of lipid bilayers, they are categorized as either unilamellar vesicles (composed of single lipid bilayer) or multi-lamellar vesicles (composed of multiple lipid bilayers). Sonication of multi-lamellar vesicles (MLVs) results in generation of small unilamellar vesicles (SUVs) while extrusion of MLVs through polycarbonate filters results in large unilamellar vesicles (LUVs) as outlined below in **Figure 2.2**. The preparation of GUVs is not described in this chapter and shall be discussed later on in the thesis.

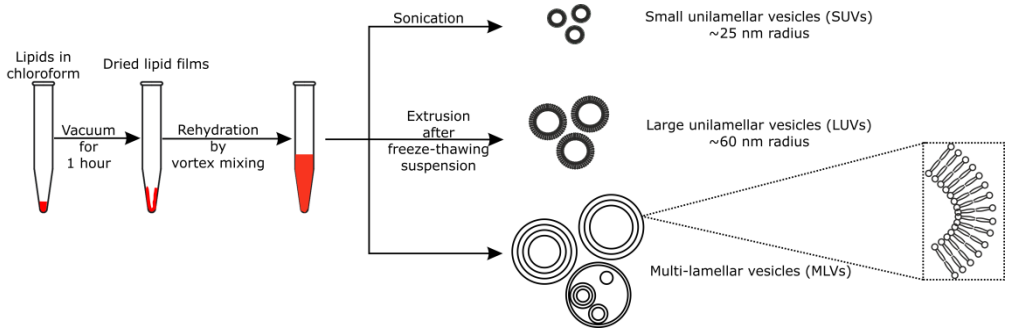

Figure 2.2: Basic strategy for preparation of lipid vesicles. A typical protocol is shown for preparation of lipid vesicles used in this thesis.

In general, the preparation of lipid vesicles involves the evaporation of the organic solvents (typically pure chloroform or mixtures of methanol: chloroform) in which the lipid (mixture) is dissolved followed by rehydration in the desired buffer. Thereafter, depending on the size/type of the lipid vesicles required, protocols diverge.
A typical protocol for the preparation of lipid vesicles is outlined below:

1. Lipid mixtures of the desired composition in organic solvents are transferred into a clean glass vial using glass syringes and dried under a slow stream of nitrogen making a uniform film on the glass vial wall. *Rehydration of non-uniform films can lead to formation of lipid clumps and might result in a low liposome yield at the end of the LUV preparation procedure. It is necessary to use an inert gas (Nitrogen/Argon) in this step to prevent lipid oxidation. Oxidized lipids can change physical/chemical properties of lipid bilayers which interfere with exploring lipid-protein interactions.*
2. The dried lipid films are then kept under vacuum for about an hour. Typical pressures for vacuum are ~ 0.1-0.5 bar. *This step is critical to formation of stable lipid membranes as residual levels of chloroform can lead to undesirable effects such as unstable lipid vesicles or lipid clumps/particles in the resulting SLBs.*

3. This step is followed by rehydration into the desired buffer followed by vortex mixing the sample which leads to the formation of multi-lamellar vesicles (MLVs). The resulting suspension will be cloudy due to light scattering by MLVs. A s*ufficiently high ionic strength (at least 75 mM NaCl) and low pH (~ 6.0) of the rehydration buffer is necessary to prepare stable SLBs when working with lipid mixtures containing a significant fraction of anionic lipids. This requirement will be discussed in detail later*.
4. To prepare small unilamellar vesicles (SUVs), the resulting suspension is sonicated using a tip sonicator until the suspension becomes clear. Sonification of the solution for an hour with sonication amplitudes of 25% and a pulse on/off time of 15/15 seconds was optimal for all liposomal preparations in this thesis. *During sonication, heating up of the suspension should be avoided to prevent lipid oxidation by carrying out sonication in an ice-bucket, preferably in a cold room*.
5. For preparation of large unilamellar vesicles (LUVs), the resulting cloudy suspension is freeze-thawed multiple times until it becomes clear. The clear suspension is now extruded using 100 nm polycarbonate filters at least 11 times to obtain the final LUV solution. *Persistent cloudiness in the suspension after freeze-thawing is an indication of incomplete evaporation of organic solvent or vesicle aggregation due to the presence of a considerable concentration of divalent cations (~ mM)*. *Use of excessive force during extrusion (likely resulting from improper assembly of extrusion chamber or high concentrations) should be avoided to prevent filter rupture.*
6. Contact with ambient air should be minimal at all times. LUVs should not be stored more than a week. SUVs are inherently unstable due to their high degree of curvature and will spontaneously fuse to form larger vesicles when stored below their phase transition temperatures.

2.4 Formation of SLBs

2.4.1 Apparatus

A chamber for preparation and imaging of SLBs, shown in **Figure 2.3A,** was constructed with assistance from Dr. Chandrashekhar Murade, a post-doctoral colleague. Drilled glass slides were annealed with appropriate tubing using epoxy glue. Using a parafilm cut-out between the glass slide and cleaned glass supports, the resulting chamber was assembled by heating for 2 minutes at ~ 70 ^{o}C to ensure that the parafilm glues to the glass slide. This approach is efficient since it allows us to reuse the glass slides; the chamber can be disassembled by heating it again and simply peeling off the parafilm from the underlying glass supports. These chambers were used in all experiments in this thesis unless specified otherwise (**Figure 2.3B**). Every chamber had a rectangular area of 2.5 cm^2 and could hold 120 µl.

To cover the available area we estimated that a lipid concentration of ~ 10 µM was required assuming an average lipid headgroup area of 0.65 nm^2.

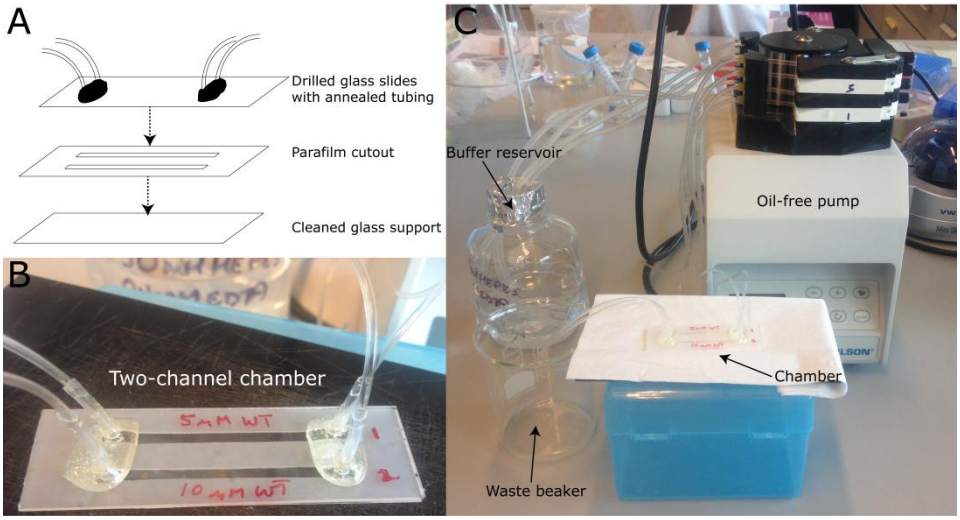

Figure 2.3 : Custom-built chamber and apparatus for SLB formation. A) Strategy used to build an imaging chamber for SLBs. B) The resulting chamber after annealing parafilm with glass substrates. C) The set-up for SLB preparation consisting of an oil-free pump used to control the flow-rate of buffers from the reservoir to the chamber.

The formation of SLBs is typically carried out using lipid vesicles as outlined in **Figure 2.4** below where lipid vesicles are mixed with the final buffer to desired concentrations and immediately added to glass supports cleaned as described in **section 2.6.3**. After a brief incubation period, unbound vesicles are washed away and the resulting SLBs can be used for further experiments. This strategy works very well for lipid vesicles prepared in deionized water if the lipids are zwitterionic or the final composition contains less than 5 mol% anionic lipids[140]. Preparation of SLBs containing 50 mol% anionic lipids (POPG in our optimization experiments) was non-trivial. Existing strategies reported in the literature were not reproducible in our hands and thus SLB formation had to be optimized.

Taking the approach outlined in **Figure 2.4**, we tested the influence of pH, ionic strength, lipid concentration, and substrate cleaning methodologies systematically in order to reproducibly get stable and homogeneous SLBs.

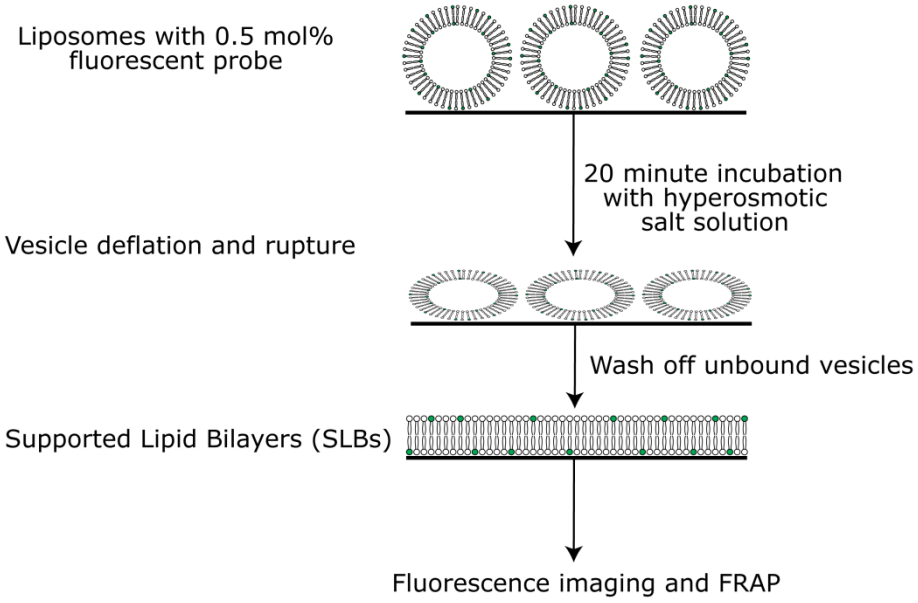

Figure 2.4: Typical strategy for formation of supported lipid bilayers (SLBs).

2.4.2 Influence of pH and ionic strength on SLB formation

It has been shown that spreading of phospholipid bilayers with a net negative charge on glass surfaces depends on pH and ionic strength[141]. The screening of the like charges of the substrate and lipid headgroups at high ionic strengths allows more vesicles to adsorb to the substrate. First the influence of pH was tested. POPC:POPG lipid vesicles were prepared in 100 mM NaCl solution (pH adjusted to 7.4) and were mixed in a 1:1 ratio with 1M NaCl solution (pH adjusted to 7.4) just before incubation on glass slides. The formation of POPC:POPG (1:1) SLBs under these conditions was not possible even upon deflating the vesicles using 1 M NaCl in the incubation fusion step at pH 7.4. Under these conditions, lipid vesicles added to glass supports remained unfused as demonstrated by the inability of the lipids to diffuse into photo-bleached areas of the SLBS (**Figure 2.5, top panel**). In contrast, lipid vesicles deflated in a pH 6.0 solution containing 1M NaCl did fuse into homogeneous SLBs in which the lipids were mobile. Thus, for all further preparations for POPC:POPG (1:1) SLBs, the initial fusion step was carried out at pH 6.0 accompanied with a high ionic strength.

After SLB formation at pH 6.0, switching the buffer pH to 7.4 did not influence the integrity of the SLBs. The SLBs remained homogeneous and the lipids stayed completely mobile. However, neutral lipids are not influenced by these conditions and form homogeneous SLBs irrespective of pH and ionic strength.

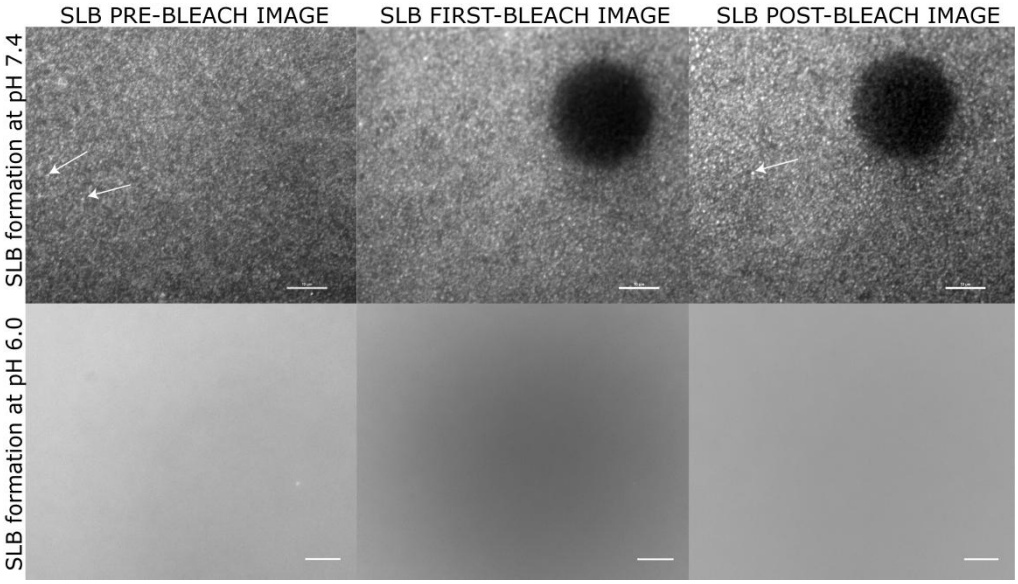

Figure 2.5: Importance of pH during SLB formation. The upper panels show fluorescent images of POPC:POPG (1:1) SLBs prepared at pH 7.4 in presence of 1M NaCl after which the buffer was switched to 50 mM HEPES, 0.1 mM EDTA, 100 mM NaCl, pH 7.4. We observed fluorescent spots (white arrows) which are most likely unfused vesicles. These are immobile as seen from the non-recovered regions in images obtained post-bleaching. The lower panels show fluorescent images of POPC:POPG (1:1) SLBs prepared at pH 6 in presence of 1M NaCl. After the SLB preparation step, the buffer was switched to 50 mM HEPES, 0.1 mM EDTA, 100 mM NaCl, pH 7.4. In this case, the lipids in the SLBs are so mobile that the bleached spot is difficult to see due to the immediate fluorescence recovery in the bleached spot. 0.5 mol% NBD-PC was incorporated in the liposome preparations for visualization of SLBs. The scale bar is 10 μm.

The results presented in **Figure 2.5** indicate that for mixtures containing more anionic lipids, the strategy to prepare the lipid vesicles in a salt containing buffer and carrying out the SLB formation at pH ~ 6.0 works. It is necessary to not only work at high ionic strength but also have a low pH to because at neutral pH, silanol groups on glass supports can deprotonate (SiO^- + H^+) and the glass surface becomes negatively charged[170] leading to increased electrostatic repulsions between the glass and vesicles. The low pH of ~ 6.0 is not expected to have a large effect on lipid charge since the pKa of POPG is ~ 3.0.

Next, we checked the influence of NaCl on the SLBs formed at pH 6 in fluorescence microscopy experiments. Briefly, 250 μM lipid vesicles were incubated on glass supports (cleaned by sonication in 2% Hellmanex® solution at 70 °C) for 20 minutes in the absence (**Figure 2.6A**) or presence (**Figure 2.6C**) of 1M NaCl solution (1:1 ratio).

After the washing step to remove unbound vesicles, we observed patches of SLBs in the absence of NaCl at pH 6.0 while the presence of NaCl ensured homogeneous SLBs. Interestingly, addition of 750 mM NaCl to the SLB patches formed in the absence of NaCl (**Figure 2.6B**) led to fusion but the SLB still contained lipid-free regions likely due to scarcity of attached lipid vesicles. In the SLB experiments NaCl was used instead of divalent cations

because calcium ions are reported to cluster POPG vesicles[143]. These results indicate that rupturing of anionic lipid vesicles that adhere to the glass occurs at low pH while fusion requires high osmotic gradients probably ensuring the deflation of lipid vesicles. The thus prepared SLBs were found to remain stable at buffer flow rates up to 150 µl/min. Higher flow rates of buffer resulted in membrane disruption.

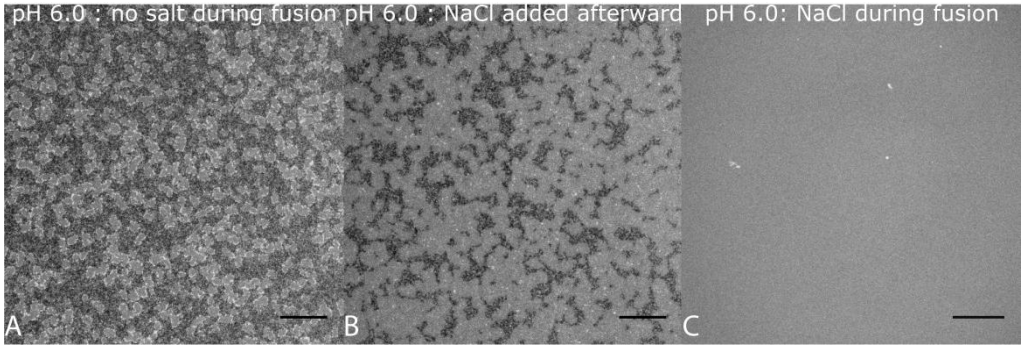

Figure 2.6: Influence of ionic strength for SLB formation. The above images show fluorescent images obtained upon addition of POPC:POPG (1:1) lipid vesicles on glass supports. When these lipid vesicles are prepared in deionized water (~ pH 6) and added to glass supports, patches of SLBs (high fluorescence intensity along edges are probably unfused vesicles see Figure 2.8) are seen. Addition of 750 mM NaCl to these SLBs results in the disappearance of intact vesicles and fusion of the SLB patches as shown in panel B. Preparation of lipid vesicles in a 100 mM NaCl containing solution and incubation on glass slides in a 1:1 ratios with 1 M NaCl leads to formation of homogeneous SLBs (panel C). The scale bar is 10 µm.

We observed an interesting effect of the net ionic strength on the formation of SLBs. Low ionic strengths (< 300 mM NaCl final concentration) during the formation of SLBs (at pH 6.0) lead to formation of defects in the resulting SLBs after switching the buffer to a pH of 7.4 (**Figure 2.7A**), while high ionic strengths (>600 mM NaCl final concentration) during the formation of SLBs (at pH 6.0) lead to formation of caps/buds in the resulting SLBs after switching the buffer to a pH of 7.4.

SLBs formed at low ionic strengths probably lead to incomplete fusion causing defects in the resulting SLBs. The defects are circular rather than rugged which is a consequence of the tendency of lipid bilayers to minimize line tension. Intermediate values of NaCl reproducibly resulted in homogeneous SLBs (**Figure 2.7B**). In SLBs formed at high ionic strengths the negative charge on the lipid headgroups are screened by counter-ions. Upon switching to a lower ionic strength buffer the headgroup repulsion increases giving rise to thinner bilayers. The excess area that results from this thinning possibly leads to budding of the SLBs. The inset in **Figure 2.7C** shows ring like structures which decrease in size as the focus is moved up in Z direction. A z-stack depicting the three-dimensional structures on SLBs is shown later in the thesis.

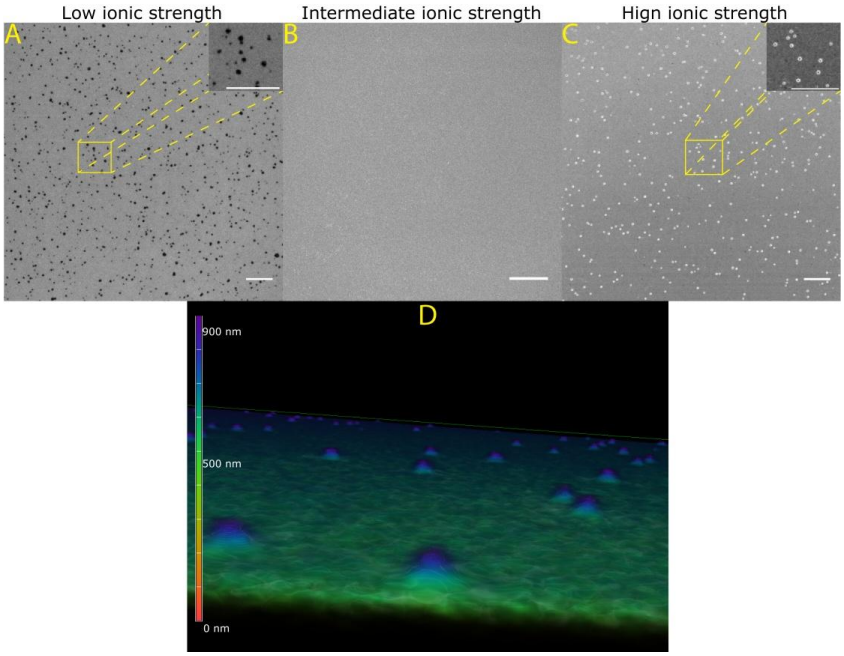

Figure 2.7: Influence of ionic strengths during SLB formation. Representative fluorescent images of POPC:POPG SLBs doped with 0.5 mol% BODIPY-PC. Incubation of liposomes was performed at varying ionic strengths and then the buffer was switched to a 50 mM HEPES, 0.1 mM EDTA, 100 mM NaCl buffered at pH 7.4 before imaging. At low ionic strengths (< 300 mM NaCl), SLBs presented defects (inset in panel A). At intermediate ionic strengths (between 300-500mM NaCl), SLBs were homogeneous while at higher ionic strengths (> 500 mM NaCl), curved three-dimensional structures resulted on the SLB surface (inset in panel C). Panel D shows a z-stack of SLBs with caps/buds (~ 800 nm in height) prepared at high ionic strengths. SLBs were fluid under all conditions as tested by FRAP. The scale bar is 10 μm.

2.4.3 Influence of lipid concentration

To optimize the pH and ionic strength for SLB formation, a very high concentration of lipid vesicles was used to ensure complete bilayer coverage. For obtaining a continuous SLB, it is critical to use a sufficient amount of lipid vesicles. To economize the lipid concentration used, we varied the lipid concentration to get the minimal concentration required for homogeneous SLB formation. As mentioned earlier, the lipid concentration corresponding to the chamber dimensions was ~ 10 μM. Addition of twice the theoretical concentration was therefore assumed to be sufficient since liposome fusion conditions were optimized as outlined in the previous section. However, we observed that for POPC:POPG (1:1), a nearly 10-fold higher lipid concentration was required for homogeneous (without cracks and islands) SLBs as shown in **Figure 2.8**.

At concentrations lower than ~ 120 μM, homogeneous SLBs were seldom observed. It is interesting to note that at low concentrations of lipids, SLB patches were seen throughout the chamber and lipid vesicles could be seen sticking to the edges supporting the fact that SLB edges are known to enhance vesicle adhesion and induce vesicle rupture, leading to the

formation of continuous SLBs[171]. For the preparation of SLBs with a high fraction of anionic lipids, an excess of lipid vesicles is thus needed to ensure maximal coverage.

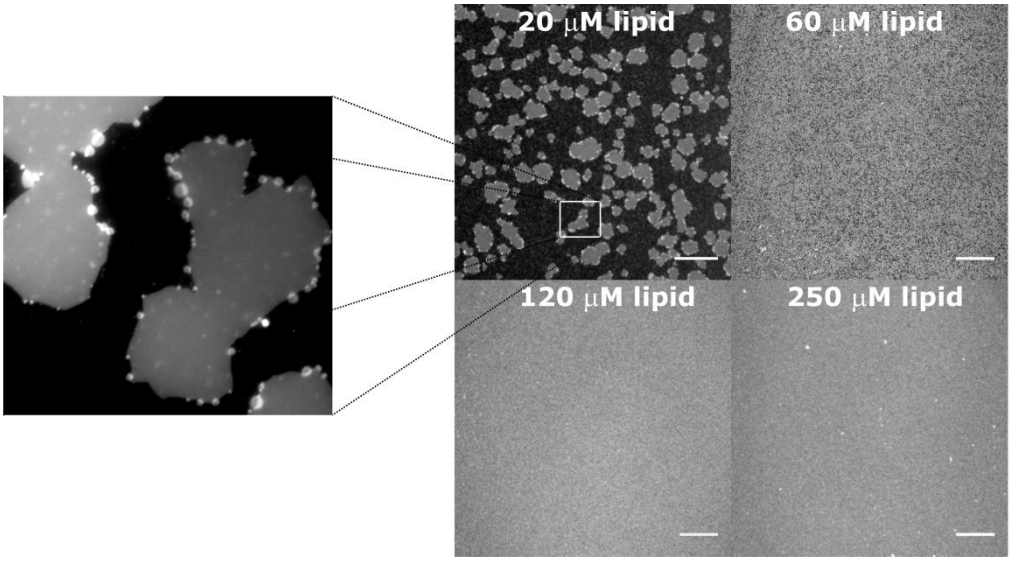

Figure 2.8: Effect of lipid concentration on formation of POPC:POPG (1:1) SLBs. The above confocal fluorescence images show patchy and non-homogeneous SLBs at 20 μM and 60 μM respectively. At low concentrations lipid vesicles are seen stuck to lipid bilayer patches (zoomed left panel image from a random area). Lipid vesicle concentrations ≥ 120 μM lead to formation of uniform SLBs. All experiments were carried out in 50 mM HEPES, 0.1 mM EDTA buffered at pH 7.4 and measured at room temperature. The scale bar is 10 μm.

2.5 Characterization of SLBs

After successful preparation of defect-free POPC:POPG SLBs, the next step was to characterize the two-dimensional lateral lipid diffusion. The macroscopic fluidity of biological lipid membranes is a property that is related to the diffusion coefficient of individual lipid molecules and is affected by the packing order of the lipid constituents[172]. Other factors that can affect lipid membrane fluidity include headgroup charge, acyl chain saturation, phase state and the presence of cholesterol. The presence of a solid substrate introduces a frictional barrier that may hinder the free diffusion of lipids and thus, prior to use of SLBs, it is critical to ensure that lipids are fluid in the formed SLBs.

2.5.1 Fluorescence Recovery After Photobleaching (FRAP)

Fluorescence recovery after photobleaching (FRAP) is a much used tool for quantifying the translational dynamics of biological molecules *in vitro*[152,153] and *in vivo*[173,174]. Available on most commercial confocal laser-scanning microscope systems, it can be used to address a number of questions regarding continuity of membrane compartments, cell division, protein localization and activity, protein interactions and dynamics with other cellular components

within a living cell to name a few. FRAP and associated techniques (fluorescence loss in photobleaching (FLIP), and inverse FRAP (iFRAP) are ideal for determining kinetic properties, including the diffusion coefficients, mobile fractions, and transport rates of target molecules in live-cell imaging. FRAP experiments rely on selectively photobleaching the fluorescence within a region of interest with a high-intensity laser, followed by monitoring the diffusion of new fluorescent molecules into the bleached area over a period of time with low-intensity laser light. Powerful single molecule techniques like (fluorescent) single particle tracking and fluorescence correlation spectroscopy have recently been developed but require sensitive instrumental setups with highly efficient cameras and detectors. The relatively simple and straightforward FRAP technique, being a bulk fluorescence technique, does not face so many technical challenges. The quantitative evaluation of the FRAP curve is however not straightforward because a number of parameters in FRAP experiments influence the obtained diffusion coefficients[175-179], making data interpretation challenging. The type of fitting model used to obtain the diffusion coefficient and the bleaching time[180] are the most critical parameters, while others like bleach radius[181], sampling rate (based on the Nyquist criterion) and attenuation ratios are less critical. It is thus important to reduce all sources of uncertainty and error in any FRAP measurement.

2.5.1.1 Type of fitting model

In order to extract diffusion coefficients from the FRAP measurements on POPC:POPG SLBs doped with 0.5 mol% NBD-PC, the fluorescence recovery curves were initially fitted with a single exponential following the assumption that we only had single diffusing fluorescent species. Data fitting revealed that a single component exponential fit could not properly fit the few initial points in the recovery curve (blue curve in **Figure 2.9A**). The possibility that the inability to fit the first part of the FRAP curve was an effect of the surface influencing lipid diffusion in the lower membrane leaflet (resulting in two components) was excluded by sodium dithionite experiments as mentioned in **section 2.8**. Thus, we opted for an alternative fitting procedure and followed the Soumpasis model[181,182] for fitting the fluorescence recovery data with circular bleach area. This model has been shown to be better than single exponential models for calculating lipid diffusion coefficients[183]. To test if the Soumpasis model was indeed better, the same raw data was fitted to both exponential and Soumpasis models. It was noted that the Soumpasis model consistently fitted the raw data better than the exponential fits (**Figure 2.9A**). As can be seen in the residuals, the Soumpasis model did include the first data points correctly. The diffusion coefficients extracted from the Soumpasis fit were consistently higher (~ 1.5 fold) than those obtained for a single exponential fit for the same raw data (**Figure 2.9B**) at any given bleach radius.

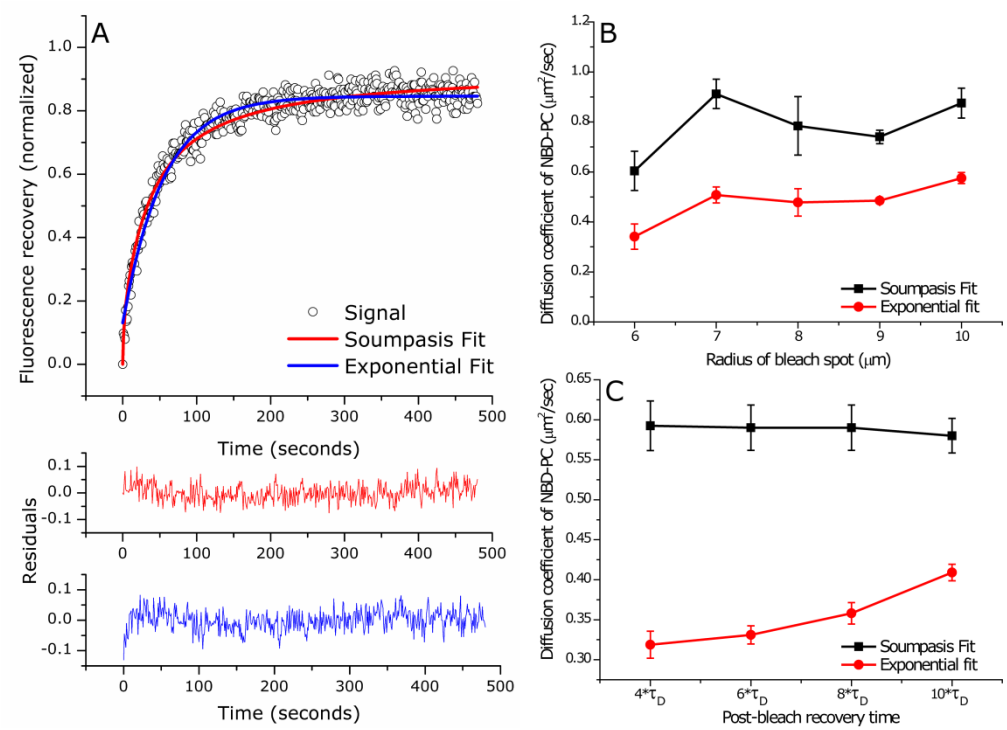

Figure 2.9: Comparison of fitting of raw FRAP data using two different fitting equations. A) Comparison of fitting models to obtain diffusion coefficients. A single exponential fit (blue curve) is not able to fit the early part of the data while the Soumpasis fit (red curve) is better. B) Effect of bleach radius on $D_{NBD\text{-}PC}$. POPC:POPG SLBs doped with 1 mol% NBD-PC were made in 50 mM HEPES, 0.1 mM EDTA buffer at pH 7.4 at room temperature. The radius of the bleach spot was varied as shown keeping the recovery time at $10*\tau_D$ (300 seconds). The same raw data was used to fit with either a Soumpasis fit or an exponential fit. C) Effect of post-bleach recovery time on $D_{NBD\text{-}PC}$. POPC:POPG SLBs doped with 1 mol% NBD-PC were made in 50 mM HEPES, 0.1 mM EDTA buffer at pH 7.4 at room temperature. The radius of the bleach spot was 8 μm. The error bars represent standard deviations obtained from 6 individual measurements on the same SLB in different regions.

Bleach radius strongly affects the recovery time in FRAP experiments since the characteristic diffusion time (τ_D) depends on the square of the bleach radius. Very small values of bleach radius (< 2 μm) will lead to noisy data affecting the obtained values of diffusion coefficients while larger bleach radii might require additional tweaking of bleach time. This is because larger bleach radii will require longer post-bleach recovery times. The post-bleach recovery time is another important parameter for fitting for FRAP curves. The typical recovery times should be at least 10-50 times the τ_D as suggested in earlier literature. To optimize the post-bleach recovery time, the fluorescence recovery data was acquired for at least 5 more minutes after the fluorescence recovery curve reached a plateau. Then, the recovery curves were fit by systematically reducing the time-points fitted until the obtained diffusion coefficient started to change. Values of diffusion coefficients obtained from Soumpasis fits are reported to be independent of the post-bleach recovery time in contrast to values obtained

from single exponential fits. To test this, post-bleach recovery times were varied for FRAP data for 8 μm bleach radius (**Figure 2.9C**) and indeed values obtained from the Soumpasis model do not depend on the post-bleach recovery time for a circular bleached spot. Thus, the use of Soumpasis model for fitting FRAP data should be preferred when absolute values of diffusion coefficients are important and when using a circular bleached spot. The change in bleach radius does not affect values of diffusion coefficient obtained which arises from lipid diffusion being a bulk property. All FRAP data in further experiments were thus fitted using a Soumpasis fit with bleach radius of 8 μm and a recovery time of 300 seconds ($10*\tau_D$) throughout the thesis unless mentioned otherwise. A number of other models have been proposed for fitting FRAP recovery data for both circular/non-circular bleach profiles and have been extensively reviewed recently[184].

2.5.1.2 Bleaching time

The bleach time in any FRAP experiment is a critical parameter as it influences the values of diffusion coefficients obtained. Longer bleaching times (resulting in the formation of coronas due to diffusion of bleached molecules into the area around the bleached spots) may result in loss of information if multiple (fast and slow) diffusing species are present[180]. Bleaching should be typically carried out at high laser powers (typically 100mW) within times that are much shorter (at least 20-fold) than the characteristic diffusion time (τ_D) of the probe in question. This is important as it avoids significant probe diffusion while bleaching. Diffusion during bleaching can result in under-sampling of fluorescence recovery leading to an underestimation of the diffusion coefficients. Bleaching times are therefore supposed to be as low as possible for any given FRAP experiment. A simple way to test if bleach times are short enough is to do image analysis on the first post-bleach image to determine the *effective radius* of the photo-bleached (circular) area. Deviations in the effective radius from the input values of bleach radius necessitate the optimization of bleach times or attenuation ratios (ratio of laser power at bleaching/laser power for acquisition) in case of instrumentation limitations. The bleach time was varied systematically during FRAP measurements and its influence on $D_{NBD\text{-}PC}$ in POPC:POPG (1:1) SLBs was probed, keeping the bleach radius constant (8 μm). As expected (**Figure 2.10**), higher bleach times resulted in lower values of $D_{NBD\text{-}PC}$ for the same SLB. Thus bleach times should be as low as possible. All FRAP data in further experiments were acquired with the bleach time of 1 second ($0.05*\tau_D$) unless mentioned otherwise.

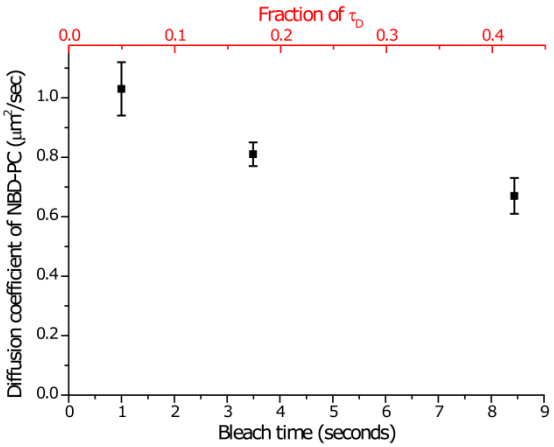

Figure 2.10: Influence of bleach time on the diffusion coefficient of NBD-PC. Values of D_{NBD-PC} in POPC:POPG SLBs obtained at different bleach times in FRAP experiments. The bleach times are also shown as a fraction of characteristic diffusion times τ_D calculated to be (top red X-axis) SLBs were prepared in 50 mM HEPES, 0.1 mM EDTA buffer at pH 7.4 at room temperature. Bleach radius was kept constant (8 µm) during the FRAP experiment. The error bars represent standard deviations obtained from 5 individual measurements on the same SLB.

Overall, the fitting model, bleach time, bleach radius and the post-bleach recovery time are the most important parameters for FRAP experiments. The best way to optimize these parameters is to first choose a bleach radius giving optimal signal/noise ratio. Next, vary the bleach time and keep it as low as possible by adjusting the attenuation ratios (sampling rates maybe increased although this will increase noise as well). And lastly, optimize the post-bleach recovery time as mentioned before.

2.6 Influence of substrate cleaning on SLB homogeneity

The final optimization step was to increase the stability of SLBs since the POPC:POPG SLBs prepared on glass supports (cleaned as outlined in **Section 2.6.1**) were susceptible to defect formation after 12-18 hours in 50 mM HEPES, 0.1 mM EDTA buffer at pH 7.4 at room temperature. To enhance the stability of SLBs over time, different glass substrate cleaning protocols were tested.

2.6.1 Pre-treatment with Hellmanex/ICN detergent: Protocol 1

Glass supports obtained from manufacturers are usually covered with dust and residual organic components. Sonication is used to get rid of dust particles but to improve cleaning and increasing wetting properties of glass supports, commercial detergents such as ICN 7X detergent (MP Biomedicals, USA) or Hellmanex® cleaning solutions (Hellma, Germany) are typically used. Glass slides were immersed in these cleaning solutions; 1% solutions (Hellmanex®) or diluted 7-fold (ICN 7X detergent), heated up to 70 °C, and sonicated for 90 minutes. Both detergents worked equally well and pre-treatment of the slides with either

of these reagents did not influence the fluidity and homogeneity of the resulting POPC:POPG (1:1) SLBs. The SLBs on detergent cleaned glass slides were defect-free (**Figure 2.11, Protocol 1**) but remained so only for 12-18 hours. We therefore introduced other/additional cleaning steps to enhance the stability of SLBs as outlined in the further sections.

2.6.2 Argon Plasma cleaning: Protocol 2

Cleaning of glass substrates with ionized plasma has been shown to be very effective for removal of organic contaminants. Ionized plasma, consisting of argon ions and electrons are generated by a strong electrical field and then accelerated by external radio frequency (RF) waves. Argon plasma is deep purple in color and emits intense ultraviolet light in a low-pressure environment (~ 200 mTorr). The collision of ionized plasma with glass surfaces increases the amount of silanol (Si-OH) groups promoting surface hydrophilicity[170,185]. The plasma cleaning protocol used here is outlined below:

i. Glass supports were first sonicated in deionized water for 5 minutes and dried under a stream of nitrogen.
ii. Next, the pre-treated slides were exposed to argon plasma for 15 minutes at 200 mTorr and then immediately transferred and stored in deionized water.
iii. After sonicating for 5 minutes, the glass supports were used for SLB formation.

On the glass slides treated with this protocol the SLBs were inhomogeneous and contained immobile patches (**Figure 2.11, Protocol 2**). It is possible that intense plasma exposure resulted in increased surface roughness preventing formation of SLBs.

2.6.3 Piranha etching: Protocol 3

Upon the failure to obtain homogeneous SLBs on surfaces cleaned with argon plasma, we resorted to cleaning glass supports by using an additional acid piranha etching step after the pre-treatment step described in **section 2.6.1**. Piranha solution is prepared by adding hydrogen peroxide to sulfuric acid (1:3) and should be done so only under a laminar hood with extra handling precautions. Due to the strong dehydrating power of sulfuric acid, the addition of hydrogen peroxide is highly exothermic. In general, the temperature of freshly prepared piranha solution can reach 100 °C in <1 minute. Atomic oxygen, an extremely reactive oxygen free radical generated by dehydration of hydrogen peroxide, rapidly and thoroughly oxidizes the organic compounds on the glass surface. Furthermore, atomic oxygen increases the number of silanol groups (SiOH) on the glass surface[170,186]. Polar silanol groups form hydrogen bonds with vicinal water molecules and promote surface hydrophilicity[170,187]. At neutral pH, silanol groups deprotonate ($SiO^- + H^+$) and the glass surface becomes negatively charged[170]. Extended piranha cleaning may result in a small increase in the roughness of glass surfaces[188]. Preparation of POPC:POPG SLBs yielded homogeneous and fluid SLBs on piranha

cleaned glass substrates according to Protocol 3. The D_{NBD-PC} in these POPC:POPG (1:1) SLBs on was ~ 2-fold higher than that obtained on SLBS on surfaces cleaned by Protocol 1 (**Figure 2.11**).

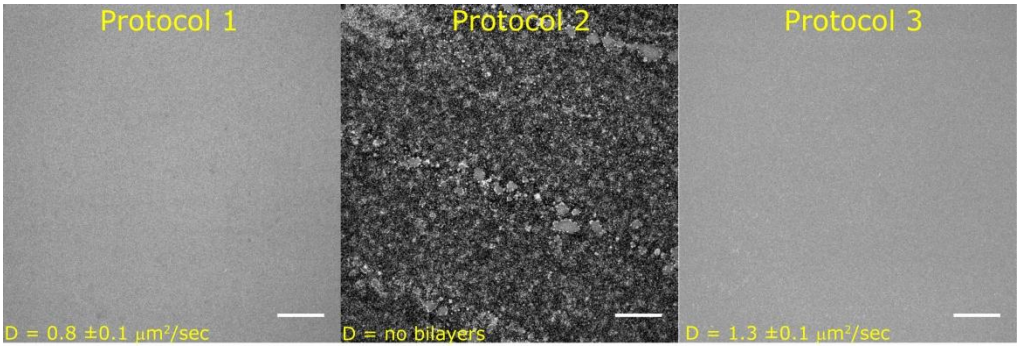

Figure 2.11: Overview of influence of surface treatment on formation of POPC:POPG (1:1) SLBs. Equimolar POPC:POPG SLBs were prepared on glass surfaces cleaned with the different protocols outlined in section **2.6**. Identical SLB preparation methods were followed using the same batch of lipid vesicles on the same day. Homogeneous SLBs failed to form on glass substrates prepared with protocol 2 while glass substrates with protocol 1/3 resulted in homogeneous SLBs.

Next, we checked the stability of POPC:POPG SLBs in time, using a qualitative approach (appearance of defects) and a quantitative approach by measuring diffusion coefficient of a lipid probe (D_{NBD-PC}). POPC:POPG SLBs prepared on glass supports cleaned according to Protocol 3 remain defect-free and yielded consistent values of diffusion coefficients for at least 3 days under ambient conditions (**Figure 2.12**).

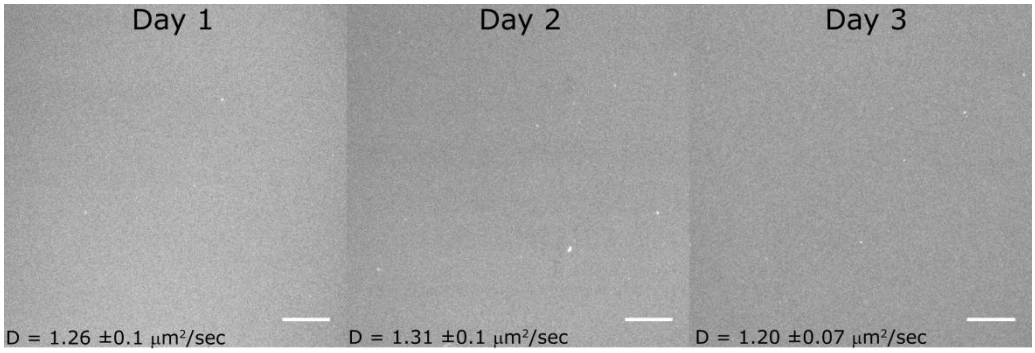

Figure 2.12: Stability of POPC:POPG (1:1) SLBs over time. Representative fluorescent images of POPC:POPG SLBs doped with 0.5 mol% NBD-PC in 50 mM HEPES, 0.1 mM EDTA buffered in pH 7.4 at room temperature. FRAP measurements and confocal images were taken every 24 hours for 3 days. The SLBs remain defect free and the values of D_{NBD-PC} do not change significantly. All scale bars are 10 μm.

Thus all further preparations of SLBs in this thesis were carried out using Protocol 3 unless mentioned otherwise.

2.7 Summary of optimized protocol for formation of POPC:POPG SLBs

After testing several parameters and factors influencing the formation of POPC:POPG SLBs, a protocol was established and followed consistently throughout the thesis.

2.7.1 Preparation of glass supports

i) Glass slides were first cleaned in 2% Hellmanex® or 1X ICN Detergent in a bath sonicator for 60 minutes at 70 °C. Glass slides were then exhaustively rinsed in deionized water and dried with N_2. *Both pre-cleaning steps are equally efficient in terms of the resulting homogeneity of the POPC:POPG (1:1) SLBs*.

ii) The dried slides were then etched with a 3:1 solution of 95% sulfuric acid (H_2SO_4) and 30% hydrogen peroxide (H_2O_2) for 7 minutes. *Longer etching times lead to brittle glass supports in my experience*.

iii) The cleaned slides were cleaned exhaustively with deionized water and used within 3 days. *For SLB preparations involving < 5% anionic lipids, the slides can be used for a week*.

2.7.2 Preparation of glass vials for liposome preparation

i) Glass vials used for drying lipids were pre-cleaned with 2% Hellmanex® or 1X ICN Detergent in a bath sonicator for 60 minutes at 70 °C. Thereafter, they were rinsed with acetone to remove any residual detergent and then with 70% ethanol and dried. *Before aliquoting lipids, it's advisable to rinse the glass vials with chloroform or the organic solvent the lipids are dissolved in*.

2.7.3 Preparation of lipid vesicles

i) Lipid mixtures of the desired composition were aliquoted in the clean glass vials (~ 0.78 mg) and rotated in a circular fashion under a slow flow of N_2 gas. Then these glass vials were kept under vacuum (0.5 bar) for 1 hour. *Add between 50-100 µl of $CHCl_3$ if total volume of aliquoted lipid is less than 25 µl to ensure uniform mixing in multi-component mixtures.*

ii) Next, the dried lipid films were re-suspended in the buffer of choice with the final lipid concentration ~ 1 mM. *For SLB formation with anionic lipids, it is necessary that this buffer contains at least 75 mM NaCl and pH ~ 6.0.*

iii) The resulting solution was either sonicated or freeze-thawed depending whether SUVs or LUVs were desired.

iv) Storage of lipid vesicles (esp. SUVs) should be in accordance with the resulting phase transition temperature of the composition.

2.7.4 Preparation of SLBs

i) The flow chamber was assembled with freshly cleaned glass supports as shown in **Figure 2.3**. Lipid vesicles were mixed in a 1:1 ratio with 1M NaCl and immediately loaded into the chambers.

ii) After an incubation time of 20 minutes, the flow chamber was rinsed with buffer of choice at a flow rate of 80 µl/min for 20 minutes to ensure maximal removal of unbound lipid vesicles.

iii) SLBs made with POPC:POPG (1:1) and POPC:POPG (3:1) lipids with the above protocol show the expected lipid mobility (~ 1.2 μm^2/sec) and homogeneity upto ~ 3 days. 100% POPC SLBs are stable until a week of preparation. *SLBs meant for longer experiments can be sealed on the top using an oil or wax to minimize lipid oxidation*.

iv) The aforementioned protocols also work with POPS and POPA lipids in an equimolar concentration with POPC lipids.

2.8 Influence of substrate interactions on membrane fluidity

Several reports in literature advocate the use of polymeric substrates like dextrans or poly-ethylene glycol on glass supports in order to prevent non-specific interactions of lipid membranes with the underlying supports. Preparations of such supports are well known and undoubtedly advantageous especially for studies with trans-membrane proteins, but they are susceptible to contamination from ambient bacteria since they are good carbon sources. In order to avoid such complications, we used bare glass supports throughout this thesis unless mentioned otherwise. To test for non-specific surface interactions between lipids and the glass supports, we used FRAP to measure two parameters:

1) Mobile fractions of different fluorescent lipid probes. We consistently obtained a value of mobile fraction close to unity indicating that lipids freely diffused on the glass supports.
2) Measuring lower leaflet diffusion selectively by monitoring fluorescence recovery curves after quenching the NBD moiety in the upper leaflet by passing a buffer containing sodium dithionite though the flow-cell.

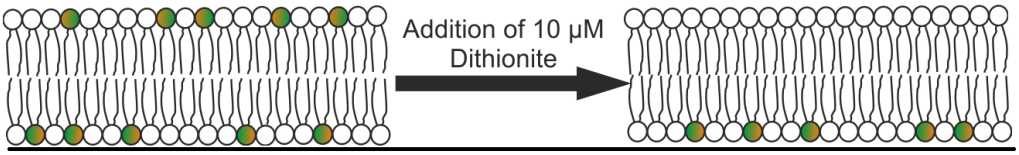

Figure 2.13: Monitoring single leaflet diffusion. POPC:POPG SLBs with 0.5 mol% NBD-PC prepared as per protocol discussed in previous sections. FRAP measurements were carried out to measure lipid diffusion. 10 μM sodium dithionite prepared in 50 mM HEPES, 0.1 mM EDTA buffer at pH 7.4 was incubated for 30 minutes and then he buffer as replaced with 50 mM HEPES, 0.1 mM EDTA buffer at pH 7.4. Since sodium dithionite bleaches only the leaflet in contact, the diffusion of lipids in the lower leaflet can be measured.

Sodium dithionite is well to known to irreversibly bleach NBD and cannot pass though the lipid bilayer. Thus, a FRAP measurement performed after the addition of dithionite reveals the $D_{NBD\text{-}PC}$ from the lower leaflet. In all measurements, $D_{NBD\text{-}PC}$ from the lower leaflet was the comparable to that obtained from the combined contributions of both leaflets indicating little influence of glass substrates in our experimental conditions.

2.9 Conclusions

The effects of several parameters affecting the formation of SLBs were examined in this chapter. Fusion conditions for lipid vesicles (pH, ionic strength, surface treatment and lipid concentration) containing a high fraction of negative lipids (> 0.25) differ from conditions required for SLB preparations involving neutral lipids. Conditions ensuring low pH, high ionic strength and lipid concentration favor the preparation of stable SLBs consisting of high amounts of anionic lipids. Altering the ionic strength across the membrane leaflets using monovalent salts can modulate the morphology of SLBs. The formation of stable and homogeneous SLBs is ensured by choosing the ionic strengths optimally. Treatment of the glass surfaces that are used as substrates for SLB formation is another key parameter influencing the stability and homogeneity of SLBs. The critical FRAP parameters and their influence mentioned in the chapter allow for precise measurements of diffusion values in such SLB systems. Although the conditions and parameters described in this chapter only cover POPC:POPG lipid systems, these conditions should, in principle, also apply to lipid systems of comparable compositions.

3

Clustering of membrane-bound alpha synuclein locally impairs lipid diffusion by increasing lipid packing

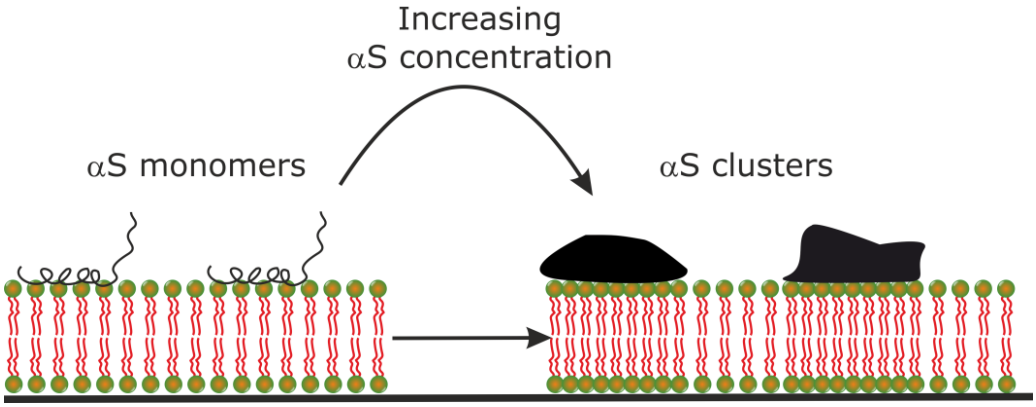

Iyer, A., Mireille M. A. E. Claessens, and V. Subramaniam. 2016. *Clustering of membrane-bound alpha synuclein locally impairs lipid diffusion by increasing lipid packing*. This chapter has been submitted for publication.

3.1 Introduction

Alpha synuclein (αS) is a 140 amino acid, intrinsically disordered monomeric protein with a yet unclear physiological function. αS consists of three domains: 1) An N-terminal domain (residues 1-60) with positively charged lysine residues that is believed to be instrumental in membrane binding of monomeric αS[91,106,189,190]; 2) A central hydrophobic domain known as NAC (Non-Aβ Component) comprising residues 61-95, which is critical to aggregation of monomers into fibrils and forms the core of the amyloid fibril; 3) A C-terminal domain (residues 96-140) that is proline rich and predominantly negatively charged at physiological pH[82].

αS is ubiquitously present in eukaryotic cells but is found in particularly high concentrations at the synaptic junctions of neuronal cells[191]. Although the function of αS is unclear, it has been suggested to be involved in the regulation of synaptic vesicle pools[71], vesicle trafficking[48,192,193] and vesicle fusion events at the synapse[194]. The mechanism by which αS regulates these processes may depend on physical membrane properties related to e.g. domain formation. Accordingly the cholesterol and sphingomylein content dependent[114] association of αS to raft-like membrane micro-domains (typically liquid ordered) in eukaryotic cells[86,135] has been suggested to be important in signal transduction events. However the association of αS with more ordered lipid domains *in vivo* seems to be in conflict with *in vitro* observations indicating selective binding of αS to liquid disordered regions in anionic lipid membranes[108,136]. This discrepancy between *in vivo* and *in vitro* observations remains unsolved.

Recent literature indicates that the function of αS is related to changes in the physical properties of lipid membranes upon interaction with monomeric αS[99,103,110,155]. The macroscopic fluidity of lipid membranes is one such property and is related to the diffusion coefficient of individual lipid molecules and is affected by the packing order of the lipid constituents[172]. Fluidity in plasma membranes and membranes of cellular organelles, is critical to a multitude of processes in living cells[172] including gene expression[149,195], activity of membrane-bound proteins such as receptor-associated protein kinases[167,196], sensor proteins[165], ion channels[166] and modulation of immune responses[197]. A decrease in membrane fluidity has been predicted to interfere with vesicle fusion and budding[198,199] and to influence the progression of neurodegenerative diseases including Parkinson's disease (PD)[31,169]. Although a lot is known about the aggregation of αS into amyloid structures in PD[83,200], it remains unclear how the intriguing interplay between lipid membranes and αS leads to neuronal cell death in PD[60,109,127,201-204]. Considering the association of αS with membrane micro-domains *in vivo* and the functional relevance of αS-membrane interactions in PD, we hereby address how physical membrane properties like membrane packing and fluidity are affected before αS amyloids are observed.

Using three truncated variants of αS (**Figure 3.1**) with comparable membrane binding affinities but different aggregation propensities, we probed how lipid order, determined from fluorescence anisotropy experiments, and effective lateral lipid diffusion (D_{LL}), determined in FRAP experiments, in SLBs were affected by the appearance of membrane-bound αS clusters. The Δ71-82-αS variant (lacking residues 71-82) is a known aggregation-deficient variant[205] and has higher net negative charge at pH 7.4 compared to WT-αS. In contrast, 1-108-αS (lacking residues 109-140) is known to aggregate into amyloids much faster than WT-αS[206,207]. The aggregation of the 1-60-αS variant (lacking residues 61-140) has not been investigated in detail yet but this αS variant remained aggregation deficient in our experimental conditions. Both 1-108-αS and 1-60-αS variants have fewer negatively-charged residues as compared to WT-αS. The differences in the net charges of the truncated variants gave us a handle to modulate the attractive and repulsive forces between αS monomers.

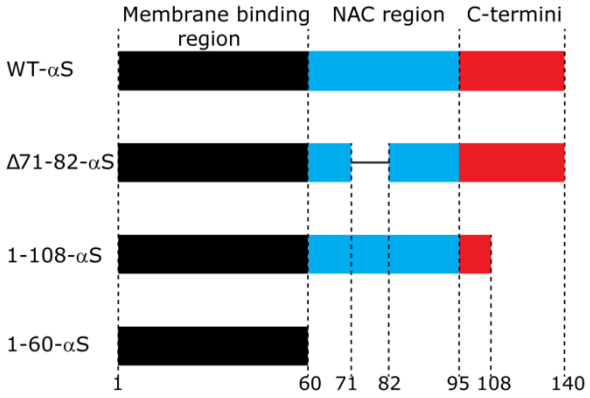

Figure 3.1: Schematic of sequences of WT-αS and the three αS truncated variants used. The truncated variants lacked a significant fraction of the C-terminus (1-108-αS), a significant fraction of the NAC region (Δ71-82-αS), or lacked both NAC and C-terminal region (1-60-αS).

Our results show that upon addition, monomeric αS immediately starts clustering on SLBs. In these early clusters, no Thioflavin-T-detectable cross-β sheet protein aggregates are present. The size of the early clusters depends on αS concentration and their formation severely impairs the effective D_{LL} in SLBs depending on the αS cluster size. The observed changes in membrane fluidity coincide with an increased lipid order upon cluster formation at high P/L ratios. Our results indicate that the clustering of αS on lipid membranes induces ordering of underlying lipids.

3.2 Results

3.2.1 Excess of αS on SLBs promotes protein clustering

To investigate the interplay between αS and lipid membranes, we chose SLBs with an equimolar lipid composition of POPC:POPG. Using this model system, we previously showed that formation of amyloid aggregates of WT-αS on the surface of POPC:POPG SLBs lead to membrane disruption and lipid extraction[125]. To probe how the clustering of membrane-bound protein that precedes amyloid formation and membrane disruption affects physical membrane properties, we used three different truncated variants (**Figure 3.1**) of αS with varying aggregation propensities. Protein mixtures for each truncated variant and WT-αS containing a fraction of AlexaFluor647 labeled monomers (1 in 10), were added to separate SLBs at varying P/L ratios (0.02 to 1.0) by varying the bulk protein concentration and imaged immediately. The addition of protein to the SLB resulted in the immediate appearance of small protein clusters on the SLBs for WT-αS and all truncated variants studied (**Figure 3.2, left panel**). On the time scales studied, the clusters were immobile and did not grow or shrink. Quantification of mean areas of the individual clusters (see Methods) showed that the area occupied by the individual clusters of WT-αS and the other truncated variants increased with increasing P/L ratios. The size of the Δ71-82-αS clusters seems to saturate around an average protein cluster size of ~ 0.30 μm^2 from a P/L ratio of 0.25 as shown in **Figure 3.2, right panel**.

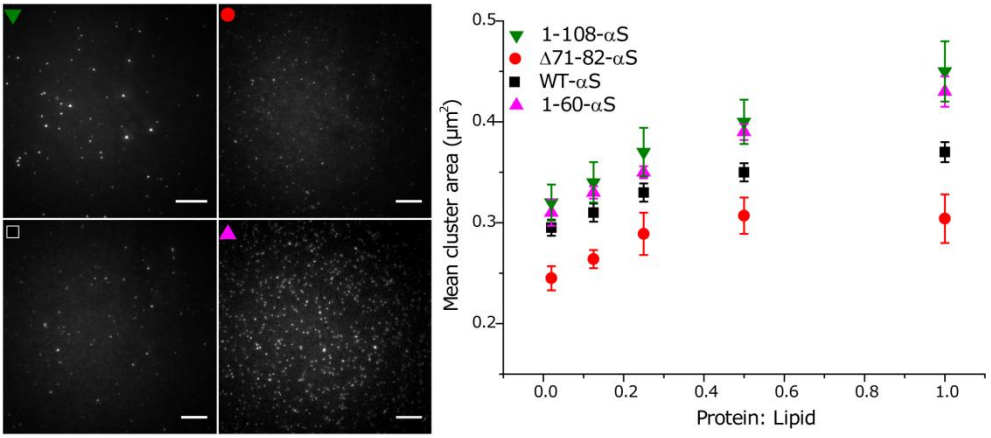

Figure 3.2: Representative fluorescence images of SLBs after addition of monomeric αS. Addition of monomeric αS (10% AlexaFluor 647 labeled αS) to POPC:POPG SLBs with varying P/L ratios led to immediate formation of clusters. The lipid concentration was calculated (from the dimensions of the flow chamber used and assuming an average lipid headgroup size of 65 nm^2) to be 10 μM. Images were acquired immediately after protein incubation (left panel). The acquired images were subjected to an intensity threshold after background subtraction (see section 4.5.5 for details) to estimate the respective mean cluster areas (right panel). The error bars are three times the standard error obtained from an average of ~ 2500 clusters. All experiments were carried out in 50 mM HEPES, 0.1 mM EDTA, pH 7.4 buffer at room temperature. Scale bar is 10 μm.

At any given P/L ratio, the largest protein cluster sizes were observed for 1-108-αS, followed by 1-60-αS and WT-αS respectively. The smallest sized clusters were formed by the Δ71-82-αS variant. Measurement of the area fractions occupied by protein clusters in the fluorescent images showed that the smallest area fraction was occupied by the Δ71-82-αS variant while the 1-60-αS and the 1-108-αS variant occupied the largest area fractions. Although, the area of individual αS clusters increased with increasing P/L ratios, the area fraction occupied with clusters did not vary much (**Figure 3.3**).

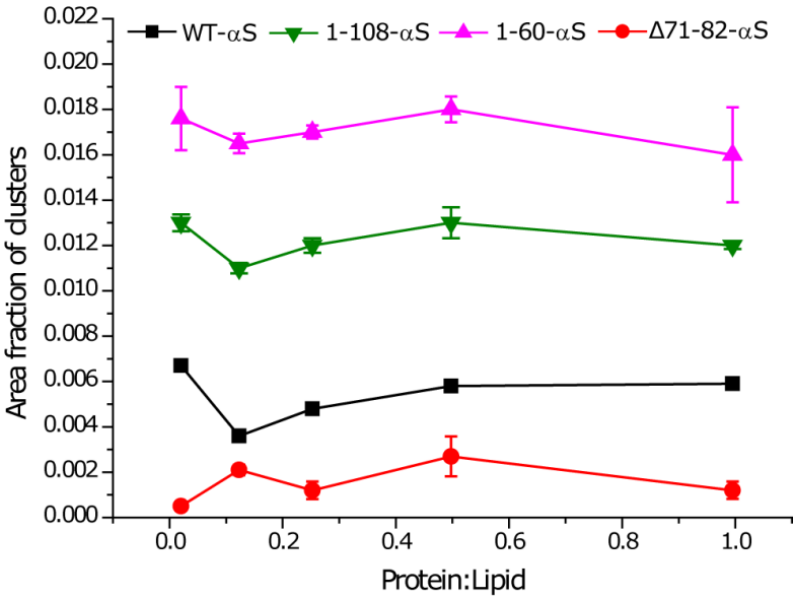

Figure 3.3: Overview of area fractions of αS clusters on POPC:POPG SLBs. The above plot depicts area fraction of αS clusters obtained from fluorescent images after image processing (See methods). All experiments were performed in 50 mM HEPES, 0.1 mM EDTA, pH 7.4 buffer at room temperature.

Given the fact that all protein binding sites are already occupied at P/L ratio of 0.02[108], the addition of more protein beyond this P/L ratio does not result in formation of new protein clusters. Instead, the cluster area increases with increasing P/L ratio with the combined area of all clusters remaining unchanged. This suggests reorganization of the membrane bound protein clusters into bigger clusters upon increasing P/L ratios. The possibility of three-dimensional growth cannot be completely excluded since the addition of αS to pre-existing clusters could be either from the bulk solution or from membrane bound protein. Although the measured cluster areas are not necessarily equilibrium values, we do not observe any cluster movement or exchange of material between clusters and the bulk solution that is fast enough to result in growth/shrinkage of clusters over the time scale of the experiments. We confirmed

that αS does not cluster in absence of lipid membranes and that the observed clustering is not a consequence of labeling αS with AlexaFluor647 dye (**Figure 3.4**).

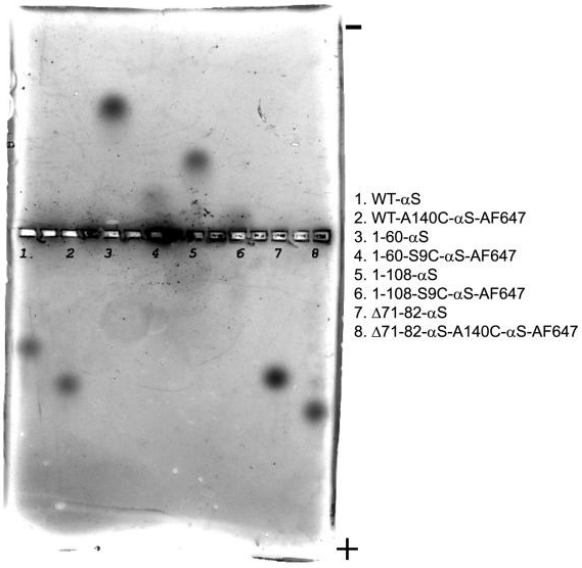

Figure 3.4: Non-denaturing agarose gel for WT-αS and truncated variant. 10 μM of WT-αS and αS truncated variants labeled with AlexaFluor647 (even numbered lanes) or unlabeled (odd numbered lanes) were aliquoted into wells in a 0.5% Agarose gel in Tris-Glycine buffer at pH 8. Since 1-60-αS and 1-108-αS have a net positive charge at pH 7.4, an agarose gel was run with wells in middle to allow migration to both charged poles. The differences in migration of a given αS variant are a result of AlexaFluor647 labeling which is known to be negatively charged leading to a different migration of the labeled αS towards the charged poles.

We therefore conclude that the formation of the protein clusters requires the presence of lipid membranes and investigated if it affected lipid membrane properties.

3.2.2 Clustering of monomeric αS to SLB surface affects lateral lipid diffusion

To explore the changes in physicochemical properties of lipid membranes due to the presence of αS clusters, we looked at changes in membrane fluidity e.g. lipid diffusion and order. Fluorescence recovery after photobleaching (FRAP) experiments were performed before (control) and immediately after αS incubation to investigate the influence of αS binding on the effective lateral lipid diffusion coefficient of NBD-PC (henceforth $D_{NBD\text{-}PC}$) in the SLBs. Upon systematically increasing the P/L ratio for monomeric WT-αS and the truncated variants from 0.02 to 1, we observed differences in the drop of the $D_{NBD\text{-}PC}$ (**Figure 3.5**) in the presence of the truncated variants compared to WT-αS.

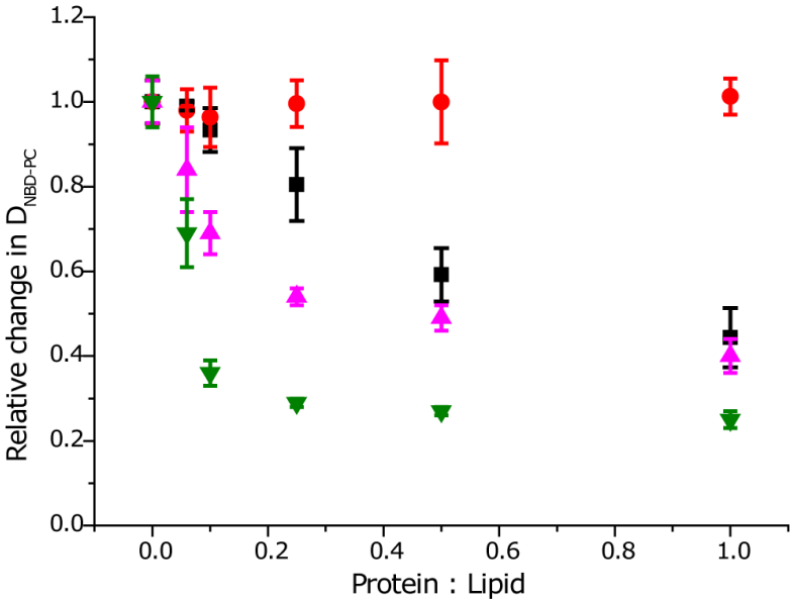

Figure 3.5: αS concentration dependent changes in D_{NBD-PC} in POPC: POPG (50:50) SLBs. Incubation of increasing concentrations of monomeric αS, or increased P/L ratios consistently resulted in a drop in the D_{NBD-PC} after protein addition for all αS variants except Δ71-82-αS (red circles). The decrease in the D_{NBD-PC} is more pronounced for the 1-108-αS (green downward triangles) and 1-60-αS (magenta upward triangles) as compared to WT-αS (black squares) for all P/L ratios. The error bars indicate standard deviations obtained from 5 individual FRAP measurements. All experiments were carried out in 50 mM HEPES buffer, 0.1 mM EDTA, pH 7.4 at room temperature.

D_{NBD-PC} dropped as a function of the P/L ratio by ~ 55% in the presence of WT-αS at a P/L ratio of 1. At all P/L ratios tested, D_{NBD-PC} remained unaffected by the presence of the Δ71-82-αS variant even though the binding affinities of WT-αS and Δ71-82-αS are comparable (**Figure 3.6**). The drop in D_{NBD-PC} was maximal in the presence of the 1-108-αS variant (~ 75%) followed by the 1-60-αS variant, at all P/L ratios. Interestingly, we did not observe any immobile fraction of NBD-PC upon binding of either truncated variants or WT-αS to the SLBs. Our results are in agreement with previous reports showing impaired lipid diffusion in liposomes upon binding of WT-αS by electron spin resonance spectroscopy[208].

Estimation of the number of amino acids involved in the formation of the membrane-bound helical domains of WT-αS and 1-108-αS variant on lipid membranes revealed (**Figure 3.6**) an identical value of ~ 79 amino acids. The size of the membrane-bound helical domain for the 1-60-αS variant corresponded to ~ 31 amino acids and ~ 47 amino acids for the Δ71-82-αS variant. Mere membrane association or the size of the membrane-bound helical domain can thus not explain the trends observed in D_{NBD-PC} with different truncated protein variants.

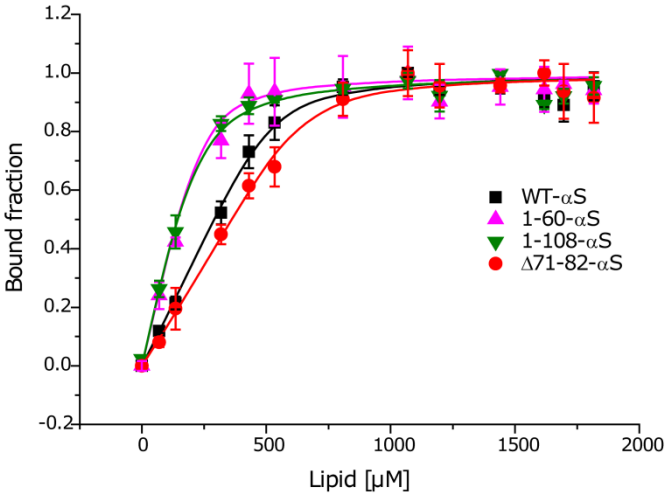

αS type	Aggregation into amyloids	Net charge at pH 7.4	Mean residue ellipticity (mdeg.cm^2.dmol^{-1})	%α-helical content	Size of helix, amino acids	Lipid concentration at 50%αSbinding
Δ71-82-αS	-	- 9.9	13077 ± 587	36 ± 2	47 ± 3	359± 24
WT-αS	+	- 8.9	20758 ± 687	56 ± 3	79 ± 4	293± 24
1-60-αS	-	+4.1	18306 ± 971	51 ± 3	31 ± 5	155± 10
1-108-αS	+++	+3.1	26684 ± 914	73 ± 3	79 ± 4	144± 17

Figure 3.6: Binding of WT-αS and other truncated variants to POPC:POPG liposomes. The bound fractions were obtained by measuring mean residual ellipticites at 222 nm by CD spectroscopy. The binding curve was quantified by fitting normalized mean residual ellipticity values (Appendix A). The error bars indicate standard deviations from three independent measurements. All experiments were carried out in 50 mM HEPES, 0.1 mM EDTA, pH 7.4 buffer at room temperature. The calculation of helicity was performed as described elsewhere[209].

The effect of αS binding on membrane fluidity was not only observed for POPC:POPG (1:1) SLBs. FRAP experiments with POPC:POPS (1:1) SLBs showed a similar αS-induced impairment of $D_{NBD\text{-}PC}$, indicating that the effective drop was not specific for the PG headgroup (**Figure 3.7A**). To enhance αS-membrane interactions, the fraction of negative lipids in the SLBs studied was high compared to physiological fractions. To account for this, we also varied the fraction of POPG in SLBs to physiologically relevant fractions and observe that the drop in $D_{NBD\text{-}PC}$ was present but less pronounced (**Figure 3.7B**). Moreover, the presence of NaCl does not seem to influence the observed changes in $D_{NBD\text{-}PC}$ upon addition of αS (**Figure 3.7C**). The drop in D_{LL} was also consistently observed for a given concentration of WT-αS, independent of the type of fluorescent lipid used to probe D_{LL} (**Figure 3.7D**).

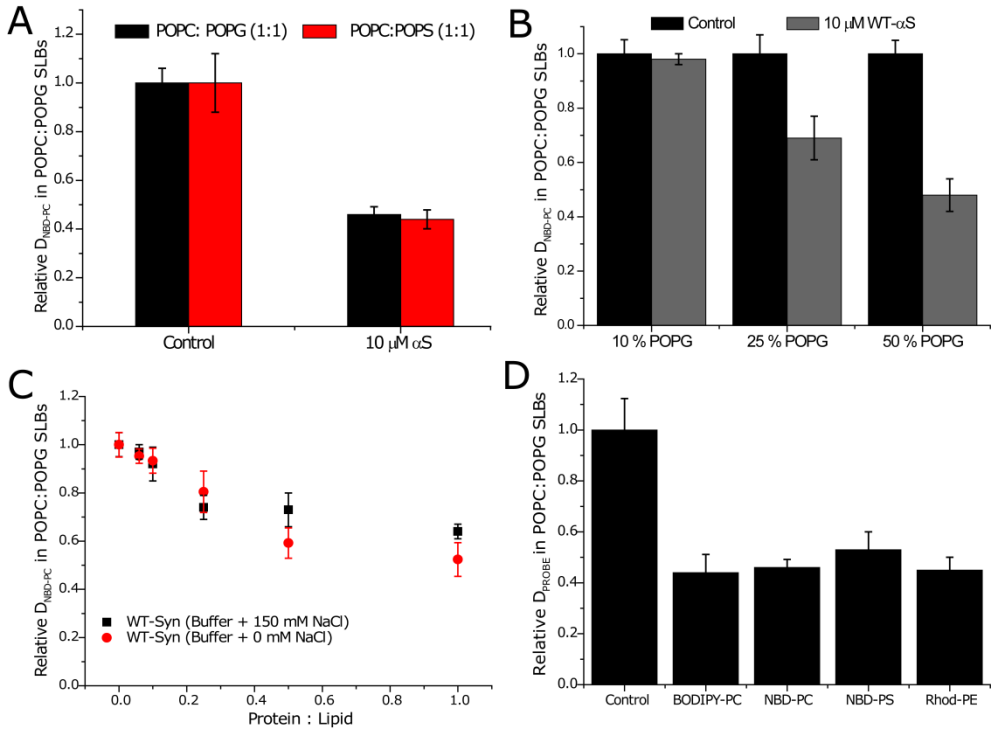

Figure 3.7: Control experiments for explaining the observed drop in lipid diffusion. A) Influence of WT-αS on the D_{NBD-PC} in SLBs with different lipid headgroups. 10 μM of WT-αS was incubated on SLBs composed of equimolar ratios of POPC:POPG (black bars) and POPC:POPS (red bars). The D_{NBD-PC} values were normalized with respect to that obtained in absence of any added protein. B) Relative change in the D_{NBD-PC} in POPC:POPG SLBs. 10 μM of WT-αS was incubated with POPC:POPG SLBs with increasing fraction of POPG lipids as shown. C) Influence of NaCl on the relative change in the D_{NBD-PC} in POPC:POPG (1:1) SLBs. 10 μM of WT-αS was incubated with POPC:POPG SLBs with (black squares) and without (red circles) 150 mM NaCl followed by measurement of D_{NBD-PC}. D) Relative change in the D_{LL} of different probes in POPC:POPG (1:1) SLBs. 10 μM of WT-αS was incubated with POPC:POPG SLBs and D_{PROBE} was measured immediately. The fluorescent lipid probe concentration was 0.5 mol% in each case. All experiments were performed in 50 mM HEPES, 0.1 mM EDTA, pH 7.4 buffer at room temperature.

Since the selected proteins (**Figure 3.1**) differ in their tendency to aggregate, interactions between membrane-bound proteins that resulted in the formation of membrane-bound protein clusters or amyloid species may be responsible for the observed changes in D_{LL}.

3.2.3 Clusters of αS on lipid bilayers do not contain amyloid signature

To check if the formation of clusters on the membrane surface resulted in amyloid formation, we monitored the aggregation of WT-αS and the truncated variants in presence and absence of POPC:POPG large unilamellar vesicles (LUVs) using ThT fluorescence. The increase in ThT fluorescence signal is indicative of amyloid formation[210,211]. As in the FRAP experiments,

the P/L ratio was varied from 0.02 to 1. The change in ThT fluorescence in time is presented in **Figure 3.8**. In the absence of vesicles, WT-αS had a long aggregation lag-time (~ 25 hours) whereas; the lag-time for 1-108-αS variant was shorter (~ 3 hours). Δ71-82-αS and the 1-60-αS failed to aggregate into amyloids over a period of 10 days. The presence of POPC:POPG liposomes could not enhance aggregation of both Δ71-82-αS and the 1-60-αS at P/L ratios as high as 1.

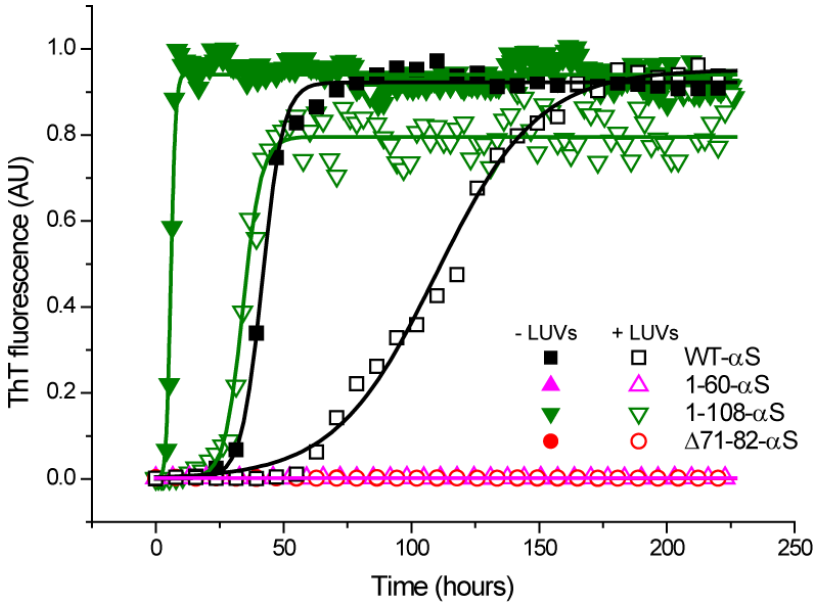

Figure 3.8: Representative aggregation of αS truncated variants. The αS truncated variants were aggregated in the presence (open symbols) and absence (closed symbols) of 1:1 POPC:POPG liposomes. 1-108-αS (green inverted triangles) aggregated with a lag-time of ~ 3 hours while the lag time of the WT-αS (black squares) was ~ 25 hours. The 1-60-αS (magenta upward triangles) and Δ71-82-αS (red circles) did not aggregate either in presence/absence of POPC:POPG liposomes over a period of ~ 10 days. 50 μM of protein of each variant in at least 6 replicates was allowed to aggregate in 50 mM HEPES, 0.1 mM EDTA, pH 7.4 buffer at 37 °C at 300 rpm in a fluorescence plate reader. ThT concentration was kept constant at 10 μM.

In the presence of POPC:POPG liposomes, we did not observe a ThT fluorescence signal for ~ 25 hours for the 1-108-αS variant and the aggregation lag-time of WT-αS was also significantly extended in the presence of the vesicles. It is therefore unlikely that the drop in D_{LL} observed soon after addition of αS to SLBs results from amyloid formation. Although recent reports have stated that lipid membranes can act as primary nucleation sites and therefore accelerate aggregation of αS into amyloids[120], we did not observe this effect. This discrepancy results possibly from differences in the physical properties of lipids chosen, and/or the experimental conditions employed in our study. Aggregation competent αS

variants showed an increase in the aggregation lag time in the presence of liposomes. The increase in the lag time can possibly be attributed to a reduced effective monomer concentration in the bulk solution resulting from monomers binding to liposomes. We also incubated ThT with SLBs in samples with P/L ratio of 1 and observed no fluorescence signal from ThT in the protein clusters.

Although accumulation of αS on SLBs resulted in protein clustering at all P/L ratios and lipid compositions for WT-αS and all truncated variants used in the study, conversion of membrane-bound protein to amyloid structures was never observed within experimental times (~ 60 min). Therefore, we conclude that the conversion to amyloid structures cannot explain the changes in D_{LL}.

3.2.4 αS binding leads to increased acyl chain packing in liposomes

In the absence of membrane-associated amyloid formation, the decrease in the D_{LL} could result from a tighter packing (increased order) of lipids upon cluster formation of αS. To test this hypothesis, steady-state fluorescence anisotropy was used to monitor if changes in membrane fluidity resulting from an increase in lipid order in POPC:POPG liposomes. DPH (1,6-Diphenyl-1,3,5-hexatriene) is a well known hydrophobic probe for structural and dynamic studies on lipid membranes[212-214]. DPH roughly resembles a cylinder with its absorption and fluorescence emission transition dipoles aligned parallel to its long molecular axis. It has negligible fluorescence in solution because of its rotational motion. In absence of rotational motion, it has a very high fluorescence polarization depending on the orientation of the long axis. DPH aligns parallel to the lipid acyl chains and therefore an increase in lipid acyl chain packing can be monitored as an increase in the fluorescence anisotropy, r [213].

At a constant DPH concentration, the P/L ratio was varied similar to that in the FRAP measurements. We observed that WT-αS and 1-60-αS showed an increase in anisotropy values with the 1-60-αS showing consistently higher values at all P/L ratios. In spite of having a comparable membrane binding affinity as WT-αS, Δ71-82-αS only shows a marginal change in the steady state anisotropy, r as shown in **Figure 3.9**.

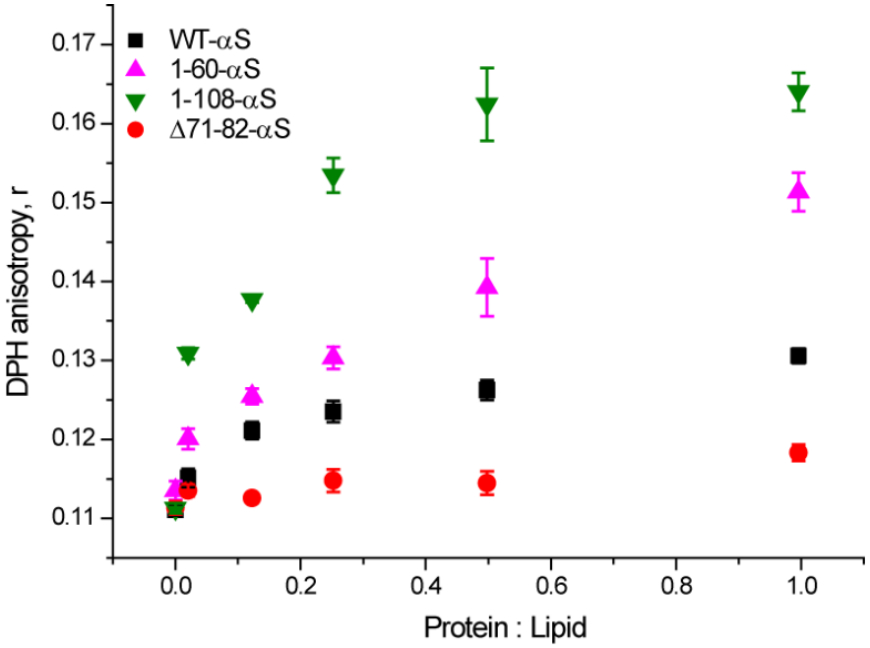

Figure 3.9: Changes in DPH anisotropy in POPC: POPG (1:1) LUVs with increasing αS concentration. Addition of monomeric αS to POPC:POPG LUVs containing 1 mol% DPH leads to a pronounced increase in the fluorescence anisotropy in all truncated variants and WT-αS (squares) except Δ71-82-αS (circles). The 1-108-αS (inverted triangles) and 1-60-αS (upward triangles) show higher anisotropy values at all P/L ratios compared to WT-αS. The error bars indicate standard deviations obtained from 3 independent measurements. All experiments were carried out in 50 mM HEPES, 0.1 mM EDTA, pH 7.4 buffer at room temperature.

The 1-108-αS variant showed a steep increase at low P/L ratios and continued to increase at higher P/L ratios. The changes in steady state anisotropy seem to be maximal for the 1-108-αS variant indicating increased packing of lipid acyl chains in the presence of clusters of this protein. Fluorescent images obtained after adding αS to POPC:POPG SLBs (L/P =10) containing 1 mol% DPH result in intense fluorescent regions beneath all αS clusters except the Δ71-82-αS variant (**Figure 3.10**).

Moreover, increasing concentration of WT-αS over DPH labeled POPC:POPG SLBs resulted in larger ordered regions corresponding with larger WT-αS clusters (**Figure 3.11**).

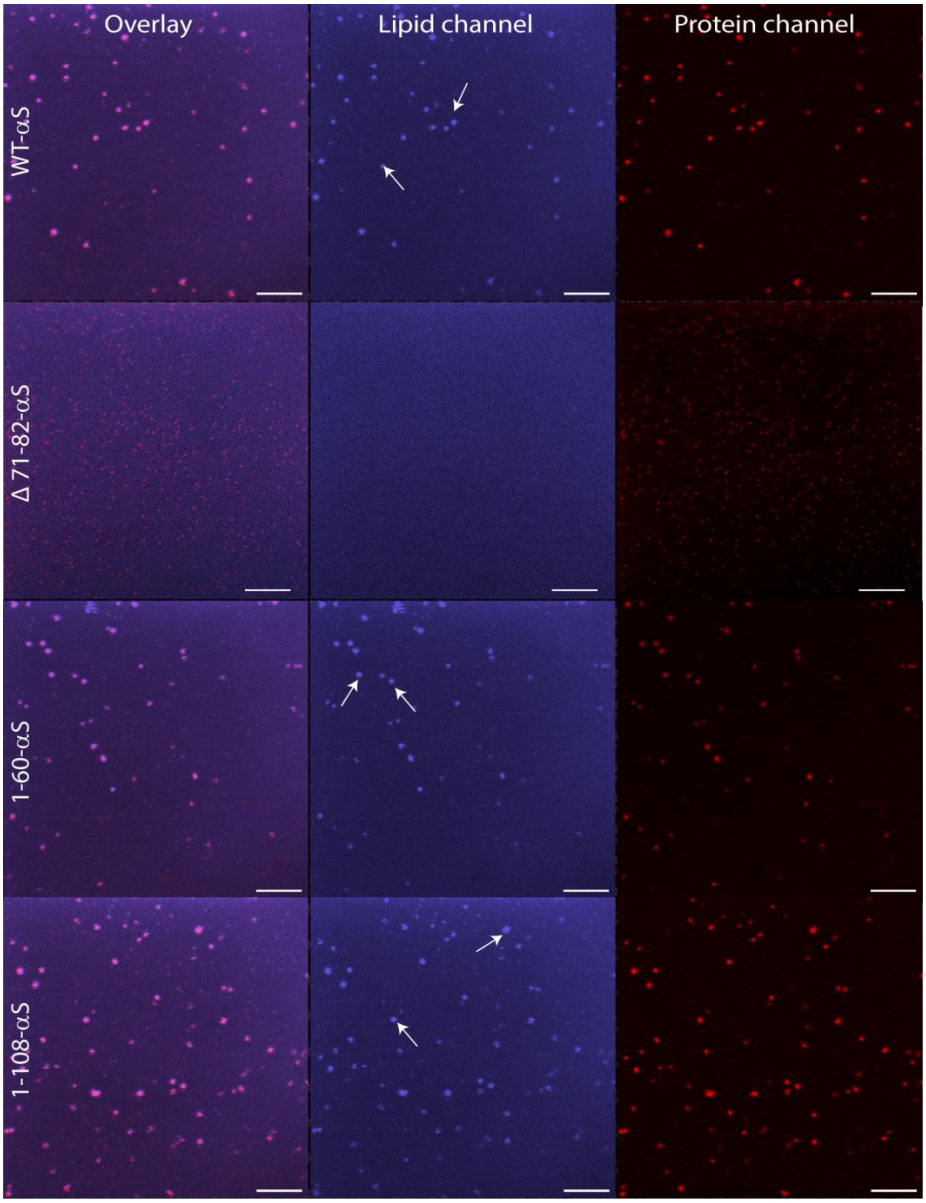

Figure 3.10: Lipid ordering in POPC:POPG SLBs observed using DPH in presence of αS constructs. αS constructs were added to 1 mol% DPH containing POPC:POPG SLBs at a lipid to protein ratio of 10. After addition of αS to SLBs, enhanced fluorescence is observed in the lipid channel below regions of αS clusters (white arrows in lipid channel) for all αS constructs except Δ71-82-αS. All experiments were carried out in 50 mM HEPES buffer, 0.1 mM EDTA, pH 7.4 at room temperature.

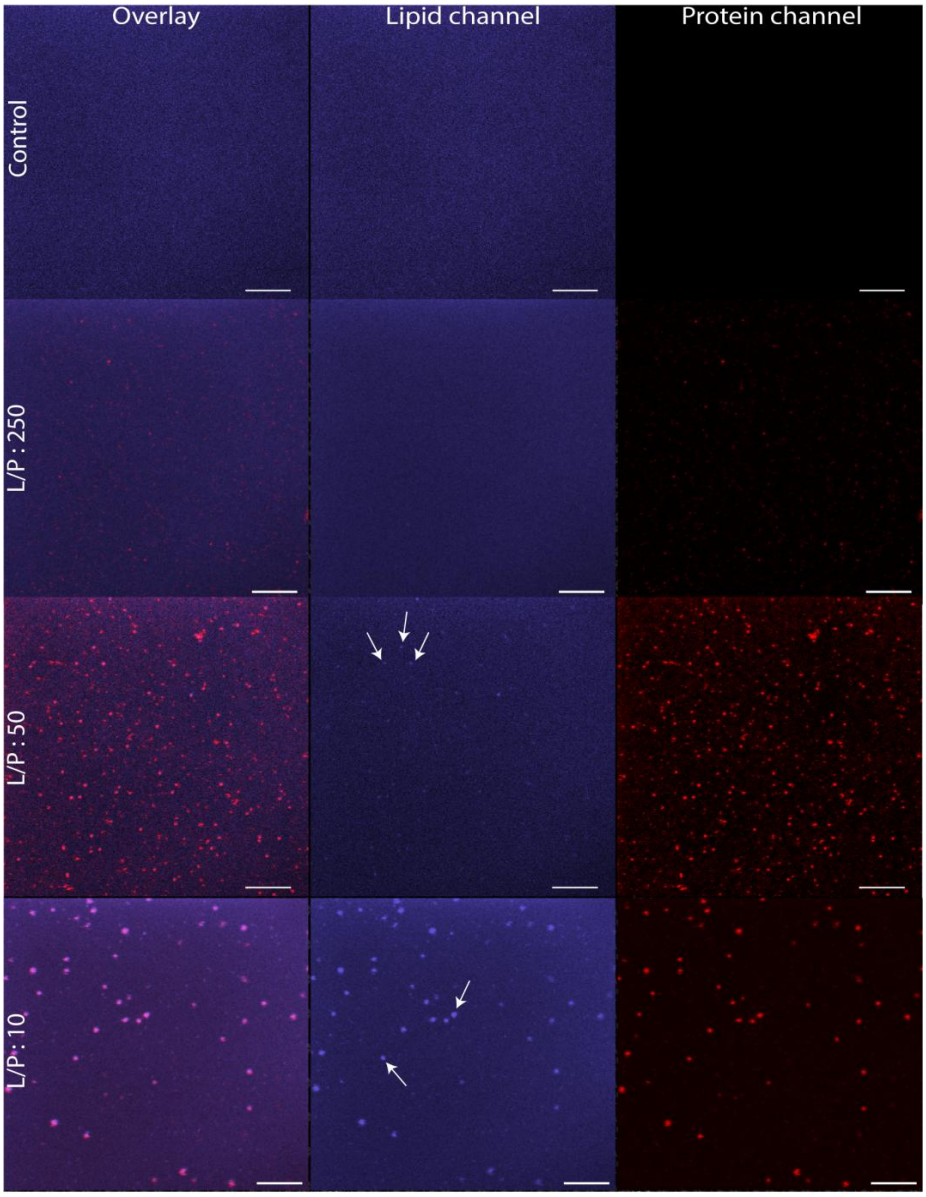

Figure 3.11: WT-αS induced lipid ordering in POPC:POPG SLBs observed using DPH. Incubation of increasing concentrations of monomeric αS, or increased P/L ratios as shown in the figure above resulted in intense fluorescent regions (white arrows in lipid channel) upon larger cluster formation (protein channel). Control images (no protein added) do not show any regions with enhanced fluorescence. POPC:POPG SLBs were labeled with 1 mol% DPH. All experiments were carried out in 50 mM HEPES buffer, 0.1 mM EDTA, pH 7.4 at room temperature.

These observations combined with the marginal changes in the steady state anisotropy of DPH in liposomes in the presence of the Δ71-82-αS variant suggest little or no influence on lipid packing. Results from steady state anisotropy and ordered domains observed in fluorescence microscopy of DPH labeled POPC:POPG SLBs seem to correlate with the protein cluster sizes hinting that the changes in lipid packing and cluster formation are linked.

3.3 Discussion

In this study, we have systematically investigated how clustering of monomeric αS and the interaction of αS clusters with lipid membranes influence physicochemical properties of lipid membranes. Upon binding to anionic membranes, WT-αS assumes a helical conformation. In this helical conformation, some hydrophobic residues line up on the polar face of the helix[215]. At the conditions of our experiments, all αS binding sites on the membrane surface are occupied, the average distance between two membrane-bound monomers is small and inter-protein collisions can result in cluster formation. Clustering of membrane-bound αS is a consequence of a complex interplay mainly between attractive hydrophobic interactions, resulting from the solvent exposed hydrophobic patches on the membrane-bound αS, and repulsive electrostatic interactions, resulting from the negatively charged unstructured solvent exposed C-terminal region of αS. Considering the interplay between attractive and repulsive forces, the net inter-protein repulsion is expected to be highest in the Δ71-82-αS and minimal in the 1-108-αS variant. Thus, the Δ71-82-αS results in smaller sized clusters due to decreased hydrophobic attraction between proteins compared to WT-αS. The removal of the negatively charged C-terminal region in two truncated variants (1-60-αS and 1-108-αS) results in larger clusters than WT-αS which is likely due to decreased electrostatic repulsions between the membrane-bound monomers. It has been reported that αS can induce local curvature on lipid membranes[110]. It is well known that binding of αS to lipid membranes is sensitive to curvature and it is plausible that this increase in local membrane curvature upon αS binding could drive further binding of αS. With increasing cluster size, the D_{LL} measured in FRAP experiment decreases. These changes in lipid diffusion are not a result of a mere association of αS monomers and the SLBs. This is because, in spite of having similar membrane-bound fractions as WT-αS; membrane-bound Δ71-82-αS has no influence on D_{LL}. Also, at P/L ratios ~ 0.02 where the lipid binding sites for αS are completely saturated, we observe no change in D_{LL}. The changes in D_{LL} are thus a consequence of interactions of the αS clusters with lipid membranes.

Interactions between membrane-bound αS molecules impaired D_{LL} in SLBs, but the mobile fraction of the fluorescent probe (either zwitterionic or negatively charged) remained close to unity at any P/L ratio. This means that the lipids are not immobilized under the protein clusters but are able to exchange continuously. Upon increasing the bulk protein concentration

systematically, we observe that that the mean cluster area increases but the total area occupied by these clusters does not change significantly. This suggests that a higher αS concentration in the bulk allows for a faster rearrangement of clusters by exchange with bulk protein. As the cluster area increases, the time a particular lipid spends under a αS cluster (first passage time) increases. Since FRAP measures an *effective* diffusion coefficient of lipids in an area that contains both regions with and without clusters; the D_{LL} obtained in presence of clusters is a weighted average of the diffusion coefficients from both regions, where large clusters have a larger effect on the effective diffusion coefficient than smaller ones. The accumulation of proteins in clusters results in an accumulation of more closely packed (charged) lipids under the clusters as seen from fluorescence microscopy and an increase in lipid order as indicated by steady state anisotropy. It is known that an increase in lipid order, by increasing cholesterol content or degree of saturation, can significantly decrease D_{LL}[216]. For a similar packing of proteins in the clusters one would expect the lipid organization under the clusters to be independent of the cluster size. Without single lipid tracking measurements, it however is difficult to ascertain if the resulting drop in D_{LL} beneath αS clusters is similar for larger and smaller clusters. However the data points from both the FRAP and DPH anisotropy experiments on SLBs covered with protein clusters of the different truncated variants collapse on a single "master" curve (**Figure 3.12**). The increase in lipid order and the decrease in D_{LL} both become visible beyond a cluster area of ~ 0.30 μm^2. The correlation between the changes in D_{LL} and *r* suggest a concerted process where the formation of clusters leads to a closer packing of lipids and a decrease of the effective D_{LL}. The correlation between the effective D_{LL} and *r* as observed in the master curve is non-trivial as it does not result from a direct interaction between proteins and lipids.

Although αS mainly binds to anionic lipids, the drop in effective D_{LL} of zwitterionic lipids suggests that αS clustering (possibly stabilized by anionic lipids) also affects effective D_{LL} of zwitterionic lipids. A similar effect on the diffusion of zwitterionic lipids has been observed for annexin a5, a peripheral protein involved in vesicle fusion events, upon its clustering on anionic lipid membranes[217]. Clustering of proteins and ordering of lipids into membrane micro-domains are both known to be involved in protein function and this interplay forms the basis for many cellular signaling processes[137]. Protein clustering and the formation of membrane domains can either be mutually exclusive or coupled depending on the cellular niche[114,168,218]. Binding studies of αS with synaptic vesicle mimics *in vitro* suggest a strong preference for membrane curvature, cholesterol content and lipid phase[105,108,219]. Synaptic vesicles are typically enriched in cholesterol and comprise of typical raft components such as GPI-anchored proteins. Lipid domains formed due to clustering of αS in our measurements could thus be important as the presence of such membrane micro-domains is usually coupled with

protein organization, recruitment and consequently protein function[133,220-222]. For example, clustering of GPI-APs on cellular membranes has been directly linked to their function[223].

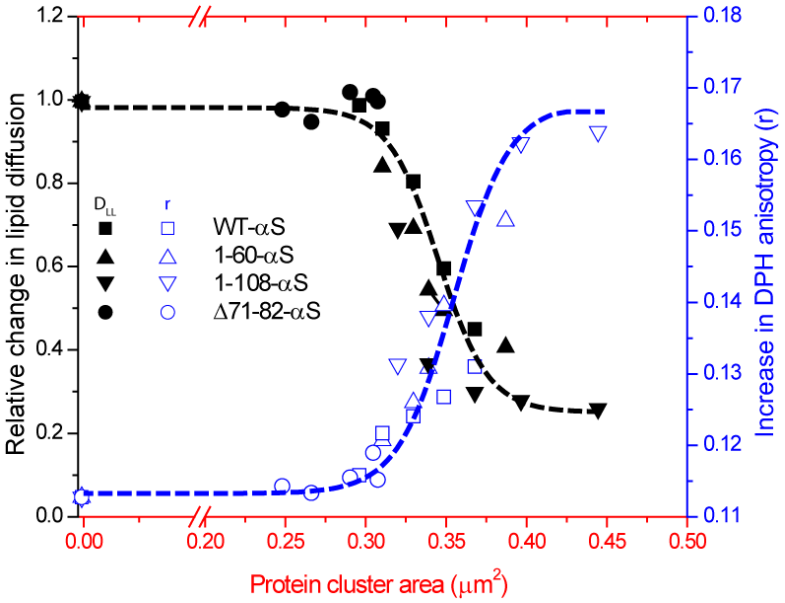

Figure 3.12: Master curve of data correlating changes in lipid diffusion and lipid packing to protein cluster areas. The above plot shows relative changes in the lipid diffusion coefficients (black closed symbols) and absolute steady state anisotropy values of DPH in liposomes (blue open symbols) against mean protein cluster areas. WT-αS is depicted as squares while the Δ71-82-αS variant is shown as circles. The 1-108-αS variant (downward triangles) results in the biggest change in lipid diffusion coefficients and DPH anisotropy followed by the 1-60-αS variant (upward triangles). The dotted lines are representative of the general trend in increasing anisotropy (blue lines) and changes in lipid diffusion (black lines).

The decreased membrane fluidities could also be relevant in the pathogenic aspect of αS. Aging cellular membranes, in particular have lower membrane fluidity and their intrinsic membrane recycling mechanisms are less efficient. The closure of transient defects in plasma membranes that would be expected to reseal quickly, would be less efficient with decreased membrane fluidities. Our finding that it is the clustering of αS which causes impaired fluidity and ordering of lipids, provides a different perspective in understanding and possibly hinting towards the functional/pathogenic role of αS.

3.4 Conclusion

Together, our data suggests that the formation of non-amyloid αS clusters upon exposure of SLBs to αS at high P/L ratios changes both the effective lipid diffusion and lipid packing. The observation that an increase in lipid order and decrease in D_{LL} as a function of the mean area of individual clusters can be plotted on a master curve suggest that the close packing of lipids in the clusters is responsible for the observed effect. Changes in physical properties of

membranes due to αS monomers or clusters could be relevant to the function of αS bound to membranes in cellular systems. Subtle changes resulting from increased αS concentrations or mutations might change αS clustering and thereby affect lipid diffusion, partitioning, re-organization and ordering which could give undesirable biological consequences and is possibly relevant in PD.

3.5 Materials and Methods

Stock solutions of 1-palmitoyl-2-oleoyl-sn-glycero-3-phosphocholine (POPC), 1-palmitoyl,2-oleoyl phosphatidylglycerol (POPG), and 1-palmitoyl-2-[6-[(7-nitro-2-1,3-benzoxadiazol-4-yl)amino]hexanoyl]-sn-glycero-3-phosphocholine(NBD-PC) in chloroform were purchased from Avanti Polar Lipids (Birmingham, AL) and used without further purification. Ethylenediaminetetraacetic acid (EDTA) was purchased from Sigma Chemicals (St. Louis, MO). Sodium chloride (NaCl), sodium hydroxide (NaOH), and 4-(2-hydroxyethyl)-1-piperazineethanessulfonic acid (HEPES) were purchased from Merck (Germany).

3.5.1 Substrate Pretreatment

Before bilayer formation, glass cover-slips were washed in 2 % Hellmanex (VWR International, Chicago, IL) at 80° C for 60 minutes, rinsed profusely with deionized water and then dried with a stream of nitrogen. The slides were etched for 8 minutes in a solution of 3:1 (v/v) concentrated sulfuric acid(H_2SO_4) and hydrogen peroxide (H_2O_2). The slides, kept immersed in deionized water throughout, were used within 3 days after treatment.

3.5.2 Supported lipid bilayer preparation

Lipid stock solutions of POPC and POPG in chloroform were mixed in 1:1 molar ratios, dried under a stream of nitrogen, and placed under vacuum for 1 hour. After drying the lipid films were rehydrated in 100 mM NaCl solution and vortexed for 5 minutes. Small unilamellar vesicles (SUVs) were prepared by sonicating the rehydrated liposome solution for 40 minutes using a Branson tip sonicator (25% amplitude). Thereafter, the SUVs were centrifuged at 13200 rpm to remove any tip residue from the sonicator probe. The SUVs were stored at 4 °C and used within 3 days. Supported lipid bilayers were formed by vesicle fusion inside a 120 µl custom built chamber (see **Figure 2.3B**) on appropriately treated glass slides. The extruded vesicles were mixed with 1M NaCl solution at a 1:1 ratio to induce fusion. After 20 minutes incubation, excess vesicles were removed from the chamber by rinsing with a 50 mM HEPES, 0.1 mM EDTA, and 750 mM NaCl, pH 7.4 buffer. Thereafter the chamber was rinsed with 50 mM HEPES, 0.1 mM EDTA, pH 7.4 buffer to remove salt. At least 3 mL of buffer were passed through the chamber to ensure complete solvent exchange.

3.5.3 Expression, purification and labeling of WT-αS variants

All αS variants were expressed in Escherichia coli strain BL21(DE3) using the pT7-7 expression plasmid and purified in the presence of 1 mM DTT as previously reported[224]. The cDNAs for the truncated variant of αS lacking 71-82 residues Δ71-82-αS were obtained from Prof. Benoit Giasson from University of Florida (USA). Since αS does not contain any cysteine residues necessary for fluorescent labeling, an alanine to cysteine mutation was introduced at residue 140 for WT-αS and Δ71-82-αS. For labeling 1-108-αS and 1-60-αS, a serine to cysteine mutation was introduced at residue 9 (S9C)[109]. S9C is typically used for FCS based measurements for estimation of binding affinities of αS to lipid membranes[225]. Prior NMR studies have confirmed that the S9C mutation in αS does not affect its membrane bound state. Prior to labeling, all cysteine containing αS variants were reduced with a six-fold molar excess of DTT for 30 min at room temperature. The samples were desalted with Pierce Zeba desalting columns, followed by the addition of a two-fold molar excess of AlexaFluor 647 C2 maleimide dye (Invitrogen) and incubated for two hours in the dark at room temperature. Free label was removed using two desalting steps. The protein labeling efficiency was estimated to be >90% from the absorption spectrum by measuring protein absorbance at 280 nm and including the correction factor for AlexaFluor 647 (0.03).

3.5.4 Protein cluster imaging and analysis

For imaging of αS clusters, a Nikon (Tokyo, Japan) A1 total internal reflection fluorescence (TIRF) microscope was used. The labeled proteins were diluted with unlabeled protein (1 in 10) in 50 mM HEPES, 0.1 mM EDTA, pH 7.4 buffer to the desired concentrations before incubating with SLBs. Visualization of SLBs was done by incorporating 0.5 mol% BODIPY-PC in the phospholipid bilayers. The proteins were incubated with the SLBs at room temperature. Images were acquired using a 100X OI, 1.48 NA TIRF objective. The acquired images consisted of 512 × 512 pixels with a pixel size of 0.158 μm under identical gain settings. The images were contrast enhanced to the same extent to make any features appear clearly. To quantify the cluster sizes, raw images were first corrected for uneven background illumination (rolling-ball method, 100 pixels) in Fiji[226]. The resulting images were subjected to an intensity threshold (consistent for all images) and the resulting pixel areas were quantified as cluster areas.

3.5.5 Fluorescence Recovery After Photobleaching (FRAP)

To determine the lateral lipid diffusion in SLBs, FRAP was performed on a NikonA1 confocal microscope equipped with a perfect focus system (PFS). A 100-mW Argon ion laser (488 nm, Coherent, CA) was used to both bleach and monitor the lipid bilayer fluorescence. In the FRAP experiment fluorescence from a circular region of interest (ROI) was bleached (radius ~ 8 μm)

in 1 second. After bleaching the increase in fluorescence intensity in the ROI was monitored for 6 minutes. All FRAP data were fitted using Soumpasis fit[182] which has been shown to better model for lipid diffusion than a single exponential fit for circular bleach geometry[183].

3.5.6 Circular dichroism (CD) spectroscopy

A Jasco J-715 spectropolarimeter was used to obtain CD spectra at protein concentrations of 3 μM. Spectra were recorded between 200 to 250 nm with a step size of 1 nm and a scanning speed of 10 nm/minute, using a 1 mm path length cuvette. The apparent dissociation constants for both the protein variants were determined by titrating them against POPC: POPG (50:50) SUVs and fitting the measured mean residue ellipticity at 222 nm to the lipid concentration as reported before[108]. The details of the fitting equation used are given in **Appendix A**.

3.5.7 Thioflavin T aggregation assay

Thioflavin T aggregation assays were carried out in a TECAN Infinite M200 micro-plate reader. For every protein variant, 50 μM of monomeric protein was allowed to aggregate in 50 mM HEPES, 0.1 mM EDTA, pH 7.4 buffer at 37 °C at 300 rpm in a fluorescence plate reader. The ThT concentration was kept constant at 10 μM.

3.5.8 Fluorescence anisotropy

POPC: POPG (50:50) LUVs with 1 mol% 1,6-Diphenyl-1,3,5-hexatriene (DPH) were prepared in 50 mM HEPES, 0.1 mM EDTA, pH 7.4 buffer at room temperature. Lipid concentration was kept constant at 10 μM. Protein concentration was varied to obtain final P/L ratios of 0.02, 0.1, 0.25, 0.5 and 1. Control samples were measured before protein addition in each sample run. Fluorescence anisotropy was recorded at 25 °C by using an excitation wavelength of 360 nm and an emission wavelength of 440 nm. The result for each condition is the average of three independent measurements.

3.6 Acknowledgements

We thank Prof. Benoit Giasson from University of Florida for providing the plasmids for the Δ71-82-αS construct, Prof. Roberta Croce from the Vrije Universiteit Amsterdam for permission to carry out CD spectroscopy measurements, Kapil Singh from University of Zürich for providing a script for FRAP data analysis, Prof. Nils Petersen from University of Alberta, Dr. Martin Stöckl from University of Konstanz and Yuval Mulla from FOM Institute AMOLF for discussions. The work presented in this chapter is part of a project titled "A Single Molecule View on Protein Aggregation" (Nr. 127) funded by Foundation for Fundamental Research on Matter (FOM).

4

Amyloids of alpha synuclein affect the integrity of supported lipid bilayers

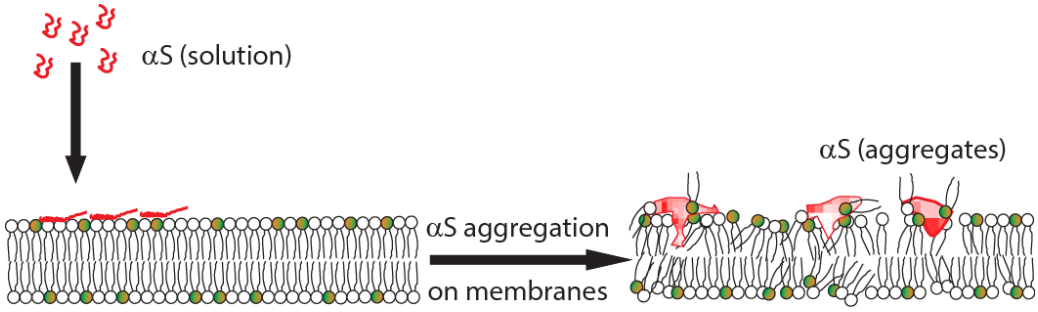

Parts of this chapter are published in:

Iyer, A., Nils O. Petersen, Mireille M. A. E. Claessens, and V. Subramaniam. 2014. *Amyloids of Alpha-Synuclein Affect the Structure and Dynamics of Supported Lipid Bilayers*. Biophys J 106:2585-2594.

4.1 Introduction

The 14.4 kDa neuronal protein αS is a major component of Lewy bodies, which are a pathological hallmark of Parkinson's disease (PD)[31]. Neuronal death has been attributed to various causes[30,44,49,191,227], all of which involve the aggregation of αS into amyloid structures. Above a critical concentration αS aggregates *in vitro* into oligomers and fibrils[228], with the details of aggregation depending on pH[229], salt[230] and temperature[229] conditions. There is increasing evidence that interactions with lipid bilayers play a role in αS aggregation[155,202], although there have been some unresolved debates in earlier literature[231,232].

αS-lipid membrane interactions depend on the negative charge on the membrane[231]. These interactions are mediated by positively charged residues located in seven imperfect repeats in the N-terminus of the protein[190,233]. These repeats are reminiscent of lipid membrane binding domains in apolipoproteins, with the first five repeats predicted and shown to form alpha helices upon binding to negatively charged SUVs[91,106]. *In vitro,* the presence of negatively charged lipid membranes accelerates αS aggregation into amyloids[231]. For other amyloid forming proteins like Aβ and IAPP, membrane integrity is affected by extensive membrane remodeling and lipid extraction[142,144,234-237]. There is increasing evidence that this is also the case for αS[103,126,127,155,238]. Further, the report of measurable amounts of lipids in Lewy bodies[44] strongly suggests that the interaction of lipid membranes with αS is relevant in the aggregation process.

One of the major reasons attributed to neuronal cell death in PD is membrane damage[239-241]. It is uncertain if certain oligomeric species or the aggregation process causes the observed membrane damage. Moreover, the exact mechanism of this damage remains to be elucidated. Both monomers and oligomers of WT-αS have been shown to cause dye leakage in model membrane vesicles, consistent with a pore-like mechanism[112,190,242,243]. However, this leakage is observed only at high surface charge densities indicating that other mechanisms maybe important at physiologically relevant charge densities. WT-αS oligomers with a putative channel-like structure have been shown to induce single ion-channel currents in lipid membranes[244]. Recent reports also indicate that addition of monomeric wild type αS (WT-αS) causes membrane damage in SLBs[126,127]. Thus, it is unclear whether membrane damage is due to αS amyloid formation on the membrane or is a result of binding of αS species to the membrane. To distinguish between these two mechanisms for membrane damage, we studied a truncated variant lacking amino acid residues 71-82 (henceforth αS(Δ71-82)) that in solution fails to form amyloids but forms spherical oligomers with a diameter of ~ 20 nm[205]. We used SLBs as a platform to visualize and measure the interactions of WT-αS and αS(Δ71-82) with membranes by confocal microscopy using fluorescently labeled SLBs and αS.

We indirectly modulated the rate of aggregation of αS on the membrane surface by varying the negative lipid composition and thereby modulating the density of membrane-bound protein. We used fluorescence recovery after photobleaching (FRAP) to measure changes in the lateral diffusion coefficients of lipids to extract quantitative information about lipid phase and fluidity. FRAP was also used to probe diffusion of αS and its aggregation on the SLB surface. We observe that formation of amyloids by WT-αS results in lipid extraction and decrease the mobility of lipids in SLBs. Neither effect is observed with the truncated variant even though it binds membranes with comparable affinity.

4.2 Results

4.2.1 WT-αS and αS(Δ71-82) bind lipid membranes with comparable affinities

In order to compare the clustering and possible aggregation of WT-αS and αS(Δ71-82) on lipid membranes, the binding of both proteins to SLBs has to be comparable. We used CD spectroscopy to measure binding affinities of αS(Δ71-82) and WT-αS to POPC:POPG (1:1) SUVs[108] (Materials and Methods). The data (**Figure 4.1A**) show that the binding affinities of both constructs to the lipid bilayer are comparable. Although the WT-αS and αS(Δ71-82) exhibit similar binding affinities to lipid membranes, they show different aggregation behavior in solution.

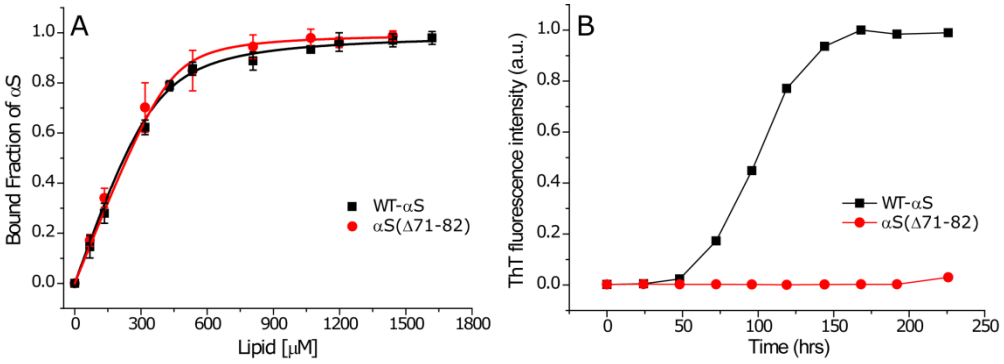

Figure 4.1: A) Binding of WT-αS and αS(Δ71-82)with POPC:POPG liposomes. Titration of WT-αS (black squares) and αS(Δ71-82) (red circles) by POPC:POPG (50:50) SUVs. The bound fractions were obtained by measuring mean residual ellipticites at 222 nm by CD spectroscopy. The binding curve was generated by fitting normalized ellipticity values to Equation 2 (solid lines), assuming equivalent binding sites (see **Appendix A** on page 154 for details). The error bars indicate standard deviations from three independent measurements. B) Aggregation kinetics of αS variants at 37 °C monitored by ThT fluorescence. The aggregation reaction was carried out using 50 mM HEPES, 0.1 mM EDTA at 300 rpm constant orbital shaking conditions in a fluorescence micro-plate reader. The protein concentration was kept at 100 μM and the ThT concentration was 10 μM.

In absence of membranes, αS(Δ71-82) does not form fibrillar amyloids[205] and aggregation arrests at an oligomeric stage[245], whereas WT-αS readily aggregates into cross-β sheet rich amyloid structures. Aggregation experiments under our experimental conditions confirmed this reported difference in aggregation behavior as shown in **Figure 4.1B**.

4.2.2 WT-αS and αS(Δ71-82) self-assemble differently on POPC:POPG (1:1) SLBs

Upon systematically varying the concentration of αS on POPC:POPG (1:1) SLBs, we observed that both WT-αS and αS(Δ71-82) organized into clusters on the SLB surface. Although the binding affinities of these proteins were comparable, there was a clear difference in the organization of these clusters (**Figure 4.2**), obtained upon incubation of 10 μM protein on SLBs after 18 hours (P/L ratio :1).

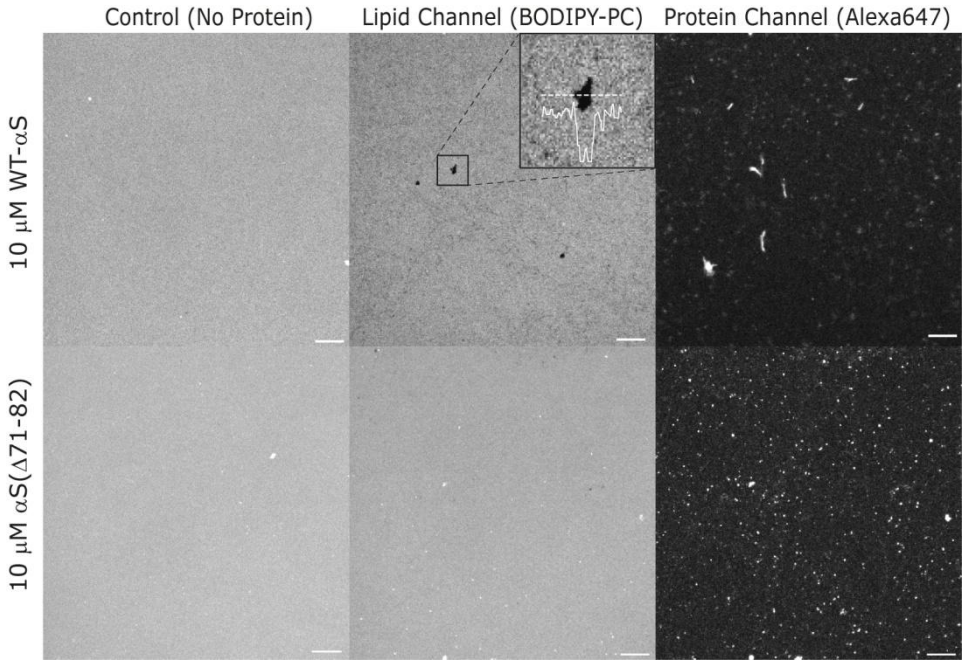

Figure 4.2: Clustering of WT-αS and αS(Δ71-82) on POPC:POPG supported lipid bilayers. Representative images of POPC:POPG (1:1) SLBs labeled with 0.25 mol% fluorescent lipid BODIPY-PC after adsorption of 10 μM αS for 18 hours. The protein images show bigger and more heterogeneous WT-αS protein aggregates on 50% POPG-containing bilayers (top panel) as compared to those of αS(Δ71-82) variant (lower panel). There appears to be little correlation between the defects on the SLBs and the bigger aggregates. The lipid images show the appearance of cracks and defects in the top panels (WT-αS). The insert shows these at an enhanced magnification. The sparse lipid clustering (seen as bright spots) was also seen in the controls and αS(Δ71-82) aggregates do not seem to have a preference for these regions. Fewer and smaller defects appear in the presence of αS(Δ71-82) and the average intensity remains the same. Images are contrasted to the same extent to facilitate comparison. All experiments were performed at room temperature in 50 mM HEPES, pH 7.4, 0.1 mM EDTA buffer. The scale bar is 10 μm.

WT-αS assembles into a heterogeneous distribution of clusters of both small and large areas, whereas clusters of αS(Δ71-82) are more homogenous in size. Upon decreasing the P/L ratio, we observe that assembly of both WT-αS (**Figure 4.3**) and αS(Δ71-82) clusters (**Figure 4.4**) are sensitive to protein concentration, with cluster size increasing as a function of protein concentration.

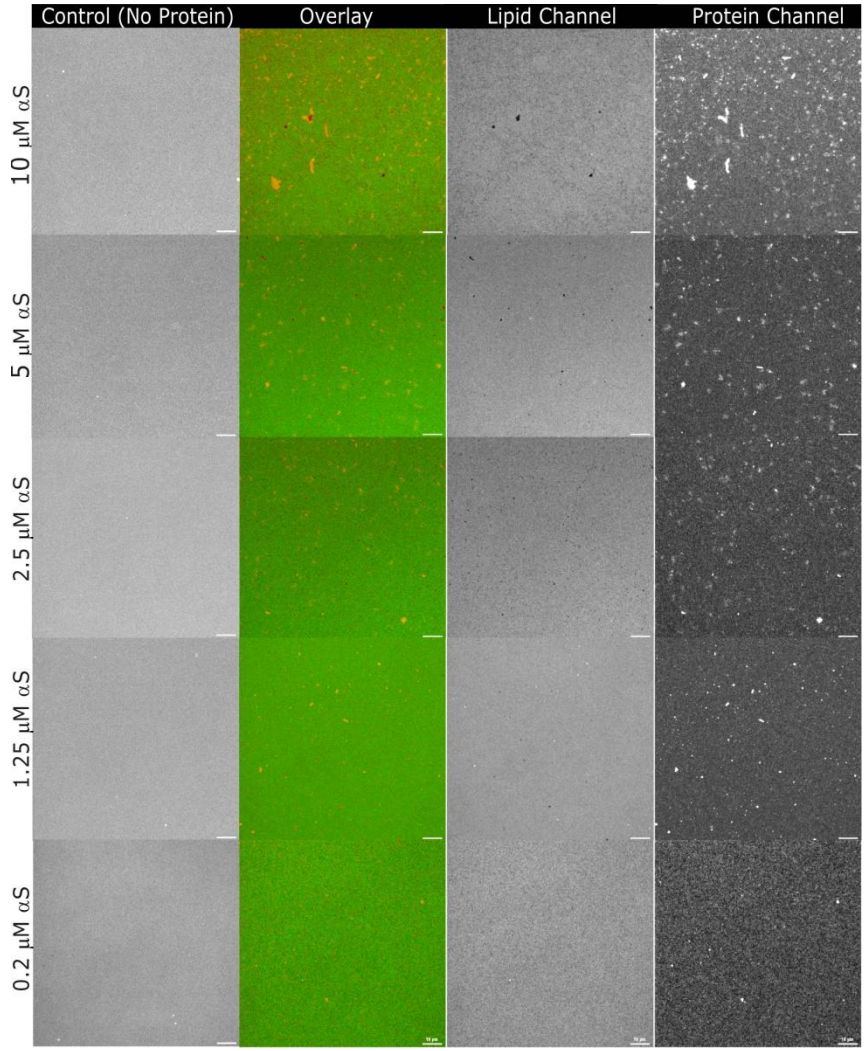

Figure 4.3: Adsorption of WT-αS on POPC:POPG (50:50) SLBs. Representative confocal images of POPC:POPG (1:1) SLBs before (control) and after addition of increasing amounts of WT-αS (labeled to AlexaFluor 647). 0.25 mol% of BODIPY-PC was incorporated as a fluorescent lipid probe in SLBs. The lipid channel clearly shows increasing membrane damage in form of defects and cracks as the protein concentration is increased from 0.2 μM WT-αS to 10 μM WT-αS. Correspondingly, the cluster sizes also seem to increase upon increasing protein concentration. Images are contrasted to the same extent to facilitate proper comparison. All images were taken at room temperature in 50 mM HEPES, 0.1 mM EDTA, pH 7.4 buffer. The scale bar is 10 μm.

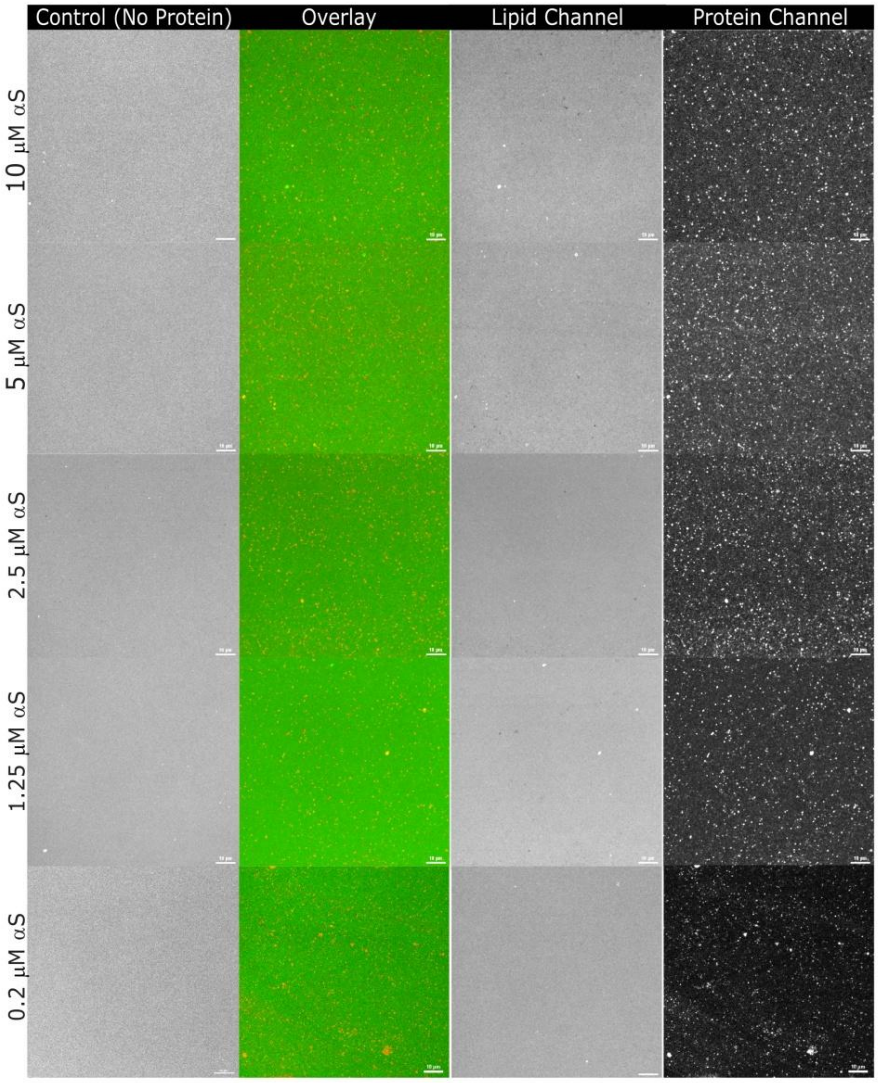

Figure 4.4: Adsorption of αS(Δ71-82) on POPC:POPG (50:50) SLBs. Representative confocal images of POPC:POPG (1:1) SLBs before (control) and after addition of increasing amounts of αS(Δ71-82) variant which was labeled to AlexaFluor 647. 0.25 mol% of BODIPY-PC was incorporated as a fluorescent lipid probe in SLBs. The above images show clearly no effect of incubation of αS(Δ71-82) as the concentration is increased from 0.20 μM to 10 μM. There is hardly any significant damage seen across this concentration range. Correspondingly the cluster sizes also do not show a difference. Images are contrasted to the same extent to facilitate proper comparison. All images were taken at room temperature in 50 mM HEPES, 0.1 mM EDTA, pH 7.4 buffer. The scale bar is 10 μm.

In order to obtain a quantitative overview of protein cluster size, we estimated average cluster areas (Materials and Methods) by fitting the measured area distribution to a log-normal distribution. **Figure 4.5** depicts the correlation between the protein concentration and average cluster areas.

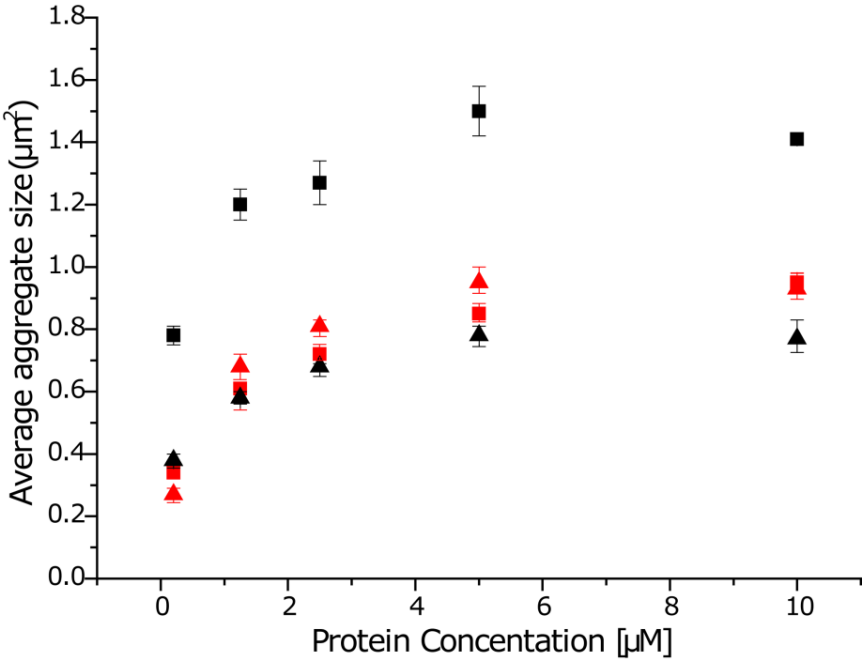

Figure 4.5: Average cluster areas of αS on SLBs with changing protein concentration and lipid composition. Average cluster areas obtained by fitting the area distributions obtained from αS aggregates on POPC:POPG SLBs. Upon increasing protein concentration, there is a two-fold increase in the average cluster areas irrespective of the lipid composition for both WT-αS and αS(Δ71-82). However, for a given protein concentration, αS(Δ71-82) clusters (red symbols) show little dependence on lipid composition contrary to that observed for the WT-αS clusters (black symbols). The clusters areas for WT-αS and αS(Δ71-82) on 50% POPG SLBs are shown by squares and as triangles for 25% POPG SLBs. The error bars indicate standard errors in each case. The statistics underlying the values presented here are shown in **Table 4.1**.

As shown in **Figure 4.5**, we also obtained αS cluster areas from incubation of WT-αS and αS(Δ71-82) on POPC:POPG (75:25) SLBs (**Figure 4.6**). This experiment was done to investigate if the percentage of negatively-charged lipids influenced the clustering of αS on SLBs.

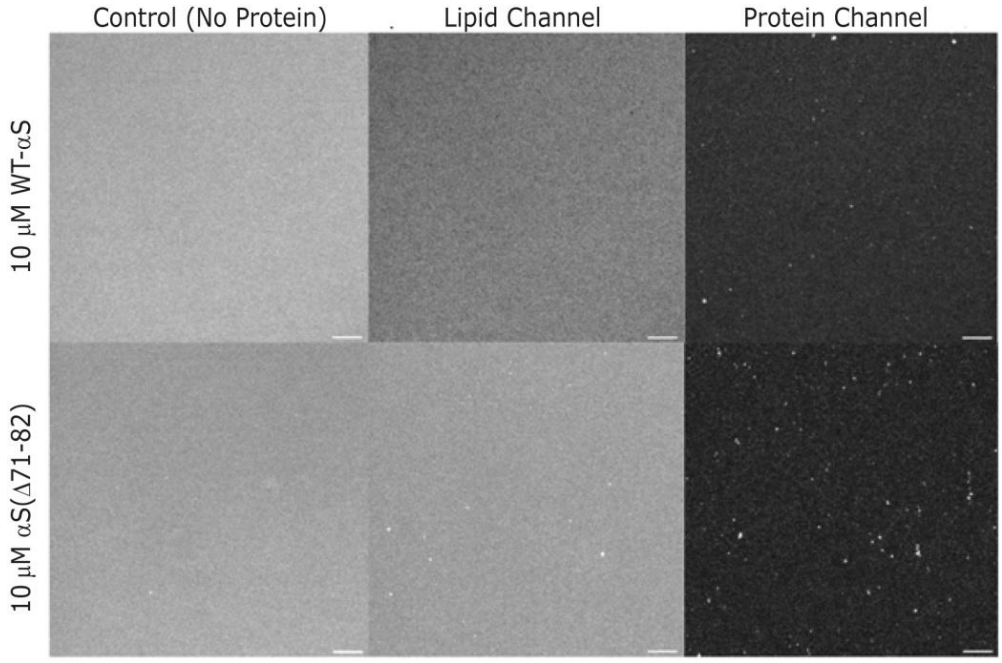

Figure 4.6: Adsorption of αS on POPC : POPG (75:25) SLBs. Representative confocal fluorescence images of SLBs before (control) and after adsorption of 10 μM αS (labeled to AlexaFluor 647) after an 18 hour incubation period. 0.25 mol% of BODIPY-PC was incorporated as a fluorescent lipid probe in SLBs. The lipid channel shows very small defects and fluorescence intensity loss with the WT-αS (top panels), whereas no such effects are seen with αS(Δ71-82) (lower panels). Images are contrasted to the same extent to facilitate proper comparison. All experiments were performed at room temperature in 50 mM HEPES, pH 7.4, 0.1 mM EDTA buffer. The scale bar is 10 μm.

Our observations show a charge-dependent increase in the size of WT-αS clusters on SLBs at high P/L ratios. The WT-αS clusters are consistently smaller on less negatively charged SLBs (i.e. 25% versus 50% POPG content). The histograms of the cluster areas (**Figure 4.7**) show a more heterogeneous distribution (larger widths) for the WT-αS clusters at all concentrations. The smallest calculated cluster area using our thresholding parameters is 0.04 μm^2 which corresponds to the pixel area in the image. We cannot make any conclusive predictions about the size or aggregation number (number of monomers) of αS structures inducing membrane damage. At these high P/L ratios (1:1), it has been previously reported that WT-αS forms amyloid structures depending on the percentage of negative charge in the lipid membranes[231].

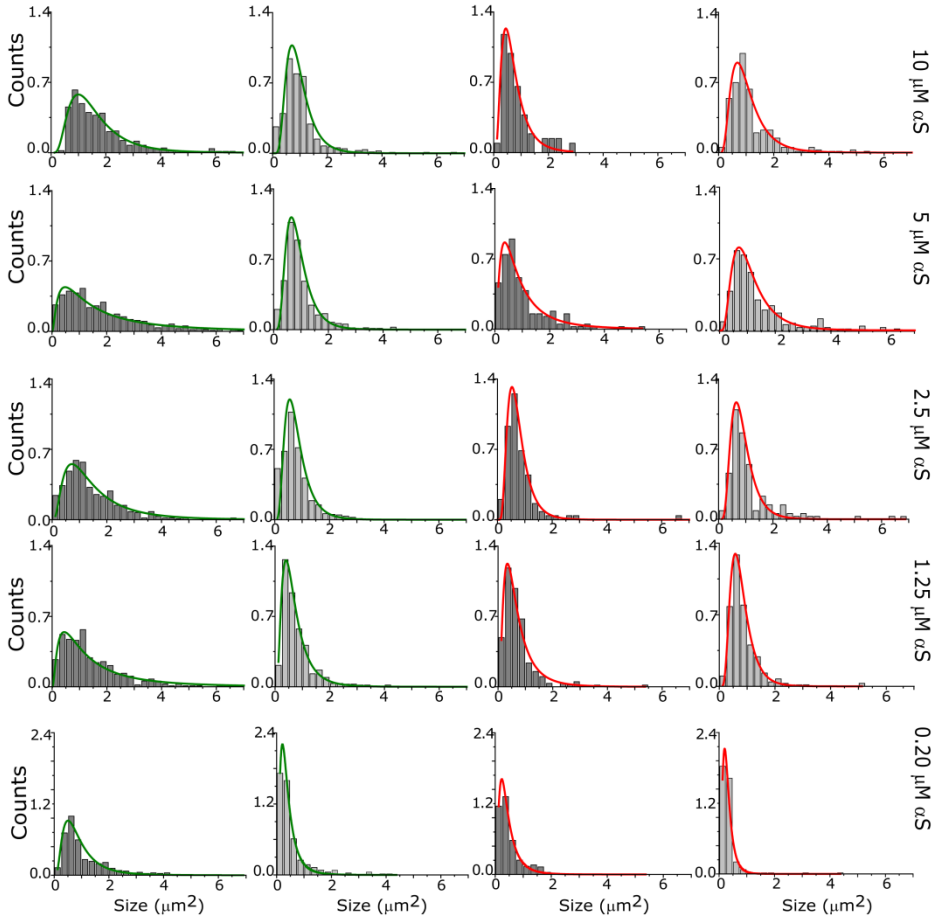

Figure 4.7: Aggregate area histograms of WT-αS and αS(Δ71-82) formed on POPC:POPG SLBs. Using the *ObjectCount* plugin in the Nikon NIS Elements software, a distribution of the aggregate areas was obtained (For details, see Figure 4.13. These distributions were area normalized to 1 and were fitted to a log-normal distribution. The WT-αS aggregate area distributions are represented by dark grey bars and the αS(Δ71-82) aggregate area distributions are represented by light gray bars. The aggregates of WT-αS, show a wider distribution (green fits) in 50% POPG SLBs as compared to the WT-αS in 25% POPG SLBs (red fits). In order to establish if the observed WT-αS clusters contain amyloid, SLBs containing 10 μM WT-αS clusters were incubated with Thioflavin T (ThT) for one hour. After washing off unbound ThT, most of the clusters seen in the protein channel were found to be positive for ThT fluorescence (Figure 4.8), confirming the formation of amyloid aggregates on the SLB surface[127,142]. The average intensities in all ThT positive clusters were at least 150 times higher than background intensities. It is interesting to note that not all clusters of WT-αS are positive for ThT fluorescence (Figure 4.8; Panel B).

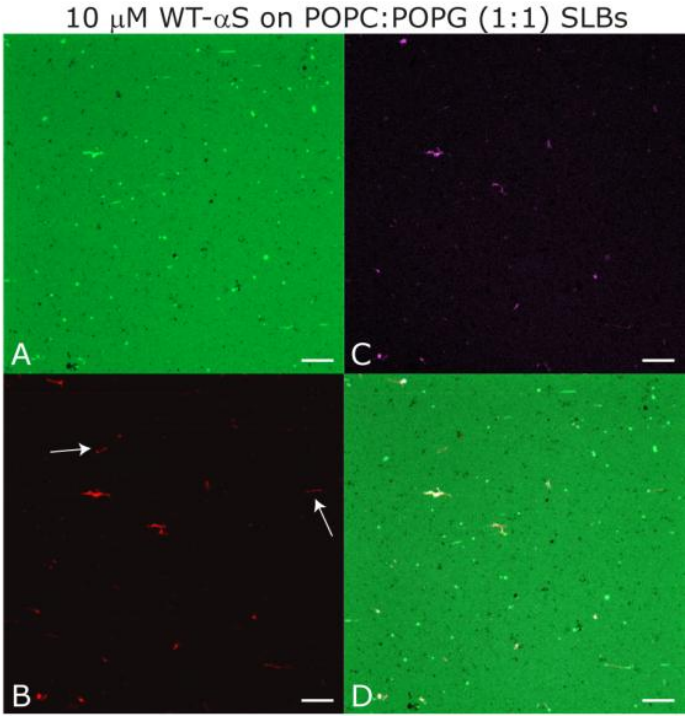

Figure 4.8: ThioflavinT (ThT) staining of WT-αS aggregates. Representative fluorescence images of POPC:POPG (1:1) SLBs depicting in the lipid channel (A) and coresponding protein channel (B) after 18 hr incubation of 10 μM labeled WT-αS on POPC:POPG SLB. The white arrows show aggregates of WT-αS which are not positive for Thioflavin T dye. (C) Fluorescence images taken after ThT staining of the WT-αS aggregates on POPC:POPG (1:1) SLBs. (D) Overlay of all channels. All images were taken at room temperature in 50 mM HEPES, 0.1 mM EDTA, pH 7.4 buffer. The scale bar is 10 μm.

To investigate if the clusters of WT-αS can reorganize and grow into bigger amyloid aggregates, we incubated the aggregates formed from 10 μM WT-αS after 18 hours on POPC:POPG (1:1) SLBs for another 24 hours. As expected for amyloid growth, we observe a marked increase in the protein aggregate size as shown in **Figure 4.9**. Closer inspection of the WT-αS amyloid aggregates show evidence of lipid fluorescence (arrows in **Figure 4.9**). This may be a result of lipids being extracted out of the membrane upon amyloid formation.

We see fewer protein aggregates at this stage which suggests that smaller aggregates fuse into bigger structures; however, an alternative explanation could be that the aggregates desorbed from the membrane.

Similar experiments were performed with POPC:POPG (50:50) SLBs at higher ionic strength. In the presence of 150 mM NaCl and identical buffer conditions similar protein clusters and membrane damage patterns were observed as in the absence of additional salt (**Figure 4.9C**).

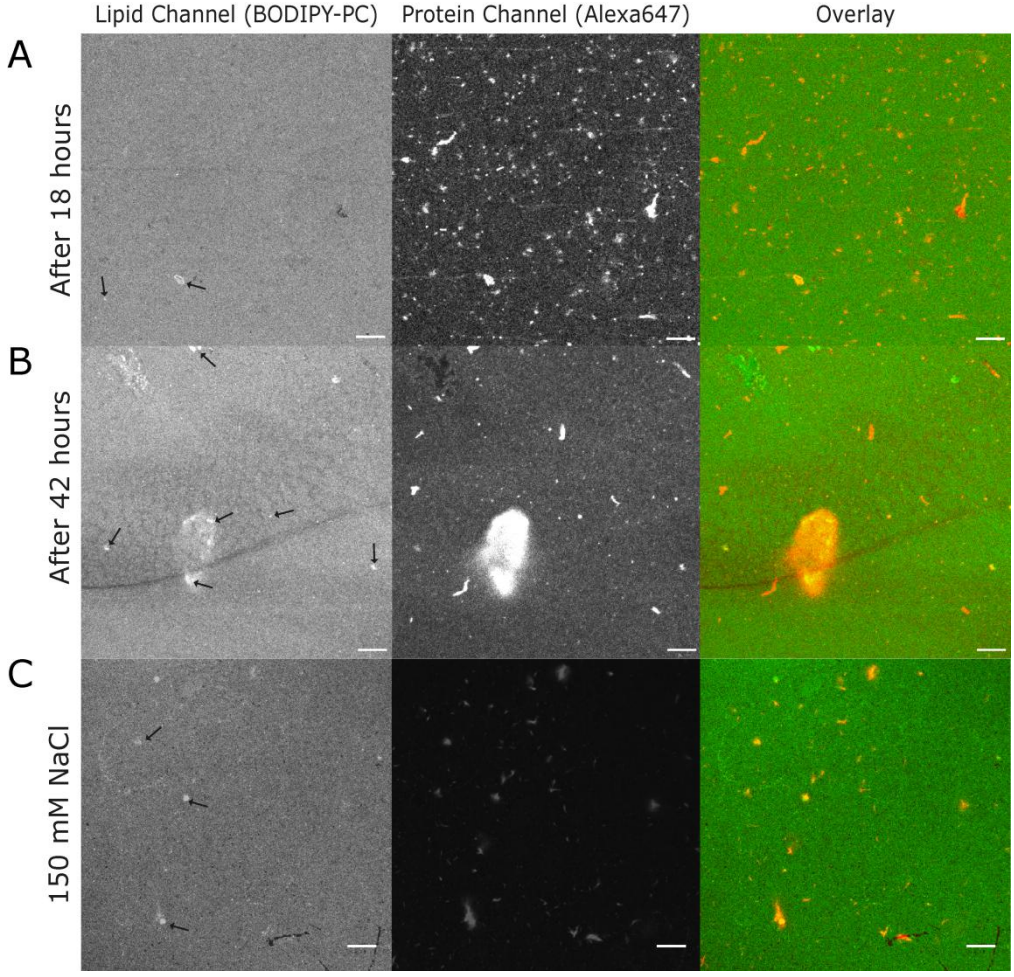

Figure 4.9: Time dependent growth of WT-αS aggregates on POPC: POPG (50:50) SLBs. Representative endpoint images obtained after incubation of 10 μM WT-αS on POPC:POPG (50:50) after 18 hours (panel A) and the same bilayer incubated for another 24 hours (panel B). Upon incubation for 18 hours, large aggregates are seen on the bilayer surface but these aggregates do not coincide with regions of high membrane damage. After 42 hours, very large aggregates appear that in some regions appear to incorporate lipids. The black arrows show lipids lining along the shape of the aggregate suggesting incorporation. C) Adsorption of αS on POPC : POPG (50:50) SLBs in presence of 150 mM NaCl. Representative images of adsorption of 10 μM WT-αS after an 18 hour incubation period in 50 mM HEPES, 150 mM NaCl, pH 7.4, 0.1 mM EDTA buffer. We observe formation of defects (Lipid channel) and macroscopic protein clusters (Protein Channel) as seen in absence of NaCl. All experiments were performed at room temperature. The scale bar is 10 μm.

4.2.3 Aggregation of αS affects lipid membrane mobility

Protein aggregation on SLBs requires that the observed clusters are mobile on the bilayer. This mobility would be affected by the protein-protein interactions required for aggregation into amyloid fibrils. The dependence of protein clustering on lipid composition further suggests that there are specific lipid-protein interactions. To characterize the aggregation state of αS, we used FRAP to probe the diffusion of WT-αS and αS(Δ71-82) on SLBs. We observed that at 10 μM protein concentration, the diffusion coefficient of WT-αS ($D_{\alpha S}$) had a much lower value (~ 0.14 μm^2/sec) than that for αS(Δ71-82) (~ 1.1 μm^2/sec) (**Figure 4.10A**) on POPC: POPG (75:25) SLBs. The αS(Δ71-82) variant diffuses much faster than the WT-αS at all protein concentrations and lipid compositions used. We attribute the faster diffusion to significantly reduced interactions between αS(Δ71-82) species as compared to that of WT-αS. Consistent with strong protein-protein interactions and amyloid formation we observed a decrease (up to 30%) in the mobile fraction of the WT-αS species with increasing concentrations of the protein (**Figure 4.10B**). The mobile fraction of αS(Δ71-82) does not change. We analyzed the average fluorescence intensities from the protein channel after incubation of labeled WT-αS and αS(Δ71-82) on POPC:POPG SLBs. SLBs incubated with different concentrations of WT-αS showed a linear increase in fluorescence intensity whereas SLBs with αS(Δ71-82) did not. Intriguingly, a similar trend was observed with WT-αS upon decreasing the percentage of negative lipids in the SLBs (**Figure 4.10C**).

After incubation for 18 hours, the unbound protein was washed off. Since the binding affinities of WT-αS and αS(Δ71-82) were comparable, the SLBs should be fully covered with αS at all concentrations used. Thus, after the washing step, the fluorescence intensity should have been comparable for SLBs incubated with WT-αS and αS(Δ71-82). The fact that we see an increase in fluorescence intensity with increasing concentration of WT-αS suggests direct adsorption of incoming WT-αS onto attached WT-αS species. A higher intensity could also be a result of compaction of existing aggregates into ordered structures, thereby creating space for incoming monomers.

To investigate the effect of αS binding on lateral mobility of lipids in POPC:POPG SLBs, we used fluorescent recovery after photo-bleaching (FRAP) using BODIPY-PC as a fluorescent lipid probe. The diffusion coefficient of BODIPY-PC in the absence of protein was found to be ~ 1.25 μm^2/sec, similar to values reported in literature for lateral diffusion of lipids in SLBs on glass surfaces[246,247]. The lipids were completely mobile (mobile fraction > 98%) and SLBs were found to be stable over an incubation period of at least 42 hours. Increasing concentrations of WT-αS (P/L ratios from 0.02 to 1) were incubated on separate SLBs for 18 hours. After 18 hour incubation with WT-αS, a drop in the diffusion coefficient of BODIPY-PC in SLBs was observed with increasing P/L ratios. At P/L ratios below 0.1, there is little effect

on the lipid bilayer fluidity, but starting from P/L ~ 0.1, we observe a drop in the diffusion coefficient of BODIPY-PC (D_B) (**Figure 4.10D**).

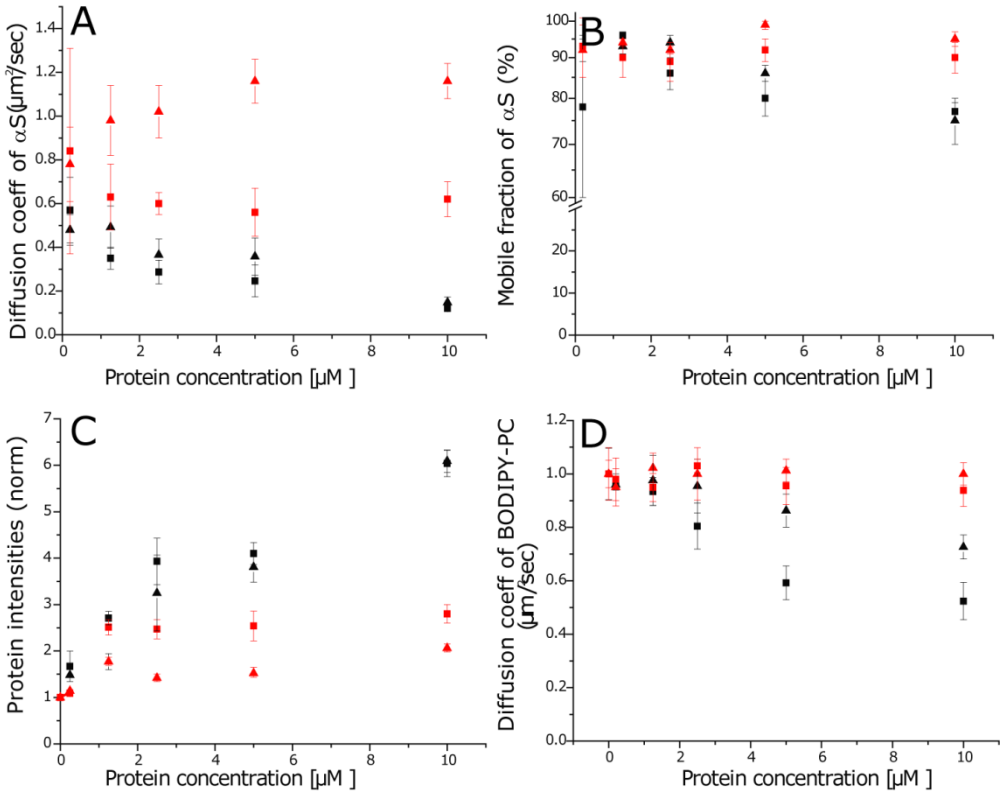

Figure 4.10: Effects of adsorption of αS on lipid and protein dynamics of the SLBs. In all the figures, measurements with WT-αS are shown with black symbols, those with αS(Δ71-82) with red symbols; measurements on 50% POPG-containing membranes are shown with square symbols and those on 25% POPG-containing membranes with triangular symbols. A) Apparent protein diffusion coefficients ($D_{\alpha S}$). B) Mobile fractions in protein channel obtained from FRAP upon incubation of WT-αS and αS(Δ71-82) on POPC:POPG SLBs in increasing concentrations. C) Average intensities (normalized to background of red channel) obtained from protein channels after 18 hour incubation and removal of unbound protein. The WT-αS clearly shows a concentration dependent rise in adsorbed protein irrespective of % of negative charge on SLBs, whereas αS(Δ71-82) intensities do not change with concentration. D) Protein concentration dependent changes in lateral diffusion coefficients of BODIPY-PC (D_B) relative to that in the absence of protein. The error bars indicate standard deviation obtained from five independent measurements in A), B), and C) and from ten independent measurements in D). All experiments were performed at room temperature in 50 mM HEPES, pH 7.4, 0.1 mM EDTA buffer. Note: the protein diffusion measurements (A and B) at 200 nM had poor signal to background and therefore much poorer fits to the recovery curves and greater variability in both diffusion coefficient and mobile fractions estimates.

The mobile fraction of BODIPY-PC remained unchanged upon incubation of WT-αS and αS(Δ71-82) at all protein concentrations and lipid compositions. D_B dropped by ~ 55% and ~ 30% on 50% POPG and 25% POPG SLBs respectively. Upon incubation of similar concentrations of αS(Δ71-82) on POPC:POPG SLBs, we found no change in the apparent diffusion coefficients of BODIPY-PC in either lipid composition as seen in **Figure 4.10D**.

The increase in the protein aggregate size coincides with the drop in D_B. Thus formation of small protein clusters is not enough to decrease the lateral diffusion of lipids, whereas aggregation of αS into larger clusters and/or amyloids with typical cross-β sheets is correlated with the decreased lateral diffusion of SLBs.

4.2.4 Amyloid formation and lipid extraction are correlated

To probe the effects of WT-αS aggregation and αS(Δ71-82) clustering on the integrity of SLBs, we systematically varied the concentration of αS on SLBs. 0.25 mol% BODIPY-PC was incorporated to visualize the SLBs. In the absence of protein, the bilayers were devoid of defects, cracks or any other inhomogeneities resolvable by our confocal microscope (**Figure 4.2; Control**). Upon adding increasing concentrations of WT-αS to separate SLBs, we observe a general loss of BODIPY-PC fluorescence intensity and appearance of defects with no lipid present (black regions in images) and patterns of elongated cracks with lower than average fluorescence intensities, suggesting damage to the SLBs (**Figure 4.2**) after 18 hours. We observed that the extent of this damage seems to reduce as the protein concentration is reduced (P/L ratio from 1 to 0.02) (**Figure 4.3**). In contrast to what was observed with WT-αS, when αS(Δ71-82) is added to the SLBs, there was much less evidence of damage to SLBs (**Figure 4.4**). αS(Δ71-82) did however form smaller clusters on the bilayer surface as seen in **Figure 4.2**. Control experiments involving SLBs incubated in buffer show no such damage over the time scale of the experiments. Moreover, these SLBs show negligible loss in BODIPY-PC fluorescence intensity over a period of at least 42 hours. The onset of aggregation of WT-αS to form amyloid structures is faster with increasing composition of negatively charged lipids[231]. Accordingly, to probe if amyloid formation was involved in the observed membrane damage, we decreased the proportion of negative lipids. Upon incubation of 10 μM protein on POPC:POPG (75:25) SLBs for 18 hours, we found that WT-αS causes fewer and smaller defects, whereas αS(Δ71-82) variants show almost no defect formation (**Figure 4.6**). We measured the lipid fluorescence in the buffer solution above the SLBs before and after incubation with protein for 18 hours. After protein incubation there is a concentration dependent increase in lipid fluorescence. This increase is about 3-4 fold larger for WT-αS than for αS(Δ71-82) (**Figure 4.11**).

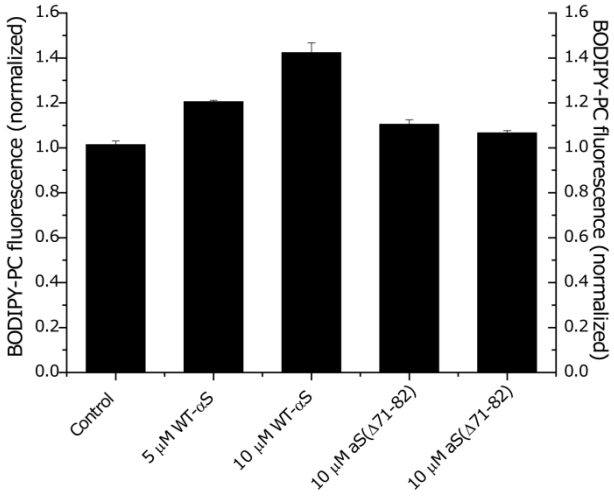

Figure 4.11: Lipid fluorescence in buffer after αS incubation on POPC:POPG SLBs. Relative increase in BODIPY-PC fluorescence seen in the buffer above the SLBs after incubation of αS variants over POPC: POPG (50:50) SLBs. All values were obtained by normalizing against the fluorescence obtained from buffer before incubation of αS variant. All experiments were performed at room temperature in 50 mM HEPES, 0.1 mM EDTA, pH 7.4 buffer.

These results suggest that the general loss of lipid fluorescence after incubation with WT-αS could be due to lipid extraction. We suggest that formation of amyloid structures in WT-αS occurs concurrently with extraction of lipids from the SLBs. To test if the loss in membrane fluidity, membrane damage and aggregate formation are influenced by the BODIPY probe, SLBs containing a small fraction of NBD-PC lipids were incubated with 5 μM and 10 μM WT-αS. Similar defects, cracks in the lipid membrane, and protein aggregate formation were observed. We conclude that the specific fluorescent probe does not influence our observations. We find the same decrease in D_B upon incubation with unlabeled protein (5 μM and 10 μM WT-αS) rather than 25% labeled and 75% unlabeled protein, confirming that there is no significant effect on D_B from adding the fluorophores.

4.3 Discussion

WT-αS and αS(Δ71-82) behave differently on SLBs. Collectively, the data presented here shows that the adsorption of protein to the membrane surface results in protein clustering. Depending on the interactions between proteins, this clustering can result in the formation of amyloid, which causes significant perturbations in the bilayer structure and dynamics. As the concentration of WT-αS is increased, the lipid structure is altered by formation of defects that appear to be devoid of lipid and by formation of a pattern of cracks with fewer lipids. Concurrently, the rate of diffusion of the lipid decreases, suggesting that diffusion is either hindered by the formation of cracks or slowed down by a strong association of lipid with protein clusters. As the concentration of αS(Δ71-82) variant is increased, there are a few

defects but there is no evidence of other perturbations to the lipid membranes. We see no cracks and D_B is unaffected. There is also minimal loss of lipid. The perturbations by the WT-αS on the SLBs become more severe as the time of incubation is increased from 18 hours to 42 hours. It is also important to note that there are no defects or lipid loss in samples without protein even after 42 hours.

The effects of the WT-αS on the membrane fluidity and integrity are generally lipid composition dependent and more pronounced at high fractions of negatively charged lipids (POPG). Changing the composition of the lipid does not change the effects of the αS(Δ71-82) variant on these membrane properties. Both WT-αS and αS(Δ71-82) are expected to adsorb on the membrane in comparable amounts owing to their comparable membrane binding. However, as the protein concentration is increased the amount of adsorbed WT-αS increases linearly whereas there is no change in the amount of adsorbed αS(Δ71-82) variant. Interestingly, the adsorption of the αS(Δ71-82) variant is lower on membranes with lower proportion of charged lipids, whereas that of the WT-αS is not. This is consistent with the additional adsorption of the WT-αS arising from protein-protein binding rather than protein-lipid binding.

Both the WT-αS and the αS(Δ71-82) variant appear to form small clusters of protein on the surface. As the concentration increases, the average area of these clusters increase by about a factor of two. At all concentrations, the average cluster area of the WT-αS is larger on the highly charged membranes. This agrees with the earlier observations that at high protein-to-lipid ratios, a high percentage of negative lipids increase the rate of aggregation of WT-αS [231]. Moreover, WT-αS is seen to form very large clusters of protein at high concentrations and longer incubation times. These large clusters are stained positively by ThT, supporting the conclusion that the proteins in the clusters tend to aggregate into amyloid fibrils. Such large ThT positive structures are not observed for the truncated variant. The largest amount of membrane damage occurs when amyloid structures form. We also observed formation of similar clusters and membrane damage at higher ionic strengths. Therefore, the most likely explanation for the observed membrane damage would be the aggregation of WT-αS into amyloids characterized by a significant cross-β sheet component on the membrane surface. The evidence for the extent of membrane damage is indirect, but support the conclusion that both lipid leaflets are removed since the fluorescence in these regions is reduced to background levels. In the cracks, the fluorescence is reduced, but not to the background levels, so these perturbations may be limited to the top leaflet. Defects in the SLBs are seen starting from P/L ratios of 1:10 and increase in frequency with higher concentrations. Vesicle permeabilization assays showed hardly any dye efflux with POPC:POPG LUVs [112], motivating us to test an alternative mechanism. Our data is consistent with a mechanism of membrane damage including lipid extraction and incorporation in amyloid structures.

Prior reports also suggest that αS variants having higher aggregation propensity cause significantly greater membrane damage in SLBs [127] or increased cell death of dopaminergic neurons in a rat model [75]. Thus aggregation into amyloids is likely to be the prerequisite for membrane damage. Previous studies on interaction of WT-αS with POPC:POPS (1:1)[106] and POPC:POPA (1:1)[231] supported lipid bilayers using atomic force microscopy (AFM)[106,231] also reveal defects and membrane disruption with formation of protein aggregates on the bilayer surface[106,231]. Recent studies with model vesicles suggest a membrane thinning mechanism[110]. WT-αS has previously been shown to cause phase separation and protein clustering to eggPG rich domains[143,248] in eggPC: eggPG (50:50) SLBs. In our experiments, we do not observe phase separation upon addition of WT-αS; this may be attributed to the choice of lipids. Aggregate sizes similar to those observed for αS have also observed for β-amyloid (1–40) on POPC/POPG SLBs [249].

The rate of diffusion of the WT-αS is lower than that of the αS(Δ71-82) variant at all concentrations and for both lipid compositions. While the WT-αS diffusion decreases at higher concentrations, that of the αS(Δ71-82) variant does not. Correspondingly, the fraction of mobile WT-αS decreases at high concentrations while the αS(Δ71-82) variant remains fully mobile. The decrease in mobile fraction of WT-αS is consistent with the formation of large amyloid aggregates and to the change in the lipid diffusion, suggesting a correlation between the two effects. The diffusivity of the WT-αS is independent of the lipid composition of the SLBs. However, the αS(Δ71-82) variant moves significantly faster on the less charged membrane. This may be related to the observation that there is less protein adsorbed, which would suggest that the protein diffusion is sensitive to protein concentration on the surface. Since there appears to be no difference in the average cluster area for the αS(Δ71-82) variant on two differently charged membranes, the difference in protein diffusion is not related to the cluster sizes.

If the changes in lipid and protein diffusion are linked, it could arise from direct protein-lipid bilayer interactions. This notion is supported by the observation that the large aggregates co-localize with lipids. The diffusion of the lipid D_B is therefore impaired by the diffusion of the protein $D_{\alpha S}$ in proportion to the amount bound to the protein as shown in equation 3 below:

$$D_B = f_a D_{\alpha S} + (1 - f_a) D_f \qquad (3)$$

Where D_f is the measured diffusion coefficient of BODIPY-PC in absence of any protein and f_a is the fraction of lipid bound. This relation assumes a rapid exchange between free and bound lipid on the time scale of the recovery of fluorescence (minutes).

Table 4.1 shows the calculated fractions (f_a) as a function of protein concentration. f_a increases with protein concentration and with the fraction of negatively-charged lipids in the SLBs in a self-consistent manner. Although BODIPY-PC exhibits reduced lateral mobility upon incubation with WT-αS, its mobile fraction remains close to unity at all protein concentrations used. This suggests that BODIPY-PC is not immobilized beneath or around the clusters. Thus the lipids in the SLBs must be able to exchange within the time scale of the measurement of fluorescence recovery.

Table 4.1: Cluster associated fractions of BODIPY-PC on POPC:POPG SLBs. The table below shows clusters associated fraction f_a obtained from equation 3. This fraction increases with the protein concentration and fraction of negative lipids. Note: the protein diffusion measurements at 200 nM had poor signal to background and therefore much poorer fits to the recovery curves and greater variability in both diffusion coefficients ($D_{\alpha S}$) and mobile fractions estimates. The error bars indicate standard deviations from 5 independent measurements.

	Protein Conc (μM)	Measured D_B (μm²/sec)	Measured $D_{\alpha S}$ (μm²/sec)	f_a (from model)	Mean cluster areas (μm²)
WT-αS on POPC:POPG (50:50) SLBs	10	0.75 ± 0.07	0.15 ± 0.02	0.39 ± 0.06	1.41 ± 0.02
	5	0.81 ± 0.06	0.36 ± 0.09	0.42 ± 0.06	1.50 ± 0.08
	2.5	0.87 ± 0.09	0.37 ± 0.07	0.33 ± 0.07	1.27 ± 0.07
	1.25	1.08 ± 0.05	0.49 ± 0.10	0.11 ± 0.04	1.21 ± 0.05
	0.20	1.14 ± 0.03	0.48 ± 0.07	0.05 ± 0.03	0.78 ± 0.03
WT-αS on POPC:POPG (75:25) SLBs	10	0.84 ± 0.04	0.12 ± 0.01	0.31 ± 0.02	0.77 ± 0.06
	5	1.04 ± 0.06	0.25 ± 0.07	0.18 ± 0.03	0.78 ± 0.03
	2.5	1.10 ± 0.10	0.29 ± 0.05	0.12 ± 0.04	0.68 ± 0.02
	1.25	1.08 ± 0.09	0.35 ± 0.05	0.09 ± 0.04	0.58 ± 0.02
	0.20	0.97 ± 0.06	0.57 ± 0.15	0.14 ± 0.11	0.38 ± 0.01
αS(Δ71-82) on POPC:POPG (50:50) SLBs	10	1.05 ± 0.04	0.62 ± 0.08	0.05 ± 0.03	0.95 ± 0.02
	5	1.02 ± 0.04	0.56 ± 0.11	0.06 ± 0.02	0.85 ± 0.01
	2.5	1.13 ± 0.09	0.60 ± 0.05	0.04 ± 0.01	0.72 ± 0.03
	1.25	1.04 ± 0.05	0.63 ± 0.15	0.04 ± 0.02	0.61 ± 0.08
	0.20	1.02 ± 0.07	0.84 ± 0.47	0.10 ± 0.05	0.34 ± 0.02
αS(Δ71-82) on POPC:POPG (75:25) SLBs	10	1.21 ± 0.06	1.16 ± 0.08	0.08 ± 0.03	0.93 ± 0.02
	5	1.21 ± 0.07	1.16 ± 0.10	0.08 ± 0.05	0.95 ± 0.05
	2.5	1.49 ± 0.02	1.02 ± 0.12	0.04 ± 0.01	0.81 ± 0.02
	1.25	1.42 ± 0.05	0.98 ± 0.16	0.03 ± 0.02	0.68 ± 0.04
	0.20	1.09 ± 0.08	0.78 ± 0.17	0.06 ± 0.04	0.27 ± 0.02

4.3.1 A model for aggregation of αS on SLBs.

Our operating model for the action of αS on SLBs is illustrated in **Figure 4.12**. αS initially binds the charged lipids in the membranes via a conformational change that involves the formation of amphipathic alpha helical structures. These adsorbed proteins interact to form small clusters which is the end point for the self-assembly of the αS(Δ71-82) variant. However in WT-αS, clustering is followed by aggregation allowing additional adsorption of the protein, and leading to amyloid-containing protein aggregates. These aggregates bind strongly to negatively-charged lipids (POPG), thereby reducing the effective mobility of the lipid mixture. The clusters weakly associate with POPC since the mobile fraction of BODIPY-PC is unchanged. If the protein aggregate detaches from the membrane it would lead to lipid loss.

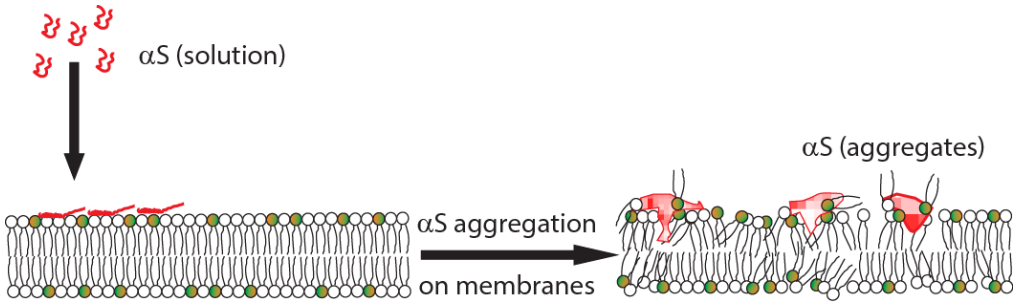

Figure 4.12: Proposed model of aS aggregation on lipid membranes.

4.4 Conclusions

We report that aggregation of WT-αS on lipid membranes leads to formation of amyloid structures which grow in time. This conversion of monomeric WT-αS to amyloid structures composed of lipids and WT-αS, is accompanied by significant membrane damage, lipid extraction, and reduced lateral mobility of lipids in SLBs. This happens more prominently at high protein to lipid ratios. The αS(Δ71-82) variant fails to form amyloids on the bilayer surface and thus is not able to damage lipid membranes. Overall, our data suggests that aggregation of WT-αS on lipid membranes affects membrane integrity. Whether the membrane damage observed in our experiments arises from a distinct amyloid species or the process of amyloid formation remains to be established.

4.5 Materials and methods

Stock solutions of 1-palmitoyl-2-oleoyl-*sn*-glycero-3-phosphocholine (POPC), 1-palmitoyl,2-oleoyl phosphatidylglycerol (POPG), and 1-palmitoyl-2-[6-[(7-nitro-2-1,3-benzoxadiazol-4-yl)amino]hexanoyl]-*sn*-glycero-3-phosphocholine (NBD-PC) in chloroform were purchased from Avanti Polar Lipids (Birmingham, AL) and used without further purification. Ethylenediaminetetraacetic acid (EDTA) was purchased from Sigma Chemicals (St. Louis, MO). Sodium chloride (NaCl), sodium hydroxide (NaOH), and 4-(2-hydroxyethyl)-1-piperazineethanessulfonic acid (HEPES) were purchased from Merck (Germany). Alexa Fluor 647 C2 maleimide and β-BODIPY® FL C5-HPC (2-(4,4-Difluoro-5,7-Dimethyl-4-Bora-3a,4a-Diaza-s-Indacene-3-Pentanoyl)-1-Hexadecanoyl-*sn*-Glycero-3-Phosphocholine was purchased from Invitrogen (Carlsbad, CA).

4.5.1 Substrate Pretreatment

Glass cover-slips were washed in 2 % Hellmanex (VWR International, Chicago, IL) at 80° C for 60 minutes, rinsed exhaustively with deionized water and then dried with a stream of nitrogen. The slides were etched for 8 minutes in a solution of 3:1 (v/v) concentrated sulfuric acid (H_2SO_4) and 30% hydrogen peroxide (H_2O_2). The slides were stored in MilliQ water, and were used within 3 days after treatment.

4.5.2 Vesicle and supported lipid bilayer preparation

Lipid stock solutions of POPC and POPG in chloroform were mixed in 1:1 or 3:1 molar ratios along with 0.25 mol% of fluorescent lipid BODIPY-PC, dried under a stream of nitrogen, and placed under vacuum for 1 h. After drying, the lipid films were rehydrated in 100 mM NaCl solution. Large unilamellar vesicles (~ 500 μM in lipids) were prepared by extruding the solution 21 times through 100 nm polycarbonate membranes. The vesicles were stored at 4 °C and used within 3 days. Supported lipid bilayers were formed by vesicle fusion inside a 120 μL custom built chamber on appropriately treated glass slides. The extruded vesicles were mixed with 1 M NaCl solution at a 1:1 ratio to induce fusion as reported before[143]. After 20 min incubation, excess vesicles were removed from the chamber by rinsing with a 50 mM HEPES, 0.1 mM EDTA, and 750 mM NaCl, pH 7.4 buffer. Thereafter the chamber was rinsed with 50 mM HEPES, 0.1 mM EDTA, pH 7.4 buffer to remove salt. At least 3 mL of buffer were passed through the chamber to ensure complete solvent exchange.

4.5.3 Expression, purification and labeling of αS

Since WT-αS does not contain any cysteine residues necessary for fluorescent labeling, an alanine to cysteine mutation was introduced at residue 140. The WT-αS-A140C variant was

expressed in Escherichia coli strain BL21 (DE3) using the pT7-7 expression plasmid and purified in the presence of 1 mM DTT as previously reported[224]. The cDNAs for the truncated variant of αS lacking 71-82 residues (αS(Δ71-82)) were obtained from Prof. Benoit Giasson from University of Florida (USA). The cDNA was cloned into a pT7-7 expression plasmid and purified. For labeling αS(Δ71-82), an alanine to cysteine mutation was introduced at residue 140 as for the WT-αS. Prior to labeling, both WT-αS-A140Cand αS(Δ71-82)-A140C were reduced with a five-fold molar excess of DTT for 30 min at room temperature. The samples were desalted with Pierce Zeba desalting columns, followed by the addition of a two-fold molar excess of Alexa 647 (AL647) C2 maleimide dye (Invitrogen) and incubated for two hours in the dark at room temperature. Free label was removed using two desalting steps. The protein labeling efficiency was estimated to be 90% from the absorption spectrum. Before use, the protein was diluted with 50 mM HEPES, 0.1 mM EDTA, pH 7.4 buffer to the desired concentrations.

4.5.4 Imaging of supported lipid bilayers and proteins

All measurements were performed on a Nikon (Tokyo, Japan) A1 confocal microscope equipped with a perfect focus system (PFS). SLBs were visualized by incorporating 0.25 mol% BODIPY-PC. To visualize the proteins, a mixture of 25% labeled and 75% unlabeled protein was used. The SLBs were prepared as reported before[143]. In a typical experiment, exactly two times the chamber volume (~ 240 µl) of the desired concentrations of the protein was flushed into the perfusion chamber with an oil-free pump. The proteins were incubated with the SLBs for 18 hours at room temperature. Thereafter the unbound protein was washed off with 50 mM HEPES, 0.1 mM EDTA, pH 7.4 for 10 minutes to remove background fluorescence from the unbound protein in the solution. While the washing step could potentially lead to desorption, within the time frame of the measurements we see less than 10% decrease in the protein fluorescence from these bilayer systems. Images were acquired using a 63X water immersion, 1.30 NA objective combined with a 2X optical zoom. The acquired images consisted of 512 × 512 pixels with a pixel size of 0.41 × 0.41 µm. All images were collected under identical conditions of power and gain. For visualization purposes only, the contrast threshold was set to a constant value, allowing comparison of all images.

4.5.5 Image processing and cluster analysis

The Nikon NIS Elements *ObjectCount* module was used for area estimation of αS clusters. Using intensity thresholding, areas of αS clusters were calculated automatically from the pixel areas in at least 10 images per protein concentration. Since the number of clusters and their sizes depend directly on the level of the threshold set, we systematically varied the threshold (**Figure 4.13**) to choose an optimum threshold.

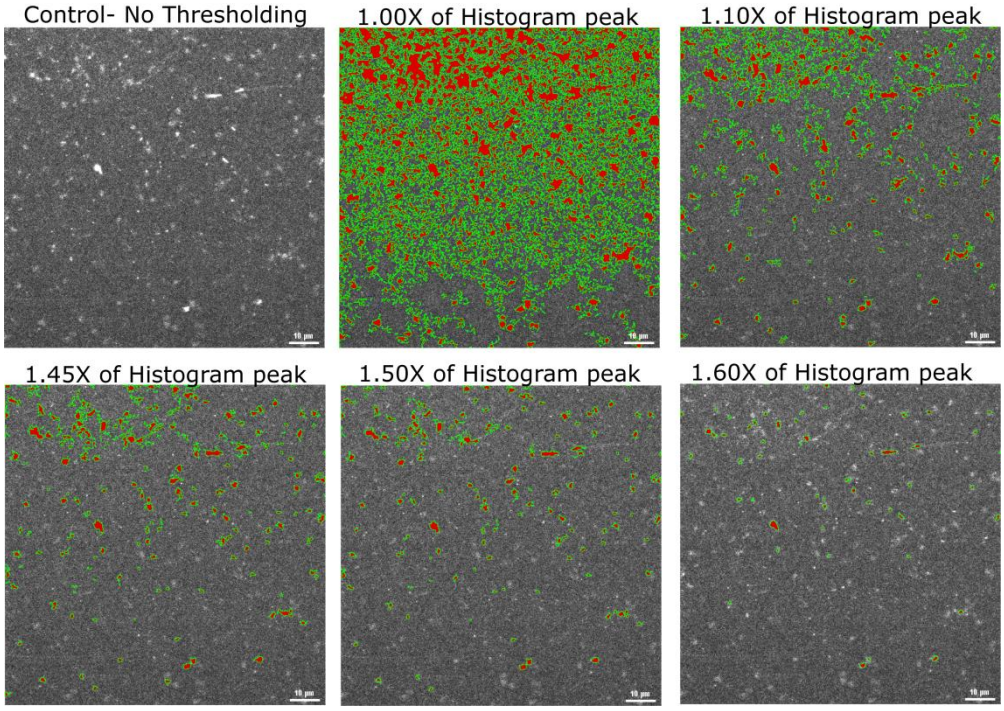

Figure 4.13: Optimizing thresholding parameters for cluster analysis. Using the Nikon NIS Elements software, the *ObjectCount* plugin was used to set an intensity threshold. To choose an optimum threshold, the thresholding point was varied along the intensity histogram in the protein channel. As seen in the figure, a thresholding value of 1.60X leads to exclusion of certain aggregates and a value up to 1.45X leads to over-estimation of cluster sizes. Thus 1.50X was chosen as a thresholding value for all images. All images were taken at room temperature in 50 mM HEPES, 0.1 mM EDTA, pH 7.4 buffer.

For each image, the intensity threshold was fixed to 1.5 times the peak intensity of its intensity histogram, avoiding under- or over-sampling. The cluster area distribution for each protein concentration was fit to a log-normal distribution to get an average cluster area[250].

4.5.6 Fluorescence Recovery After Photobleaching (FRAP)

FRAP was used to determine the diffusivity of lipids in the bilayer and of the labeled protein on the lipid bilayer after incubation. FRAP was performed on a NikonA1 confocal microscope. A 100-mW Argon ion laser (488 nm, Coherent, CA) was used to both bleach and monitor the lipid bilayer fluorescence. A 30-mW laser (647 nm, Coherent, CA) was used to bleach and monitor protein fluorescence. In the FRAP experiment, fluorescence from a circular region of interest (ROI) was bleached (radius ~ 12 μm) in 1.5 s. After bleaching, the increase in fluorescence intensity in the ROI was monitored for 8 minutes. During the experiment there was only a minimal drop in the fluorescence intensity in the reference ROI. All FRAP data were fitted using the Soumpasis fit[182] which has been shown to better model membrane/protein

diffusivity than a single exponential fit[183], yielding the diffusion coefficients and mobile fractions of the probed entity.

4.5.7 Circular dichroism (CD) spectroscopy

A Jasco J-715 spectropolarimeter was used to obtain CD spectra at protein concentrations of 3 μM in solution. Spectra were recorded between 190 to 260 nm with a step size of 0.5 nm and a scanning speed of 10 nm/min using a 1 mm path length cuvette. The apparent dissociation constants (Kd_{app}) for both proteins were determined by titrating them against POPC:POPG (50:50) SUVs and fitting the measured mean residue ellipticity at 222 nm, *R,* to the solution of the binding equilibrium equation:

$$P + \frac{L}{n} \leftrightarrow R \qquad (1)$$

By assuming equilibrium binding and applying the law of mass action, solving for *R (*detailed calculations in **Appendix A**), we obtain:

$$R = R_O - (R_O - R_f)\frac{Kd_{app} + P + \frac{L}{n} + \sqrt{(Kd_{app} + P + \frac{L}{n})^2 - 4P\frac{L}{n}}}{2P} \qquad (2)$$

where *R* is the measured signal (MRE at 222 nm, corrected for dilution) at a given lipid concentration, *L* is the total lipid concentration, and *P* is the total concentration of the protein. Kd_{app} is the apparent macroscopic dissociation equilibrium constant, and *n* is the binding stoichiometry (lipids/protein). R_f and R_o are the final (corrected for dilution) and initial mean residue ellipticities respectively. This equation assumes that all lipid-binding sites are equivalent and that Kd_{app} does not depend on the lipid/protein ratio[108]. Since αS adopts a helical conformation upon membrane binding[91], titration of WT-αS and αS(Δ71-82) with POPC/POPG (1:1) SUVs allows an estimate of Kd_{app} from the characteristic band at 222 nm.

4.6 Acknowledgements

The authors thank Prof. Benoit I. Giasson from University of Florida for providing the plasmids for the 71-82 synuclein construct, Kapil Dev Singh from University of Zürich for providing a script for data analysis, and Nathalie Schilderink from University of Twente for assistance with αS expression, purification, and labeling. This work was supported by "Stichting voor Fundamenteel Onderzoek der Materie" (FOM), Nederland as a part of the FOM program titled "A Single Molecule View on Protein Aggregation". N.O.P.'s visit to the Netherlands was supported by visitors travel grant 040.11.389 from the Netherlands Organization for Scientific Research (NWO).

5

The impact of N-terminal acetylation of alpha synuclein on phospholipid membrane binding & fibril structure

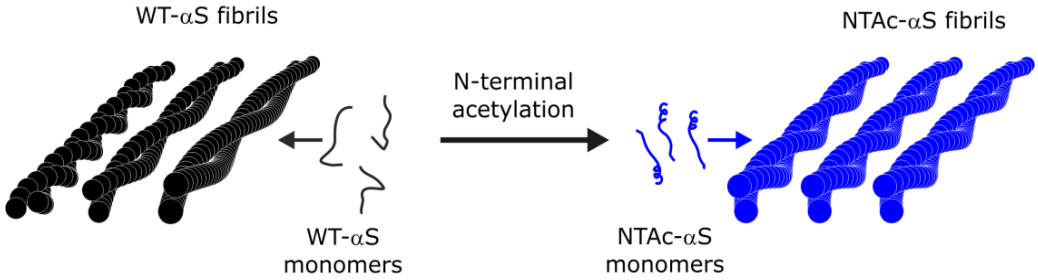

Iyer, A., Schilderink, N, Roeters, S., Hommersom, B., Heeren, R., Woutersen, S., Claessens, M. M. A. E and Subramaniam, V. *Effect of N-terminal acetylation in alpha synuclein on its membrane binding properties and fibril structure*. This chapter has been submitted for publication.

5.1 Introduction

Alpha synuclein (αS) is an intrinsically disordered monomeric protein found in particularly high concentrations at the synaptic junctions of neuronal cells[56,191,251]. Its physiological function and precise role in the etiology of Parkinson's disease (PD) remain, to date, unknown. The binding of αS to phospholipid membranes observed *in vitro* is thought to be relevant for its function in eukaryotic cells and may facilitate the αS aggregation cascade that possibly leads to neuronal cell death in PD. The phospholipid membrane binding and aggregation of αS have been extensively characterized *in vitro*[80,120,126,155,190,200,252]. Although αS is known to be subject to posttranslational modifications[56,84], most of these investigations used αS that was recombinantly expressed in bacteria, and are thus not post-translationally modified. Post-translational modifications (PTMs) such as phosphorylation, ubiquitination or acetylation are used by eukaryotic cells to modulate protein conformation and/or function. More than 90% of eukaryotic cellular proteins are N-terminally acetylated[253,254] and it is now established that N-terminal acetylation is the predominant PTM in αS[87,88].

In vivo, the influence of N-terminal acetylation of αS on its aggregation into amyloid fibrils is unknown, while existing *in vitro* reports are contradictory[115,255,256]. Considering the critical role of the N-terminal residues of αS in phospholipid membrane binding[84,102,257], N-terminal acetylation may considerably affect, and perhaps even regulate, membrane binding. We therefore probed how this αS modification impacts αS's affinity for phospholipid membranes and investigated how it affects the aggregation into amyloid fibrils. In this chapter, the membrane binding properties of bacterially expressed N-terminally acetylated αS (NTAc-αS) and αS purified from human erythrocytes (Endo-αS) was assessed by systematically varying charge density and cholesterol content of both large unilamellar vesicles (LUVs) and highly curved small unilamellar vesicles (SUVs) using circular dichroism (CD) spectroscopy.

Our observations show that N-terminal acetylation does not significantly influence the membrane binding affinity of αS as a function of membrane anionic charge, cholesterol content and curvature. The effect of acetylation is more pronounced in the kinetics of αS aggregation into amyloid fibrils. We used atomic force microscopy (AFM) and two-dimensional infra red spectroscopy (2D-IR) to extract qualitative and quantitative information on the structure of fibrils of NTAc-αS and Endo-αS (henceforth acetylated-αS) and WT-αS. Our results suggest that the fibril structure of both types of acetylated-αS is a well-defined distribution of different beta sheet structures differing markedly from the WT-αS.

5.2 Results and Discussion

To confirm that the bacterially expressed NTAc-αS was correctly acetylated, we first characterized the purified WT-αS, acetylated-αS using electrospray ionization mass spectrometry (ESI-MS) and acetic acid gel electrophoresis. The ESI-MS results show that all three αS variants were monomeric with WT-αS having the expected molecular weight of 14459 Da. The molecular weight of NTAc-αS (14502 Da) confirms the presence of a single acetyl group in NTAc-αS. The molecular weight of NTAc-αS was identical to that of Endo-αS suggesting the absence of any other post-translational modifications in Endo-αS (**Figure 5.1A**).

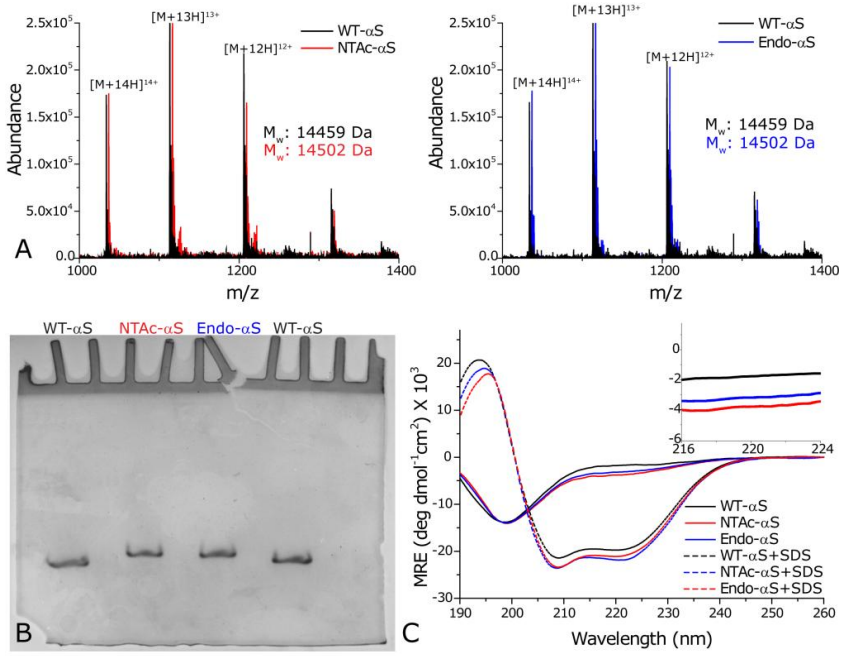

Figure 5.1: Biochemical characterization of αS variants. A) ESI-MS data of purified monomeric WT-αS, NTAc-αS and Endo-αS respectively. All samples were prepared in 10 mM ammonium acetate buffer with the concentration of αS monomers kept constant at 15 μM. For a given m/z value, the corresponding charge state is indicated. Molecular weights (M_w) were calculated as follows: m/z value = $[M+xH]^{x+}$. M_w = (m/z value * x) - x. B) Acetic acid gel electrophoresis data of monomeric WT-αS, NTAc-αS and Endo-αS. 5 μM of each protein samples was loaded into gels and as shown above, the relative migration of WT-αS was more than that of acetylated-αS which migrated at similar positions. C) CD spectra showing the conformational transition from a random coil to a α-helix upon the addition of SDS micelles. The inset shows the slightly higher absorbance of acetylated-αS at 222 nm compared to WT-αS. All data obtained with WT-αS is depicted with black, with NTAc-αS with red and with Endo-αS with blue colors respectively.

The slower migration of both acetylated-αS in the acetic acid gel electrophoresis experiment compared to WT-αS confirmed the loss of a positive charge upon αS acetylation[255] and the absence of any high molecular weight species (**Figure 5.1B**) in our preparations.

To address the possible effect of N-terminal acetylation on the secondary structure of free and phospholipid membrane bound αS, we acquired CD spectra of both acetylated-αS's and WT-αS in buffer with and without phospholipid membrane-mimicking SDS micelles. The resulting spectra showed typical random coil and helix conformations for all three proteins in buffer solution and on SDS micelles respectively (**Figure 5.1C**). The slightly higher absorbance in the 222 nm region for the unstructured acetylated-αS (**Figure 5.1C, inset**) agrees with the higher helical content of αS in solution observed in NMR experiments[255]. These NMR experiments indicate that N-terminal acetylation impacts the first 12 residues in αS resulting in a small increase in the helical propensity[255]. The stabilization of α-helical structure in N-terminally acetylated-αS is not unique but is generally observed in other proteins with this PTM[258,259]. The strength of αS/lipid phospholipid membrane interactions is often quantified using spectroscopic methods, in particular CD[108,120,260] and pulsed EPR[101,261]. Recent studies using NMR suggest that NTAc-αS has a slightly higher affinity than WT-αS for phospholipid vesicles[255,262]. To systematically characterize the binding of both acetylated-αS and WT-αS to phospholipid membranes in more detail using CD spectroscopy[108], we varied the percentage of the anionic lipid POPS (100, 75, 50, 25 and 0 %) in small unilamellar POPC:POPS vesicles (SUVs) as shown in **Figure 5.2**. To be able to compare αS binding to the membranes of various phospholipid compositions, we determined the phospholipid concentration at which 50% of the αS was bound to vesicles (L_{50}). At the conditions used, the L_{50} approximates the equilibrium dissociation constants (K_d). The L_{50} values as a function of the fraction of anionic lipids are given in **Table 5.1**.

Table 5.1: L_{50} values (μM) of monomeric αS for different lipid compositions. [a]The binding data in these cases could not be fitted to the binding equation. N.D: Not determined.

Lipid and protein	POPS (100)	POPC:POPS (25:75)	POPC:POPS (50:50)	POPC:Chol (50:50)	POPS:Chol (50:50)	POPC:POPS (75:25)	POPC (100)
				SUVs			
WT-αS	57 ± 4	333 ± 7	294 ± 8	> 2500 [a]	539 ± 30	638 ± 11	> 2500 [a]
NTAc-αS	54 ± 4	302 ± 10	310 ± 18	> 2500 [a]	455 ± 32	576 ± 15	1905 ± 65
Endo-αS	57 ± 5	257± 18	263 ± 16	> 2500 [a]	445 ± 31	524 ± 26	1967 ± 136
				LUVs			
WT-αS	572 ± 72	N.D	> 2000 [a]	> 2500 [a]	N.D	N.D	> 2500 [a]
NTAc-αS	500± 32	N.D	> 2000 [a]	> 2500 [a]	N.D	N.D	> 2500 [a]
Endo-αS	547± 21	N.D	> 2000 [a]	> 2500 [a]	N.D	N.D	> 2500 [a]

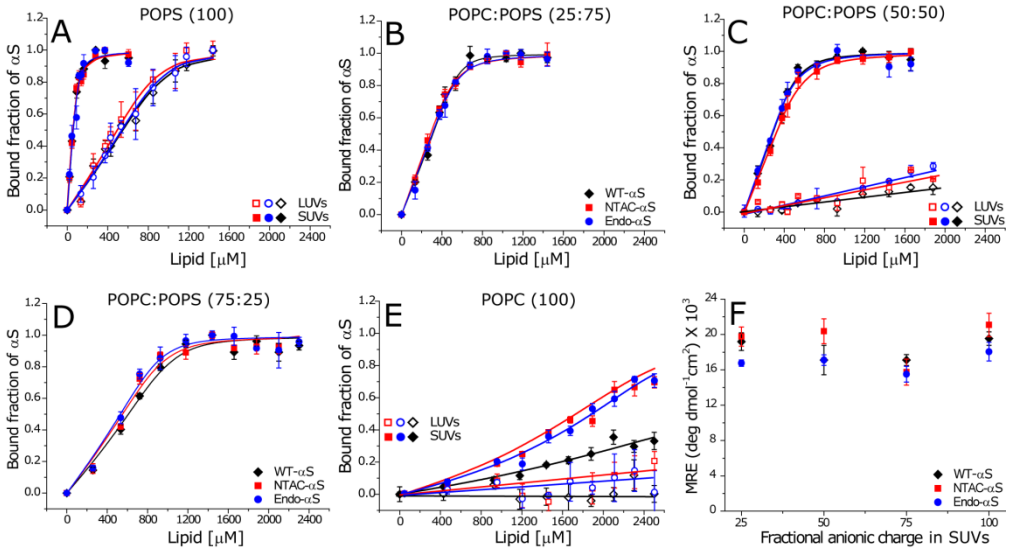

Figure 5.2: Membrane binding characteristics of WT-αS, NTAc-αS and Endo-αS. All data obtained with WT-αS is depicted with black diamonds/lines, with NTAc-αS with red squares/lines and with Endo-αS with blue circles/lines. Open symbols in panel A/C/E represent data obtained in the presence of LUVs and closed symbols represent data obtained in presence of SUVs. A-D) Binding curves of αS to 100% POPS liposomes (panel A), 25:75 POPC:POPS (panel B), 50:50 POPC:POPS (panel C) and 75:25 POPC:POPS (panel D) showing no differences in membrane binding of acetylated-αS compared to WT-αS. E) Binding curves of αS to POPC liposomes show hardly any binding of αS to membranes of this composition but acetylated-αS has a slightly higher affinity for 100% POPC SUVs than WT-αS. F) Average mean residual ellipticities (MRE) values were obtained from the plateau phase of the binding curve obtained from CD spectroscopy measurements showing insignificant differences for either WT-αS or either acetylated-αS indicating a similar size of helical domain on lipid membranes. All measurements were performed at room temperature in the presence of 10 mM Tris, 100 mM KCl buffered at pH 7.4. The error bars in all binding curves represent standard deviations from 3 independent measurements. The binding curves for LUVs (open symbols) shown in panel C and E could not be fitted using the solution to a simple quadratic equation[108] and the depicted lines are only a guide to the eye.

The L_{50} values for both acetylated-αS molecules are comparable for all percentages of POPS in SUVs tested (**Figure 5.2A-E; solid symbols**) and show little difference from the L_{50} values found for WT-αS with the exception of POPC SUVs (**Figure 5.2E; solid symbols**). Binding of WT-αS to POPC SUVs was slightly weaker than binding of acetylated-αS. Considering that acetylated-αS has considerable α-helical structure in solution[255], the loss in conformational entropy upon binding to phospholipid membranes is probably lower for acetylated-αS than that for the unstructured WT-αS . Because the final helical content of both membrane bound αS's is comparable (**Figure 5.2F**), the net free energy gain upon binding of WT-αS to POPC membranes is larger, resulting in a slightly lower affinity of WT-αS for membranes of zwitterionic lipids. Upon increasing the fraction of POPS in the phospholipid membrane, electrostatic interactions between lysines and negatively charged headgroups dominate and likely mask the contribution of the conformational entropy.

Next, we investigated the influence of αS acetylation on the membrane curvature dependent binding of αS. It is known that WT-αS binds better to SUVs (25-40 nm diameter) than LUVs

(100-200 nm diameter). The higher affinity of WT-αS possibly results from the presence of intrinsic defects in SUVs which result in increased exposure of the hydrophobic acyl regions to αS[104,108]. **Figure 5.2A, C and E** show that with decreasing liposome curvature the L_{50} values increase by at least an order of magnitude for the POPS liposomes. As shown in **Figure 5.2C and E** we could not determine the L_{50} values for the LUVs composed of 1:1 POPC:POPS or POPC or 1:1 POPC:Chol (**Figure 5.3**) because hardly any phospholipid membrane binding was detectable by CD spectroscopy. Previous reports comparing the binding of NTAc-αS and WT-αS to SUVs and LUVs of similar equimolar mixtures of anionic and neutral phospholipids (DOPS and DOPC/DOPE) using NMR found no influence of acetylation on the apparent dissociation constants[262]. Although we observe a lower affinity of αS to LUVs of most POPC:POPS mixtures compared to SUVs of the same composition, the L_{50} values for both acetylated-αS species are comparable to the values for WT-αS indicating that acetylation has no significant influence αS binding to liposomes. N-terminal acetylation only seems to affect the (weak) binding of αS to zwitterionic POPC vesicles.

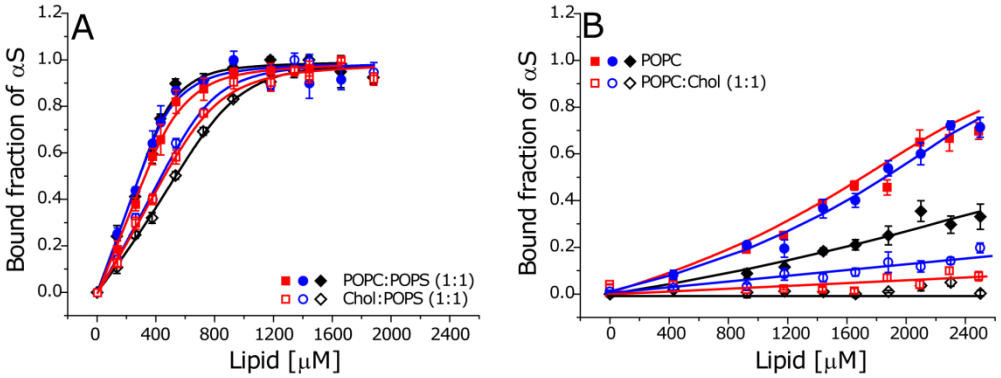

Figure 5.3: Membrane binding characteristics of WT-αS, NTAc-αS and Endo-αS to SUVs containing cholesterol. A) Binding curves comparing the affinity of αS to 1:1 Chol:POPS SUVs (open symbols) and 1:1 POPC:POPS SUVs (closed symbols). B) Binding curves of αS to 1:1 POPC:Chol SUVs (open symbols) and POPC SUVs (closed symbols). The binding curves for LUVs (open symbols) shown in panel B could not be fitted using the solution to a simple quadratic equation[108] and the depicted lines are only a guide to the eye. All measurements were performed at room temperature in the presence of 10 mM Tris, 100 mM KCl buffered at pH 7.4. The error bars in all binding curves represent standard deviations from 3 independent measurements.

Cholesterol is a critical component of cellular membranes and has been shown to affect the binding of αS[263]. Estimations of the plasma membrane composition in existing literature report an equimolar ratio of cholesterol and phospholipids[151,264]. To test the effect of the presence of cholesterol on the binding of acetylated-αS, we used vesicles composed of 1:1 mixtures of cholesterol and either POPC or POPS. We observed that the presence of cholesterol in SUVs of the anionic lipid POPS decreases the binding affinity by ~ 2 fold for both acetylated-αS and WT-αS. Inclusion of cholesterol in SUVs of the zwitterionic phospholipid POPC nearly abolished

membrane binding of both acetylated and WT-αS (**Figure 5.3B**) in CD spectroscopy measurements. The observations that cholesterol can promote the lipid ordering at the equimolar phospholipid/cholesterol ratios used in our study[216,265,266] and the reduced affinity of αS for such ordered lipid phases[136] may explain these observations. Acetylation does not seem to have any effect on binding of αS to cholesterol containing membranes.

Although we did not observe significant changes in phospholipid membrane binding affinity of αS after acetylation, the acetylation may affect the tendency of αS to aggregate into amyloid fibrils. The impact of N-terminal αS acetylation on its aggregation rate is unclear, with contradicting reports in the existing literature[115,116,255,256]. To probe the influence of acetylation on aggregation into amyloid fibrils, fibril growth was examined using a Thioflavin T (ThT) fluorescence assay. The normalized ThT fluorescence of both acetylated-αS and WT-αS exhibit a typical sigmoidal shape (**Figure 5.4A-C**).

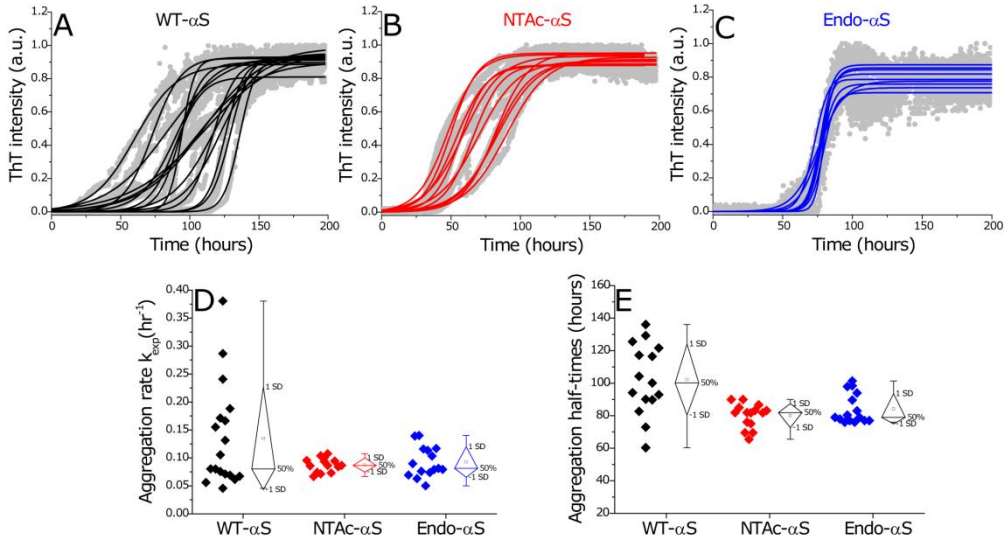

Figure 5.4: Aggregation kinetics of WT-αS, NTAc-αS and Endo-αS at 37 °C monitored by measuring ThT fluorescence. The aggregation reaction was carried out with a protein concentration of 35 μM of WT-αS (black symbols), NTAc-αS (red symbols) and Endo-αS (blue symbols) using PBS buffer at 300 rpm in a TECAN fluorescence micro-plate reader at 37 °C (panel A-C). The exponential phase aggregation rates (panel D) and the corresponding aggregation half-times (panel E) were obtained from the aggregation curves as mentioned elsewhere[252]. The ThT concentration was 5 μM.

The aggregation lag times and aggregation rates obtained from sigmoidal fits are highly variable for WT-αS while narrow distributions are found for the acetylated-αS (**Figure 5.4-E)**. Although, surface induced aggregation can lead to variability in fibrillization kinetics, both WT-αS and acetylated-αS monomeric samples were monitored on the same micro-plate under identical conditions. It is therefore reasonable to assume that the heterogeneity in fibrillization kinetics reported by ThT is a result of N-terminal acetylation in αS. The narrow lag-time

distribution observed for acetylated-αS compared to WT-αS suggests that acetylation results in the nucleation of a more homogenous population of fibrils. Morphological analysis of samples obtained at the plateau phase of ThT fluorescence using AFM and scanning transmission electron microscopy confirmed that both acetylated-αS and WT-αS formed fibrillar aggregates (**Figure 5.5A**).

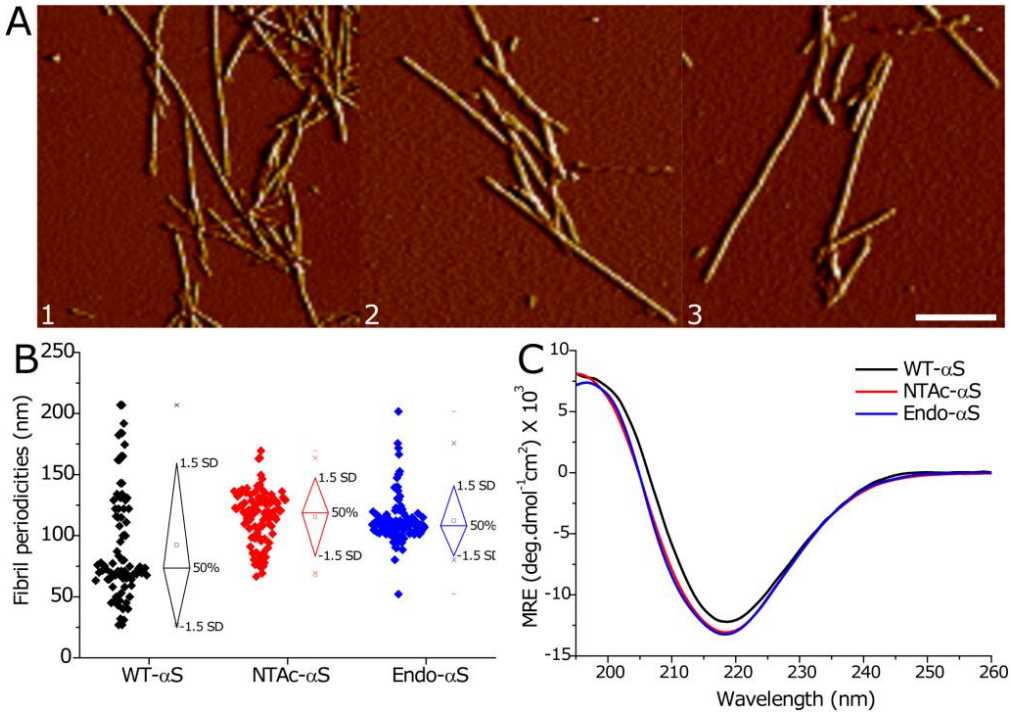

Figure 5.5: AFM and CD spectroscopy of WT-αS and acetylated-αS fibrils. A) AFM amplitude images depicting fibrillar aggregates of WT-αS (panel 1), NTAc-αS (panel 2) and Endo-αS (panel 3). The scale bar is 250 nm. B) Fibril periodicities measured from AFM images show slightly higher values for acetylated-αS compared to WT-αS. C) CD spectroscopy of purified αS fibrils show slightly higher β sheet content in acetylated-αS fibrils than WT-αS fibrils. All fibrils were prepared in PBS buffer solutions and purified after aggregation to remove monomers.

Fibril heights of WT-αS and both acetylated-αS species obtained from AFM images are comparable while the fibril periodicity (helical pitch of twisted fibrils) distributions indicate that acetylated-αS fibrils have slightly higher periodicities (**Table 5.2**). The periodicity distribution of WT-αS fibrils is much broader compared to that of acetylated-αS fibrils (**Figure 5.5B**). The spread in the periodicity distribution possibly reflects the heterogeneity in aggregation rates observed in ThT experiments. The presence of EDTA in aggregation mixtures has been reported to result in homogenous fibril preparations possibly by restriction of conformations accessible to a monomer[267]. Acetylation seems to also influence the conformational ensemble

of the monomeric αS in solution as evidenced by NMR measurements and may thereby also affect the nucleation of a more homogenous population of fibrils.

	Fibril height (nm)	Fibril periodicity (nm)	Mean fibril length (μm)	Number of fibrils, n
WT-αS	6.8 ± 1	84 ± 44	1.83 ± 0.8	233
NTAc-αS	6.1 ± 1	115 ± 21	0.56 ± 0.2	165
Endo-αS	6.7 ± 1	112 ± 19	0.74 ± 0.3	320

Table 5.2: Overview of structural parameters for αS fibrils obtained from atomic force microscopy. Error bars represent standard deviations.

The differences in fibril morphology are also reflected in the secondary structure observed for αS fibrils. Although the CD spectroscopy showed a characteristic negative peak at ~ 218 nm for both acetylated-αS and WT-αS fibrils, the acetylated-αS fibrils had slightly higher β sheet content (**Figure 5.5C**). Similar differences in calculated CD spectra have been recently reported for αS with and without N-terminal acetylation by MD simulations[268]. The mean fibril length of WT-αS was ~ 6 fold higher than the acetylated-αS fibril length (**Figure 5.6**).

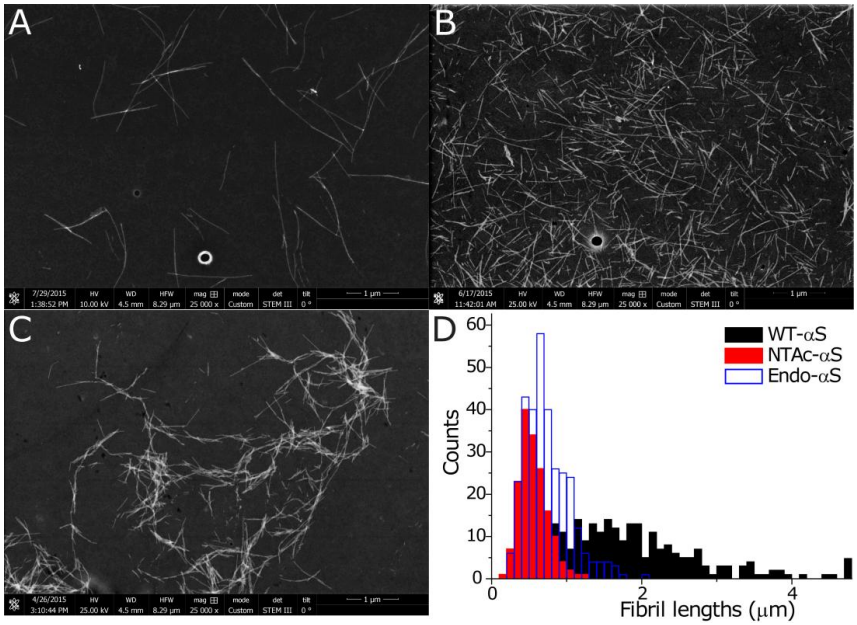

Figure 5.6: STEM measurements of WT-αS, NTAc-αS and Endo-αS fibrils. Representative dark-field images of WT-αS (panel A), Endo-αS (panel B) and NTAc-αS (panel C) fibrils obtained post aggregation in PBS buffer at 37 °C with constant shaking at 1000 rpm. The fibrils were purified with a 100 kDa cutoff filter to remove the residual monomers before STEM imaging. The length distributions (panel D) were obtained using the *Simple Neurite Tracer* plugin[226] in Fiji software show a much smaller mean length acetylated-αS fibrils as compared to WT-αS fibrils.

Since fibril lengths can be influenced by stochastic shear forces arising during sample preparations, it cannot be ascertained conclusively if differences in the apparent mean fibril lengths result from acetylation of αS. The broader fibril periodicity distribution from AFM measurements observed for WT-αS fibrils and the differences between the CD spectra of WT-αS and acetylated-αS fibrils may result from a difference in molecular conformation. To investigate this possibility, we measured two-dimensional infrared (2D-IR) spectra in the amide-I region (1600-1700 cm^{-1}), which provide information on secondary protein structure[269-273]. There are significant differences between the 2D-IR spectra of WT-αS fibrils and acetylated-αS fibrils (**Figure 5.7A**).

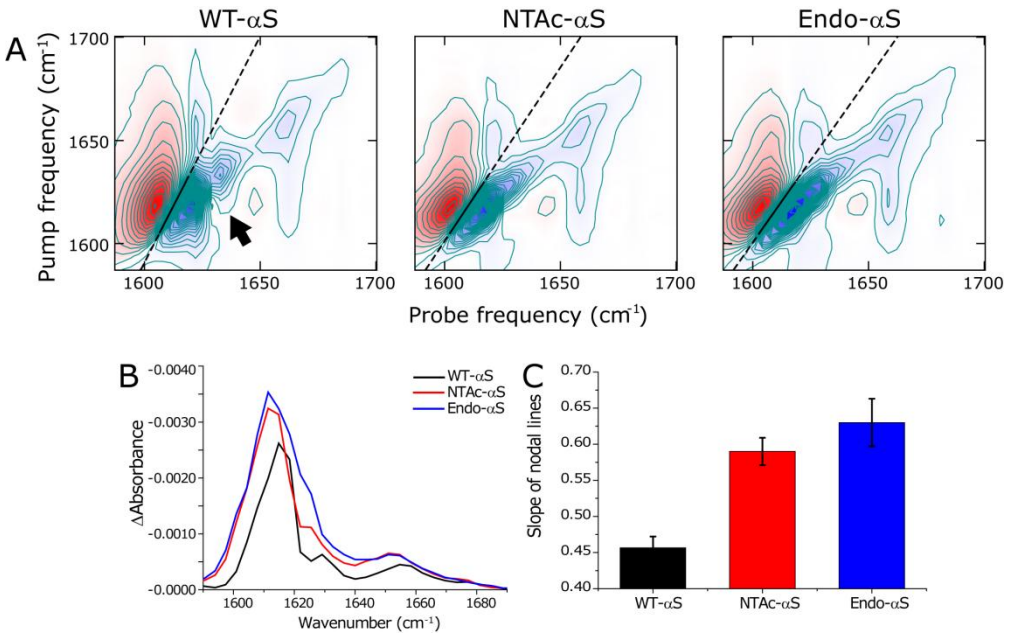

Figure 5.7: 2D-IR spectra of αS fibrils. A) 2D-IR spectra showing solid straight lines are fits through the zero crossings in the β sheet region. The steeper slope of the line in the WT-αS fibril spectrum shows that the spectral heterogeneity is less in this spectrum as compared to the acetylated-αS spectra. The arrow indicates a cross peak between the ~ 1620 cm^{-1} and the 1632 cm^{-1} peak, which is only present in the WT-αS spectrum, indicating coupling between modes resulting from two different types of β sheet structure. All fibrils were prepared in deuterated PBS buffer solutions and purified after aggregation to remove monomers. B) Diagonal slices of the 2D-IR spectra, to aid the recognition of the diagonal peaks described in the main text. To avoid distortion of the lineshapes as a result of a large spectral width of the pump as compared to the anharmonicity that results in a distorting positive contribution of the induced absorption to the bleach signal that is plotted here, we plot the average between the diagonals that are blue shifted by one and by two probe pixels. C) The nodal slopes were obtained from the fitted straight lines through the zero crossings in the β sheet region, showing a comparable spectral inhomogeneity for acetylated-αS fibrils, and a smaller inhomogeneity for WT-αS fibrils. We obtained the nodal slopes by calculating the frequencies where the signal goes through zero, in between the induced absorption (red peak at lower probe frequency in panel A) and the bleach (blue peak at higher probe frequency in panel A), for each pump pixel in the 1600-1622 cm-1 region by interpolation of the data point right before and right after the zero crossing, and subsequently fitting a straight line through the interpolated zero crossings.

We assign the four IR-active modes (visible on the diagonal of the 2D-IR) spectra as follows: the peak at (ν_{probe}, ν_{pump}) = (1657, 1657) cm^{-1} is indicative of turns[274,275], and the peaks at (1620, 1620) cm^{-1}, (1632. 1632) cm^{-1} and (1683, 1683) cm^{-1} are indicative of β sheet structure[275-278] (**Figure 5.7B**). The most notable spectral differences distinguishing WT-αS from NTAc-αS fibrils are the cross peak patterns and the spectral inhomogeneity. The cross peak at (ν_{probe} , ν_{pump}) = (1657, 1620) cm^{-1} shows that the vibrational modes in the turns are spatially close enough to couple to the vibrational modes in the β sheets. Likewise, the cross peak in the WT-αS spectrum at (1632, 1620) cm^{-1} (arrow in **Figure 5.7A**) reveals vibrational coupling between different beta sheet modes. The latter cross peak is not observed in the spectra of the acetylated αS's, indicating a clear structural difference. The slanted shape of the diagonal peaks indicates spectral inhomogeneity: when scanning the excitation frequency ν_{pump} over the absorption band, the response shifts to higher ν_{probe} with increasing ν_{pump} (in the absence of spectral inhomogeneity the peak shape is parallel to the ν_{pump} axis)[269]. If there are many oscillators with a slightly different environment leading to a large spectral inhomogeneity, the slope of the response will go towards 45°. WT-αS fibrils have a relatively smaller degree of spectral heterogeneity in the β sheet region than acetylated-αS fibrils which is evinced by the different slopes of the nodal lines[269] (black lines in **Figure 5.7A/C** for quantitative analysis). This increased spectral heterogeneity of acetylated-αS fibrils can be due to increased solvent exposure of the β sheets, and/or to a broader conformational distribution[269,279]. The former scenario is not likely, since experiments using the polarity-sensitive FE-dye[280] show that the core of acetylated-αS fibrils is just as polar as that of WT-αS fibrils (**Figure 5.8**).

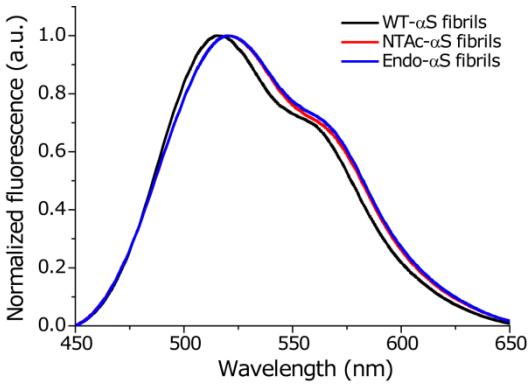

Figure 5.8: Fluorescence emission spectra of FE dye bound to αS fibrils. 20 μM of WT-αS (black), NTAc-αS (red) and Endo-αS fibrils (blue) were incubated for 1 hour with 2 μM FE dye in PBS buffer at room temperature. The fluorescence emission spectra were acquired using an excitation wavelength of 420 nm and excitation/emission slit widths at 5 nm.

The smaller fibril-to-fibril heterogeneity of acetylated-αS as compared to WT-αS fibrils as measured by AFM (**Figure 5.5B**) suggests that the larger spectral inhomogeneity observed in the 2D-IR measurements for the acetylated-αS fibrils is not the result of a random distribution of structures, but of a well-defined distribution of different beta sheet structures present within one fibrillar repeating unit[281]. Recent micro-electron diffraction experiments indicated insignificant differences in the intermolecular spacing of β sheets of NTAc-αS and WT-αS, which also explains similarities in heights of NTAc-αS and WT-αS fibrils from our AFM experiments[59]. It is therefore likely that the different arrangement of αS monomers in acetylated-αS fibrils as shown in 2D-IR measurements do not significantly influence the intermolecular spacing between β sheets. The similarities in fibril structures and vibrational signatures of acetylated-αS fibrils in our measurements suggest that NTAc-αS faithfully mimics Endo-αS, the purification of which is cumbersome.

Under our experimental conditions, N-terminal acetylation seems to have little influence on membrane binding of αS to phospholipid membranes. In line with this observation the sub-cellular localization and distribution of αS has been observed to be unaffected by N-terminal acetylation[115]. This suggests that if N-terminal acetylation of αS plays a regulatory role in the function of the protein, it should act in conjunction with either a physicochemical cue or another binding partner. N-terminal acetylation in αS may not be directly used to tune membrane binding but is possibly required to adjust the interaction strength with other partners like Soluble N-ethylmaleimide-sensitive factor Attachment Receptors (SNAREs), actin[251], tubulin[282,283] or specific lipids[116]. Further studies targeted at elucidating binding partners of monomeric αS could yield more insight into the impact of N-terminal acetylation in regulating interactions.

Although we do not observe major differences in aggregation rates of both acetylated-αS and WT-αS, N-terminal acetylation does result in a high degree of homogeneity in aggregation lag times and fibril morphologies. Structural polymorphs of αS and Aβ fibrils have been shown to result in significantly different toxicities in neuronal cell cultures[57,58,284] and considering that *in vitro* preparations of WT-αS fibrils have significant polymorphism, acetylated-αS fibrils are more relevant for such studies.

5.3 Materials and Methods

5.3.1 Expression, purification and labeling of αS

WT-αS was expressed in Escherichia coli strain BL21(DE3) using the pT7-7 expression plasmid and purified in the presence of 1 mM DTT as previously reported[224]. Endogenous αS was purified from freshly collected human RBCs provided by Sanquin blood bank, the Netherlands. The purification protocol used is similar to that described elsewhere[87], except using first an

anion exchange column for bulk purification (GE Healthcare, Source 15Q) followed by further purification with a hydrophobic interaction column (GE Healthcare, HiTrap Phenyl HP). NTAc-αS protein was produced by co-expression of both the αS plasmid and the N-terminal acetylation B complex plasmid in E. coli. The N-acetylation B complex plasmid was kindly provided by Dr. Daniel Mulvihill. The purification protocol is the same as for WT-αS.

5.3.2 Mass Spectrometry

Electrospray ionization (ESI) mass spectra were acquired on a Thermo Finnigan LTQ FT-ICR in positive mode. The sample was inserted by means of a syringe pump. The spray voltage was operated between 1-1.5 kV. The final concentration of αS monomers was 15 μM in 10 mM ammonium acetate buffer.

5.3.3 Acetic acid gel Electrophoresis

Proteins were separated based on the difference in acetylation of the N-terminus by acetic acid-urea polyacrylamide gel electrophoresis using a protocol as described elsewhere[285].

5.3.4 Preparation of liposomes

Stock solutions of 1-palmitoyl-2-oleoyl-sn-glycero-3-phosphocholine (POPC), 1-palmitoyl-2-oleoyl-sn-glycero-3-phospho-L-serine (POPS) and cholesterol from ovine wool were purchased from Avanti Polar Lipids (Birmingham, AL) and used without further purification. Tris salt and Potassium chloride (KCl) were purchased from Merck (Germany). Lipid stock solutions of POPC and POPS in chloroform were mixed in appropriate molar ratios, dried under a stream of nitrogen, and placed under vacuum for 1 hr. After drying the lipid films were rehydrated in 10 mM Tris, 100 mM KCl solution and vortexed for 5 minutes. Small unilamellar vesicles (SUVs) were prepared by sonicating the rehydrated liposome solution for 40 minutes using a Branson tip sonicator. Thereafter, the SUVs were centrifuged at 13200 rpm to remove any tip residue from the sonicator probe. For preparation of large unilamellar vesicles (LUVs), the rehydrated liposome solution (after the vortexing step) was subjected to multiple cycles of free-thawing in liquid nitrogen until the resulting solution was clear. Thereafter, the solution was extruded through a polycarbonate membrane of pore size 100 nm. The SUVs and LUVs were stored at 4 °C and used within 2 days.

5.3.5 Circular dichroism (CD) spectroscopy

A Jasco J-715 spectropolarimeter was used to obtain CD spectra at a protein concentration of 3 μM. By measuring the increase in absorbance at 222 nm that is indicative of a transition of the monomeric protein from a random to a helical conformation upon lipid association, a binding curve could be generated by titrating αS with liposomes. The binding curves were

then normalized assuming saturation of MRE values in the plateau phase of the binding curve represents saturation of protein binding sites on the lipid membrane. The normalization of the binding curve for incomplete saturation (in case of zwitterionic membranes) was performed using average MRE values (**See Figure 5.2F**) obtained at saturation conditions for respective variant of αS. Fitting of the binding curves was done using a binding equation as reported before[108] (see **Appendix A** for details). For measurement of CD spectra of αS fibrils, samples were first purified using a 100 kDa cut-off filter to remove monomeric αS. The effective concentration of fibrillar protein was estimated as given in **Appendix B**. Thereafter, CD spectra were recorded between 195 to 260 nm with a step size of 1 nm and a scanning speed of 10 nm/min using a 1 mm path length cuvette at room temperature.

5.3.6 Thioflavin T aggregation assays

All aggregation assays were carried out in a TECAN InfinitePro200 multi-plate fluorescence plate reader using a protein concentration of 35 μM in PBS buffer a 37 °C under constant orbital shaking at 300 rpm.

5.3.7 Atomic Force Microscopy

For AFM measurements, 20 μl of 10 μM fibril suspension was incubated on freshly cleaved mica (15 x 15 mm) for 5 minutes. Samples were thereafter washed with D_2O and dried using N_2 gas. AFM images were acquired in tapping mode on a Dimension 3100 Scanning Probe Microscope (Bruker) using NSG01 gold probes with a resonant frequency between 87-230 kHz and a tip radius ~ 10 nm. Fibril heights were measured using NanoScope Analysis v1.5 software and for the measurements of periodicities, fibrils in AFM images were traced using a custom written script in MATLAB using the DIPimage toolbox (version 2.3, TU Delft, Delft, The Netherlands) was used[286]. The script is based on quantitative analysis of AFM images mentioned elsewhere[224].

5.3.8 Two-dimensional IR (2DIR) spectroscopy

The 2DIR spectra were measured on a setup described elsewhere[287]. In short, a commercially available mode-locked Ti:sapphire oscillator system whose output is amplified by a Ti:sapphire regenerative amplifier was used to create 35 fs, 800 nm pulses of ~ 3.1 mJ at a repetition rate of 1 kHz. These were converted in an optical parametric amplifier into ~ 100 fs, ~ 6100 nm pulses of ~ 20 μJ with an approximately Gaussian distribution that has a full width half max (FWHM) of ~ 150 cm^{-1}. The IR beam was then split into a pump, probe and a reference beam. The pump beam is led through a Fabri-Perrot interferometer, and thereby reduced in bandwidth to a FWHM of ~ 12 cm^{-1}. The pump beam was then rotated 90° with respect to the probe beam by a λ/2 plate, and subsequently overlapped with the probe pulse

in the sample in a ~ 200 µm focus. All spectra were obtained at a pump-probe delay of 1.5 ps. After the sample, the probe and reference beam was coupled into to an OrielMS260i spectrograph that disperses the light onto a 32 pixel MCT-array with a resolution of 3.9 cm^{-1}. Fibril samples for 2D-IR measurements were prepared in deuterated PBS buffers at 37 °C, 1000 rpm constant shaking. Prior to measurements, monomers were removed via ultra-centrifugation at 25000 rpm.

5.3.9 Scanning Transmission Electron Microscopy (STEM)

Fibrils were aggregated in PBS buffer, diluted with D_2O, and then prepared for STEM dark-field imaging. Typically, a 5 µl drop of 20 µM fibril samples were adsorbed on 300 mesh formvar coated copper grids for 5 minutes and then washed 5 times with D_2O. The grids were thereafter dried at 37°C and then transferred under vacuum into the STEM setup. Dark-field digital images of fibrils were acquired using a FEI Verios 460 microscope operating at 25 kV electron beam energy. Before recording the dark-field STEM images, condenser stigmators were carefully adjusted to give a circular beam profile when the beam was viewed on the grids, and the beam was carefully centered and spread to produce uniform illumination over the field of view. Histograms for fibril length were obtained from these data using the *Simple Neurite Tracer* plugin in Fiji software[226,288].

5.4 Acknowledgements

The authors thank Dr. Daniel Mulvihill (University of Kent, Kent, U.K.) for the N-acetylation B complex construct, Prof. Roberta Croce (Vrije Universiteit Amsterdam) for access to the CD spectrometer, Dr. Arshdeep Sidhu (University of Twente) for advice on AFM imaging/analysis and Dr. Volodymyr Shvadchak for discussions and providing the polarity sensitive FE dye. The authors thank the Sanquin blood bank for providing human red blood cells for obtaining endogenous αS. The work presented here is part of a project titled "A Single Molecule View on Protein Aggregation" (Nr. 127) funded by Foundation for Fundamental Research on Matter (FOM). We also acknowledge the European Research Council (ERC) for funding through grant 210999 and the Netherlands Organization for Scientific Research (NWO).

5.5 Experimental contributions

2D-IR experiments were carried out in collaboration with Mr. Steven Roeters from the University of Amsterdam. Mass Spectrometry measurements were carried out in collaboration with Mr. Bob Hommersom from FOM Institute AMOLF. CD spectroscopy measurements for estimation of binding affinities were carried out in collaboration with Nathalie Schilderink from the University of Twente.

6

The role of N- and C-terminal domains of alpha synuclein in amyloid fibril morphology

6.1 Introduction

Although the mechanism by which neuronal cell death occurs in Parkinson's disease (PD) is unclear, the self assembly of monomeric alpha synuclein (αS) into amyloid fibrils plays an important role in PD[46,56,59,289]. *In vitro* produced αS fibrils have not only been shown to be cytotoxic but also seed endogenous αS *in vivo* on cell membranes in a recent report[128]. In addition, some fibrillar species of αS that are structurally and morphologically different (polymorphs) show varying cytotoxic effects[57,59,128] suggesting that the differences in the organization of αS monomers in fibrils are related to cytotoxicity. Elucidating the details of the self-assembly of αS amyloid fibrils is a key step to understanding the structural features of these fibril polymorphs that could increase our insights into their role in the mechanism of cell death in PD. What triggers the aggregation of monomeric αS into amyloid fibrils in cells is unknown, but *in vitro* aggregation has been shown to crucially depend on physicochemical parameters like pH, buffer, ionic strength, shaking condition, and temperature[200,229,267].

The amino acid sequence of αS comprises three regions. Residues 1-60 are involved in membrane binding[189], residues 61-95 contain the amyloidogenic NAC domain that is necessary for amyloid formation[205,245,290,291] and the highly charged C-terminal region comprises residues 96-140[83]. The structural features of αS amyloid fibrils resemble those of fibrils of other amyloidogenic peptides and proteins. Their width ranges between 40-110 Å and the fibril core contains hydrophobic "cross-β" structures made up of arrays of β strands running perpendicular to the long axis of the fibrils[21,292,293]. Reports on fibril structure obtained with solid-state NMR have shown that αS fibrils characterized so far contain at least four to five β strands and agree largely on the C-terminal region being solvent exposed and disordered in the resulting amyloid fibrils[281,294]. Although high resolution techniques have increased our understanding of the structure of amyloid fibrils[58,59,83,200,281], the molecular events occurring during and leading to the self assembly process into specific fibril polymorphs remain obscure. It becomes increasingly evident that structural differences in amyloid fibrils prepared from the same peptide sequence under different ionic strengths can differ in cellular toxicity suggesting that toxicity is directly related to subtle details of fibril structure[57,58,281,295]. Thus, it is necessary to understand the factors that could potentially affect fibril structure and morphology. Disruption of the existing long range interactions between the N-terminal, NAC and C-terminal regions of monomeric αS are reported to influence its aggregation in amyloids. The hypothesis that the C-terminus of monomeric αS "flips-back" on its NAC region is suggested to auto-inhibit αS aggregation[296-299] by preventing self-associative interactions of the NAC region. Removal of the C-terminus of monomeric αS increases its aggregation rate into amyloid fibrils[81,83,206,300,301]. This idea is also supported by independent

measurements by disrupting these long range interactions in αS using urea, and by changing pH and changing ionic strengths in SAXS and NMR experiments[296-299]. Addition of polyamines, increasing ionic strength or truncation of terminal residues likely disrupt these interactions, exposing the hydrophobic regions and triggering αS aggregation into amyloids[206,233,302,303]. Subtle conformational differences in the monomeric state induced by the aforementioned factors could affect the structure and morphology of the resulting fibrils as shown in **Chapter 5**.

Given the relevance of long-range interactions between the terminal regions in the monomeric αS in the aggregation process of αS, we aimed to investigate if removal of the terminal regions could also affect fibril structure and morphology. To test this hypothesis, we used both N and C-terminal truncated variants of αS for aggregation studies keeping the NAC fibril core intact (**Figure 6.1A**). We investigated the influence of these truncations on the assembly of fibrillar structures of αS using circular dichroism and Fourier transform infrared spectroscopy and atomic force microscopy (AFM) supplemented by scanning transmission electron microscopy (STEM). Our results show that truncations in the N-terminus of monomeric αS do not significantly influence the aggregation rates or fibril structures while aggregation of C-terminal truncated variants of αS result in morphologically different fibrillar structures. In particular, 1-108-αS fibrils have different fibril morphology. These fibrils likely comprise of strongly twisted β sheets and cannot seed the aggregation of the highly charged WT-αS monomers. The strong aggregation of the 1-108 fibrils suggests that the core of these fibrils is more solvent exposed. The incorporation of 1-108-αS monomers into WT-αS fibrils proceeds much faster than incorporation of WT-αS monomers and switches fibril morphology to that of 1-108-αS fibrils. The observation of switching of fibril morphology is interesting since seeds are conventionally thought to act as templates. These results indicate that truncations in the C-terminal domain of αS can result in structural changes in the resulting fibrils.

6.2 Results

6.2.1 Increasing net charge of αS influences aggregation rate

To investigate how removal of regions flanking the NAC domain in αS affected their aggregation propensity, we used Thioflavin T (ThT) as a reporter dye. ThT is a well known molecule that has a very weak fluorescence in solution and exhibits intense fluorescence upon binding to cross-β structures[210,211]. Aggregation of WT-αS and all truncated variants show typical sigmoidal growth profiles (**Figure 6.1B**). Truncations of both N-terminal and C-terminal residues influenced the aggregation rates to different extents. The exponential phase aggregates rates and aggregation half-times were extracted from normalized

aggregation curves (**see methods**). The removal of residues 1-20 (21-140-αS) did not significantly influence the exponential phase aggregation rate compared to WT-αS while removal of residues 1-60 (61-140-αS) resulted in a 6 fold decrease in the aggregation rate (**Figure 6.1C**). In line with earlier reports removal of the C-terminal residues in 1-108-αS and 1-124-αS both accelerated the rate of aggregation into fibrils[81,83,206,300,301,304].

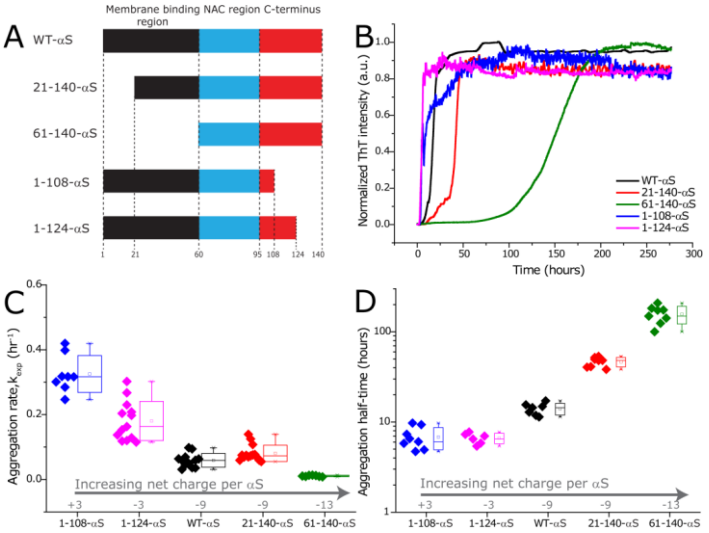

Figure 6.1: αS truncated variants and aggregation properties. A) Scheme of truncated variants used in the study. B) Aggregation kinetics of truncated αS variants. The panel shows representative normalized aggregation curves of the truncated variants monitored using ThT fluorescence. αS aggregation was carried out using 35 μM protein for each variant with 5 μM ThT in PBS buffer and constant shaking at 300 rpm at 37 °C. C) Aggregation rates and D) Aggregation half times of truncated variants. The estimation of aggregation rates and half times were performed as reported previously[252]. In the above panels (B,C and D), WT-αS is depicted with black, 21-140-αS by red, 61-140-αS by green, 1-108-αS by and 1-124-αS by magenta line/diamonds respectively. Box lengths in panel C and D represent standard deviation in the plotted data. Net proteins charges are calculated using the *ProtParam* tool from ExPASy server.

As expected, the aggregation half-times increased in the order of increasing net charge of the monomeric protein as 1-108-αS≈1-124-αS<WT-αS<1-124-αS<61-140-αS (**Figure 6.1D**) while the opposite relation between net charge and aggregation rate was observed (**Figure 6.1C**).

6.2.2 Removal of C-terminal residues strongly affects structure of αS fibrils

The removal of amino acid residues from regions flanking the NAC region may not only affect aggregation rates but also the morphology of the assembled fibrils. To get an overview of the fibril morphologies, we used scanning transmission electron microscopy (STEM). WT-αS, 21-140-αS and 61-140-αS fibrils form typical μm long rod-like fibrils (**Figure 6.2A-C**) while the 1-108-αS and 1-124-αS fibrils were morphologically different and formed higher order fibrillar aggregates[206,300,305](**Figure 6.2D/E**). In both 1-108-αS and 1-124-αS samples

isolated rod-like fibrils were sparsely observed to protrude out from higher order fibrillar aggregates.

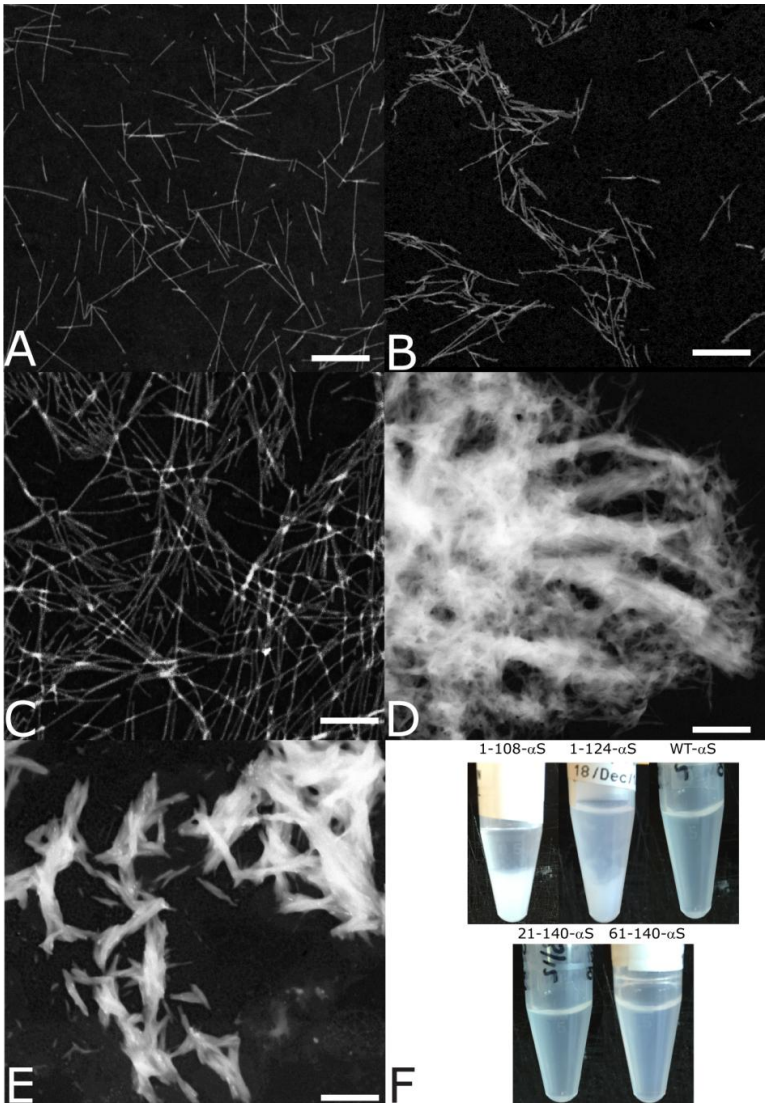

Figure 6.2: STEM images of αS truncated variants. The above panels show STEM images of WT-αS fibrils (panel A) and truncated variants (panel B-E). The 21-140-αS (panel B) and 61-140-αS (panel C) fibrils are micrometers long have a rod-like morphology like WT-αS fibrils while 1-124-αS (panel D) and 1-108-αS (panel E) fibrils mainly organize into higher order fibrillar aggregates. The scale bar is 0.5 µm. Panel F shows aggregated solutions of αS fibrils and settled aggregates (densely white) in stagnant tubes after 12 hours post aggregation.

To quantify possible structural differences in αS fibrils, atomic force microscopy (AFM) measurements were performed in tapping mode on WT-αS and truncated αS fibrils in ambient

air conditions (**Figure 6.3A-E**). Compared to WT-αS fibrils, 21-140-αS and 61-140-αS fibrils are morphologically similar while fibrils of 1-108-αS and 1-124-αS organize in higher order fibrillar aggregates; only sparse individual fibrils are observed in case of 1-108-αS and 1-124-αS fibrils.

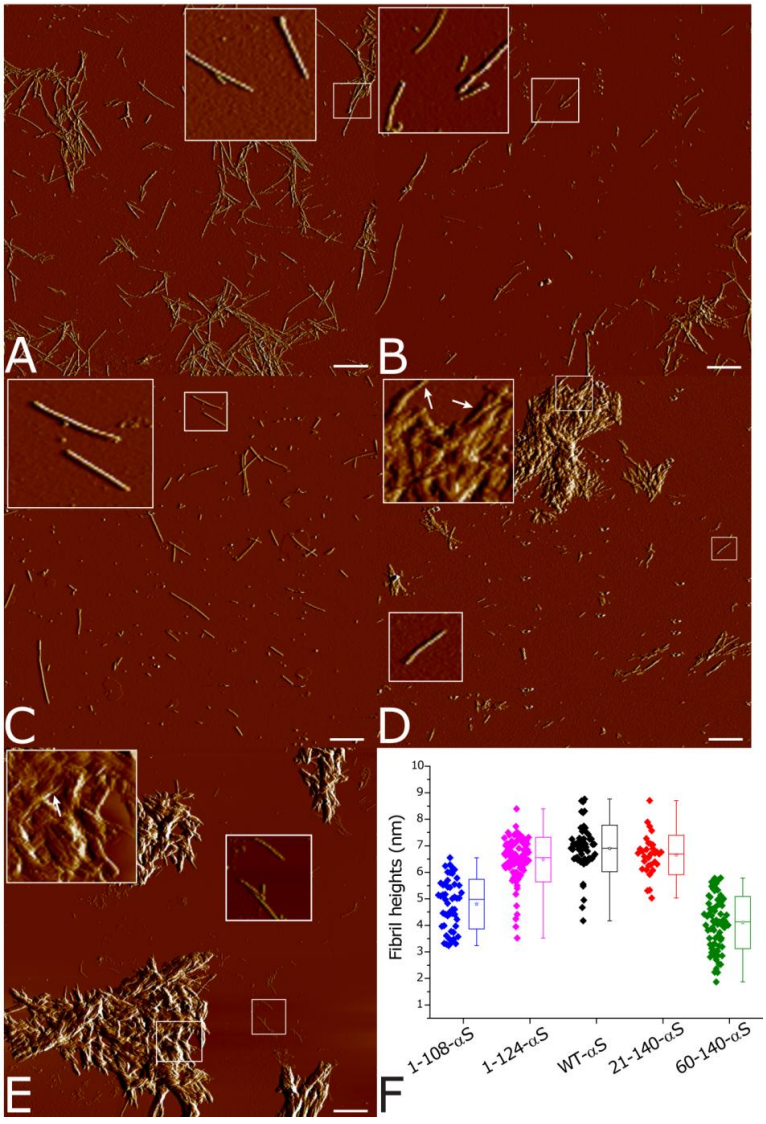

Figure 6.3: AFM amplitude images of αS fibrils on mica. Purified fibrils of WT-αS (panel A) and truncated variants were imaged on mica under tapping mode in air. The 21-140-αS (panel B) and 61-140-αS (panel C) fibrils show typical fibrillar morphology while 1-124-αS (panel D) and 1-108-αS (panel E) fibrils show both fibrillar and supra-fibrillar structures (inset).Fibril heights are shown in panel F. The scale bar is 1 μm.

The height distribution measured from AFM images corresponds to fibril diameters and is plotted in **Figure 6.3F**. WT-αS fibrils have an average height of ~ 7 nm similar to previous reports[267,306,307](**Figure 6.3F and Table 1**) and comparable heights were measured for the 21-140-αS and 1-124-αS fibrils; however, fibril heights decreased with substantial truncations in either N or C-terminus of monomeric αS as seen for fibrils of the 1-108-αS and 60-140-αS variants (**Table 6.1**). Periodicity measurements were performed on fibrils greater than 0.5 µm in length.

Table 6.1: Quantitative comparison of WT-αS and truncated variant fibril morphologies.

Fibril type/ Parameter	Mean fibril height (nm)	# of fibrils, n	Mean fibril periodicity (nm)	# of fibrils, n	Net charge of monomer
1-108-αS	4.7 ± 0.9	74	52 ± 9	22	+3
1-124-αS	6.4 ± 0.8	81	46 ± 8	15	-3
WT-αS	6.9 ± 0.9	56	95 ± 39	56	-9
21-140-αS	6.7 ± 0.7	32	128 ± 57	32	-9
60-140-αS	4.1 ± 1.0	80	51 ± 20	80	-13

The generally observed wide distribution of fibril heights likely represents the structural polymorphism of the samples. Since the height of higher order fibrillar aggregates was extremely heterogeneous ranging between ~ 150-400 nm, height distributions of fibrils obtained from 1-108-αS and 1-124-αS variants were obtained from individual fibrils only. The insets for 1-108-αS and 1-124-αS fibrils show that fibril periodicities are comparable in both the higher order aggregates and individual fibrils (**Figure 6.4**).

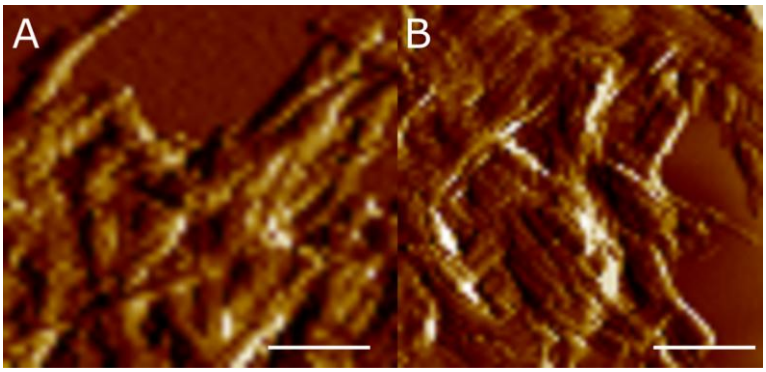

Figure 6.4: Zoomed AFM images of higher ordered aggregates 1-108-αS and 1-124-αS. Panel A depicts AFM images from inset of 1-124-αS fibrils and that of 1-108-αS fibrils are depicted in panel B. The scale bar is 1 µm.

In general, fibril periodicities were affected for all truncation variants of αS suggesting that residues that are known not to be involved directly in the fibril core can still affect fibril structure (**Table 6.1**)[306,307].

6.2.3 C-terminal truncated variants of αS comprise of strongly twisted β-sheets

Next, we investigated if secondary structures of the amyloid fibrils of WT-αS and truncated αS variants differed. The far-UV CD spectra of the WT-αS fibrils had a single broad minimum centered at ~ 219 nm arising from the $n\pi^*$ transition typical of a β sheet conformation (**Figure 6.5A**) while the minimum in the spectrum of the N-terminal truncated variants was blue-shifted by 2 nm. In contrast, the CD spectra of the 1-124-αS and 1-108-αS fibrils in the $n\pi^*$ transition region were red-shifted by 3 nm and 12 nm respectively. The positive maximum arising from the $\pi\pi^*$ transition was red shifted by ~ 5 nm for the 1-108-αS fibrils while the 21-140-αS fibrils spectra were blue shifted by ~ 4 nm compared to WT-αS. The CD spectrum of the 1-108-αS fibrils was very different from that of the other truncated variants.

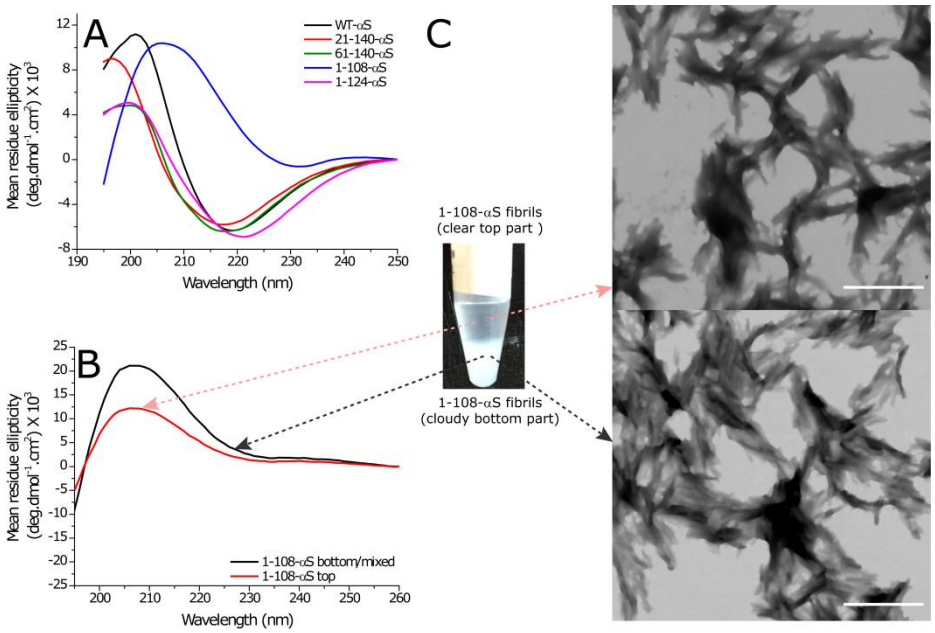

Figure 6.5: Secondary structure measurement of αS truncated variants. A) CD spectra of WT-αS and truncated variants. B) CD spectra and STEM images (panel C) of 1-108-aS fibrils obtained from cloudy (bottom part of tube or after mixing the tube) and clear solutions of aggregated samples.

Heterogeneous suspensions composed of solid-phase material with an uneven distribution of chromophores can result in changes in both intensity and in a red-shift of CD peaks,

a phenomenon known as differential absorption flattening (DAF)[308,309]. To establish if DAF effects are present in the 1-108-αS fibrils, CD spectra and STEM images were obtained from clear and cloudy solutions of 1-108-αS fibrils obtained after aggregates settled down (**Figure 6.5B/C**). We observe no peak shifts in CD spectra and STEM images indicate 1-108-αS fibrils give rise to aggregates with a comparable morphology suggesting that the secondary structures of 1-108-αS is similar in both solution phases and although plausible, DAF effects are unlikely. A negative minimum in the CD spectra at ~ 230 nm is suggestive of increased β-turns in other protein structures[310,311]. It is however improbable that the 1-108 fibril is highly enriched in β-turns as this would not result in a stable fibril structure. A red-shift of the $n\pi^*$(215-218 nm)and $\pi\pi^*$ transition region (195-200 nm) in CD spectra of C-terminal truncated αS fibrils could be a consequence of strongly twisted β-sheets[312] as reported recently for the ILQINS hexapeptide[313]. To probe for such possible structural differences in 1-108-αS fibrils and minimize misinterpretation due to scattering artifacts, we obtained FTIR spectra of all αS fibril samples. The FTIR spectra show a typical absorption in the amide I region corresponding to β-sheet structures (**Figure 6.6, left panel**) for all αS fibrils except the 1-108-αS fibrils for which a very broad peak in the amide I region is observed. To get more information on the peak positions, the second-derivative of the amide I infrared spectra were obtained (**Figure 6.6, right panel**).

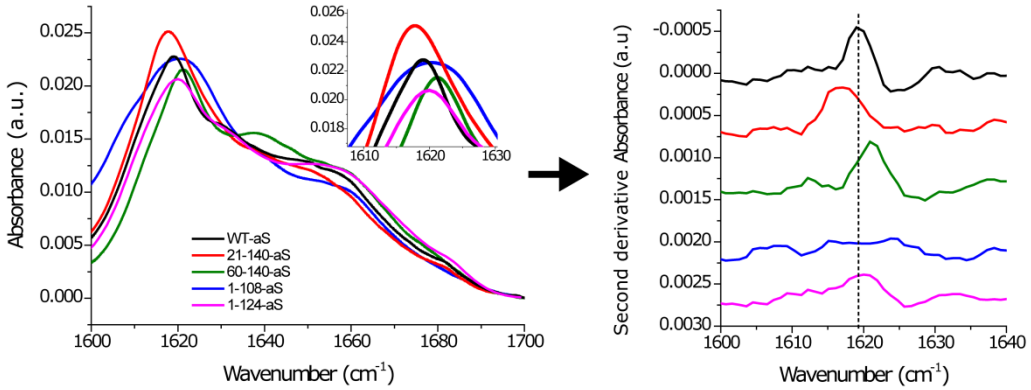

Figure 6.6: FTIR spectra of fibrils of WT-αS and truncated variants (left panel) and accompanying second derivatives plotted with an offset on the y-axes (right panel). The color coding in the right panel is same as that in the FTIR spectra (left panel).

WT-αS fibrils have an absorption spectrum with an amide I band with a maximum at ~ 1619 cm^{-1} which corroborates existing reports. 21-140-αS fibrils exhibited a slightly blue shifted amide I band at ~ 1617 cm^{-1} while that of 1-124-αS and 61-140-αS fibrils have a slight red shifted amide I band at 1621 cm^{-1}. 1-108-αS fibrils, in contrast, produce a spectrum with a very broad amide I band in the FTIR spectra, which upon taking the second derivative

is indistinguishable. These FTIR data suggest that although subtle structural differences exist in all truncation variants, the structure of the 1-108-αS fibrils is significantly different from WT-αS.

6.2.4 1-108-αS fibrils cores are incompatible for WT-αS monomers

To test the hypothesis that the fibril structure of WT-αS and 1-108-αS are different, we performed cross-seeding aggregation experiments. It is known that addition of preformed fibrils, i.e. seeds, to a solution of αS monomers accelerates aggregation process by bypassing the rate-determining step of primary nucleation[200,252,314]. Thus by monitoring the rate of incorporation of monomers of one type into preformed fibrils of another type (cross-seeding rate), structural differences in the fibril core can be gauged qualitatively. This is a reasonable assumption since both WT-αS and 1-108-αS have the identical random coil conformation in their respective monomeric states and a delay or non-existence of seeding is indicative of a different fold or slightly different conformation of a given fibril core. Self-seeding aggregation experiments using 1% seeds show a faster incorporation of 1-108-αS monomers compared to WT-αS monomers (**Figure 6.7B/C**).

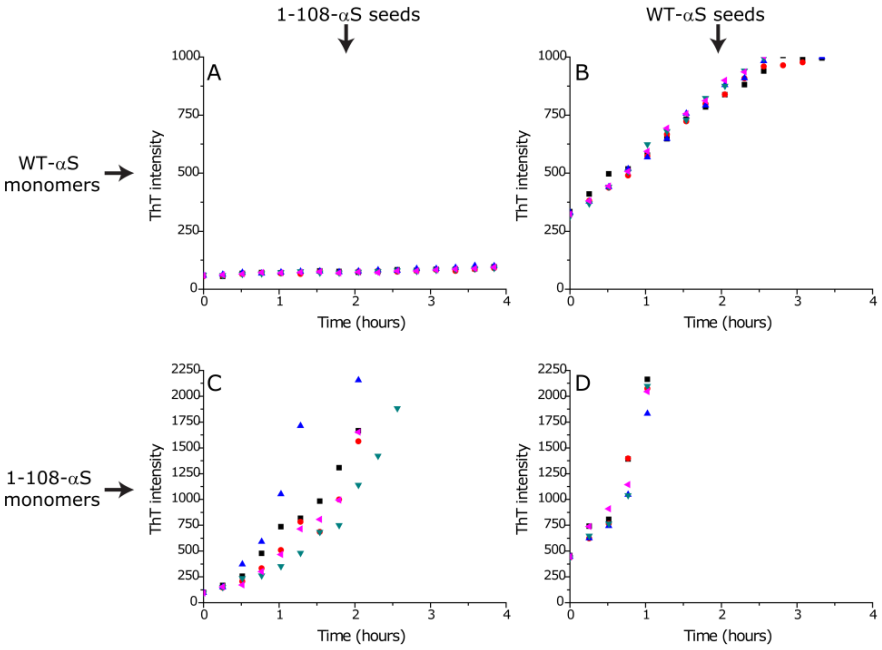

Figure 6.7: Seeding/Cross-seeding rates of WT-αS (black symbols) and 1-108-αS (blue symbols). Panel A and panel C depict initial data points of aggregation of WT-αS and 1-108-αS monomers respectively with 1-108-αS seeds while panel B and D depict that of WT-αS and 1-108-αS monomers with WT-αS seeds. Panel A does not show any increase in the ThT intensities compared to other panels within first 4 hours. The monomer concentration was 35 μM in PBS buffer at 37 °C at quiescent conditions.

In cross-seeding experiments, WT-αS seeds seem to be slightly more efficient in incorporating 1-108-αS monomers (**Figure 6.7D**) than WT-αS monomers while WT-αS monomers could not be seeded with 1-108-αS seeds under our experimental conditions (**Figure 6.7A**). Subsequently, to characterize the self-seeded and cross-seeded fibril populations, STEM images were obtained upon aggregation completion i.e. at the plateau phase of seeded aggregation experiments. Self-seeded aggregation showed elongated and bundled fibrils for WT-αS and 1-108-αS respectively (**Figure 6.8A/C**) while cross-seeding of 1-108-αS monomers with WT-αS seeds showed higher ordered aggregates (**Figure 6.8B**).

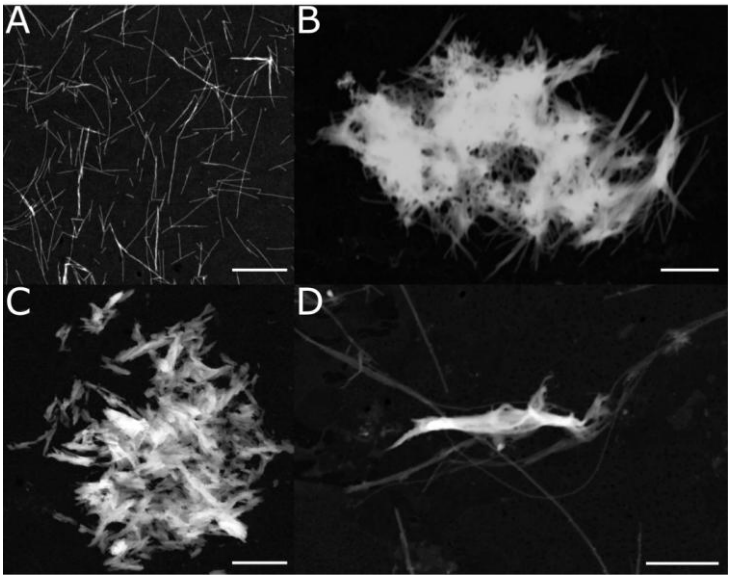

Figure 6.8: STEM images of Self- and Cross-seeded fibrils of WT-αS and 1-108-αS. Representative images of αS fibrils obtained from self-seeding of WT-αS monomers (panel A) and cross-seeding of 1-108-αS monomers (panel B) with WT-αS fibrils. Representative images of 1-108-αS fibrils obtained from self-seeding of 1-108-αS monomers (panel C) and cross-seeding of WT-αS monomers (panel D). As shown in panel D, WT-αS monomers grow into fibrillar structures over time without any bundling in presence of 1-108-αS seeds (white bundle in center of panel D). Seed concentration was kept constant at 1% (v/v). Fibrils were imaged at the plateau stage of seeded aggregation curves. Scale bar in all panels in 0.5 μm.

Cross seeding of WT-αS monomers with 1-108-αS seeds with showed an enhanced presence of elongated "rod-like" fibrils which are likely WT-αS fibrils while 1-108-αS seeds were sparsely observed (**Figure 6.8D**) corroborating observations from ThT self/cross-seeding experiments. To further establish if structure of the fibril cores were different, we used a polarity sensitive FE dye to probe the polarity of the environment in the fibril core[280].

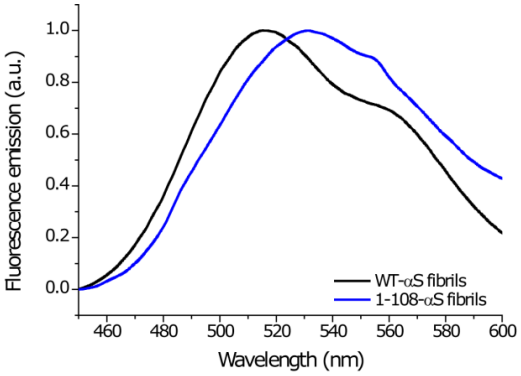

Figure 6.9: Fluorescence emission spectra of FE dye. 20 µM of WT-αS (black) and 1-108-αS (blue) fibrils (blue) were incubated for 1 hour with 2 µM FE dye in PBS buffer at room temperature. The fluorescence emission spectra (λ_{exc}=420 nm) of 1-108-αS fibrils is more red shifted with a higher band ratio of emission peaks.

Compared to the spectra of WT-αS fibrils, the red-shifted fluorescence emission band observed for the 1-108-αS fibrils is indicative of a relatively more solvent exposed fibril core. These data coupled with the CD and FTIR observations are indicative of a different fibril structure for the 1-108-αS fibrils.

6.3 Discussion

In this study, we have investigated if terminal regions in αS could influence the fibril structure and morphology of αS. Compared to WT-αS, the exponential phase aggregation rate of the 21-140-αS variant was comparable while that for the 61-140-αS variant was ~ 6 fold slower. The latter is likely to be a result of removal of residues involved in the hydrophobic core of the fibrils while the results in the former case suggest that the first 20 residues are probably not involved directly in fibril assembly in line with earlier reports[294,300,301]. Overall, the differences in the aggregation rates of proteins with either an N- and C-terminal truncation seem to correlate well with the net charge of monomeric αS. The net charge of monomeric αS can also be modulated with pH and affects aggregation rate in a similar way[200,229].

It is possible that the differences in the net charge of the monomeric protein due to removal of terminal regions also impact the resulting fibril morphologies. Aggregation of WT-αS and N-terminal truncated variants resulted in up to micrometer long "rod-like" fibrils while the C-terminal truncated variants of αS formed a heterogeneous mixture of "rod-like" fibrils and higher order fibrillar aggregates. A closer inspection of 1-124-αS and 1-108-αS higher order fibrillar aggregates in AFM revealed "rod-like" fibrils with periodicities identical to isolated "rod-like" fibrils corroborating previous reports showing higher ordered fibril networks and cylindrical aggregates of αS are composed of individual fibrils[206,300,305]. The absence of higher order fibrillar aggregates of WT and N-terminal truncated variants of αS in either AFM or STEM images in our fibril preparation conditions results suggest that the impact of C-terminal

residues (in particular 109-140 region) in fibril morphology is more significant than that of N-terminal residues. The C-terminus of WT-αS comprising of 32 amino acids, has been shown to collapse on WT-αS fibrils upon drying resulting in a ~ 17% decrease in fibril height in AFM images compared to those in liquid[306] which explains the slightly lower heights for 1-124-αS fibrils and similar heights for 21-140-αS fibrils. The ~ 40% decrease in height of the 61-140-αS fibrils compared to WT-αS fibrils is likely a result of a reduced number residues that make up the fibril core which in WT-αS fibrils comprises residues 34-96[58,281,315-317]. But the 30% decrease in fibril height for the 1-108-αS fibrils is peculiar and cannot be explained using the same argument. This suggests that 1-108-αS fibrils have a different fibril structure or alternatively that the αS monomers within fibril have a different orientation.

Compared to WT-αS, all truncation variants except 1-108-αS fibrils showed slight shifts (~ 2-3 nm) in the $n\pi^*$ transition region in the CD spectra but show significant shifts in the $\pi\pi^*$ transition regions. In contrast, the CD spectrum of the 1-108-αS fibrils was strongly red-shifted in both transition regions. A red-shift in CD spectra can sometimes be attributed to DAF effects which arise in heterogeneous suspensions with an uneven distribution of chromophores. We reasoned that a decrease in sample heterogeneity should reduce the magnitude of the DAF effects. CD spectra of clear solutions were obtained from the top of the aggregated solutions of 1-108-αS fibrils after aggregates settled down. We saw no differences in peak position between these two samples. The clear top solution seems to simply contain a lower concentration of protein fibrils which is expected since most of the protein aggregates have settled on the bottom of the sample. Although the aggregated solutions of both 1-108-αS and 1-124-αS fibrils both contained higher ordered aggregates that settled over time, the CD spectra of 1-124-αS fibrils did not show strong red shifts like 1-108-αS fibrils. DAF effects can therefore not explain the spectral differences between WT-αS and 1-108-αS fibrils. In general, the electronic transitions of the amide bond are affected by solvent and environment. Since the $n\pi^*$ transition is much weaker than the $\pi\pi^*$ transition, the peak position of the $n\pi^*$ transition is an unreliable indicator of environment of the chromophores; the peptide bond in our case[318]. The wavelength of the $\pi\pi^*$ transition in a peptide bond in CD spectra is known to red shift in water because the excited state in the $\pi\pi^*$ transition is more polar than the ground state. The higher polarity of the excited state stems from an intramolecular charge transfer from the nitrogen atoms to the oxygen atoms, resulting in a charged nitrogen atom that is able to form hydrogen bonds with the aqueous solvents[318]. Formation of additional hydrogen bonds results in the apparent red shift while a reduced interaction with protic solvents will lead to a blue shift in the CD spectra in the $\pi\pi^*$ transition region. Compared to WT-αS, the observed shifts in the CD spectra of 21-140-αS and 1-108-αS fibrils can be attributed to differences in solvent exposure of their respective peptide bonds. These differences can arise from an altered orientation of the monomer in the

21-140-αS and 1-108-αS fibril structures. We choose to study the 1-108-αS fibrils in more detail because of the unexplained decrease in fibril heights, an unusual CD spectra and formation of higher ordered aggregates.

For this purpose FTIR spectra were obtained from all fibril samples. The amide I mode in the FTIR spectra is generated primarily by backbone carbonyl stretching motions causing delocalization of their vibrational motions and is known to be sensitive to the secondary structure of protein[269,319]. Although all αS fibril forms used in the study are evidently composed of β-sheet structures and do not show significant shifts or broadening, the FTIR spectrum of 1-108-αS fibrils was very broad compared to WT-αS fibrils. The second derivative amide I spectra showed significantly different positions of the amide I maxima for WT-αS and peak broadening for 1-108-αS fibrils. The broad peak could be a result of increased solvent exposure of the β-sheets, and/or to a broader conformational distribution of comprising β-sheets[269,279]. To test the former scenario, experiments using the polarity-sensitive FE-dye were carried out and show that indeed the core of 1-108-αS fibrils is indeed more solvent exposed than that of WT-αS fibrils (**Figure 6.9**) corroborating results from CD spectroscopy. The increased solvent exposure of the hydrophobic β-sheets in 1-108-αS fibrils is expected to impose an energetic penalty and might explain the higher order association of the 1-108-αS fibrils.

Individual β-strands in β sheets in amyloid fibrils are typically slightly twisted as a result of chirality of the carbon atoms in proteins. An increase in twisting of β-sheets in the 1-108-αS fibrils possibly encompasses a tilting of the monomer. In the 1-108-αS fibril monomers are no longer stacked perpendicular to the fibril axis. Besides the chirality of the carbon atoms, the highly charged C-terminal tails in WT-αS fibrils probably also affect the orientation of the residues in the fibril core and the absence of this region in the 1-108-αS fibrils probably releases the energetic penalty associated with the close packing of "like" charged tails. This electrostatic repulsion together with the twisted orientation of the core segments possibly accounts for the different appearance of the 1-108-αS fibrils on the microscopic scale. It has been recently shown that WT-αS fibrils, depending on ionic strength of buffer used, can have completely different morphologies arising from altered orientation of αS monomer within the fibril core[58,281]. To ascertain if the core of the fibril structures were compatible, cross-seeding experiments were performed. In fibril assembly, the unfavorable loss of conformational entropy of free αS monomers upon association to fibrils is compensated for by corresponding inter-protein interactions. It is unclear from our preliminary results whether the absence of cross-seeding of WT-αS monomers by 108-αS seeds is caused by a strongly twisted β-conformation that is formed of different beta strands than the WT-αS fibrils or if the 1-108-αS fibrils cannot accommodate the initial binding of the WT-αS monomers with their

highly negatively charged C-terminus. Further experiments are needed to exclude the possibility of either mechanism.

It is conventionally believed that seeds act as templates that direct the conformation of the incoming monomers during fibril growth. Our contrary observations that 1-108-αS monomers result in 1-108-αS fibril-like morphology with WT-αS seeds and can be seeded into WT-αS seeds much faster than WT-αS monomers is peculiar but not unprecedented. Previously, a PD related point variant of αS (A30P-αS) has been shown to result in A30P-αS like fibrils with WT-αS seeds and incorporation of WT-αS monomers into A30P seeds proceeded at a rate much faster than that in presence of WT-αS seeds[320]. WT-αS fibrils prepared under different ionic strengths are morphologically and structurally dissimilar and differ in the extent of cellular toxicities[57,58]. Our observations of a higher seeding rate of 1-108-αS monomers into WT-αS seeds and switching of WT-αS morphology to a 1-108-αS fibril like morphology could explain why 1-108-αS aggregates are more toxic than WT-αS aggregates *in vivo*.

6.4 Materials and Methods

6.4.1 Expression, purification and labeling of αS variants

All αS variants were expressed in Escherichia coli strain BL21(DE3) using the pT7-7 expression plasmid and purified in the presence of 1 mM DTT as previously reported[224].

6.4.2 Thioflavin T (ThT) aggregation assay

Thioflavin T aggregation assays were carried out in a TECAN Infinite M200 micro-plate reader. For every protein variant, a final concentration of 80 μM of monomeric protein was allowed to aggregate in PBS (137 mM NaCl, 3 mM KCl, 10 mM Phosphate) buffer at 37 °C under constant shaking maintained at 300 rpm. Prior to loading on the plate reader, all prepared protein samples were filtered using a 100 kDa membrane to get rid of any aggregates resulting from addition of concentrated PBS during sample preparation. The ThT concentration was kept constant at 5 μM. The aggregation half-times in unseeded experiments were calculated from normalized aggregation curves and represent the time for 50% monomer conversion. The exponential phase aggregation rate (k_{exp}) in unseeded experiments was determined as the rate of increase of the logarithm of ThT fluorescence intensity corresponding to monomer conversion below 30% as reported previously[252]. Briefly, kexp = (ln(0.3) – ln(0.02))/($t_{30\%}$ – $t_{2\%}$), where $t_{30\%}$ and $t_{2\%}$ are the times needed for 30% and 2% monomer conversion to fibrils, respectively. For self/cross-seeding experiments, aggregation was carried out using 1% seeds of a given fibrillar species at 37 °C using 35 μM αS monomers in PBS buffer under quiescent conditions. Seeds were prepared by sonicating freshly prepared and filtered (using a 100 kDa filter) αS fibrils in PBS buffer for 5 minutes. The initial aggregation rate in seeded experiments

was determined similarly by measuring the increase of the ThT signal within the first 3000 seconds of the measurement.

6.4.3 Scanning Transmission Electron Microscopy

Fibrils were aggregated in PBS buffer, diluted with MilliQ water, and then prepared for STEM dark-field imaging. Typically, a 5 µl drop of 20 µM fibril samples were adsorbed on 300 mesh formvar coated copper grids for 5 minutes and then washed 5 times with water. The grid was dried at 37°C and then transferred under vacuum into the STEM setup. Before recording the dark-field STEM images, condenser stigmators were carefully adjusted to give a circular beam profile when the beam was viewed on the grids, and the beam was carefully centered and spread to produce uniform illumination over the field of view. Dark-field digital images of fibrils were acquired using a FEI Verios 460 microscope operating at 25 kV electron beam energy. Histograms for fibril length were calculated from these data using the *Simple Neurite Tracer*[288] plugin in Fiji software[226].

6.4.4 Atomic Force Microscopy

For AFM a measurement, 20 µl of the 10 µM fibril suspension was incubated on freshly cleaved mica (15 x 15 mm) for 5 minutes. Samples were thereafter washed with MilliQ water and dried using N_2 gas. Thereafter samples were kept in 37 ^{o}C for 1 hour to remove any residual solvent. AFM images were acquired in tapping mode on a Dimension 3100 Scanning Probe Microscope (Bruker) using NSG01 gold probes with a resonant frequency between 87-230 kHz and a tip radius < 10 nm. Fibril heights were measured using NanoScope Analysis v1.5 software and for the measurements of fibril periodicities, fibrils in AFM images were traced using a custom written script in MATLAB using the DIPimage toolbox (version 2.3, TU Delft, Delft, The Netherlands) was used[286]. For measurement of periodicities only fibrils greater than 0.5 µm were analyzed.

6.4.5 Circular dichroism (CD) spectroscopy

A Chirascan^{TM} CD spectrometer was used to obtain CD spectra of fibrils prepared in PBS (137 mM NaCl, 3 mM KCl, 10 mM Phosphate) buffer at an effective protein concentration of 10 µM. The effective concentration of fibrillar protein was estimated as given in **Appendix B.** Fibril samples were first purified using a 100 kDa cut-off filter to remove monomeric protein. Spectra were recorded between 200 to 260 nm with a step size of 1 nm and a scanning speed of 10 nm/min using a 1-mm path length cuvette at room temperature.

6.4.6 Fourier Transform Infrared spectroscopy

αS monomers were vacuum dried overnight and re-suspended in PBS (137 mM NaCl, 3 mM KCl, 10 mM Phosphate) buffer prepared in D_2O. Re-suspended monomeric αS samples in PBS were thereafter purified using a 100 kDa cut-off filter to remove any aggregates and then kept under constant shaking at 1000 rpm at 37 °C. Before measurements, αS fibril samples were first purified using a 100 kDa cut-off filter to remove monomeric protein and the final concentration for each fibril sample for FTIR was ~ 150 μM. 15 μl of fibril solution was placed between 2 mm thick CaF_2 windows with a 50 μm spacer. Each spectrum was an average of 32 scans. All measurements were carried out in at room temperature.

6.4.7 Steady-state Fluorescence spectroscopy

The emission spectra of FE dye were obtained with a Cary Eclipse spectrofluorimeter (Varian). Spectral slits were set at 5 nm and samples were excited at 420 nm. Fluorescence emission spectra were recorded from 450-600 nm at room temperature using a 10 mm path cuvette after incubation of FE dye for 1 hour with αS fibril samples in PBS buffer. Experiments were performed in triplicates at final concentrations of 20 μM fibrils and 2 μM FE dye.

6.5 Acknowledgements

The authors thank Nathalie Schilderink, Kirsten van Leijenhorst-Groener for assistance in protein expression and purification, Prof. Roberta Croce from the Vrije Universiteit Amsterdam and Prof. J. Antoinette Killian from the Utrecht University for access to the CD spectrometer. The authors also thank Dr. Volodymyr Shvadchak for discussions and providing the polarity sensitive FE dye. The work presented here is part of a project titled "A Single Molecule View on Protein Aggregation" (Nr. 127) funded by Foundation for Fundamental Research on Matter (FOM).

6.6 Experimental contributions

FTIR measurements were carried out in collaboration with Mr. Steven Roeters from the University of Amsterdam.

7

Summary & Conclusions

"Alpha synuclein (αS) is an intrinsically disordered protein involved in PD with a yet unknown physiological function". The previous sentence has presented itself in various permutations in several research papers on this protein in the last decade. It is amazing how much we actually know about this protein and how little this helps us to understand PD (**Figure 7.1**).

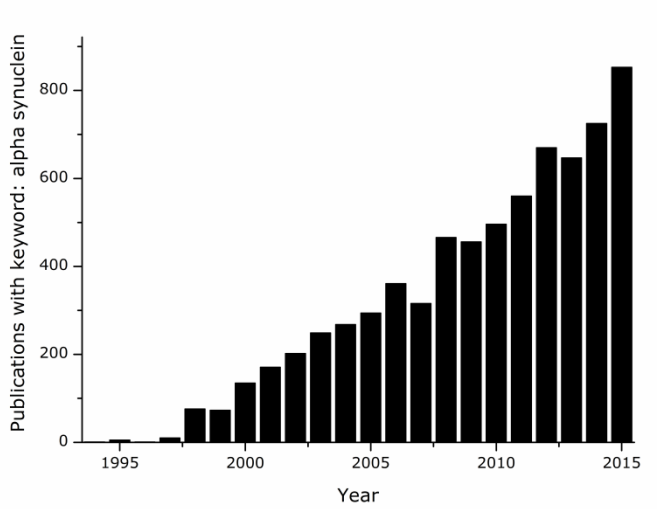

Figure 7.1: Bar plot of number of publications recorded in Pubmed from the keyword: alpha synuclein.

Ever since the discovery of αS as a presynpatic protein involved in PD, a lot of effort has been put towards elucidating what triggers the aggregation of αS into amyloid structures in the brain. Association with (specific) cellular membranes has been hypothesized to be one of these triggers that facilitates amyloid formation, but this idea is clouded by the fact that the physiological function of αS probably also involves association with physiological cell membranes. Further, whether association of αS with membranes facilitates or prevents aggregation into amyloids is also controversial. The observation that aggregation of αS into amyloid fibrils could be a protective step adds to this controversy. The process of uncovering one "face" of αS has only revealed more faces. Key to understanding this complicated protein is to unravel why it is present in micromolar concentrations at the pre-synaptic membranes. Understanding interactions with lipid membranes is critical to uncover its possible functional or pathological role. In this thesis, we investigated both the possible functional and pathological role of αS-lipid membrane interactions.

To probe interactions of αS with lipid membranes, we chose POPC:POPG in equimolar ratios as a model phospholipid membrane composition. The high fraction of anionic lipid was deliberately chosen since it was well known that interactions of αS with lipid membranes *per se* depended on fraction of anionic lipids. Preparation of SLBs with a high fraction of anionic

lipids on glass surfaces is known to be difficult. In order to have a defect-free and reproducible SLB system with a high faction of anionic lipids, preparation protocols were rigorously optimized. It was found that the combination of low pH, high ionic strength and high lipid concentration favors the preparation of stable SLBs consisting of high amounts of anionic lipids. Treatment of the glass surfaces on which the SLBs are deposited is critical and requires multiple-cleaning steps. The details of the optimization and characterization protocols are described in **Chapter 2**.

The physiological function of αS remains an enigma despite several promising reports suggesting many putative roles ranging from synaptic vesicle regulation at the neurological synapse to antioxidant and chaperone-like functions. Considering the association of αS with membrane micro-domains *in vivo* and to probe the functional relevance of αS-membrane interactions in PD, we investigated how physical membrane properties like membrane packing and fluidity in SLBs were affected by αS binding. Monomeric αS was observed to organize into clusters on the SLBs used in this thesis as described in **Chapter 3**. Using truncated variants of αS with comparable membrane binding affinities, we saw that the driving force for αS cluster formation is a complex interplay of electrostatic and hydrophobic interactions. Clustering of αS on SLBs immediately lead to impaired lipid diffusion and a marked increase in packing order of underlying lipids. The increased lipid packing order in SLBs was not only shown using fluorescence anisotropy measurements but also, for the first time, in confocal fluorescence microscopy experiments using the lipid-order sensitive DPH dye. We concluded that the clustering of αS on lipid bilayers induces ordering and results in impaired lipid diffusion. Given the sensitivity of αS binding to membrane curvature and its ability induce local curvature in lipid membranes upon binding[110], it is plausible that an increase in local membrane curvature upon αS binding exposes the acyl region in such curved regions and allows further binding of αS. The dense accumulation of αS on the membrane surface could be a strong driving force for membrane cluster formation. The fact that αS can create ordered regions in lipid membranes could be could be relevant to the function of αS since ordering of lipids is often coupled to protein function *in vivo*.

Next, we aimed to elucidate the possible mechanisms by which amyloid formation of αS on the membrane causes membrane damage. We looked at the result of αS-SLB interactions at longer time scales as described in **Chapter 3** in **Chapter 4**. At these longer timescales, the accumulation of WT-αS on lipid bilayers resulted in the formation of amyloid structures (depending on the protein to lipid ratio) which grew in size over time. The formation of amyloid aggregates on SLBs was required for SLB damage to occur. The conversion of membrane bound monomers to amyloid structures led to significant membrane damage and lipid extraction. An αS variant that was not able to assemble into amyloid was unable to damage lipid bilayers. There is accumulating evidence in the literature and from this chapter

that αS-phospholipid interactions are only significant when the membrane contains a very high anionic lipid fraction (>0.4). Such high fractions of anionic lipids are rarely found in physiological cell membranes. It is therefore likely that other damage mechanisms are more relevant in physiological environment. To probe alternative mechanisms of lipid membrane damage, experiments have been carried out in a collaboration project with pre-formed αS oligomers (Chaudhary et al, manuscript in preparation).

New reports suggest that more than 95% of αS is N-terminally acetylated in physiological environment. After this seminal report the impact of this post-translational modification in αS on binding to phospholipid bilayers and aggregation into amyloid fibrils was investigated. The obtained results can be found in **Chapter 5** and show that N-terminal acetylation seems to have little influence on the lipid binding characteristics of αS. The impact of N-terminal acetylation on the membrane binding affinity of αS as a function of membrane anionic charge density, cholesterol content and curvature was negligible. Although N-terminal acetylation does not seem to affect the membrane binding characteristics of αS it is possible that N-terminal acetylation plays an important role in regulating interactions of αS with other proteins in the cytoplasm or on the cell membrane like SNAREs, actin or tubulin. Further studies targeted at elucidating such binding partners (lipids or proteins) of monomeric αS could yield more insight into the impact of N-terminal acetylation in regulating interactions. Although we did not observe major differences in aggregation rates of both N-terminal acetylated-αS and WT-αS, N-terminal acetylation of αS resulted in a high degree of homogeneity in aggregation lag times and fibril morphologies as observed with AFM and 2D-IR studies.

Lastly to probe which physicochemical interactions were involved in αS amyloid formation in the absence of lipid membranes, we looked at different N-terminal and C-terminal truncated variants of αS. Our observations suggest that truncations in the N-terminal region of αS do not affect the resulting fibril morphology while truncations in the C-terminal region of αS result in very different fibril structures as shown in **Chapter 6**. Our preliminary results show that the C-terminal truncated fibrils can incorporate C-terminal truncated monomers but do not incorporate full-length αS suggesting that the core of the WT and C-terminal truncated αS fibrils is different. Additional experiments are planned to ascertain differences in fibril structures using 2D-IR spectroscopy.

7.1 Outlook

In this thesis, we used SLBs to understand the physicochemical factors behind interactions of αS with lipid membranes. The use of SLBs has greatly added to the understanding of the interactions between proteins and lipid membranes and the described methodologies to prepare SLBs with a high fraction of anionic lipids will allow studies not only pertaining to αS

but also in a wide range of other biological and non-biological systems. On the basis of the results and conclusions presented in this thesis and keeping in mind recent developments, I present here some prospects for future work which will serve to answer several open questions and increase our current understanding on αS and its involvement in PD:

- What is the structural arrangement of WT-αS monomers in protein clusters on lipid membranes and do they differ from that of NTAc-αS monomers? It would be interesting to isolate the initial αS clusters and investigate their biophysical properties using FTIR and CD spectroscopy. Using single molecule FRET, insights into the molecular arrangement of the monomer within these clusters can be gained. These results would help understand the biochemical factors that play a role in the structural transition of non-amyloid containing αS clusters into amyloid αS aggregates.
- It is likely that changes in cell membrane composition which occur in cellular aging could be relevant in the pathology of PD. It would be interesting to probe if changes in membrane fluidities as a consequence of altered membrane composition could trigger aggregation of αS in contrast to our observations in thesis.
- The use of the physiologically relevant NTAc-αS with known PD point mutations in studies directed in understanding aggregation kinetics and fibril assembly of αS would be more relevant to PD.
- Does N-terminal acetylated αS have other protein/lipid binding partners? Is N-terminal acetylation a regulatory modification to diminish promiscuous interactions or a silent modification? How does N-terminal acetylation of αS affect aggregation in vivo?

References

(1) Dobson, C. M. Protein misfolding, evolution and disease Trends Biochem. Sci. 1999, 24, 329-332.

(2) Theillet, F. X.; Binolfi, A.; Frembgen-Kesner, T.; Hingorani, K.; Sarkar, M.; Kyne, C.; Li, C. G.; Crowley, P. B.; Gierasch, L.; Pielak, G. J.; Elcock, A. H.; Gershenson, A.; Selenko, P. Physicochemical Properties of Cells and Their Effects on Intrinsically Disordered Proteins (IDPs) Chem. Rev. 2014, 114, 6661-6714.

(3) Uversky, V. N.; Dunker, A. K. Understanding protein non-folding Biochimica Et Biophysica Acta-Proteins and Proteomics 2010, 1804, 1231-1264.

(4) Dyson, H. J.; Wright, P. E. Intrinsically unstructured proteins and their functions Nat. Rev. Mol. Cell Biol. 2005, 6, 197-208.

(5) Xie, H. B.; Vucetic, S.; Iakoucheva, L. M.; Oldfield, C. J.; Dunker, A. K.; Uversky, V. N.; Obradovic, Z. Functional anthology of intrinsic disorder. 1. Biological processes and functions of proteins with long disordered regions J Proteome Res 2007, 6, 1882-1898.

(6) Chiti, F.; Dobson, C. M. Protein misfolding, functional amyloid, and human disease Annu. Rev. Biochem. 2006, 75, 333-366.

(7) Stefani, M. Protein Folding and Misfolding, Relevance to Disease, and Biological Function; CRC Press, Taylor & Francis Group, 2008.

(8) Bukau, B.; Weissman, J.; Horwich, A. Molecular chaperones and protein quality control Cell 2006, 125, 443-451.

(9) Hartl, F. U.; Hayer-Hartl, M. Protein folding - Molecular chaperones in the cytosol: from nascent chain to folded protein Science 2002, 295, 1852-1858.

(10) Ciechanover, A.; Brundin, P. The ubiquitin proteasome system in neurodegenerative diseases: Sometimes the chicken, sometimes the egg Neuron 2003, 40, 427-446.

(11) Hartl, F. U.; Bracher, A.; Hayer-Hartl, M. Molecular chaperones in protein folding and proteostasis Nature 2011, 475, 324-332.

(12) Kayed, R.; Head, E.; Thompson, J. L.; McIntire, T. M.; Milton, S. C.; Cotman, C. W.; Glabe, C. G. Common structure of soluble amyloid oligomers implies common mechanism of pathogenesis Science 2003, 300, 486-489.

(13) Glabe, C. G.; Kayed, R. Common structure and toxic function of amyloid oligomers implies a common mechanism of pathogenesis Neurology 2006, 66, S74-S78.

(14) Schleiden, M. J. Beiträge zur phytogenesis Archiv für Anatomie, Physiologie und Wissenschaftliche Medicin 1838, 13, 137-176.

(15) Virchow, R. Zur Cellulose-Frage Virchows Archiv fur pathologische Anatomie und Physiologie 1854, 416-426.

(16) Friedreich, N.; Kekulé, F. A. Zur Amyloidfrage Virchows Archiv fur pathologische Anatomie und Physiologie 1859, 16, 50-65.

(17) Cohen, A. S.; Calkins, E. Electron microscopic observations on a fibrous component in amyloid of diverse origins Nature 1959, 183, 1202-1203.

(18) Shirahama, T.; Cohen, A. S. High-resolution electron microscopic analysis of the amyloid fibril J. Cell Biol. 1967, 33, 679-708.

(19) Shirahama, T.; Cohen, A. S. Reconstitution of amyloid fibrils from alkaline extracts J. Cell Biol. 1967, 35, 459-464.

(20) Eanes, E. D.; Glenner, G. G. X-ray diffraction studies on amyloid filaments J. Histochem. Cytochem. 1968, 16, 673-677.

(21) Chiti, F.; Webster, P.; Taddei, N.; Clark, A.; Stefani, M.; Ramponi, G.; Dobson, C. M. Designing conditions for in vitro formation of amyloid protofilaments and fibrils Proc. Natl. Acad. Sci. U.S.A. 1999, 96, 3590-3594.

(22) Maroteaux, L.; Campanelli, J. T.; Scheller, R. H. Synuclein - a Neuron-Specific Protein Localized to the Nucleus and Presynaptic Nerve-Terminal J. Neurosci. 1988, 8, 2804-2815.

(23) Ueda, K.; Fukushima, H.; Masliah, E.; Xia, Y.; Iwai, A.; Yoshimoto, M.; Otero, D. A. C.; Kondo, J.; Ihara, Y.; Saitoh, T. Molecular-Cloning of Cdna-Encoding an Unrecognized Component of Amyloid in Alzheimer-Disease Proc. Natl. Acad. Sci. U.S.A. 1993, 90, 11282-11286.

(24) Jakes, R.; Spillantini, M. G.; Goedert, M. Identification of 2 Distinct Synucleins from Human Brain FEBS Lett. 1994, 345, 27-32.

(25) Iwai, A.; Masliah, E.; Yoshimoto, M.; Ge, N. F.; Flanagan, L.; Desilva, H. A. R.; Kittel, A.; Saitoh, T. The Precursor Protein of Non-a-Beta Component of Alzheimers-Disease Amyloid Is a Presynaptic Protein of the Central-Nervous-System Neuron 1995, 14, 467-475.

(26) Iwai, A.; Yoshimoto, M.; Masliah, E.; Saitoh, T. Non-a-Beta Component of Alzheimers-Disease Amyloid (Nac) Is Amyloidogenic Biochemistry 1995, 34, 10139-10145.

(27) Weinreb, P. H.; Zhen, W. G.; Poon, A. W.; Conway, K. A.; Lansbury, P. T. NACP, a protein implicated in Alzheimer's disease and learning, is natively unfolded Biochemistry 1996, 35, 13709-13715.

(28) Iwai, A.; Masliah, E.; Yoshimoto, M.; Saitoh, T. The Precursor Protein of Non-a-Beta Component of Alzheimers-Disease Amyloid (Nacp) Is a Presynaptic Protein of the Central-Nervous-System Neurobiol. Aging 1994, 15, S58-S58.

(29) Iwai, A.; Masliah, E.; Sundsmo, M. P.; DeTeresa, R.; Mallory, M.; Salmon, D. P.; Saitoh, T. The synaptic protein NACP is abnormally expressed during the progression of Alzheimer's disease Brain Res. 1996, 720, 230-234.

(30) Polymeropoulos, M. H.; Lavedan, C.; Leroy, E.; Ide, S. E.; Dehejia, A.; Dutra, A.; Pike, B.; Root, H.; Rubenstein, J.; Boyer, R.; Stenroos, E. S.; Chandrasekharappa, S.; Athanassiadou, A.; Papapetropoulos, T.; Johnson, W. G.; Lazzarini, A. M.; Duvoisin, R. C.; Di Iorio, G.; Golbe, L. I.; Nussbaum, R. L. Mutation in the alpha-synuclein gene identified in families with Parkinson's disease Science 1997, 276, 2045-2047.

(31) Spillantini, M. G.; Schmidt, M. L.; Lee, V. M.; Trojanowski, J. Q.; Jakes, R.; Goedert, M. Alpha-synuclein in Lewy bodies Nature 1997, 388, 839-840.

(32) Wakabayashi, K.; Matsumoto, K.; Takayama, K.; Yoshimoto, M.; Takahashi, H. NACP, a presynaptic protein, immunoreactivity in Lewy bodies in Parkinson's disease Neurosci. Lett. 1997, 239, 45-48.

(33) Spillantini, M. G.; Crowther, R. A.; Jakes, R.; Hasegawa, M.; Goedert, M. alpha-synuclein in filamentous inclusions of Lewy bodies from Parkinson's disease and dementia with Lewy bodies Proc. Natl. Acad. Sci. U.S.A. 1998, 95, 6469-6473.

(34) Conway, K. A.; Harper, J. D.; Lansbury, P. T. Accelerated in vitro fibril formation by a mutant alpha-synuclein linked to early-onset Parkinson disease Nat. Med. 1998, 4, 1318-1320.

(35) Singleton, A. B.; Farrer, M.; Johnson, J.; Singleton, A.; Hague, S.; Kachergus, J.; Hulihan, M.; Peuralinna, T.; Dutra, A.; Nussbaum, R.; Lincoln, S.; Crawley, A.; Hanson, M.; Maraganore, D.; Adler, C.; Cookson, M. R.; Muenter, M.; Baptista, M.; Miller, D.; Blancato, J.; Hardy, J.; Gwinn-Hardy, K. alpha-Synuclein locus triplication causes Parkinson's disease Science 2003, 302, 841.

(36) Rockenstein, E.; Hansen, L. A.; Mallory, M.; Trojanowski, J. Q.; Galasko, D.; Masliah, E. Altered expression of the synuclein family mRNA in Lewy body and Alzheimer's disease Brain Res. 2001, 914, 48-56.

(37) Chiba-Falek, O.; Lopez, G. J.; Nussbaum, R. L. Levels of alpha-synuclein mRNA in sporadic Parkinson disease patients Movement Disorders 2006, 21, 1703-1708.

(38) Bennett, M. C. The role of alpha-synuclein in neurodegenerative diseases Pharmacol. Ther. 2005, 105, 311-331.

(39) Kruger, R.; Kuhn, W.; Muller, T.; Woitalla, D.; Graeber, M.; Kosel, S.; Przuntek, H.; Epplen, J. T.; Schols, L.; Riess, O. Ala30Pro mutation in the gene encoding alpha-synuclein in Parkinson's disease Nat. Genet. 1998, 18, 106-108.

(40) Zarranz, J. J.; Alegre, J.; Gomez-Esteban, J. C.; Lezcano, E.; Ros, R.; Ampuero, I.; Vidal, L.; Hoenicka, J.; Rodriguez, O.; Atares, B.; Llorens, V.; Tortosa, E. G.; del Ser, T.; Munoz, D. G.; de Yebenes, J. G. The new mutation, E46K, of alpha-synuclein causes Parkinson and Lewy body dementia Ann. Neurol. 2004, 55, 164-173.

(41) Pasanen, P.; Myllykangas, L.; Siitonen, M.; Raunio, A.; Kaakkola, S.; Lyytinen, J.; Tienari, P. J.; Poyhonen, M.; Paetau, A. A novel alpha-synuclein mutation A53E associated with atypical multiple system atrophy and Parkinson's disease-type pathology Neurobiol. Aging 2014, 35, 2180-2185.

(42) Proukakis, C.; Dudzik, C. G.; Brier, T.; MacKay, D. S.; Cooper, J. M.; Millhauser, G. L.; Houlden, H.; Schapira, A. H. A NOVEL alpha-SYNUCLEIN MISSENSE MUTATION IN PARKINSON DISEASE Neurology 2013, 80, 1062-1064.

(43) Kiely, A. P.; Asi, Y. T.; Kara, E.; Limousin, P.; Ling, H.; Lewis, P.; Proukakis, C.; Quinn, N.; Lees, A. J.; Hardy, J.; Revesz, T.; Houlden, H.; Holton, J. L. alpha-Synucleinopathy associated with G51D SNCA mutation: a link between Parkinson's disease and multiple system atrophy? Acta Neuropathologica 2013, 125, 753-769.

(44) Gai, W. P.; Yuan, H. X.; Li, X. Q.; Power, J. T.; Blumbergs, P. C.; Jensen, P. H. In situ and in vitro study of colocalization and segregation of alpha-synuclein, ubiquitin, and lipids in Lewy bodies Exp. Neurol. 2000, 166, 324-333.

(45) Serpell, L. C.; Berriman, J.; Jakes, R.; Goedert, M.; Crowther, R. A. Fiber diffraction of synthetic alpha-synuclein filaments shows amyloid-like cross-beta conformation Proc. Natl. Acad. Sci. U.S.A. 2000, 97, 4897-4902.

(46) Stefanis, L. alpha-Synuclein in Parkinson's Disease Cold Spring Harbor Perspectives in Medicine 2012, 2, a009399.

(47) Cookson, M. R. alpha-Synuclein and neuronal cell death Mol Neurodegener 2009, 4, 9.

(48) Cooper, A. A.; Gitler, A. D.; Cashikar, A.; Haynes, C. M.; Hill, K. J.; Bhullar, B.; Liu, K. N.; Xu, K. X.; Strathearn, K. E.; Liu, F.; Cao, S. S.; Caldwell, K. A.; Caldwell, G. A.; Marsischky, G.; Kolodner, R. D.; LaBaer, J.; Rochet, J. C.; Bonini, N. M.; Lindquist, S. alpha-synuclein blocks ER-Golgi traffic and Rab1 rescues neuron loss in Parkinson's models Science 2006, 313, 324-328.

(49) Fiskum, G.; Starkov, A.; Polster, B. M.; Chinopoulos, C. Mitochondrial mechanisms of neural cell death and neuroprotective interventions in Parkinson's disease Ann. N. Y. Acad. Sci. 2003, 991, 111-119.

(50) McLean, P. J.; Kawamata, H.; Ribich, S.; Hyman, B. T. Membrane association and protein conformation of alpha-synuclein in intact neurons - Effect of Parkinson's disease-linked mutations J. Biol. Chem. 2000, 275, 8812-8816.

(51) Quilty, M. C.; King, A. E.; Gai, W. P.; Pountney, D. L.; West, A. K.; Vickers, J. C.; Dickson, T. C. Alpha-synuclein is upregulated in neurones in response to chronic oxidative stress and is associated with neuroprotection Exp. Neurol. 2006, 199, 249-256.

(52) Ellis, C. E.; Murphy, E. J.; Mitchell, D. C.; Golovko, M. Y.; Scaglia, F.; Barcelo-Coblijn, G. C.; Nussbaum, R. L. Mitochondrial lipid abnormality and electron transport chain impairment in mice lacking alpha-synuclein Mol. Cell. Biol. 2005, 25, 10190-10201.

(53) Lotharius, J.; Brundin, P. Pathogenesis of Parkinson's disease: Dopamine, vesicles and alpha-synuclein Nature Reviews Neuroscience 2002, 3, 932-942.

(54) Dawson, T. M.; Dawson, V. L. Molecular pathways of neurodegeneration in Parkinson's disease Science 2003, 302, 819-822.

(55) Goedert, M. Alpha-synuclein and neurodegenerative diseases Nature Reviews Neuroscience 2001, 2, 492-501.

(56) Breydo, L.; Wu, J. W.; Uversky, V. N. Alpha-synuclein misfolding and Parkinson's disease Biochim. Biophys. Acta 2012, 1822, 261-285.

(57) Peelaerts, W.; Bousset, L.; Van der Perren, A.; Moskalyuk, A.; Pulizzi, R.; Giugliano, M.; Van den Haute, C.; Melki, R.; Baekelandt, V. Alpha-synuclein strains cause distinct synucleinopathies after local and systemic administration Nature 2015, 522, 340-344.

(58) Bousset, L.; Pieri, L.; Ruiz-Arlandis, G.; Gath, J.; Jensen, P. H.; Habenstein, B.; Madiona, K.; Olieric, V.; Bockmann, A.; Meier, B. H.; Melki, R. Structural and functional characterization of two alpha-synuclein strains Nat Commun 2013, 4, 2575.

(59) Rodriguez, J. A.; Ivanova, M. I.; Sawaya, M. R.; Cascio, D.; Reyes, F. E.; Shi, D.; Sangwan, S.; Guenther, E. L.; Johnson, L. M.; Zhang, M.; Jiang, L.; Arbing, M. A.; Nannenga, B. L.; Hattne, J.; Whitelegge, J.; Brewster, A. S.; Messerschmidt, M.; Boutet, S.; Sauter, N. K.; Gonen, T.; Eisenberg, D. S. Structure of the toxic core of alpha-synuclein from invisible crystals Nature 2015, 525, 486-490.

(60) Andreasen, M.; Lorenzen, N.; Otzen, D. Interactions between misfolded protein oligomers and membranes: A central topic in neurodegenerative diseases? Biochim. Biophys. Acta 2015, 1848, 1897-1907.

(61) Chen, S. W.; Drakulic, S.; Deas, E.; Ouberai, M.; Aprile, F. A.; Arranz, R.; Ness, S.; Roodveldt, C.; Guilliams, T.; De-Genst, E. J.; Klenerman, D.; Wood, N. W.; Knowles, T. P. J.; Alfonso, C.; Rivas, G.; Abramov, A. Y.; Valpuesta, J. M.; Dobson, C. M.; Cremades, N. Structural characterization of toxic oligomers that are kinetically trapped during α-synuclein fibril formation Proceedings of the National Academy of Sciences 2015, 112, E1994-E2003.

(62) Lorenzen, N.; Otzen, D. E. Oligomers of alpha-synuclein: picking the culprit in the line-up Amyloids in Health and Disease 2014, 56, 137-148.

(63) Horrocks, M. H.; Lee, S. F.; Gandhi, S.; Iljina, M.; Tosatto, L.; Dobson, C. M.; Klenerman, D. Single-Molecule Characterisation of Alpha-Synuclein Oligomers Biophys. J. 2014, 106, 267a-267a.

(64) Fecchio, C.; De Franceschi, G.; Relini, A.; Greggio, E.; Dalla Serra, M.; Bubacco, L.; Polverino de Laureto, P. alpha-Synuclein Oligomers Induced by Docosahexaenoic Acid Affect Membrane Integrity PLoS One 2013, 8, e82732.

(65) Lee, M.; Hyun, D. H.; Halliwell, B.; Jenner, P. Effect of the overexpression of wild-type or mutant alpha-synuclein on cell susceptibility to insult J. Neurochem. 2001, 76, 998-1009.

(66) Manning-Bog, A. B.; McCormack, A. L.; Purisai, M. G.; Bolin, L. M.; Di Monte, D. A. Alpha-synuclein overexpression protects against paraquat-induced neurodegeneration J. Neurosci. 2003, 23, 3095-3099.

(67) Hashimoto, M.; Hsu, L. J.; Rockenstein, E.; Takenouchi, T.; Mallory, M.; Masliah, E. alpha-synuclein protects against oxidative stress via inactivation of the c-Jun N-terminal kinase stress-signaling pathway in neuronal cells J. Biol. Chem. 2002, 277, 11465-11472.

(68) Hayashi, S.; Wakabayashi, K.; Ishikawa, A.; Nagai, H.; Saito, M.; Maruyama, M.; Takahashi, T.; Ozawa, T.; Tsuji, S.; Takahashi, H. An autopsy case of autosomal-recessive juvenile parkinsonism with a homozygous exon 4 deletion in the parkin gene Movement Disorders 2000, 15, 884-888.

(69) Moore, D. J.; West, A. B.; Dawson, V. L.; Dawson, T. M. Molecular pathophysiology of Parkinson's disease Annu. Rev. Neurosci. 2005, 28, 57-87.

(70) Jenco, J. M.; Rawlingson, A.; Daniels, B.; Morris, A. J. Regulation of phospholipase D2: Selective inhibition of mammalian phospholipase D isoenzymes by alpha- and beta-synucleins Biochemistry 1998, 37, 4901-4909.

(71) Murphy, D. D.; Rueter, S. M.; Trojanowski, J. Q.; Lee, V. M. Y. Synucleins are developmentally expressed, and alpha-synuclein regulates the size of the presynaptic vesicular pool in primary hippocampal neurons J. Neurosci 2000, 20, 3214-3220.

(72) Zhu, M.; Qin, Z. J.; Hu, D. M.; Munishkina, L. A.; Fink, A. L. alpha-synuclein can function as an antioxidant preventing oxidation of unsaturated lipid in vesicles Biochemistry 2006, 45, 8135-8142.

(73) Bussell, R.; Eliezer, D. A structural and functional role for 11-mer repeats in alpha-synuclein and other exchangeable lipid binding proteins J. Mol. Biol. 2003, 329, 763-778.

(74) Sharon, R.; Bar-Joseph, I.; Frosch, M. P.; Walsh, D. M.; Hamilton, J. A.; Selkoe, D. J. The formation of highly soluble oligomers of alpha-synuclein is regulated by fatty acids and enhanced in Parkinson's disease Neuron 2003, 37, 583-595.

(75) Winner, B.; Jappelli, R.; Maji, S. K.; Desplats, P. A.; Boyer, L.; Aigner, S.; Hetzer, C.; Loher, T.; Vilar, M.; Campionic, S.; Tzitzilonis, C.; Soragni, A.; Jessberger, S.; Mira, H.; Consiglio, A.; Pham, E.; Masliah, E.; Gage, F. H.; Riek, R. In vivo demonstration that alpha-synuclein oligomers are toxic Proc. Natl. Acad. Sci. USA 2011, 108, 4194-4199.

(76) Danzer, K. M.; Haasen, D.; Karow, A. R.; Moussaud, S.; Habeck, M.; Giese, A.; Kretzschmar, H.; Hengerer, B.; Kostka, M. Different species of alpha-synuclein oligomers induce calcium influx and seeding J. Neurosci. 2007, 27, 9220-9232.

(77) Kalia, L. V.; Kalia, S. K.; McLean, P. J.; Lozano, A. M.; Lang, A. E. alpha-Synuclein oligomers and clinical implications for Parkinson disease Ann. Neurol. 2013, 73, 155-169.

(78) Stefanovic, A. N.; Stockl, M. T.; Claessens, M. M.; Subramaniam, V. alpha-Synuclein oligomers distinctively permeabilize complex model membranes The FEBS journal 2014, 281, 2838-2850.

(79) Stefanovic, A. N. D.; Stockl, M. T.; Claessens, M. M. A. E.; Subramaniam, V. Alpha-synuclein oligomers distinctively permeabilize model plasma and mitochondrial membranes European Biophysics Journal with Biophysics Letters 2013, 42, S156-S156.

(80) Fusco, G.; De Simone, A.; Gopinath, T.; Vostrikov, V.; Vendruscolo, M.; Dobson, C. M.; Veglia, G. Direct observation of the three regions in alpha-synuclein that determine its membrane-bound behaviour Nat Commun 2014, 5, 3827.

(81) Crowther, R. A.; Jakes, R.; Spillantini, M. G.; Goedert, M. Synthetic filaments assembled from C-terminally truncated alpha-synuclein FEBS Lett. 1998, 436, 309-312.

(82) Kim, T. D.; Paik, S. R.; Yang, C. H. Structural and functional implications of C-terminal regions of alpha-synuclein Biochemistry 2002, 41, 13782-13790.

(83) Levitan, K.; Chereau, D.; Cohen, S. I.; Knowles, T. P.; Dobson, C. M.; Fink, A. L.; Anderson, J. P.; Goldstein, J. M.; Millhauser, G. L. Conserved C-terminal charge exerts a profound influence on the aggregation rate of alpha-synuclein J. Mol. Biol. 2011, 411, 329-333.

(84) Anderson, J. P.; Walker, D. E.; Goldstein, J. M.; de Laat, R.; Banducci, K.; Caccavello, R. J.; Barbour, R.; Huang, J.; Kling, K.; Lee, M.; Diep, L.; Keim, P. S.; Shen, X.; Chataway, T.; Schlossmacher, M. G.; Seubert, P.; Schenk, D.; Sinha, S.; Gai, W. P.; Chilcote, T. J. Phosphorylation of Ser-129 is the dominant pathological modification of alpha-synuclein in familial and sporadic Lewy body disease J. Biol. Chem. 2006, 281, 29739-29752.

(85) Paleologou, K. E.; Schmid, A. W.; Rospigliosi, C. C.; Kim, H. Y.; Lamberto, G. R.; Fredenburg, R. A.; Lansbury, P. T.; Fernandez, C. O.; Eliezer, D.; Zweckstetter, M.; Lashuel, H. A. Phosphorylation at Ser-129 but not the phosphomimics S129E/D inhibits the fibrillation of alpha-synuclein J. Biol. Chem. 2008, 283, 16895-16905.

(86) Zabrocki, P.; Bastiaens, I.; Delay, C.; Barnmens, T.; Ghillebert, R.; Pellens, K.; De Virgilio, C.; Van Leuven, F.; Winderickx, J. Phosphorylation, lipid raft interaction and traffic of alpha-synuclein in a yeast model for Parkinson Biochim. Biophys. Acta 2008, 1783, 1767-1780.

(87) Bartels, T.; Choi, J. G.; Selkoe, D. J. alpha-Synuclein occurs physiologically as a helically folded tetramer that resists aggregation Nature 2011, 477, 107-110.

(88) Fauvet, B.; Mbefo, M. K.; Fares, M. B.; Desobry, C.; Michael, S.; Ardah, M. T.; Tsika, E.; Coune, P.; Prudent, M.; Lion, N.; Eliezer, D.; Moore, D. J.; Schneider, B.; Aebischer, P.; El-Agnaf, O. M.; Masliah, E.; Lashuel, H. A. Alpha-synuclein in central nervous system and from erythrocytes, mammalian cells, and Escherichia coli exists predominantly as disordered monomer J. Biol. Chem. 2012, 287, 15345-15364.

(89) Wang, W.; Perovic, I.; Chittuluru, J.; Kaganovich, A.; Nguyen, L. T.; Liao, J.; Auclair, J. R.; Johnson, D.; Landeru, A.; Simorellis, A. K.; Ju, S.; Cookson, M. R.; Asturias, F. J.; Agar, J. N.; Webb, B. N.; Kang, C.; Ringe, D.; Petsko, G. A.; Pochapsky, T. C.; Hoang, Q. Q. A soluble alpha-synuclein construct forms a dynamic tetramer Proc. Natl. Acad. Sci. USA 2011, 108, 17797-17802.

(90) Burre, J.; Vivona, S.; Diao, J.; Sharma, M.; Brunger, A. T.; Sudhof, T. C. Properties of native brain alpha-synuclein Nature 2013, 498, E4-6; discussion E6-7.

(91) Davidson, W. S.; Jonas, A.; Clayton, D. F.; George, J. M. Stabilization of alpha-synuclein secondary structure upon binding to synthetic membranes J. Biol. Chem. 1998, 273, 9443-9449.

(92) Wang, L.; Das, U.; Scott, D. A.; Tang, Y.; McLean, P. J.; Roy, S. alpha-synuclein multimers cluster synaptic vesicles and attenuate recycling Curr. Biol. 2014, 24, 2319-2326.

(93) Busch, D. J.; Oliphint, P. A.; Walsh, R. B.; Banks, S. M.; Woods, W. S.; George, J. M.; Morgan, J. R. Acute increase of alpha-synuclein inhibits synaptic vesicle recycling evoked during intense stimulation Molecular biology of the cell 2014, 25, 3926-3941.

(94) Lee, H. J.; Choi, C.; Lee, S. J. Membrane-bound alpha-synuclein has a high aggregation propensity and the ability to seed the aggregation of the cytosolic form J. Biol. Chem. 2002, 277, 671-678.

(95) Eliezer, D.; Kutluay, E.; Bussell, R.; Browne, G. Conformational properties of alpha-synuclein in its free and lipid-associated states J. Mol. Biol. 2001, 307, 1061-1073.

(96) Jao, C. C.; Hegde, B. G.; Chen, J.; Haworth, I. S.; Langen, R. Structure of membrane-bound alpha-synuclein from site-directed spin labeling and computational refinement Proc. Natl. Acad. Sci. U.S.A. 2008, 105, 19666-19671.

(97) Lokappa, S. B.; Ulmer, T. S. alpha-Synuclein Populates Both Elongated and Broken Helix States on Small Unilamellar Vesicles J. Biol. Chem. 2011, 286, 21450-21457.

(98) Cheng, C. Y.; Varkey, J.; Ambroso, M. R.; Langen, R.; Han, S. I. Hydration dynamics as an intrinsic ruler for refining protein structure at lipid membrane interfaces Proc. Natl. Acad. Sci. U.S.A. 2013, 110, 16838-16843.

(99) Ulmer, T. S.; Bax, A.; Cole, N. B.; Nussbaum, R. L. Structure and dynamics of micelle-bound human alpha-synuclein J. Biol. Chem. 2005, 280, 9595-9603.

(100) Ulmer, T. S.; Bax, A. Comparison of structure and dynamics of micelle-bound human alpha-synuclein and Parkinson disease variants J. Biol. Chem. 2005, 280, 43179-43187.

(101) Robotta, M.; Braun, P.; van Rooijen, B.; Subramaniam, V.; Huber, M.; Drescher, M. Direct evidence of coexisting horseshoe and extended helix conformations of membrane-bound alpha-synuclein ChemPhysChem 2011, 12, 267-269.

(102) Bodner, C. R.; Dobson, C. M.; Bax, A. Multiple tight phospholipid-binding modes of alpha-synuclein revealed by solution NMR spectroscopy J. Mol. Biol. 2009, 390, 775-790.

(103) Ouberai, M. M.; Wang, J.; Swann, M. J.; Galvagnion, C.; Guilliams, T.; Dobson, C. M.; Welland, M. E. alpha-Synuclein senses lipid packing defects and induces lateral expansion of lipids leading to membrane remodeling J. Biol. Chem. 2013, 288, 20883-20895.

(104) Nuscher, B.; Kamp, F.; Mehnert, T.; Odoy, S.; Haass, C.; Kahle, P. J.; Beyer, K. Alpha-synuclein has a high affinity for packing defects in a bilayer membrane: a thermodynamics study J. Biol. Chem. 2004, 279, 21966-21975.

(105) Middleton, E. R.; Rhoades, E. Effects of curvature and composition on alpha-synuclein binding to lipid vesicles Biophys. J. 2010, 99, 2279-2288.

(106) Jo, E.; McLaurin, J.; Yip, C. M.; St George-Hyslop, P.; Fraser, P. E. alpha-Synuclein membrane interactions and lipid specificity J. Biol. Chem. 2000, 275, 34328-34334.

(107) Rhoades, E.; Ramlall, T. F.; Webb, W. W.; Eliezer, D. Quantification of alpha-synuclein binding to lipid vesicles using fluorescence correlation spectroscopy Biophys. J. 2006, 90, 4692-4700.

(108) Shvadchak, V. V.; Falomir-Lockhart, L. J.; Yushchenko, D. A.; Jovin, T. M. Specificity and kinetics of alpha-synuclein binding to model membranes determined with fluorescent excited state intramolecular proton transfer (ESIPT) probe J. Biol. Chem. 2011, 286, 13023-13032.

(109) Bussell, R., Jr.; Ramlall, T. F.; Eliezer, D. Helix periodicity, topology, and dynamics of membrane-associated alpha-synuclein Protein Sci. 2005, 14, 862-872.

(110) Braun, A. R.; Sevcsik, E.; Chin, P.; Rhoades, E.; Tristram-Nagle, S.; Sachs, J. N. alpha-Synuclein induces both positive mean curvature and negative Gaussian curvature in membranes J. Am. Chem. Soc. 2012, 134, 2613-2620.

(111) Braun, A. R.; Lacy, M. M.; Ducas, V. C.; Rhoades, E.; Sachs, J. N. alpha-Synuclein-Induced Membrane Remodeling Is Driven by Binding Affinity, Partition Depth, and Interleaflet Order Asymmetry J. Am. Chem. Soc. 2014, 136, 9962-9972.

(112) van Rooijen, B. D.; Claessens, M. M.; Subramaniam, V. Lipid bilayer disruption by oligomeric alpha-synuclein depends on bilayer charge and accessibility of the hydrophobic core Biochim. Biophys. Acta 2009, 1788, 1271-1278.

(113) Martinez, Z.; Zhu, M.; Han, S. B.; Fink, A. L. GM1 specifically interacts with alpha-synuclein and inhibits fibrillation Biochemistry 2007, 46, 1868-1877.

(114) Fortin, D. L.; Troyer, M. D.; Nakamura, K.; Kubo, S.; Anthony, M. D.; Edwards, R. H. Lipid rafts mediate the synaptic localization of alpha-synuclein J. Neurosci 2004, 24, 6715-6723.

(115) Fauvet, B.; Fares, M. B.; Samuel, F.; Dikiy, I.; Tandon, A.; Eliezer, D.; Lashuel, H. A. Characterization of semisynthetic and naturally Nalpha-acetylated alpha-synuclein in vitro and in intact cells: implications for aggregation and cellular properties of alpha-synuclein J. Biol. Chem. 2012, 287, 28243-28262.

(116) Bartels, T.; Kim, N. C.; Luth, E. S.; Selkoe, D. J. N-alpha-acetylation of alpha-synuclein increases its helical folding propensity, GM1 binding specificity and resistance to aggregation PLoS One 2014, 9, e103727.

(117) Fantini, J.; Carlus, D.; Yahi, N. The fusogenic tilted peptide (67-78) of alpha-synuclein is a cholesterol binding domain Biochim. Biophys. Acta 2011, 1808, 2343-2351.

(118) Sethuraman, A.; Belfort, G. Protein structural perturbation and aggregation on homogeneous surfaces Biophys. J. 2005, 88, 1322-1333.

(119) Gray, J. J. The interaction of proteins with solid surfaces Curr. Opin. Struct. Biol. 2004, 14, 110-115.

(120) Galvagnion, C.; Buell, A. K.; Meisl, G.; Michaels, T. C.; Vendruscolo, M.; Knowles, T. P.; Dobson, C. M. Lipid vesicles trigger alpha-synuclein aggregation by stimulating primary nucleation Nat. Chem. Biol. 2015, 11, 229-234.

(121) Hoyer, W. G.; Cherny, D.; Subramaniam, V.; Jovin, T. M. Rapid self-assembly of alpha-synuclein observed by in situ atomic force microscopy J. Mol. Biol. 2004, 340, 127-139.

(122) Morriss-Andrews, A.; Shea, J. E. Kinetic pathways to peptide aggregation on surfaces: The effects of beta-sheet propensity and surface attraction J. Chem. Phys. 2012, 136, 065103.

(123) Goldsbury, C.; Kistler, J.; Aebi, U.; Arvinte, T.; Cooper, G. J. S. Watching amyloid fibrils grow by time-lapse atomic force microscopy J. Mol. Biol. 1999, 285, 33-39.

(124) Zhu, M.; Souillac, P. O.; Ionescu-Zanetti, C.; Carter, S. A.; Fink, A. L. Surface-catalyzed amyloid fibril formation J. Biol. Chem. 2002, 277, 50914-50922.

(125) Iyer, A.; Petersen, Nils O.; Claessens, Mireille M. A. E.; Subramaniam, V. Amyloids of alpha-synuclein affect the structure and dynamics of supported lipid bilayers Biophys. J. 2014, 106, 2585-2594.

(126) Rabe, M.; Soragni, A.; Reynolds, N. P.; Verdes, D.; Liverani, E.; Riek, R.; Seeger, S. On-surface aggregation of alpha-synuclein at nanomolar concentrations results in two distinct growth mechanisms ACS Chem. Neurosci. 2013, 4, 408-417.

(127) Reynolds, N. P.; Soragni, A.; Rabe, M.; Verdes, D.; Liverani, E.; Handschin, S.; Riek, R.; Seeger, S. Mechanism of membrane interaction and disruption by alpha-synuclein J. Am. Chem. Soc. 2011, 133, 19366-19375.

(128) Mahul-Mellier, A. L.; Vercruysse, F.; Maco, B.; Ait-Bouziad, N.; De Roo, M.; Muller, D.; Lashuel, H. A. Fibril growth and seeding capacity play key roles in α-synuclein-mediated apoptotic cell death Cell Death Differ. 2015, 22, 2107-2122.

(129) Legler, D. F.; Micheau, O.; Doucey, M. A.; Tschopp, J.; Bron, C. Recruitment of TNF receptor 1 to lipid rafts is essential for TNFalpha-mediated NF-kappaB activation Immunity 2003, 18, 655-664.

(130) Pan, L.; Wu, H.; Shen, C.; Shi, Y.; Jin, W.; Xia, J.; Zhang, M. Clustering and synaptic targeting of PICK1 requires direct interaction between the PDZ domain and lipid membranes EMBO J. 2007, 26, 4576-4587.

(131) Kay, J. G.; Grinstein, S. Phosphatidylserine-mediated cellular signaling Adv. Exp. Med. Biol. 2013, 991, 177-193.

(132) Lang, T.; Rizzoli, S. O. Membrane Protein Clusters at Nanoscale Resolution: More Than Pretty Pictures Physiology 2010, 25, 116-124.

(133) Strahl, H.; Burmann, F.; Hamoen, L. W. The actin homologue MreB organizes the bacterial cell membrane Nat. Commun. 2014, 5, 1-11.

(134) Goswami, D.; Gowrishankar, K.; Bilgrami, S.; Ghosh, S.; Raghupathy, R.; Chadda, R.; Vishwakarma, R.; Rao, M.; Mayor, S. Nanoclusters of GPI-Anchored Proteins Are Formed by Cortical Actin-Driven Activity Cell 2008, 135, 1085-1097.

(135) Pike, L. J. Lipid rafts: heterogeneity on the high seas Biochem. J. 2004, 378, 281-292.

(136) Stockl, M.; Fischer, P.; Wanker, E.; Herrmann, A. Alpha-synuclein selectively binds to anionic phospholipids embedded in liquid-disordered domains J. Mol. Biol. 2008, 375, 1394-1404.

(137) Bagatolli, L. A.; Ipsen, J. H.; Simonsen, A. C.; Mouritsen, O. G. An outlook on organization of lipids in membranes: searching for a realistic connection with the organization of biological membranes Prog. Lipid Res. 2010, 49, 378-389.

(138) Ramanathan, M.; Shrestha, L. K.; Mori, T.; Ji, Q. M.; Hill, J. P.; Ariga, K. Amphiphile nanoarchitectonics: from basic physical chemistry to advanced applications PCCP 2013, 15, 10580-10611.

(139) Tamm, L. K.; McConnell, H. M. Supported phospholipid bilayers Biophys. J. 1985, 47, 105-113.

(140) Lin, W.-C.; Yu, C.-H.; Triffo, S.; Groves, J. T. In Current Protocols in Chemical Biology; John Wiley & Sons, Inc.: 2009.

(141) Cremer, P. S.; Boxer, S. G. Formation and Spreading of Lipid Bilayers on Planar Glass Supports J. Phys. Chem. B 1999, 103, 2554-2559

(142) Domanov, Y. A.; Kinnunen, P. K. Islet amyloid polypeptide forms rigid lipid-protein amyloid fibrils on supported phospholipid bilayers J. Mol. Biol. 2008, 376, 42-54.

(143) Pandey, A. P.; Haque, F.; Rochet, J. C.; Hovis, J. S. Clustering of alpha-synuclein on supported lipid bilayers: role of anionic lipid, protein, and divalent ion concentration Biophys. J. 2009, 96, 540-551.

(144) Sasahara, K.; Morigaki, K.; Okazaki, T.; Hamada, D. Binding of islet amyloid polypeptide to supported lipid bilayers and amyloid aggregation at the membranes Biochemistry 2012, 51, 6908-6919.

(145) Sasahara, K.; Morigaki, K.; Shinya, K. Amyloid aggregation and deposition of human islet amyloid polypeptide at membrane interfaces FEBS J. 2014, 281, 2597-2612.

(146) Gozen, I.; Dommersnes, P.; Czolkos, I.; Jesorka, A.; Lobovkina, T.; Orwar, O. Fractal avalanche ruptures in biological membranes Nat Mater 2010, 9, 908-912.

(147) Janmey, P. A.; Kinnunen, P. K. J. Biophysical properties of lipids and dynamic membranes Trends Cell Biol. 2006, 16, 538-546.

(148) Welti, R.; Li, W. Q.; Li, M. Y.; Sang, Y. M.; Biesiada, H.; Zhou, H. E.; Rajashekar, C. B.; Williams, T. D.; Wang, X. M. Profiling membrane lipids in plant stress responses - Role of phospholipase D alpha in freezing-induced lipid changes in Arabidopsis J. Biol. Chem. 2002, 277, 31994-32002.

(149) Los, D. A.; Mironov, K. S.; Allakhverdiev, S. I. Regulatory role of membrane fluidity in gene expression and physiological functions Photosynth. Res. 2013, 116, 489-509.

(150) van Meer, G.; de Kroon, A. I. P. M. Lipid map of the mammalian cell J. Cell Sci. 2011, 124, 5-8.

(151) van Meer, G.; Voelker, D. R.; Feigenson, G. W. Membrane lipids: where they are and how they behave Nat. Rev. Mol. Cell Biol. 2008, 9, 112-124.

(152) Haque, F.; Pandey, A. P.; Cambrea, L. R.; Rochet, J. C.; Hovis, J. S. Adsorption of alpha-synuclein on lipid bilayers: modulating the structure and stability of protein assemblies J. Phys. Chem. B 2010, 114, 4070-4081.

(153) Jurkiewicz, P.; Cwiklik, L.; Vojtíšková, A.; Jungwirth, P.; Hof, M. Structure, dynamics, and hydration of POPC/POPS bilayers suspended in NaCl, KCl, and CsCl solutions Biochim. Biophys. Acta 2011, 609-616.

(154) Picas, L.; Rico, F.; Scheuring, S. Direct measurement of the mechanical properties of lipid phases in supported bilayers Biophys. J. 2012, 102, L01-03

(155) Hellstrand, E.; Grey, M.; Ainalem, M. L.; Ankner, J.; Forsyth, V. T.; Fragneto, G.; Haertlein, M.; Dauvergne, M. T.; Nilsson, H.; Brundin, P.; Linse, S.; Nylander, T.; Sparr, E. Adsorption of alpha-synuclein to supported lipid bilayers: positioning and role of electrostatics ACS Chem. Neurosci. 2013, 4, 1339-1351.

(156) Gregory, S. M.; Lai, A. L.; Yang, S. T.; Tamm, L. K. Control of fusion activities of HIV GP41 and Ebola virus fusion domains by membrane lipids Abstracts of Papers of the American Chemical Society 2013, 245.

(157) Tamm, L. K.; Lee, J.; Liang, B. Y. Capturing Glimpses of an Elusive HIV Gp41 Prehairpin Fusion Intermediate Structure 2014, 22, 1225-1226.

(158) Yang, S. T.; Kiessling, V.; Simmons, J. A.; White, J. M.; Tamm, L. K. HIV gp41-mediated membrane fusion occurs at edges of cholesterol-rich lipid domains Nat. Chem. Biol. 2015, 11, 424-431.

(159) Filippov, A.; Antzutkin, O. N. Influence of Alzheimer's beta-amyloid peptide on the lateral diffusion of lipids in raft-forming bilayers Mendeleev Commun. 2013, 23, 316-318.

(160) Wan, C.; Kiessling, V.; Tamm, L. K. Coupling of cholesterol-rich lipid phases in asymmetric bilayers Biochemistry 2008, 47, 2190-2198.

(161) Saez-Cirion, A.; Nir, S.; Lorizate, M.; Agirre, A.; Cruz, A.; Perez-Gil, J.; Nieva, J. L. Sphingomyelin and cholesterol promote HIV-1 gp41 pretransmembrane sequence surface aggregation and membrane restructuring J. Biol. Chem. 2002, 277, 21776-21785.

(162) Zigoneanu, I. G.; Yang, Y. J.; Krois, A. S.; Haque, M. E.; Pielak, G. J. Interaction of α-synuclein with vesicles that mimic mitochondrial membranes Biochim. Biophys. Acta, 1818, 512-519.

(163) Stefanovic, A. N. D.; Stockl, M. T.; Claessens, M. M. A. E.; Subramaniam, V. alpha-Synuclein oligomers distinctively permeabilize complex model membranes FEBS J. 2014, 281, 2838-2850.

(164) Marom, M.; Azem, A. The use of cardiolipin-containing liposomes as a model system to study the interaction between proteins and the inner mitochondrial membrane Methods Mol Biol 2013, 1033, 147-155.

(165) Tokishita, S.; Mizuno, T. Transmembrane Signal-Transduction by the Escherichia-Coli Osmotic Sensor, Envz - Intramolecular Complementation of Transmembrane Signaling Mol. Microbiol. 1994, 13, 435-444.

(166) Sukharev, S. Mechanosensitive channels in bacteria as membrane tension reporters FASEB J. 1999, 13, S55-S61.

(167) Wood, J. M. Osmosensing by bacteria: Signals and membrane-based sensors Microbiol. Mol. Biol. Rev. 1999, 63, 230-262.

(168) Weaver, T. E.; Conkright, J. J. Function of surfactant proteins B and C Annu. Rev. Physiol. 2001, 63, 555-578.

(169) Maccarrone, M.; Bernardi, G.; Agro, A. F.; Centonze, D. Cannabinoid receptor signalling in neurodegenerative diseases: a potential role for membrane fluidity disturbance Br. J. Pharmacol. 2011, 163, 1379-1390.

(170) Reinhardt, K. A.; Kern, W. Handbook of silicon wafer cleaning technology; 2nd ed.; William Andrew: Norwich, NY, 2008.

(171) Weirich, K. L.; Israelachvili, J. N.; Fygenson, D. K. Bilayer Edges Catalyze Supported Lipid Bilayer Formation Biophys. J. 2010, 98, 85-92.

(172) Shinitzky, M. Membrane fluidity in malignancy. Adversative and recuperative Biochim. Biophys. Acta 1984, 738, 251-261.

(173) Llopis, P. M.; Sliusarenko, O.; Heinritz, J.; Jacobs-Wagner, C. In Vivo Biochemistry in Bacterial Cells Using FRAP: Insight into the Translation Cycle Biophys. J. 2012, 103, 1848-1859.

(174) Hardy, L. R. Fluorescence recovery after photobleaching (FRAP) with a focus on F-actin Curr Protoc Neurosci 2012, Chapter 2, Unit 2 17.

(175) Blumenthal, D.; Goldstien, L.; Edidin, M.; Gheber, L. A. Universal Approach to FRAP Analysis of Arbitrary Bleaching Patterns Scientific Reports 2015, 5, 11655.

(176) Deschout, H.; Hagman, J.; Fransson, S.; Jonasson, J.; Rudemo, M.; Loren, N.; Braeckmans, K. Straightforward FRAP for quantitative diffusion measurements with a laser scanning microscope Opt. Express 2010, 18, 22886-22905.

(177) Hallen, M. A.; Layton, A. T. Expanding the scope of quantitative FRAP analysis J. Theor. Biol. 2010, 262, 295-305.

(178) Sprague, B. L.; McNally, J. G. FRAP analysis of binding: proper and fitting Trends Cell Biol. 2005, 15, 84-91.

(179) Tilley, L.; Parker, P.; Adisa, A.; Rug, M.; Hibbs, A.; Newbold, C.; Klonis, N. Confocal FRAP studies to monitor protein dynamics in live cells Molecular biology of the cell 2002, 13, 501a-501a.

(180) Weiss, M. Challenges and artifacts in quantitative photobleaching experiments Traffic 2004, 5, 662-671.

(181) Axelrod, D.; Koppel, D. E.; Schlessinger, J.; Elson, E.; Webb, W. W. Mobility measurement by analysis of fluorescence photobleaching recovery kinetics Biophys. J. 1976, 16, 1055-1069.

(182) Soumpasis, D. M. Theoretical analysis of fluorescence photobleaching recovery experiments Biophys. J. 1983, 41, 95-97.

(183) Seu, K. J.; Cambrea, L. R.; Everly, R. M.; Hovis, J. S. Influence of lipid chemistry on membrane fluidity: tail and headgroup interactions Biophys. J. 2006, 91, 3727-3735.

(184) Loren, N.; Hagman, J.; Jonasson, J. K.; Deschout, H.; Bernin, D.; Cella-Zanacchi, F.; Diaspro, A.; McNally, J. G.; Ameloot, M.; Smisdom, N.; Nyden, M.; Hermansson, A. M.; Rudemo, M.; Braeckmans, K. Fluorescence recovery after photobleaching in material and life sciences: putting theory into practice Q. Rev. Biophys. 2015, 48, 323-387.

(185) Eichler, M.; Michel, B.; Hennecke, P.; Klages, C. P. Effects on Silanol Condensation during Low Temperature Silicon Fusion Bonding J. Electrochem. Soc. 2009, 156, H786-H793.

(186) McIntire, T. M.; Smalley, S. R.; Newberg, J. T.; Lea, A. S.; Hemminger, J. C.; Finlayson-Pitts, B. J. Substrate changes associated with the chemistry of self-assembled monolayers on silicon Langmuir 2006, 22, 5617-5624.

(187) Ashley, K. M.; Meredith, J. C.; Amis, E.; Raghavan, D.; Karim, A. Combinatorial investigation of dewetting: polystyrene thin films on gradient hydrophilic surfaces Polymer 2003, 44, 769-772.

(188) Seu, K. J.; Pandey, A. P.; Haque, F.; Proctor, E. A.; Ribbe, A. E.; Hovis, J. S. Effect of surface treatment on diffusion and domain formation in supported lipid bilayers Biophys. J. 2007, 92, 2445-2450.

(189) Zarbiv, Y.; Simhi-Haham, D.; Israeli, E.; Elhadi, S. A.; Grigoletto, J.; Sharon, R. Lysine residues at the first and second KTKEGV repeats mediate alpha-Synuclein binding to membrane phospholipids Neurobiol. dis 2014, 70, 90-98.

(190) Lorenzen, N.; Lemminger, L.; Pedersen, J. N.; Nielsen, S. B.; Otzen, D. E. The N-terminus of alpha-synuclein is essential for both monomeric and oligomeric interactions with membranes FEBS Lett. 2014, 588, 497-502.

(191) Nemani, V. M.; Lu, W.; Berge, V.; Nakamura, K.; Onoa, B.; Lee, M. K.; Chaudhry, F. A.; Nicoll, R. A.; Edwards, R. H. Increased expression of alpha-synuclein reduces neurotransmitter release by inhibiting synaptic vesicle reclustering after endocytosis Neuron 2010, 65, 66-79.

(192) Scott, D.; Roy, S. alpha-Synuclein Inhibits Intersynaptic Vesicle Mobility and Maintains Recycling-Pool Homeostasis J. Neurosci 2012, 32, 10129-10135.

(193) Vargas, K. J.; Makani, S.; Davis, T.; Westphal, C. H.; Castillo, P. E.; Chandra, S. S. Synucleins Regulate the Kinetics of Synaptic Vesicle Endocytosis J. Neurosci 2014, 34, 9364-9376.

(194) Burre, J.; Sharma, M.; Tsetsenis, T.; Buchman, V.; Etherton, M. R.; Sudhof, T. C. Alpha-synuclein promotes SNARE-complex assembly in vivo and in vitro Science 2010, 329, 1663-1667.

(195) Mironov, K. S.; Maksimov, E. G.; Maksimov, G. V.; Los, D. A. Feedback between Fluidity of Membranes and Transcription of the desB Gene for the omega 3-Desaturase in the Cyanobacterium Synechocystis Mol. Biol. 2012, 46, 134-141.

(196) Hohmann, S. Osmotic stress signaling and osmoadaptation in yeasts Microbiol. Mol. Biol. Rev. 2002, 66, 300-372.

(197) Deliconstantinos, G. Physiological aspects of membrane lipid fluidity in malignancy Anticancer Res. 1987, 7, 1011-1021.

(198) George, J. M.; Yang, M. L. In Madame Curie Bioscience Database [Internet]. Landes Bioscience: Austin (TX), 2000.

(199) Hanin, I.; Yoshida, M.; Fisher, A. Alzheimer's and Parkinson's Diseases : Recent Developments 1995, 724.

(200) Buell, A. K.; Galvagnion, C.; Gaspar, R.; Sparr, E.; Vendruscolo, M.; Knowles, T. P.; Linse, S.; Dobson, C. M. Solution conditions determine the relative importance of nucleation and growth processes in alpha-synuclein aggregation Proc. Natl. Acad. Sci. USA 2014, 111, 7671-7676.

(201) Chaudhary, H.; Stefanovic, A. N.; Subramaniam, V.; Claessens, M. M. Membrane interactions and fibrillization of alpha-synuclein play an essential role in membrane disruption FEBS Lett. 2014, 588, 4457-4463.

(202) Burke, K. A.; Yates, E. A.; Legleiter, J. Biophysical insights into how surfaces, including lipid membranes, modulate protein aggregation related to neurodegeneration Frontiers in neurology 2013, 4, 1-17.

(203) van Maarschalkerweerd, A.; Vetri, V.; Langkilde, A. E.; Fodera, V.; Vestergaard, B. Protein/lipid coaggregates are formed during alpha-synuclein-induced disruption of lipid bilayers Biomacromolecules 2014, 15, 3643-3654.

(204) Dikiy, I.; Eliezer, D. Folding and misfolding of alpha-synuclein on membranes Biochim. Biophys. Acta 2012, 1818, 1013-1018.

(205) Giasson, B. I.; Murray, I. V.; Trojanowski, J. Q.; Lee, V. M. A hydrophobic stretch of 12 amino acid residues in the middle of alpha-synuclein is essential for filament assembly J. Biol. Chem. 2001, 276, 2380-2386.

(206) Hoyer, W.; Cherny, D.; Subramaniam, V.; Jovin, T. M. Impact of the acidic C-terminal region comprising amino acids 109-140 on alpha-synuclein aggregation in vitro Biochemistry 2004, 43, 16233-16242.

(207) Ariesandi, W.; Chang, C. F.; Chen, T. E.; Chen, Y. R. Temperature-Dependent Structural Changes of Parkinson's Alpha-Synuclein Reveal the Role of Pre-Existing Oligomers in Alpha-Synuclein Fibrillization PLoS One 2013, 8, e53487.

(208) Ramakrishnan, M.; Jensen, P. H.; Marsh, D. Association of alpha-synuclein and mutants with lipid membranes: spin-label ESR and polarized IR Biochemistry 2006, 45, 3386-3395.

(209) Scholtz, J. M.; Qian, H.; York, E. J.; Stewart, J. M.; Baldwin, R. L. Parameters of Helix-Coil Transition Theory for Alanine-Based Peptides of Varying Chain Lengths in Water Biopolymers 1991, 31, 1463-1470.

(210) Naiki, H.; Higuchi, K.; Hosokawa, M.; Takeda, T. Fluorometric determination of amyloid fibrils in vitro using the fluorescent dye, thioflavin T1 Anal. Biochem. 1989, 177, 244-249.

(211) LeVine, H., 3rd Quantification of beta-sheet amyloid fibril structures with thioflavin T Methods Enzymol. 1999, 309, 274-284.

(212) Suzuki, M.; Miura, T. Effect of amyloid beta-peptide on the fluidity of phosphatidylcholine membranes: Uses and limitations of diphenylhexatriene fluorescence anisotropy Bba-Biomembranes 2015, 1848, 753-759.

(213) Lentz, B. R. Use of fluorescent probes to monitor molecular order and motions within liposome bilayers Chem. Phys. Lipids 1993, 64, 99-116.

(214) Mulders, F.; van Langen, H.; van Ginkel, G.; Levine, Y. K. The static and dynamic behaviour of fluorescent probe molecules in lipid bilayers Biochim. Biophys. Acta, Biomembr. 1986, 859, 209-218.

(215) Shvadchak, V. V.; Subramaniam, V. A Four-Amino Acid Linker between Repeats in the alpha-Synuclein Sequence Is Important for Fibril Formation Biochemistry 2014, 53, 279-281.

(216) Lindblom, G.; Oradd, G. Lipid lateral diffusion and membrane heterogeneity Biochim. Biophys. Acta 2009, 1788, 234-244.

(217) Vats, K.; Knutson, K.; Hinderliter, A.; Sheets, E. D. Peripheral protein organization and its influence on lipid diffusion in biomimetic membranes ACS Chem. Biol. 2010, 5, 393-403.

(218) Jensen, M. O.; Mouritsen, O. G. Lipids do influence protein function-the hydrophobic matching hypothesis revisited Biochim. Biophys. Acta 2004, 1666, 205-226.

(219) Cole, N. B.; Murphy, D. D.; Grider, T.; Rueter, S.; Brasaemle, D.; Nussbaum, R. L. Lipid droplet binding and oligomerization properties of the Parkinson's disease protein alpha-synuclein J. Biol. Chem. 2002, 277, 6344-6352.

(220) de Kruijff, B. Lipid-Protein Interactions - Editorial Biochim. Biophys. Acta, Biomembr. 2004, 1666, 1.

(221) Perez-Gil, J. Protein modulation of membrane structure. Preface Biochim. Biophys. Acta 2008, 1778, 1527.

(222) Stockl, M.; Nikolaus, J.; Herrmann, A. Visualization of lipid domain-specific protein sorting in giant unilamellar vesicles Methods Mol. Biol. 2010, 606, 115-126.

(223) Sharma, P.; Varma, R.; Sarasij, R. C.; Ira; Gousset, K.; Krishnamoorthy, G.; Rao, M.; Mayor, S. Nanoscale organization of multiple GPI-anchored proteins in living cell membranes Cell 2004, 116, 577-589.

(224) van Raaij, M. E.; Segers-Nolten, I. M.; Subramaniam, V. Quantitative morphological analysis reveals ultrastructural diversity of amyloid fibrils from alpha-synuclein mutants Biophys. J. 2006, 91, L96-98.

(225) Rhoades, E.; Ramlall, T. F.; Webb, W. W.; Eliezer, D. Quantification of alpha-synuclein binding to lipid vesicles using fluorescence correlation spectroscopy Biophys. J. 2006, 90, 4692-4700.

(226) Schindelin, J.; Arganda-Carreras, I.; Frise, E.; Kaynig, V.; Longair, M.; Pietzsch, T.; Preibisch, S.; Rueden, C.; Saalfeld, S.; Schmid, B.; Tinevez, J. Y.; White, D. J.; Hartenstein, V.; Eliceiri, K.; Tomancak, P.; Cardona, A. Fiji: an open-source platform for biological-image analysis Nat. Methods 2012, 9, 676-682.

(227) Farrer, M. J. Genetics of Parkinson disease: paradigm shifts and future prospects Nat. Rev. Genet. 2006, 7, 306-318.

(228) van Raaij, M. E.; van Gestel, J.; Segers-Nolten, I. M.; de Leeuw, S. W.; Subramaniam, V. Concentration dependence of alpha-synuclein fibril length assessed by quantitative atomic force microscopy and statistical-mechanical theory Biophys. J. 2008, 95, 4871-4878.

(229) Hoyer, W.; Antony, T.; Cherny, D.; Heim, G.; Jovin, T. M.; Subramaniam, V. Dependence of alpha-synuclein aggregate morphology on solution conditions J. Mol. Biol. 2002, 322, 383-393.

(230) Munishkina, L. A.; Henriques, J.; Uversky, V. N.; Fink, A. L. Role of protein-water interactions and electrostatics in alpha-synuclein fibril formation Biochemistry 2004, 43, 3289-3300.

(231) Zhu, M.; Li, J.; Fink, A. L. The association of alpha-synuclein with membranes affects bilayer structure, stability, and fibril formation J. Biol. Chem. 2003, 278, 40186-40197.

(232) Necula, M.; Chirita, C. N.; Kuret, J. Rapid anionic micelle-mediated alpha-synuclein fibrillization in vitro J. Biol. Chem. 2003, 278, 46674-46680.

(233) Goers, J.; Uversky, V. N.; Fink, A. L. Polycation-induced oligomerization and accelerated fibrillation of human alpha-synuclein in vitro Protein Sci. 2003, 12, 702-707.

(234) Pifer, P. M.; Yates, E. A.; Legleiter, J. Point mutations in Abeta result in the formation of distinct polymorphic aggregates in the presence of lipid bilayers PLoS One 2011, 6, e16248.

(235) Hane, F.; Drolle, E.; Gaikwad, R.; Faught, E.; Leonenko, Z. Amyloid-beta aggregation on model lipid membranes: an atomic force microscopy study J Alzheimers Dis 2011, 26, 485-494.

(236) Last, N. B.; Rhoades, E.; Miranker, A. D. Islet amyloid polypeptide demonstrates a persistent capacity to disrupt membrane integrity Proc Natl Acad Sci U S A 2011, 108, 9460-9465.

(237) Khemtemourian, L.; Domenech, E.; Doux, J. P.; Koorengevel, M. C.; Killian, J. A. Low pH acts as inhibitor of membrane damage induced by human islet amyloid polypeptide J. Am. Chem. Soc. 2011, 133, 15598-15604.

(238) Hellstrand, E.; Nowacka, A.; Topgaard, D.; Linse, S.; Sparr, E. Membrane Lipid Co-Aggregation with alpha-Synuclein Fibrils PLoS One 2013, 8, e77235.

(239) Lashuel, H. A.; Hartley, D.; Petre, B. M.; Walz, T.; Lansbury, P. T., Jr. Neurodegenerative disease: amyloid pores from pathogenic mutations Nature 2002, 418, 291.

(240) Hashimoto, M.; Rockenstein, E.; Crews, L.; Masliah, E. Role of protein aggregation in mitochondrial dysfunction and neurodegeneration in Alzheimer's and Parkinson's diseases Neuromolecular Med. 2003, 4, 21-36.

(241) Pacheco, C.; Aguayo, L. G.; Opazo, C. An extracellular mechanism that can explain the neurotoxic effects of a-synuclein aggregates in the brain Frontiers in Physiology 2012, 3, 297.

(242) Stockl, M.; Claessens, M. M. A. E.; Subramaniam, V. Kinetic measurements give new insights into lipid membrane permeabilization by alpha-synuclein oligomers Molecular Biosystems 2012, 8, 338-345.

(243) van Rooijen, B. D.; Claessens, M. M.; Subramaniam, V. Membrane Permeabilization by Oligomeric alpha-Synuclein: In Search of the Mechanism PLoS One 2010, 5, e14292.

(244) Quist, A.; Doudevski, L.; Lin, H.; Azimova, R.; Ng, D.; Frangione, B.; Kagan, B.; Ghiso, J.; Lal, R. Amyloid ion channels: A common structural link for protein-misfolding disease Proc. Natl. Acad. Sci. U.S.A. 2005, 102, 10427-10432.

(245) Waxman, E. A.; Mazzulli, J. R.; Giasson, B. I. Characterization of hydrophobic residue requirements for alpha-synuclein fibrillization Biochemistry 2009, 48, 9427-9436.

(246) Hovis, J. S.; Boxer, S. G. Patterning and composition arrays of supported lipid bilayers by microcontact printing Langmuir 2001, 17, 3400-3405.

(247) Murray, D. H.; Tamm, L. K.; Kiessling, V. Supported double membranes J Struct Biol 2009, 168, 183-189.

(248) Pandey, A. P.; Haque, F.; Rochet, J. C.; Hovis, J. S. alpha-Synuclein-induced tubule formation in lipid bilayers J. Phys. Chem. B 2011, 115, 5886-5893.

(249) Ding, H.; Schauerte, J. A.; Steel, D. G.; Gafni, A. beta-Amyloid (1-40) peptide interactions with supported phospholipid membranes: a single-molecule study Biophys. J. 2012, 103, 1500-1509.

(250) Armstrong, R. A. Size frequency distributions of abnormal protein deposits in Alzheimer's disease and variant Creutzfeldt-Jakob disease Folia Neuropathol 2007, 45, 108-114.

(251) Bellani, S.; Sousa, V. L.; Ronzitti, G.; Valtorta, F.; Meldolesi, J.; Chieregatti, E. The regulation of synaptic function by alpha-synuclein Commun. Integr. Biol. 2010, 3, 106-109.

(252) Shvadchak, V. V.; Claessens, M. M.; Subramaniam, V. Fibril breaking accelerates alpha-synuclein fibrillization J. Phys. Chem. B 2015, 119, 1912-1918.

(253) Arnesen, T.; Van Damme, P.; Polevoda, B.; Helsens, K.; Evjenth, R.; Colaert, N.; Varhaug, J. E.; Vandekerckhove, J.; Lillehaug, J. R.; Sherman, F.; Gevaert, K. Proteomics analyses reveal the evolutionary conservation and divergence of N-terminal acetyltransferases from yeast and humans Proc. Natl. Acad. Sci. USA 2009, 106, 8157-8162.

(254) Johnson, M.; Coulton, A. T.; Geeves, M. A.; Mulvihill, D. P. Targeted amino-terminal acetylation of recombinant proteins in E. coli PLoS One 2010, 5, e15801.

(255) Maltsev, A. S.; Ying, J. F.; Bax, A. Impact of N-terminal acetylation of alpha-synuclein on its random coil and lipid binding properties Biochemistry 2012, 51, 5004-5013.

(256) Kang, L. J.; Moriarty, G. M.; Woods, L. A.; Ashcroft, A. E.; Radford, S. E.; Baum, J. N-terminal acetylation of alpha-synuclein induces increased transient helical propensity and decreased aggregation rates in the intrinsically disordered monomer Protein Sci. 2012, 21, 911-917.

(257) Bartels, T.; Ahlstrom, L. S.; Leftin, A.; Kamp, F.; Haass, C.; Brown, M. F.; Beyer, K. The N-terminus of the intrinsically disordered protein alpha-synuclein triggers membrane binding and helix folding Biophys. J. 2010, 99, 2116-2124.

(258) Chakrabartty, A.; Doig, A. J.; Baldwin, R. L. Helix capping propensities in peptides parallel those in proteins Proc. Natl. Acad. Sci. USA 1993, 90, 11332-11336.

(259) Jarvis, J. A.; Ryan, M. T.; Hoogenraad, N. J.; Craik, D. J.; Hoj, P. B. Solution structure of the acetylated and noncleavable mitochondrial targeting signal of rat chaperonin 10 J. Biol. Chem. 1995, 270, 1323-1331.

(260) Shvadchak, V. V.; Yushchenko, D. A.; Pievo, R.; Jovin, T. M. The mode of alpha-synuclein binding to membranes depends on lipid composition and lipid to protein ratio FEBS Lett. 2011, 585, 3513-3519.

(261) Drescher, M.; Veldhuis, G.; van Rooijen, B. D.; Milikisyants, S.; Subramaniam, V.; Huber, M. Antiparallel arrangement of the helices of vesicle-bound alpha-synuclein J. Am. Chem. Soc. 2008, 130, 7796-7797.

(262) Dikiy, I.; Eliezer, D. N-terminal acetylation stabilizes N-terminal helicity in lipid- and micelle-bound alpha-synuclein and increases its affinity for physiological membranes J. Biol. Chem. 2014, 289, 3652-3665.

(263) Fantini, J.; Yahi, N. The driving force of alpha-synuclein insertion and amyloid channel formation in the plasma membrane of neural cells: key role of ganglioside- and cholesterol-binding domains Adv. Exp. Med. Biol. 2013, 991, 15-26.

(264) Marsh, D. Cholesterol-induced fluid membrane domains: A compendium of lipid-raft ternary phase diagrams Biochim. Biophys. Acta, Biomembr. 2009, 1788, 2114-2123.

(265) Ferreira, T. M.; Coreta-Gomes, F.; Ollila, O. H.; Moreno, M. J.; Vaz, W. L.; Topgaard, D. Cholesterol and POPC segmental order parameters in lipid membranes: solid state 1H-13C NMR and MD simulation studies Phys. Chem. Chem. Phys. 2013, 15, 1976-1989.

(266) de Almeida, R. F. M.; Fedorov, A.; Prieto, M. Sphingomyelin/phosphatidylcholine/cholesterol phase diagram: Boundaries and composition of lipid rafts Biophys. J. 2003, 85, 2406-2416.

(267) Sidhu, A.; Segers-Nolten, I.; Subramaniam, V. Solution conditions define morphological homogeneity of alpha-synuclein fibrils Biochim. Biophys. Acta 2014, 1844, 2127-2134.

(268) Rossetti, G.; Musiani, F.; Abad, E.; Dibenedetto, D.; Mouhib, H.; Fernandez, C. O.; Carloni, P. Conformational ensemble of human alpha-synuclein physiological form predicted by molecular simulations Phys. Chem. Chem. Phys. 2015.

(269) Zanni, M. T.; Hamm, P. Concepts and Methods of 2D Infrared Spectroscopy; Cambridge University Press, 2011.

(270) Cho, M. Infrared spectroscopy: Mapping protein-protein contacts Nat. Chem. 2012, 4, 339-341.

(271) Buchanan, L. E.; Dunkelberger, E. B.; Zanni, M. T. Examining Amyloid Structure and Kinetics with 1D and 2D Infrared Spectroscopy and Isotope Labeling; Springer Berlin Heidelberg: Heidelberg, 2011.

(272) Baiz, C.; Reppert, M.; Tokmakoff, A. An Introduction to Protein 2D IR Spectroscopy; CRC Press, 2013.

(273) Middleton, C. T.; Marek, P.; Cao, P.; Chiu, C. C.; Singh, S.; Woys, A. M.; de Pablo, J. J.; Raleigh, D. P.; Zanni, M. T. Two-dimensional infrared spectroscopy reveals the complex behaviour of an amyloid fibril inhibitor Nat. Chem. 2012, 4, 355-360.

(274) Karjalainen, E. L.; Ravi, H. K.; Barth, A. Simulation of the amide I absorption of stacked beta-sheets J. Phys. Chem. B 2011, 115, 749-757.

(275) Barth, A. Infrared spectroscopy of proteins Biochim. Biophys. Acta 2007, 1767, 1073-1101.

(276) Krimm, S.; Bandekar, J. Vibrational spectroscopy and conformation of peptides, polypeptides, and proteins Adv. Protein Chem. 1986, 38, 181-364.

(277) Susi, H.; Byler, D. M. Fourier transform infrared study of proteins with parallel beta-chains Arch. Biochem. Biophys. 1987, 258, 465-469.

(278) Surewicz, W. K.; Mantsch, H. H. New insight into protein secondary structure from resolution-enhanced infrared spectra Biochim. Biophys. Acta 1988, 952, 115-130.

(279) Manas, E. S.; Getahun, Z.; Wright, W. W.; DeGrado, W. F.; Vanderkooi, J. M. Infrared spectra of amide groups in alpha-helical proteins: Evidence for hydrogen bonding between helices and water J. Am. Chem. Soc. 2000, 122, 9883-9890.

(280) Celej, M. S.; Caarls, W.; Demchenko, A. P.; Jovin, T. M. A triple-emission fluorescent probe reveals distinctive amyloid fibrillar polymorphism of wild-type alpha-synuclein and its familial parkinson's disease mutants Biochemistry 2009, 48, 7465-7472.

(281) Gath, J.; Bousset, L.; Habenstein, B.; Melki, R.; Bockmann, A.; Meier, B. H. Unlike twins: an NMR comparison of two alpha-synuclein polymorphs featuring different toxicity PLoS One 2014, 9, e90659.

(282) Alim, M. A.; Ma, Q. L.; Takeda, K.; Aizawa, T.; Matsubara, M.; Nakamura, M.; Asada, A.; Saito, T.; Kaji, H.; Yoshii, M.; Hisanaga, S.; Ueda, K. Demonstration of a role for alpha-synuclein as a functional microtubule-associated protein J. Alzheimers Dis. 2004, 6, 435-449.

(283) Zhou, R. M.; Huang, Y. X.; Li, X. L.; Chen, C.; Shi, Q.; Wang, G. R.; Tian, C.; Wang, Z. Y.; Jing, Y. Y.; Gao, C.; Dong, X. P. Molecular interaction of alpha-synuclein with tubulin influences on the polymerization of microtubule in vitro and structure of microtubule in cells Mol. Biol. Rep. 2010, 37, 3183-3192.

(284) Petkova, A. T.; Leapman, R. D.; Guo, Z.; Yau, W. M.; Mattson, M. P.; Tycko, R. Self-propagating, molecular-level polymorphism in Alzheimer's beta-amyloid fibrils Science 2005, 307, 262-265.

(285) Smith, B. J. Acetic Acid-urea polyacrylamide gel electrophoresis of proteins Methods in molecular biology 1984, 1, 63-73.

(286) Faas, F. G.; Rieger, B.; van Vliet, L. J.; Cherny, D. I. DNA deformations near charged surfaces: electron and atomic force microscopy views Biophys. J. 2009, 97, 1148-1157.

(287) Huerta-Viga, A.; Shaw, D. J.; Woutersen, S. pH dependence of the conformation of small peptides investigated with two-dimensional vibrational spectroscopy J. Phys. Chem. B 2010, 114, 15212-15220.

(288) Longair, M. H.; Baker, D. A.; Armstrong, J. D. Simple Neurite Tracer: open source software for reconstruction, visualization and analysis of neuronal processes Bioinformatics 2011, 27, 2453-2454.

(289) Eisenberg, D.; Jucker, M. The Amyloid State of Proteins in Human Diseases Cell 2012, 148, 1188-1203.

(290) Karpinar, D. P.; Balija, M. B.; Kugler, S.; Opazo, F.; Rezaei-Ghaleh, N.; Wender, N.; Kim, H. Y.; Taschenberger, G.; Falkenburger, B. H.; Heise, H.; Kumar, A.; Riedel, D.; Fichtner, L.; Voigt, A.; Braus, G. H.; Giller, K.; Becker, S.; Herzig, A.; Baldus, M.; Jackle, H.; Eimer, S.; Schulz, J. B.; Griesinger, C.; Zweckstetter, M. Pre-fibrillar alpha-synuclein variants with impaired beta-structure increase neurotoxicity in Parkinson's disease models EMBO J. 2009, 28, 3256-3268.

(291) Cho, M. K.; Nodet, G.; Kim, H. Y.; Jensen, M. R.; Bernado, P.; Fernandez, C. O.; Becker, S.; Blackledge, M.; Zweckstetter, M. Structural characterization of α- synuclein in an aggregation prone state Protein Sci. 2009, 18, 1840-1846.

(292) Astbury, W. T.; Beighton, E.; Parker, K. D. The cross-beta configuration in supercontracted proteins Biochim. Biophys. Acta 1959, 35, 17-25.

(293) Sunde, M.; Serpell, L. C.; Bartlam, M.; Fraser, P. E.; Pepys, M. B.; Blake, C. C. F. Common core structure of amyloid fibrils by synchrotron X-ray diffraction J. Mol. Biol. 1997, 273, 729-739.

(294) Vilar, M.; Chou, H. T.; Luhrs, T.; Maji, S. K.; Riek-Loher, D.; Verel, R.; Manning, G.; Stahlberg, H.; Riek, R. The fold of alpha-synuclein fibrils Proc. Natl. Acad. Sci. U.S.A. 2008, 105, 8637-8642.

(295) Nielsen, S. B.; Macchi, F.; Raccosta, S.; Langkilde, A. E.; Giehm, L.; Kyrsting, A.; Svane, A. S. P.; Manno, M.; Christiansen, G.; Nielsen, N. C.; Oddershede, L.; Vestergaard, B.; Otzen, D. E. Wildtype and A30P Mutant Alpha-Synuclein Form Different Fibril Structures PLoS One 2013, 8.

(296) Bertoncini, C. W.; Jung, Y. S.; Fernandez, C. O.; Hoyer, W.; Griesinger, C.; Jovin, T. M.; Zweckstetter, M. Release of long-range tertiary interactions potentiates aggregation of natively unstructured alpha-synuclein Proc. Natl. Acad. Sci. U.S.A. 2005, 102, 1430-1435.

(297) Trexler, A. J.; Rhoades, E. Single Molecule Characterization of alpha-Synuclein in Aggregation-Prone States Biophys. J. 2010, 99, 3048-3055.

(298) Dedmon, M. M.; Lindorff-Larsen, K.; Christodoulou, J.; Vendruscolo, M.; Dobson, C. M. Mapping long-range interactions in alpha-synuclein using spin-label NMR and ensemble molecular dynamics simulations J. Am. Chem. Soc. 2005, 127, 476-477.

(299) Zhou, W. B.; Long, C. M.; Reaney, S. H.; Di Monte, D. A.; Fink, A. L.; Uversky, V. N. Methionine oxidation stabilizes non-toxic oligomers of alpha-synuclein through strengthening the auto-inhibitory intra-molecular long-range interactions Bba-Mol Basis Dis 2010, 1802, 322-330.

(300) Murray, I. V. J.; Giasson, B. I.; Quinn, S. M.; Koppaka, V.; Axelsen, P. H.; Ischiropoulos, H.; Trojanowski, J. Q.; Lee, V. M. Y. Role of alpha-synuclein carboxy-terminus on fibril formation in vitro Biochemistry 2003, 42, 8530-8540.

(301) Qin, Z.; Hu, D.; Han, S.; Hong, D. P.; Fink, A. L. Role of different regions of alpha-synuclein in the assembly of fibrils Biochemistry 2007, 46, 13322-13330.

(302) Antony, T.; Hoyer, W.; Cherny, D.; Heim, G.; Jovin, T. M.; Subramaniam, V. Cellular polyamines promote the aggregation of alpha-synuclein J. Biol. Chem. 2003, 278, 3235-3240.

(303) Fernandez, C. O.; Hoyer, W.; Zweckstetter, M.; Jares-Erijman, E. A.; Subramaniam, V.; Griesinger, C.; Jovin, T. M. NMR of alpha-synuclein-polyamine complexes elucidates the mechanism and kinetics of induced aggregation EMBO J. 2004, 23, 2039-2046.

(304) Zibaee, S.; Jakes, R.; Fraser, G.; Serpell, L. C.; Crowther, R. A.; Goedert, M. Sequence Determinants for Amyloid Fibrillogenesis of Human alpha-Synuclein J. Mol. Biol. 2007, 374, 454-464.

(305) Semerdzhiev, S. A.; Dekker, D. R.; Subramaniam, V.; Claessens, M. M. A. E. Self-Assembly of Protein Fibrils into Suprafibrillar Aggregates: Bridging the Nano- and Mesoscale Acs Nano 2014, 8, 5543-5551.

(306) Sweers, K. K. M.; van der Werf, K. O.; Bennink, M. L.; Subramaniam, V. Atomic Force Microscopy under Controlled Conditions Reveals Structure of C-Terminal Region of alpha-Synuclein in Amyloid Fibrils Acs Nano 2012, 6, 5952-5960.

(307) Sweers, K. K. M.; Segers-Nolten, I. M. J.; Bennink, M. L.; Subramaniam, V. Structural model for alpha-synuclein fibrils derived from high resolution imaging and nanomechanical studies using atomic force microscopy Soft Matter 2012, 8, 7215-7222.

(308) Wallace, B. A.; Lees, J. G.; Orry, A. J. W.; Lobley, A.; Janes, R. W. Analyses of circular dichroism spectra of membrane proteins Protein Sci. 2003, 12, 875-884.

(309) Castiglioni, E.; Abbate, S.; Longhi, G.; Gangemi, R.; Lauceri, R.; Purrello, R. Absorption flattening as one cause of distortion of circular dichroism spectra of Delta-RuPhen(3) center dot H2TPPS complex Chirality 2007, 19, 642-646.

(310) Momotani, Y.; Arie, R.; Takagi, T. Novel transient circular dichroic spectra with a trough near 230 nm observed in the denaturation processes of lectins by sodium dodecyl sulfate Biochim. Biophys. Acta 1981, 668, 193-196.

(311) Smith, J. A.; Pease, L. G. Reverse turns in peptides and proteins CRC Crit Rev Biochem 1980, 8, 315-399.

(312) Manning, M. C.; Illangasekare, M.; Woody, R. W. Circular-Dichroism Studies of Distorted Alpha-Helices, Twisted Beta-Sheets, and Beta-Turns Biophys. Chem. 1988, 31, 77-86.

(313) Lara, C.; Reynolds, N. P.; Berryman, J. T.; Xu, A. Q.; Zhang, A. F.; Mezzenga, R. ILQINS Hexapeptide, Identified in Lysozyme Left-Handed Helical Ribbons and Nanotubes, Forms Right-Handed Helical Ribbons and Crystals J. Am. Chem. Soc. 2014, 136, 4732-4739.

(314) Yagi, H.; Kusaka, E.; Hongo, K.; Mizobata, T.; Kawata, Y. Amyloid fibril formation of alpha-synuclein is accelerated by preformed amyloid seeds of other proteins: implications for the mechanism of transmissible conformational diseases J. Biol. Chem. 2005, 280, 38609-38616.

(315) Heise, H.; Celej, M. S.; Becker, S.; Riedel, D.; Pelah, A.; Kumar, A.; Jovin, T. M.; Baldus, M. Solid-state NMR reveals structural differences between fibrils of wild-type and disease-related A53T mutant alpha-synuclein J. Mol. Biol. 2008, 380, 444-450.

(316) Lv, G.; Kumar, A.; Giller, K.; Orcellet, M. L.; Riedel, D.; Fernandez, C. O.; Becker, S.; Lange, A. Structural comparison of mouse and human alpha-synuclein amyloid fibrils by solid-state NMR J. Mol. Biol. 2012, 420, 99-111.

(317) Comellas, G.; Lemkau, L. R.; Nieuwkoop, A. J.; Kloepper, K. D.; Ladror, D. T.; Ebisu, R.; Woods, W. S.; Lipton, A. S.; George, J. M.; Rienstra, C. M. Structured Regions of alpha-Synuclein Fibrils Include the Early-Onset Parkinson's Disease Mutation Sites J. Mol. Biol. 2011, 411, 881-895.

(318) Nielsen, E. B.; Schellman, J. A. The absorption spectra of simple amides and peptides J. Phys. Chem. 1967, 71, 2297-2304.

(319) Buchanan, L. E.; Carr, J. K.; Fluitt, A. M.; Hoganson, A. J.; Moran, S. D.; de Pablo, J. J.; Skinner, J. L.; Zanni, M. T. Structural motif of polyglutamine amyloid fibrils discerned with mixed-isotope infrared spectroscopy Proc. Natl. Acad. Sci. U.S.A. 2014, 111, 5796-5801.

(320) Yonetani, M.; Nonaka, T.; Masuda, M.; Inukai, Y.; Oikawa, T.; Hisanaga, S.; Hasegawa, M. Conversion of wild-type alpha-synuclein into mutant-type fibrils and its propagation in the presence of A30P mutant J. Biol. Chem. 2009, 284, 7940-7950.

Nederlandse samenvatting

"Alfa-synucleine (αS) is een intrinsiek ongeordend eiwit met een vooralsnog onbekende fysiologische functie dat betrokken is bij de ziekte van Parkinson (PZ)". De vorige zin is, de laatste tien jaar, in verscheidene variaties verschenen in tal van onderzoeksartikelen over dit eiwit. Het is verbijsterend hoeveel we weten van dit eiwit en hoe weinig het ons eigenlijk heeft geholpen om PZ te begrijpen. Sinds de ontdekking dat het pre-synaptische eiwit αS betrokken is bij PZ, is er veel onderzoek gedaan naar wat de aggregatie van αS in amyloïdestructuren in de hersenen veroorzaakt. Er werd geopperd dat de binding tussen αS en specifieke cellulaire membranen een van de oorzaken kan zijn voor amyloïdevorming, maar dit idee wordt verstoord door het feit dat αS voor zijn reguliere fysiologische functie waarschijnlijk ook membranen bindt. Of de binding tussen αS en membranen aggregatie versnelt of juist voorkomt, is controversieel. De waarneming dat aggregatie van αS in amyloïdefibrillen een beschermingsmechanisme van de cel zou kunnen zijn, maakt het plaatje nog controversiëler. Hét gezicht van αS blijkt dus niet te bestaan. Een belangrijke stap in het leren begrijpen van dit eiwit, is uitvinden waarom het eiwit in micromolaire concentraties aanwezig is in het pre-synaptisch membraan. Hiervoor is het essentieel om de interactie tussen αS en membranen te begrijpen, om zo te ontrafelen wat de mogelijke functionele en pathologische rollen zijn van het eiwit. In dit proefschrift hebben we de mogelijke functionele en pathologische rollen van αS-membraan interacties onderzocht.

Om interacties tussen αS en lipidemembranen te bekijken, hebben we als model gekozen voor phospholipide membraancompositie: POPC:POPG (1-op-1 molratio). Het hoge aandeel van anionische lipiden is opzettelijk gekozen omdat bekend is dat de interactie tussen αS en membranen afhankelijk is van de hoeveelheid anionische lipiden. Het maken van bilagen op glas met een hoog gehalte anionische lipiden is moeilijk. Om dit voor elkaar te krijgen zijn de protocollen sterk geoptimaliseerd. Hier bleek dat een combinatie van een lage pH, hoge ionsterkte en een hoge lipidenconcentratie de stabiliteit van de dubbellagen met veel negatief geladen lipiden bevordert. Een kritische stap is ook het voorbereiden van het glasoppervlak; er zijn verschillende schoonmaakstappen nodig. De details van de protocollen voor het optimaliseren en karakteriseren worden beschreven in **Hoofdstuk 2**.

De fysiologische functie van αS blijft een enigma, ondanks dat veelbelovend onderzoek diverse suggesties biedt voor mogelijke functies van αS. Deze variëren van synaptische vesikelregulatie bij de neurologische synaps tot *anti-oxidant* en chaperone-achtige functies. Gezien de binding van αS met het membraan micro-domeinen *in vivo* en vanwege de functionele relevantie van αS-membraan interacties in PZ, hebben we onderzocht hoe de fysische eigenschappen, zoals membraan-ordening en vloeibaarheid in de bilaag, door αS binding worden beïnvloed. We hebben gezien dat op het membraan αS monomeren zich organiseren in clusters, dit staat in **Hoofdstuk 3**. Door deletie-mutanten van αS met vergelijkbare affiniteiten voor het membraan te gebruiken, zagen we dat de drijvende kracht

achter klontering een complex samenspel is van electrostatische en hydrofobe interacties. Samenklontering van αS op membranen hindert de diffusie van lipiden en zorgt voor een toename in membraanordering. De toename in ordening is niet alleen aangetoond met fluorescentie-anisotropiemetingen in oplossing maar ook, voor het eerst, met confocale fluorescentiemicroscopie experimenten met de orde-gevoelige kleurstof DPH. We concluderen dat de klontering van αS op bilagen ordening veroorzaakt en diffusie vertraagt. Gezien de gevoeligheid van αS-binding voor membraankromming, en het vermogen om kromming te veroorzaken[110], is het waarschijnlijk dat een toename in membraankromming door αS-binding acylketens blootstelt en zo verdere binding van αS veroorzaakt. De dichte accumulatie van αS op het membraan zou een sterk drijvende kracht kunnen zijn voor de vorming van geordende membraandomeinen. Het feit dat αS geordende domeinen in membranen kan maken zou relevant kunnen zijn voor de functie van αS, aangezien ordening van lipiden vaak gekoppeld is aan de eiwitfunctie *in vivo*.

Hierna hebben we ons gericht op hoe amyloïdeformatie op het membraan membraanschade kan veroorzaken. We hebben gekeken naar de resultaten van αS-membraan interacties op langere tijdschalen in **Hoofdstuk** 3 en **Hoofdstuk 4**. Op langere tijdschalen leidt de ophoping van αS op bilagen tot de vorming van amyloïdestructuren (afhankelijk van de lipide-eiwit ratio) die groeiden in de tijd. De vorming van amyloïdeklonten veroorzaakte membraanschade en leidde tot extractie van lipiden. Een αS-mutant die niet in staat was tot amyloïdevorming gaf geen membraanschade. Er is ook steeds meer bewijs in de literatuur dat αS-membraaninteracties alleen significante schade kunnen aanrichten als de membranen zeer veel anionische lipiden bevat (>40%). Zulke hoge percentages worden maar zelden gevonden in fysiologische celmembranen. Om alternatieve mechanismen achter membraanschade te bekijken, zijn experimenten uitgevoerd in een samenwerkingsproject met vooraf gevormde αS-oligomeren (Chaudhary, Iyer et al., manuscript in voorbereiding).

Recente literatuur suggereert dat in fysiologische omstandigheden meer dan 95% van het αS geacytyleerd is aan de N-terminus van het eiwit. Daarom is hier de invloed van deze post-translationele modificatie van αS op de binding aan bilagen en klontering in amyloïdefibrillen onderzocht. De bevindingen staan beschreven in **Hoofdstuk 5** en laten zien dat acetylatie van de N-terminus weinig invloed lijkt te hebben op de membraanbinding van αS. De invloed van acetylatie van de N-terminus op membraanaffiniteit als functie van membraanlading, cholesterolhoeveelheid en kromming was verwaarloosbaar. Acetylatie van de N-terminus speelt mogelijk nog wel een rol in het reguleren van interacties van αS met andere eiwitten in het cytoplasma of op het celmembraan, zoals SNAREs, actine of tubuline. Onderzoek naar het ophelderen van de functie van zulke bindingspartners (lipiden dan wel eiwitten) van monomeer αS kan meer inzicht geven in de invloed van acetylatie van de N-terminus op het

reguleren van interacties. Ook al hebben we geen grote verschillen waargenomen in de klonteringskinetiek tussen het geacetyleerde αS en het 'gewone' αS, was de tijd totdat de aggregatie begon veel constanter voor het geacetyleerde eiwit en was de morfologie van de fibrillen van dit eiwit veel homogener.

Als laatste is onderzocht welke fysico-chemische interacties betrokken zijn bij αS amyloidevorming in de afwezigheid van membranen. Hiervoor hebben we gekeken naar αS mutanten die een deel van de N-terminus en C-terminus missen. Onze waarnemingen suggereren dat het verkorten van de N-terminus geen effect heeft op fibrilmorfologie, terwijl het verkorten van de C-terminus de fibrilstructuuren sterk beïnvloedt (**Hoofdstuk 6)**. Onze voorlopige resultaten laten zien dat fibrillen van αS met een verkorte C-terminaal domein geen "normaal" αS kan incorporeren. Dit suggereert dat de kern van αS fibrillen gemaakt van het eiwit dat aan de C-terminus verkort is anders is dan die van "normaal" αS fibrillen. Experimenten met 2D-IR spectroscopie zijn gepland om verschillen in fibirlstructuur vast te stellen.

Vooruitzicht

In dit manuscript hebben we lipidemembranen op een glasoppervlak gebruikt om beter te begrijpen hoe fysicochemische factoren αS interacties met membranen beïnvloeden. Het gebruik van zulke membranen heeft veel inzichten gebracht op het gebied van eiwit-membraan interacties en de protocollen die zijn ontwikkeld om zulke membranen met een hoge lading te maken kunnen ook toegepast worden op andere eiwitten. Op basis van de resultaten en conclusies gepresenteerd in dit werk, en recente literatuur, opper ik hier mogelijkheden voor toekomstig werk dat antwoorden zou kunnen geven op openstaande vragen en meer inzicht zal bieden in ons begrip van αS en zijn betrokkenheid bij PZ:

- Wat is de structuur van 'gewone' αS-monomeren in eiwitklonten op membranen en is deze anders voor de monomeren die geacetyleerd zijn aan de N -terminus? Het zou interessant zijn om de initiële αS clusters te isoleren en de biofysische eigenschappen te bestuderen met FTIR en CD-spectroscopie. Op het niveau van enkele moleculen kan met Förster resonante energie overdacht (FRET) inzicht verkregen worden in de moleculaire ordening van de monomeren binnen deze klonten. De resultaten zouden helpen de biochemische factoren die een rol spelen in de structurele transitie van non-amyloïdeklonten in amyloïdeklonten te begrijpen.
- Het is waarschijnlijk dat veranderingen in de compositie van het celmembraan die ontstaan als cellen ouder worden, relevant zijn voor de pathologie van PZ. Het zou interessant zijn om veranderingen in membraanfluïditeit als gevolg van veranderde membraancompositie te bekijken, en te zien of dit aggregatie van αS kan veroorzaken.
- Het gebruik van fysiologisch relevante N-terminaal geacetyleerd αS met bekende PD-mutaties in studies gericht op aggregatiekinetiek en fibrilvorming zouden relevanter zijn voor PD.
- Speelt N-terminale acetylatie van αS een rol bij het binden van andere eiwitten en/of lipiden? Heeft de N-terminale acetylatie een regulerende functie, voorkomt het promiscue interacties, of heeft het geen effect? Hoe beïnvloedt N-terminale acetylatie aggregatie *in vivo*?

Appendices

A. Determination of membrane binding affinities from CD spectroscopy

CD spectroscopy can be used to measure membrane binding affinities of αS to lipid vesicles using the structural transition from a disordered monomers in solution to a membrane bound helical coils . The membrane bound fraction of αS (X_B) at any given point lies between two extremes: $X_B = 0$ in absence of lipid membranes and $X_B = 1$ at saturating conditions. In such a situation, the observed CD signal (CD_{obs}) can be described as:

$$CD_{obs} = X_B CD_B + X_F CD_F \qquad (1)$$

By assuming $X_F + X_B = 1$ and that the CD signals of free form of αS in the presence of buffer (CD_F) or the bound form of αS in presence of lipid vesicles under saturating condition (CD_B), the fraction of αS bound to lipid vesicles can be expressed as:

$$X_B = \frac{CD_{obs} - CD_F}{CD_B - CD_F} \qquad (2)$$

The binding equilibrium between αS and lipid membranes can be described as follows:

$$\alpha S_{free} + \left[L_{free}\right]_n \Leftrightarrow \alpha SL_{bound} \qquad (3)$$

where n represents the number of lipid molecules interacting with one molecule of αS (binding stoichiometry) and $\left[L_{free}\right]_n$ represents the free lipid concentration. The equilibrium dissociation constant K_D can thus be written as:

$$K_D = \frac{[\alpha S_{free}]\left[L_{free}\right]}{\alpha SL_{bound}} \qquad (4)$$

Since,

$$[\alpha S_{total}] = [\alpha S_{free}] + [\alpha SL_{bound}] \qquad (5)$$

$$[L_{total}] = n(\left[L_{free}\right] + [\alpha SL_{bound}]) \qquad (6)$$

The equation (4) can be rearranged to obtain

$$\frac{\alpha SL_{bound}}{\alpha S_{total}} = \frac{(\alpha SL_{bound})}{\alpha SL_{bound} + \alpha S_{free}} = \frac{n\left[L_{free}\right]}{K_D + n\left[L_{free}\right]} \qquad (7)$$

Equation (7) connects the fraction of bound protein (relative to total protein) to the free lipid concentration and assuming n=1:

1. When $[L_{free}] = K_D$, exactly half the protein is bound.
2. At the start of the binding curve, when $[L_{free}] << K_D$, the fraction of bound protein is directly proportional to the lipid concentration.
3. At the end of the curve, when $[L_{free}] >> K_D$, all of the protein is bound (and therefore bound fraction of protein becomes independent of lipid concentration.). The equation (7) would result in a hyperbolic binding curve (with asymptotes of slope 1/ K_D and 0). It is important to note that the independent variable derived above is $[L_{free}]$ which is not known but rather $[L_{total}]$ is known. Typically, it is assumed (known as free ligand

approximation) that $[L_{free}]$ is fairly close to $[L_{total}]$ or that the concentration of bound lipid is negligible relative to total lipid concentration such that:

$$[L]_{total} \approx [L_{free}] \Leftrightarrow L_{bound} \ll [L_{total}] \qquad (8)$$

This assumption works fairly well as long as binding is relatively weak (i.e. the K_D is at least five-fold higher than αS_{total}. As binding becomes tighter or involving multiple binding sites per protein (n≠1), and K_D becomes comparable to the total protein concentration, the aforementioned assumption breaks down and the apparent binding curve deviates from the hyperbola. Therefore, in such cases it is important to explicitly account for the free and total lipid concentration. Thus from equation (4) we have:

$$K_D = \frac{(\alpha S_{free})([L_{free}])}{\alpha SL_{bound}}$$

Substituting from equation (5),

$$K_D = \frac{(\alpha S_{total} - \alpha SL_{bound})(\frac{[L_{total}]}{n} - \alpha SL_{bound})}{\alpha SL_{bound}} \qquad (9)$$

Rearranging the above equation, we obtain:

$$[\alpha SL_{bound}]^2 - (K_D + \alpha S_{total} + \frac{[L_{total}]}{n})\alpha SL_{bound} + \frac{\alpha S_{total}[L_{total}]}{n} = 0$$

The above equation, upon solving using the quadratic formula for a relevant root gives the solution for the concentration of bound protein/lipid as:

$$\alpha SL_{bound} = \frac{(K_D + \alpha S_{total} + \frac{[L_{total}]}{n}) - \sqrt{(K_D + \alpha S_{total} + \frac{[L_{total}]}{n})^2 - \frac{4\alpha S_{total}[L_{total}]}{n}}}{2}$$

Therefore, the bound fraction can be given as:

$$X_B = \frac{\alpha SL_{bound}}{\alpha S_{total}} = \frac{(K_D + \alpha S_{total} + \frac{[L_{total}]}{n}) - \sqrt{(K_D + \alpha S_{total} + \frac{[L_{total}]}{n})^2 - \frac{4\alpha S_{total}[L]_{total}}{n}}}{2\alpha S_{total}}$$

The above equation can now be used to fit CD_{obs} obtained by varying the lipid vesicle concentration at a fixed protein concentration or titrating a known concentration of protein with known concentration of lipid vesicles. When lipids are titrated, both protein and lipid concentrations vary at each point, and therefore have to be treated as independent variables while fitting. Using the values of K_D (in M), and the binding stoichiometry n, obtained from the fit, the concentration of protein bound to the vesicles (αS_{bound}), the protein free in solution (αS_{free}) for any given $\frac{L_{free}}{\alpha S_{free}}$ can be calculated as follows:

$$\alpha SL_{bound} = X_B[\alpha S_{total}] \qquad \alpha S_{free} = [\alpha S_{total}] - \alpha SL_{bound}$$

B. Standard curve for estimation of fibril concentrations from CD spectroscopy

Estimation of αS fibril concentrations in aggregated suspensions can be difficult given their heterogeneity and measurement errors during absorption spectroscopy due to light scattering. Yet, accurate concentrations are needed for calculations of mean residual ellipticites in CD spectroscopy and enable comparison of CD spectra of different fibril samples. A simpler way to measure protein concentration in fibril suspensions is by using hexfluoroisopropanol (HFIP). It is known that addition of 30% HFIP to αS fibrils leads to complete dissolution of fibrils into stabilized helical species. By measuring MRE values for known concentrations of monomeric αS obtained after addition of 30% HFIP, a standard curve of CD signals versus known concentrations of αS can be generated as shown below.

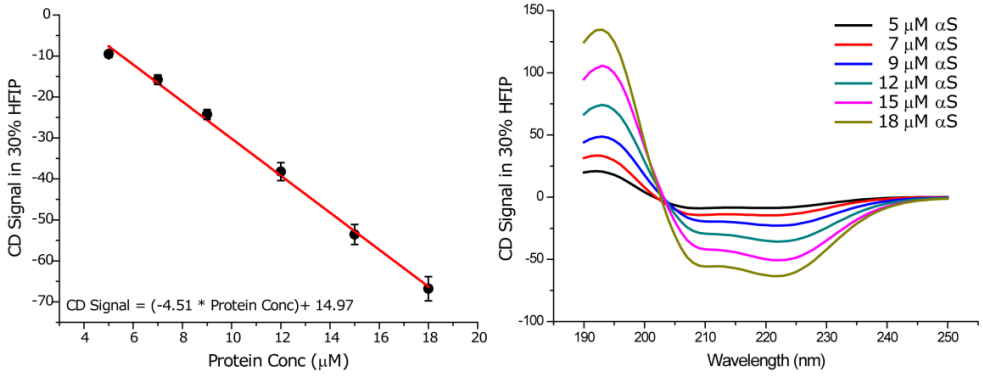

Figure B2: Standard curve of CD (at 222 nm) signals plotted against αS concentrations (left panel) obtained from CD spectra (right panel) from known concentration of αS.

Based on this equation, a raw CD signal can be used to calculate the protein concentration of a given fibril sample. The following steps should be followed:

1. Measure the CD spectra of a 200 μl fibril solution to get CD signal (CD_{before}). (*Avoid cloudy suspensions to avoid differential flattening effects*.)
2. Add 30% HFIP (final concentration) to the fibril suspension and wait for 2 minutes.
3. Measure the CD spectra of fibril solution again and note CD signal at 222 nm (CD_{after}).
4. Use CD_{after} to calculate effective protein concentration (P) using equation in
5. **Figure B2**.
6. Using values of P, to obtain MRE values for raw signal CD_{before} using the following equation:

$$MRE\ [\theta] = \frac{CD_{before} * 0.1}{Pathlength\ of\ cuvette\ (in\ cm) * P\ (in\ Molar) *\ No\ of amino\ acids\ in\ protein/peptide}$$

7. It is important that the experimental parameters like step-size, bandwidth, averaging and buffers be identical to that used for obtaining the standard curve.

C. List of abbreviations

AFM	Atomic force microscopy
BODIPY-PC	2-(4,4-Difluoro-5,7-Dimethyl-4-Bora-3a,4a-Diaza-s-Indacene-3-Pentanoyl)-1-Hexadecanoyl-sn-Glycero-3-Phosphocholine
CD	Circular dichroism
$D_{\alpha S}$	Lateral lipid diffusion coefficient of alpha synuclein
D_B	Lateral lipid diffusion coefficient of BODIPY-PC probe
$D_{NBD\text{-}PC}$	Lateral lipid diffusion coefficient of NBD-PC probe
D_{LL}	Lateral lipid diffusion coefficient of a given lipid
DOPA	1,2-dioleoyl-*sn*-glycero-3-phosphate
DOPC	1,2-dioleoyl-*sn*-glycero-3-phosphocholine
DPPC	1,2-dipalmitoyl-*sn*-glycero-3-phosphocholine
DOPG	1,2-dioleoyl-*sn*-glycero-3-phospho-(1'-*rac*-glycerol)
DPPG	1,2-dipalmitoyl-*sn*-glycero-3-phospho-(1'-*rac*-glycerol)
DOPS	1,2-dioleoyl-*sn*-glycero-3-phospho-L-serine
DPPS	1,2-dipalmitoyl-*sn*-glycero-3-phospho-L-serine
EDTA	Ethylenediaminetetraacetic acid
Endo-αS	Endogenous alpha synuclein isolated from red blood cells
ESI-MS	Electro-spray ionization mass spectrometry
FRET	Förster resonance energy transfer
FTIR spectroscopy	Fourier transform infra red spectroscopy
GUVs	Giant unilamellar vesicles
HEPES	4-(2-hydroxyethyl)-1-piperazineethanessulfonic acid
LUVs	Large unilamellar vesicles
MAS-NMR	Magic angle spinning nuclear magnetic resonance
MLVs	Multi-lamellar vesicles
NaCl	Sodium chloride
NaOH	Sodium hydroxide
NBD-PC	1-palmitoyl-2-[6-[(7-nitro-2-1,3-benzoxadiazol-4yl)amino] hexanoyl]-sn-glycero-3-phosphocholine
NBD-PS	1-palmitoyl-2-{12-[(7-nitro-2-1,3-benzoxadiazol-4-yl)amino] dodecanoyl}-sn-glycero-3-phosphoserine
NTAc-αS	N-terminally acetylated alpha synuclein (expressed in *E.coli*)
PEG	Polyethylene glycol
POPA	1-palmitoyl-2-oleoyl-*sn*-glycero-3-phosphate
POPC	1-palmitoyl-2-oleoyl-sn-glycero-3-phosphocholine

POPG	1-palmitoyl-2-oleoyl-*sn*-glycero-3-phospho-(1'-*rac*-glycerol)
POPS	1-palmitoyl-2-oleoyl-*sn*-glycero-3-phospho-L-serine
PTM	Post-translational modification
Rhod-PE	1,2-dioleoyl-sn-glycero-3-phosphoethanolamine-N-(lissamine rhodamine B sulfonyl)
SDS	Sodium dodecyl sulphate
SLBs	Supported lipid bilayers
ssNMR	solid state nuclear magnetic resonance
SUVs	Small unilamellar vesicles
STEM	Scanning transmission electron microscopy
WT-αS	Wild type alpha synuclein
XRD	X-Ray diffraction
1-60-αS	Truncated variant of wild type alpha synuclein lacking residues 61-140
1-108-αS	Truncated variant of wild type alpha synuclein lacking residues 109-140
21-140-αS	Truncated variant of wild type alpha synuclein lacking residues 1-20
61-140-αS	Truncated variant of wild type alpha synuclein lacking residues 1-60
2D-IR	Two dimensional infrared spectroscopy
αS(Δ71-82)	Truncated variant of wild type alpha synuclein lacking residues 71-82

D. List of publications

In preparation/Submitted/Under review:

1. **Iyer, A.**, Schilderink, N., Claessens, M. M. A. E. and Subramaniam, V. Clustering of membrane bound alpha synuclein locally impairs lipid diffusion by increasing lipid packing. (*manuscript submitted*)

2. **Iyer, A.**, Schilderink, N, Roeters, S., Hommersom, B., Woutersen, S., Claessens, M. M. A. E and Subramaniam, V. Effect of N-terminal acetylation in alpha synuclein on its membrane binding properties and fibril structure. (*manuscript submitted*)

3. Raaijmakers, M.J.T., **Iyer, A.**, Subramaniam, V., Blum, C., Wessling, M. and Benes, N.E., Fluorescent protein thin films by interfacial polymerization. (*manuscript in preparation*)

4. *Roeters, S., ***Iyer, A.**, Woutersen, S. and Subramaniam, V. Evidence for intramolecular beta-sheet structure in alpha synuclein fibrils grown under physiological conditions. (*manuscript submitted*) *equal contribution

5. *Chaudhary, H., ***Iyer, A.**, Subramaniam, V. and Claessens, M. M. A. E. Oligomers of alpha synuclein initiate membrane damage from pre-existing defects. (*manuscript submitted)* *equal contribution

6. Stefanovic, A., Leijenhorst-Groener, K.V.L., **Iyer, A.**, Chaudhary, H., Nolten, I.S., Claessens, M. M. A. E and Subramaniam, V. Cytotoxicity and uptake mechanism of extracellularly administered α-synuclein oligomers. *(manuscript under revision in Biomolecules)*

7. Dominguez, J., **Iyer, A.**, Cox, R., Scheidelaar, S., Dörr, J., Koorengevel, M., Subramaniam, V., and Killian, J.A., Preferences in lipid solubilization by the styrene-maleic acid copolymer in membranes of mixed lipid composition. (*manuscript in preparation*)

8. ***Iyer, A.**,*Roeters, S., Woutersen, S., Claessens, M. M. A. E and Subramaniam, V. The C-terminus of alpha synuclein plays a major role in the fibril morphology. (*manuscript under preparation*) *equal authorship

9. *Kumar, S.,***Iyer, A**. and Swaminathan, R., Effect of macromolecular crowding by dextrans and Ficolls on the rate of acetylcholine esterase catalysis. (*manuscript under preparation*) *equal contribution

Accepted/Online:

10. **Iyer, A.**, Nils O. Petersen, Claessens, M. M. A. E, and Subramaniam, V. 2014. Amyloids of Alpha-Synuclein Affect the Structure and Dynamics of Supported Lipid Bilayers. Biophys J 106:2585-2594.

11. **Iyer, A.**, A. Chandra, and R. Swaminathan. 2014. Hydrolytic enzymes conjugated to quantum dots mostly retain whole catalytic activity. Biochim Biophys Acta 1840:2935–2943.

Acknowledgements

I called up my mom on that late Saturday night and said "Ma, My PhD thesis is ready!" I got a reply "So, did you know that our Prime Minister has started a new pension scheme?" I smiled. If you are a PhD already, you know how exactly WHY. Those long hours of (last-minute) experiments, frustrations of irreproducible experiments, further frustrations on the reproducibility of the irreproducible experiments, the glimmer of hope in a seemingly simple experiment, the unparalleled joy of manuscript submissions/acceptances and of course the curses accompanying the manuscript rejections; all seemed to be colligating like pieces of a kaleidoscope now. My thoughts are probably recapitulated better in the immortal words of the mortal Taylor Swift "*I don't know about you, but I am feeling 22*".

I have had the privilege of having two great supervisors who have; in simple words literally carved the researcher in me and keep at it persistently. These few words will do very little justice to the role they have played. I have learnt patience and consistence from you, Vinod a.k.a The BIG BOSS, who hired me in spite of the glaring mistake in my PhD motivation letter (*which a very select few know of*). Vinod, I have learnt from you not only the very basics of scientific approach but also those witty one-liners that have kind of ingrained in me. I have enjoyed and will always remember: scientific/non-scientific discussions with you leading to your proverbial circular head-nods culminating with a "Look, adi…" and going to completely unrelated photonics conferences (which, I still maintain were useful). Mireille, if my PhD was a Harry Potter movie, you were like Sirius Black to me. I have learnt so much from you when it comes to approaching science. I am still amazed by the clarity of thought I have been left with after numerous discussions with you. Your ability to separate the scientific and layman thinking is something I truly admire and hope to learn it too. I have bugged you with my manuscripts/presentations/posters/abstracts persistently (even while you were on holidays) and you have reciprocated the same way…with red lines in the corrected manuscripts…persistently.

I owe a lot to my parents for their undying unconditional love and who thought that I was going to cure Parkinson's disease when I got the PhD position (my mom still does). My sister Chitra and her hubby Karthik kept motivating me in tough times. My friends, who have most likely skipped the text of this thesis up till now and opened this section first are probably gloating/complaining mentally about who got the most ink-space in my acknowledgments. Prince, Naveen and Kartikey were, have and will be the best BHASADI's ever. The weekend getaways to east european countries, the homemade dinners, the unspoken jealousy when either of us published an article and of course the sporadic (regular) visits to Holland Casino (HC, as we fondly call it). Omkar a.k.a SIR and Himanshu a.k.a Netaji who were close colleagues in the two years I spent in the University of Twente have been like elder brothers to me. Guiding me right from day one; from *kortings, koopzondags* to *kruidnotens;* everywhere. Chandu bhaiiya, I owe my experimental chamber building skills to you!

Martin Stöckl, your unconditional help in educating me on lipids is something I will remember life-long. I wish we get to do some science together in future. My friends in Twente including Ravi, Deepak, Merel, Mitava, Aditi, Harshita, Somnath, Aditya Tushar and Yashaswini; you guys made sure conversations were never boring. Jasper, with you, discussing science has never been more illuminating. The best moments I have had in Twente and will always cherish were of course in our office ZH165; where the sun (lights) never set. My office buddies: Slav, Burcu and Himanshu; it is impossible to put a word for the times we have spent together in that office. If you ask me still to put one word, it would be surely "*supercalifragilisticexpialidocious*". Those Bulgarian-Turkish debates are something I still remember. BTW, the jury is still out on who's better ;). Nana, I thank you for all fun we've had at conferences and for berating me for forgetting to include you in this section. You will get your Porsche soon. All my colleagues at the Nanobiophysics group including Harmen, Senthil, Maurice, Arshdeep, Kristian, Amin, Federica, Maurice, Martijn, Jord, Niels and Pim made sure there was something for discussing during coffee or beer. The unconditional administrative and technical support of Sylvia, Robert, Kees, Kirsten, Yvonne, Wilma, Irene played a big role in this thesis. Sylvia, talking to you always made me happy no matter whatever the media: personally, via email or Whatsapp! Nathalie, you deserve a special mention since you were not only a good friend/colleague but my predominant protein-source as well. You stood by me during all this time whether I was high or low, in UT or AMOLF. It has been great working with you!

Moving to AMOLF halfway through my PhD was a decision I am glad I made. I had a great time in AMOLF. I met a different brand of researchers in AMOLF with radically different ways in scientific approaches. My first colleagues Theresa, Vova, Niels, Lara, Leffert and Galja were simply great and our coffee discussions are something I still cherish. Yuval and Agata, discussions with you have always given me a different perspective and always an after-thought, which is very unique and special. I think the best way to discuss your contribution to this thesis is to argue it over coffee or a beer! You guys have been close friends and I hope this goes a long way. Galja, you have been around unconditionally every time I needed coffee and your ability to laugh is something unique you have. Anders, I promise to be the life member of the "Elite coffee club"! Every other Bio-softie including Bart, Viktoria, Marjolein, Celine, Federica, Mick and Cristina has been a tremendous source of motivation and help; scientifically/technically/logically and all the other "allys". Gijsje, I thank you specially for adopting me into your group when Vinod had to leave for VU.

The Photonics/Solar cell crowd at AMOLF including Benjamin, Parisa, Sander and Cristina are people with whom I've shared a lot of laughs and frustrations. The sporadic interactions with "Tans-ies", "Rein-ies" and "Jeroen-ies" at AMOLF made me feel home after the move to AMOLF. It has been really a wonderful journey with you guys. Steven, Sergey, Roeland,

Konrad, Juan, Olga, Bob, Sergey, Fatemeh and Michiel: collaborating has been great and I look forward for more. This work would not have reached here without the unconditional administrative and technical support of all the excellent staff in ICT, HR department, secretaries and the technical workshop at AMOLF. Petra, thank you so much for making the transition to AMOLF smooth and helping me in the Dutch summary. Sabine, I thank you for all the help in administrative stuff at AMOLF. I owe a lot of my Dutch language speaking skills to the blackjack card dealers in HC and of course to Hinco Schoenmaker at AMOLF.

Marija and Praveen, discussing science with you guys has never been so exciting with you guys. I wish we have awesome collaborations in future! Saptaswa, I can honestly say I have never laughed so much in my life as much I did during the CHAINS conference in last December! Marie, Lotta, Cheryl, Lars, Sunny, Alex and Eli are some close buddies with whom I share a bond called *That-night-at-Marie's*. My M.Tech buddies; Samir, Himanshu, Anup, Rajesh, Neha, Deblina, Debatosh and Kapil have always made sure that I never flew too high. Kapil, I am indebted to you for your help in providing R scripts for data processing which saved me a lot of time. Finally, I would like to take this opportunity to thank the unacknowledged majority of people that have "karmically" helped me reach here.

As I have been often reminded of my pathological condition of verbal diarrhea, I am pretty sure I have exceeded the word limit for the acknowledgement section. If there isn't one yet, there will surely be one for future PhDs graduating from the University of Twente. After all, if biophysicists aren't trend-setters, who are? With this last textual bit, I shall be no longer be someone who is allowed to mess up experiments, someone who is allowed to fixate on side issues or someone who is allowed to work at his own pace. I am glad…

Aditya Iyer

6th April 2016

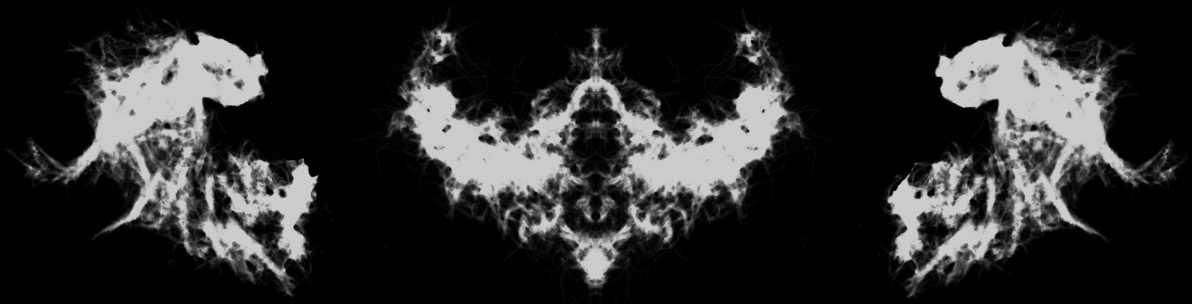

ISBN 9789036540865